New Insights on Rhyolitic and Mixed Rhyolitic-Basaltic Magmatism and Volcanism at Krafla Central Volcano, Iceland

Shane M. Rooyakkers

Department of Earth and Planetary Sciences

McGill University

Montreal

February 2020

© Shane Rooyakkers 2020

ABSTRACT

This work documents processes of rhyolitic and mixed rhyolitic-basaltic magmatism and volcanism at Krafla central volcano, northeast Iceland, from two perspectives: 1) field studies of the mixed basalt-rhyolite Halarauður eruption associated with major caldera collapse at ca. 110 ka, and 2) petrologic and geochemical studies of erupted products from the Halarauður event and six additional rhyolitic or mixed rhyolitic-basaltic eruptions, spanning the full ca. 190 k.y. history of rhyolitic volcanism at Krafla.

The Halarauður eruption is the largest known eruption from the Krafla system. Its deposits, exposed up to ~7 km from the present-day caldera and originally interpreted as welded fall deposits, are here reinterpreted as the proximal remnants of a once expansive ignimbrite sheet that was largely eroded away during the last glaciation. A total erupted magma volume of 7 ± 6 km^3 is proposed based on reconstruction of the original distribution of outflow deposits, assuming a range of dispersal scenarios and erosion rates. Poor preservation and large uncertainties in volume estimates highlight the inherent challenges of studying ignimbrite eruptions in Iceland, and resultant biases in records of its Quaternary explosive volcanism.

Three major stratigraphic units, H1-H3, are recognised in a revised eruptive stratigraphy for the Halarauður event. Whole-rock compositions of the extremely crystal-poor (<1-2 modal% macrocrysts) juvenile products span a continuous range between 50.0 - 74.6 wt% SiO$_2$, reflecting mixing of rhyolite with underplating basalt. Evolved compositions (andesite to rhyolite) and marked compositional heterogeneity are typical of early-erupted units (H1 and lower to middle parts of H2), which tapped the upper, poorly mixed regions of the chamber, while later-erupted deposits (upper H2 through H3), tapped from denser hybrid magma and underplating basalt from lower levels, grade smoothly upward from andesite to basalt. Unusual lithofacies characteristics of the deposits, including the only spatter-rich ignimbrite deposits described in Iceland, and an exceptionally rare welded basaltic ignimbrite unit with only one known equivalent globally, reveal complex eruptive dynamics involving interplay between caldera collapse and eruption style. The eruption began with opening of ring fracture vents and rapid column collapse, emplacing small-volume, valley-ponded pumice- and spatter-bearing lithic breccias (unit H1). As collapse progressed, variably hybridised and degassed magma from deeper levels was squeezed through a developing ring fault conduit system. Spatial heterogeneities in ascent rates and outgassing through this variably dilated fault system caused coeval formation of collapsing plumes and spatter fountains at separate vents. Spatter was entrained into flows from the more explosive vents, which deposited proximal spatter agglomerates and more distal spatter-bearing ignimbrite (unit H2). Overlying very strongly welded (lava-like) ignimbrite deposits (H3; basaltic andesite to basalt) reflect uncharacteristically high mass flux venting of mafic magma from deep levels of the chamber, which was squeezed through a mature and dilated ring fault system by the

subsiding roof block. The explosive venting of large volumes of basalt in the Halarauður event contrasts with the large-volume effusive basaltic eruptions typical of Iceland, highlighting the explosive potential of large basaltic bodies if they encounter rhyolite.

Petrologic studies of Halarauður products provide evidence for a major and rapid destabilisation of the Krafla magmatic system after accumulation and storage of large magma bodies at shallow depth. Discrete macrocryst populations with very subtle or no zoning and in equilibrium with endmember whole-rock compositions (e.g., An_{60-76} plagioclase and Mg# 68-75 augite native to the endmember basalt) record separate storage of large, well-mixed, melt-dominant bodies of evolved basalt (50.0 wt% SiO_2, 5.0 wt% MgO; Mg# 38) and high-silica rhyolite (74.6 wt% SiO_2) under stable P-T conditions prior to their interaction. Geobarometry and MELTS modeling constrain storage of the evolved basalt to <1-1.5 kbar (~4-6 km depth), overlapping with the presently active basaltic chamber or storage zone beneath the caldera. A second population of calcic plagioclase (cores An_{81-91}) associated with primitive basaltic glass selvages of Mg# 49-55 occurs sparsely in the volumetrically minor H1 deposits and very rarely in later-erupted units, implying interaction of a second, small batch of more primitive basalt with the upper parts of the Halarauður system. Crystals from all three magmas show little or no evidence for dissolution or re-equilibration with surrounding hybrid melt; application of experimentally measured crystal growth rates to narrow (<100 μm) plagioclase overgrowth rims imply pre-eruptive mixing timescales with rhyolite of <15 hours for the primitive basalt, and at most two months but possibly as short as several tens of hours for the evolved basalt. Rapid destabilisation of the magmatic system and ascent of multiple basaltic magmas from depth likely reflect a major rifting episode in the Krafla system. Large bodies of crystal-poor magma may thus be stored at shallow depth in Iceland's rift zones, but can be rapidly mobilised for eruption.

Other Krafla eruptions involving rhyolite vary widely in size and style, but all rhyolites have high-silica compositions (73.7-75.8 wt% SiO_2) and similar trace element systematics. Macrocrysts (plagioclase ± augite ± pigeonite ± orthopyroxene ± fayalite ± titanomagnetite) in all rhyolites (excluding one aphyric unit) principally record crystal growth from evolved melts. Most crystal cores have compositions appropriate for equilibrium with melts equivalent in composition to their respective whole-rock, and basalt-derived crystals are rare, although some crystals derive from less evolved, co-genetic, intermediate or silicic magmas. Evidence for late-stage fractional crystallisation from mineral compositions and zoning patterns are not consistent with generation of Krafla high-silica rhyolites in a single step by partial melting of hydrothermally altered basalts. Additionally, comparisons with experimental work reveal difficulties in producing high-silica rhyolite compositions by partial melting alone, and trace element models for basalt partial melting provide a poor fit to the observed compositions. Instead, MELTS trace element models suggest a dominant role for assimilation-fractional crystallisation (AFC) in generating Krafla rhyolites. We

thus propose that the absence of intermediate erupted compositions reflects the presence of uneruptible intermediate mush bodies at depth.

Parallel REE patterns among the ca. 110 ka Halarauður rhyolite and all younger units imply that the overall processes that produce Krafla rhyolites have been similar across much of the system's lifespan. The ca. 190 ka oldest (un-named) rhyolite is distinct from all younger units with respect to both REE patterns and incompatible element ratios, reflecting a distinct source and possibly deeper crustal melting prior to establishment of a large and long-lived shallow mafic system. By contrast, similar chemistries and crystal populations reveal a common parentage for three rhyolite ridges (each ~0.15 km^3) erupted subglacially around the caldera margins at ca. 65 ka. More recent eruptions have been smaller in volume (each $\leq$0.02 km^3) and focused in the central-eastern region of the caldera. Products from this period are either aphyric, reflecting possible superheating by adjacent basalt, or show textual evidence for basalt-rhyolite interaction, implying a triggering role for basalt in recent events. Basalt-rhyolite interaction in the C.E. 1724 Víti eruption, which formed a small maar crater in the central caldera region, were syn-eruptive and too rapid for crystals to record. Compositional overlap between Víti products and quenched rhyolite magma recently sampled from ~2.1 km depth in the IDDP-1 well suggests that the IDDP-1 rhyolite is either the same magma body that was tapped in the Víti event, or a separate body derived from the same source. Rapid basalt triggering of the Víti eruption raises the possibility that the IDDP-1 body could produce a similar explosive event if intercepted by ascending basalt.

RÉSUMÉ

Le but de ce travail est de documenter des processus en lien avec le magmatisme et le volcanisme rhyolitique et rhyolitique-basaltique du volcan central de Krafla, au nord-est de l'Islande, et est abordé sous deux angles: 1) l'étude sur le terrain de l'éruption mixte basalte-rhyolite Halarauður associée à un effondrement majeur de la caldeira à ca. 110 ka, et 2) l'étude pétrologique et géochimique des produits d'éruption de l'événement de Halarauður et six autres éruptions rhyolitiques ou mixtes rhyolitiques-basaltiques, couvrant la totalité de l'histoire du volcanisme rhyolitique à Krafla sur la période de ca. 190 ka.

L'éruption de Halarauður est la plus grande éruption connue du système de Krafla. Ses dépôts, exposés jusqu'à environ 7 km de la caldeira actuelle et interprétés à l'origine comme des dépôts soudés de retombée volcanique, sont ici réinterprétés comme les restes proximaux d'une couche d'ignimbrite qui devait autrefois être plus large et qui a été en grande partie érodée lors de la dernière glaciation. Le volume total de l'éruption magmatique proposé est de 7 ± 6 km3 sur la base de la reconstruction de la distribution d'origine des dépôts de coulées, et en supposant plusieurs scénarios de dispersion et de taux d'érosion. Une mauvaise conservation et de grandes incertitudes dans les estimations du volume mettent en évidence les défis inhérents à l'étude des éruptions d'ignimbrites en Islande et les biais qui en résultent dans les enregistrements de son volcanisme explosif quaternaire.

Trois grandes unités stratigraphiques, H1-H3, sont reconnues dans une stratigraphie éruptive révisée pour l'événement de Halarauður. Les compositions roche totale des produits juvéniles extrêmement pauvres en cristaux (<1-2% de macrocristaux modaux) couvrent une plage continue entre 50.0 – 74.6 wt% SiO2, reflétant le mélange de la rhyolite avec le basalte sous-jacent. Les compositions plus évoluées (andésite à rhyolite) et une hétérogénéité de composition marquée, sont typiques des unités d'éruption précoce (H1 et parties inférieures à moyennes de H2), et proviennent des régions supérieures mal mélangées de la chambre magmatique, tandis que les dépôts des éruptions ultérieures (H2 supérieur vers H3), proviennent d'un magma hybride plus dense et de basalte sous-jacent à des niveaux inférieurs, évoluant graduellement de l'andésite au basalte. Les caractéristiques inhabituelles des lithofaciès des dépôts, y compris les dépôts d'ignimbrite riches en débris décrits en Islande, ainsi qu'une unité soudée d'ignimbrite basaltique exceptionnellement rare avec un seul équivalent connu dans le monde, révèlent une dynamique éruptive complexe impliquant une interaction entre l'effondrement de la caldeira et le style d'éruption. L'éruption a commencé avec l'ouverture de cheminées associées à des failles en anneau et l'effondrement rapide de la colonne, mettant en place de petites quantités de brèches lithiques contenant de la pierre ponce et des projections de débris (unité H1). Au fur et à mesure de la progression de l'effondrement, du magma

variablement hybride et dégazé provenant de niveaux plus profonds est comprimé par un système de conduits de faille en anneau en développement. Les hétérogénéités spatiales des taux de remontée et du dégazage à travers ce système de failles à dilatation variable ont provoqué la formation contemporaine de panaches d'effondrement et de fontaines à projection sur des cheminées différentes. Les débris de projection ont été entraînés par les écoulements des évents les plus explosifs, qui déposaient des agglomérats de débris proximaux et des ignimbrites plus distales contenant des débris (unité H2). Les dépôts d'ignimbrites superposés très soudés (de type lave) (H3; andésite basaltique à basalte) reflètent un flux de masse inhabituellement élevé évacuant le magma mafique des niveaux profonds de la chambre, lui-même comprimé entre un système de failles en anneau matures et dilatées, et par le bloc de toit en train de s'affaisser. Le relâchement explosif de grands volumes de basalte dans l'événement de Halarauður contraste avec les éruptions basaltiques effusives de grand volume typiques de l'Islande, mettant en évidence le potentiel explosif des grands corps basaltiques s'ils rencontrent de la rhyolite.

L'étude pétrologique des produits de l'Halarauður fournit des preuves d'une déstabilisation majeure et rapide du système magmatique de Krafla après l'accumulation et le stockage de grands corps magmatiques à faible profondeur. Les populations discrètes de macrocristaux avec un zonage très léger ou inexistant et en équilibre avec les compositions roche totale des endmembers (par exemple, le plagioclase An60-76 et l'augite Mg# 68-75 originaire du endmember du basalte) enregistrent un stockage séparé de produits de fusion massifs et bien mélangées de basalte évolué (50.0% en poids de SiO_2, 5.0% en poids de MgO; Mg# 38) et de rhyolite à haute teneur en silice (74.6% en poids de SiO_2) dans des conditions PT stables avant leur interaction. La géobarométrie et la modélisation en utilisant MELTS contraignent le stockage du basalte évolué à <1-1,5 kbar (~ 4-6 km de profondeur), chevauchant la chambre basaltique ou la zone de stockage actuellement active sous la caldeira. Une deuxième population de plagioclases calciques (cœurs An81-91) associée à des bordures de verre basaltique primitif de Mg# 49-55 se trouve clairsemée dans les dépôts H1 de volume très faible et très rarement dans des unités à éruption tardive, ce qui implique l'interaction d'une deuxième batch de basalte plus primitif avec les parties supérieures du système de l'Halarauður. Les cristaux des trois magmas montrent peu ou pas de preuves de dissolution ou de rééquilibrage avec le produit de fusion hybride environnant ; l'application des taux de croissance cristalline mesurés expérimentalement pour réduire la croissance des bordures des plagioclases (<100 μm) implique des échelles de temps de mélange pré-éruptif avec de la rhyolite <15 heures pour le basalte primitif, et un maximum de plusieurs dizaines d'heures à deux mois pour le basalte évolué. La déstabilisation rapide du système magmatique et l'ascension de plusieurs magmas basaltiques en profondeur reflètent probablement un épisode majeur de rifting dans le système de Krafla. Des grands corps magmatiques pauvres en cristaux peuvent ainsi être stockés à faible profondeur dans les zones du rift islandais, mais peuvent être rapidement mobilisés pour une éruption.

D'autres éruptions de Krafla impliquant de la rhyolite varient considérablement en taille et en style, mais toutes les rhyolites ont des compositions à haute teneur en silice (73.7 à 75.8 wt% SiO2) et une systématique en éléments traces similaire. Les macrocristaux (plagioclase ± augite ± pigeonite ± orthopyroxene ± fayalite ± titanomagnetite) dans toutes les rhyolites (à l'exception d'une unité aphyrique) enregistrent principalement la croissance cristalline à partir du produit de fusion évolué. La plupart des cœurs cristallins ont des compositions adéquates pour atteindre l'équilibre avec un magma fondu équivalent en composition à leur roche totale respective, et les cristaux dérivés des basaltes sont rares, bien certains cristaux proviennent de magmas intermédiaires ou siliciques co-génétiques moins évolués. Des évidences d'une cristallisation fractionnée tardive provenant de la composition ainsi que du « zoning » des minéraux ne sont pas consistant avec la génération de rhyolites à haute teneur en silice à Krafla, en une seule étape et par fusion partielle des roches basaltiques altérées. De plus, les comparaisons avec les travaux expérimentaux révèlent des difficultés à produire par fusion partielle seule des compositions rhyolitiques à haute teneur en silice, et les modèles d'éléments traces pour la fusion partielle de basalte ne correspondent pas exactement aux compositions observées. Au lieu de cela, les modèles d'éléments traces MELTS suggèrent un rôle dominant de l'assimilation-cristallisation fractionnée (AFC) dans la génération de rhyolites de Krafla. Nous proposons donc que l'absence de compositions volcaniques intermédiaires reflète la présence en profondeur de corps de roches fondues de compositions intermédiaires non éruptibles.

Les patterns parallèles de REE de la rhyolite de ca. 110 ka de Halarauður et de toutes les unités plus jeunes impliquent que les processus globaux qui produisent les rhyolites de Krafla ont été similaires sur une grande partie de la durée de vie du système. La plus ancienne rhyolite de ca. 190 ka (non nommée) est distincte de toutes les unités plus jeunes en ce qui concerne à la fois les patterns de REE et les ratios d'éléments incompatibles, reflétant une source distincte et une fusion crustale probablement plus profonde avant la mise en place d'un système mafique peu profond de grande taille et à longue durée de vie. Par contraste, des compositions chimiques et des populations de cristaux similaires révèlent une parenté commune pour trois des crêtes de rhyolite (chacune ~ 0,15 km3) qui sont entrées en éruption sous le glacier autour des marges de la caldeira à ca. 65 ka. Les éruptions plus récentes ont été de plus petit volume (chacune <0.02 km3) et concentrées dans la région centre-est de la caldeira. Les produits de cette période sont soit aphyriques, reflétant une surchauffe possible par le basalte adjacent, soit présentent des preuves d'une interaction basalte-rhyolite, impliquant que le basalte a eu un rôle déclencheur lors d'événements récents. L'interaction basalte-rhyolite dans l'éruption de C.E.1724 de Víti, qui a formé un petit cratère de type Maar dans la région centrale de la caldeira était syn-éruptive et trop rapide pour que les cristaux enregistrent l'évènement. Le chevauchement de la composition entre les produits d'éruption de Víti ainsi que le verre magmatique rhyolitique récemment échantillonné à une profondeur d'environ 2.1 km dans le puits IDDP-1, suggèrent que la rhyolite IDDP-1est soit le même corps magmatique qui a été prélevé de

l'événement de Víti, soit un corps distinct dérivée de la même source. Le déclenchement rapide de l'éruption basaltique de Víti soulève la possibilité que le corps magmatique IDDP-1 puisse produire un événement explosif similaire s'il est intercepté par un basalte ascendant.

ACKNOWLEDGEMENTS

If you are reading this, I survived…

…five Montreal winters.

First, an enormous thank you to the most incredible supervisor, Dr. John Stix. John, I literally cannot thank you enough for your amazing support, mentorship and humour. Thank you for giving me every possible opportunity, for always going the extra mile for your students and putting our needs before your own, and for trusting me with the freedom to take this project in the directions that interested me most. Your seemingly limitless enthusiasm is truly infectious, and it's honestly impossible not to feel excited and motivated after a chat with you. You have taught me so much, not just about volcanoes and doing science, but also about getting the best out of people. Thank you.

Kim Berlo's contributions as secondary supervisor are acknowledged. I have been lucky during this work to have a large and talented group of collaborators from whom I could draw ideas and technical know-how. Thank you to my co-authors Simon Barker, Bruce Charlier, Rachel Hampton, Daniele Morgavi, Diego Perugini, Maurizio Petrelli, and Francesco Vetere for your important contributions to this work. Thank you also to Daniele, Diego, Maurizio and Francesco for making me feel so welcome in Perugia – those three months were one of the highlights of my Ph.D.

Many others helped me along the way. Thank you to Ásgrímur Guðmundsson and Kristján Sæmundsson for extremely valuable insights on the geology of Krafla. The invaluable technical assistance of Lang Shi, who helped with microprobe analyses and electron microscopy, was called upon many times – thank you, Lang. Thanks also to: David Martineau, Carla Gonzalez, Clara Waelkens and Frances Gray for field assistance; Hugh Tuffen for helpful discussions and field insights; the McGill Volcano Group (+ Becky!) for fun and camaraderie; Stephan Kolzenburg, Becky Paisley, Monika Rusiecka and Clara Waelkens for insightful discussions about all things volcanic that helped to bring many ideas together; Marion Saby for translating the abstract; Bill Minarik for tips and guidance in advisory meetings; and to my former M.Sc. supervisor, Colin Wilson, who has continued to be a helpful source of knowledge and advice.

This work would not have been possible without the incredible support of Landsvirkjun, the National Power Company of Iceland, who generously hosted us at the Krafla Power Station during our four field campaigns. Thank you especially to Sigurður Markússon for overseeing the logistics of our stays, and to Ásgrímur Guðmundsson for arranging access to core samples.

During this work I was fortunate to receive financial support from Robert Wares and Eric Mountjoy fellowships, and a GEOTOP scholarship. My sincere thanks to the benefactors, Robert Wares and Anita Mountjoy, and to GEOTOP – your support is extremely appreciated. This work was funded by research grants to John Stix and Kim Berlo.

Finally, and most importantly, many thanks to my amazing friends and family for all the love, support and fun over these Ph.D. years and beyond. Mum and Dad - an extra special thanks for everything you've done for me, and for encouraging curiosity in a little boy who asked a lot of questions. Maybe now I'll go find a "real" job?

TABLE OF CONTENTS

3. GENERATION, ASSEMBLY AND ERUPTION OF KRAFLA RHYOLITES: INSIGHTS FROM PETROLOGY

4. UNRAVELLING PRE- AND SYN-ERUPTIVE PROCESSES IN A LARGE MIXED BASALT-RHYOLITE ERUPTION: A PETROLOGIC STUDY OF THE HALARAUÐUR IGNIMBRITE

LIST OF FIGURES

LIST OF TABLES

PUBLICATIONS ARISING FROM THIS THESIS

Journal Articles

Rooyakkers, S. M., Stix, J., Berlo, K., and Barker, S. J., 2020, Emplacement of unusual rhyolitic to basaltic ignimbrites during collapse of a basalt-dominated caldera: The Halarauður eruption, Krafla (Iceland): Geological Society of America Bulletin, (in press).

Conference Abstracts

Rooyakkers, S. M., Stix, J., Berlo, K., and Barker, S. J., 2019, The Halarauður eruption, Krafla, Iceland: A rare example of ignimbrite formation at a basalt-dominated caldera. Oral presentation at IUGG General Assembly, Montréal, Québec, Canada, July 8-18.

Rooyakkers, S. M., Stix, J., Berlo, K., and Barker, S. J., 2018, Spatter-rich and lava-like ignimbrites of the Halarauður eruption, Krafla (Iceland): An unusually violent eruption from a basalt-dominated caldera. Poster presented at AGU Fall Meeting, Washington, D.C., USA, December 11-15.

Rooyakkers, S. M., Stix, J., Berlo, K., Barker, S. J., and Tuffen, H., 2017, Mafic spatter-rich and lava-like welded ignimbrites linked with collapse of a basaltic caldera: The Halarauður eruption, Krafla, Iceland. Poster presented at AGU Fall Meeting, New Orleans, Louisiana, USA, December 10-14.

1. Introduction

1.1. MOTIVATION FOR RESEARCH

In 2008, silicic glass ranging in composition from dacite to rhyolite was found among cuttings from the bottom of well KJ-39 (2571 m depth), drilled by Landsvirkjun (the National Power Company of Iceland) for geothermal exploration in the central region of Krafla caldera in northeast Iceland, indicating that an evolved magma body or zone of partial melt was intercepted during drilling (Mortensen et al., 2010). The following year, well 1 of the Iceland Deep Drilling Project (IDDP), a government-industry consortium exploring the possibility of exploiting supercritical hydrothermal fluids for energy production (Friðleifsson and Elders, 2005; Friðleifsson et al., 2014), was drilled vertically approximately 1 km north of the KJ-39 wellhead (approximately 2 km northwest of the site where KJ-39 encountered melt in the eastward-slanted well), and unexpectedly intersected compositionally distinct molten rhyolite at 2104 m depth (Elders et al., 2011; Zierenberg et al., 2013; Mortensen et al., 2014; Schiffman et al., 2014). These occurrences mark the first times anywhere in the world that rhyolitic magma or melt has been encountered during drilling.

The presence of rhyolite magma or melt at shallow depths beneath the caldera is somewhat unexpected given the predominance of basalt at Krafla, and the deeper level ($\geq$3 km) at which magma bodies within the caldera had previously been detected (Einarsson, 1978), and thus raises important questions regarding its origin, volume, characteristics, and potential eruptibility. It also presents an unprecedented opportunity to study both the presence of molten rhyolite at shallow depths and the interface between the magmatic and hydrothermal systems *in situ*. In response, plans are currently in development to drill again into the IDDP-1 rhyolite body and develop the

Krafla Magma Testbed (KMT; http://kmt.is), a multi-borehole facility designed for scientific exploration and engineering tests at the magma-hydrothermal interface (Eichelberger et al., 2019).

Despite current interest in the present-day system, past rhyolitic magmatism and volcanism at Krafla have received limited attention. Petrologic studies have outlined the broad chemical characteristics of the various Krafla rhyolites and offered contrasting views on their petrogenesis, advocating for an origin either by fractional crystallisation of mantle-derived basalt accompanied by crustal assimilation (Nicholson, 1990; Nicholson et al., 1991), or by low-degree partial melting of altered basaltic crust around the margins of basaltic magma bodies (Jónasson, 1994, 2007). Further detailed petrologic studies are needed to resolve the controversial origin of Krafla rhyolites and constrain the dynamics and timescales of their generation, assembly, storage, and mobilisation for eruption. Additionally, the style and dynamics of past rhyolitic eruptions at Krafla are poorly understood. Subglacial emplacement of the Hrafntinnuhryggur rhyolite ridge in the southeastern caldera region was studied in detail by Tuffen and Castro (2009), but the large mixed basalt-rhyolite Halarauður eruption linked with formation of the caldera has been studied only in outline (Calderone et al., 1990), and the dynamics of other rhyolitic eruptions at Krafla have not been investigated. This thesis research is motivated by the need to fill such gaps in order to provide context for understanding the modern system, including the presently active magma or melt bodies beneath the caldera, and for assessing the hazards posed by possible future rhyolitic eruptions.

1.2. THESIS OVERVIEW AND STRUCTURE

The central purpose of this thesis is to expand understanding of rhyolitic magmatism and volcanism at Krafla. Some key questions that will be addressed include:

1. What were the style and dynamics of the large, partially rhyolitic eruption linked by previous workers with formation of the Krafla caldera? How large was the event and what were the associated hazards?

2. What magmatic processes occurred in the build-up to this event and other rhyolitic eruptions at Krafla?

3. What insights can detailed microanalytical studies of minerals and glasses in erupted products offer into the processes of rhyolite petrogenesis at Krafla and similar Icelandic systems?

4. What role (if any) do mafic magmas play in mobilising rhyolitic magmas and/or triggering their eruptions at Krafla?

5. Is there a genetic relationship between any recently erupted rhyolites and the presently active rhyolitic magma or melt bodies?

These questions, and many others, are addressed in five interrelated chapters, structured around the central theme of understanding the processes and dynamics of rhyolitic magmatism at Krafla from petrogenesis to eruption. Chapter 2 has been published as Rooyakkers et al. (2020), and the only changes to the published work in the thesis are for the sake of formatting consistency. Chapters 3 and 4 are written in the style of journal articles. Each chapter serves as a self-contained study, but all chapters are closely linked by the common theme of rhyolitic magmatism and volcanism at Krafla and commonly build on the findings of preceding chapters.

Chapter 1 introduces the motivation for this research and summarises the present state of knowledge. We introduce the Krafla volcanic system and its place within the unique tectonic and volcanic setting of Iceland. Previous ideas around rhyolitic magmatism and volcanism at Krafla

and elsewhere in Iceland, on which this thesis builds, are outlined, and we highlight gaps in understanding that this research aims to address.

Chapter 2 presents a detailed field-based study of the mixed basalt-rhyolite Halarauður eruption, the largest known eruption from the Krafla system. We explore the link between this event and major caldera collapse, present a new eruptive stratigraphy, and re-evaluate previous interpretations of the style and volume of the event. Our findings highlight the major hazards associated with large rhyolitic eruptions at Krafla and similar systems, but also the inherent difficulties in reconstructing the histories of such events in frequently glaciated areas such as Iceland and the resultant biases in the geological record of explosive volcanism.

Chapter 3 takes a broader standpoint, examining the subvolcanic processes that ultimately drive rhyolitic eruptions. We present a petrologic study of rhyolites from seven eruptions spanning the full history of rhyolitic volcanism at Krafla, with particular focus on detailed microanalysis of minerals, melt inclusions and matrix glasses. A large new petrologic dataset offers a wealth of new insights on the processes and dynamics of rhyolite generation, storage and mobilisation in Icelandic rift zones.

Chapter 4 returns to the Halarauður eruption, exploring the subvolcanic processes that occurred in the build-up to, and during, this major event. New whole-rock and crystal-chemical data are linked to the stratigraphic framework outlined in Chapter 2, allowing magmatic interactions in the system to be traced through time and linked with progression of the eruption. The origin of the Halarauður magmas, pre-eruptive configuration of the magmatic system, and timescales of basalt-rhyolite interactions are explored.

Chapter 5 integrates and summarises the findings of this thesis research. We revisit some of the key questions raised in Chapter 1, and identify some areas ripe for future research.

1.3. TECTONICS AND GEOLOGY OF ICELAND

1.3.1. Tectonic Setting and Neovolcanic Zones

Iceland is the subaerial portion of the Iceland Basalt Plateau, a ~350,000 km^2 region of thickened oceanic crust and anomalous topography that rises >3000 m above the abyssal floor of the North Atlantic Ocean (e.g., Gudmundsson, 2000; Thordarson and Larsen, 2007, and references therein). The plateau is transected by the Mid-Atlantic ridge system, marking the boundary between the North American and Eurasian plates, and its formation is widely attributed to the anomalously high magmatic flux resulting from interaction between the spreading ridge and a deep-seated mantle plume over the last ~24 Ma (e.g. Vink, 1984; White, 1997; Wolfe et al., 1997; Bijwaard and Spakman, 1999; Allen et al., 1999; Smallwood and White, 2002; Parnell-Turner et al., 2014). Because of its thickened crust, deformation across the plateau is more complex and more widely distributed than is typical for an oceanic plate boundary. Across Iceland, the boundary splits into a series of segments that are variably oblique to the relative plate spreading vector (Einarsson, 2008). Within each segment, extension occurs by diking and normal faulting, mainly in the fissure swarms of the volcanic systems, and any transcurrent component of plate motion is accommodated by strike-slip faulting on "bookshelf" faults that run transverse to that segment (Einarsson, 1991a, 2008). Due to westward drift of the ridge relative to the deep-seated roots of the mantle plume, successive eastward jumps of the rift systems have occurred occasionally through Iceland's history

(Einarsson, 1991a, 2008). Thorough reviews of Icelandic geodynamics are provided by Gudmundsson (2000), Sigmundsson (2006), Einarsson (2008), and Sigmundsson et al. (2020).

The modern surface expressions of Iceland's unique tectonic setting are its neovolcanic zones (Fig. 1.1), which are areas of active volcanism encompassing all products erupted during the Bruhnes magnetic epoch (<0.8 Ma; Jóhannesson and Sæmundsson, 1998). The neovolcanic zones are of two main types: axial rift zones and flank zones. The axial rift zones mark the trace of the divergent North American-Eurasian plate boundary across Iceland, and are characterised by tholeiitic volcanism and pronounced extensional tectonics (Jakobsson, 1972, 1979; Sæmundsson, 1974, 1978, 1979; Imsland, 1983). Spreading in the rift zones generally occurs in discrete episodes, concurrent with volcanic activity (e.g., Sigurdsson and Sparks, 1978; Björnsson et al., 1979; Brandsdóttir and Einarsson, 1979; Björnsson, 1985). Individual episodes, commonly referred to as "fires", are usually confined to a single volcanic system and can last for years to decades (Thordarson and Höskuldsson, 2008). Core structures of the rift zones are the West (WVZ) and North (NVZ) Volcanic Zones, which are linked by the Mid-Iceland Belt (MIB) and connected to the Mid-Atlantic Ridge system by the Tjörnes Fracture Zone (TFZ) in the north and the Reykjanes Volcanic Zone (RVZ) in the south (Thordarson and Larsen, 2007) (Fig. 1.1). The East Volcanic Zone (EVZ) is a propagating axial rift that will eventually take over from the waning WVZ (Fig. 1.1) (Thordarson and Larsen, 2007). The flank zones (also known as lateral rift zones), including the Snæfellsnes Volcanic Belt (SVB) in west Iceland and the Öræfi Volcanic Belt (ÖVB) to the east of the plate boundary in south Iceland, are areas of intraplate volcanism and poorly developed extensional tectonics (Fig. 1.1) (Sæmundsson, 1978, 1979; Thordarson and Larsen, 2007). Flank zone magmas are subalkaline (also called "transitional") to mildly alkaline in composition (Jakobsson, 1972, 1979; Imsland, 1983).
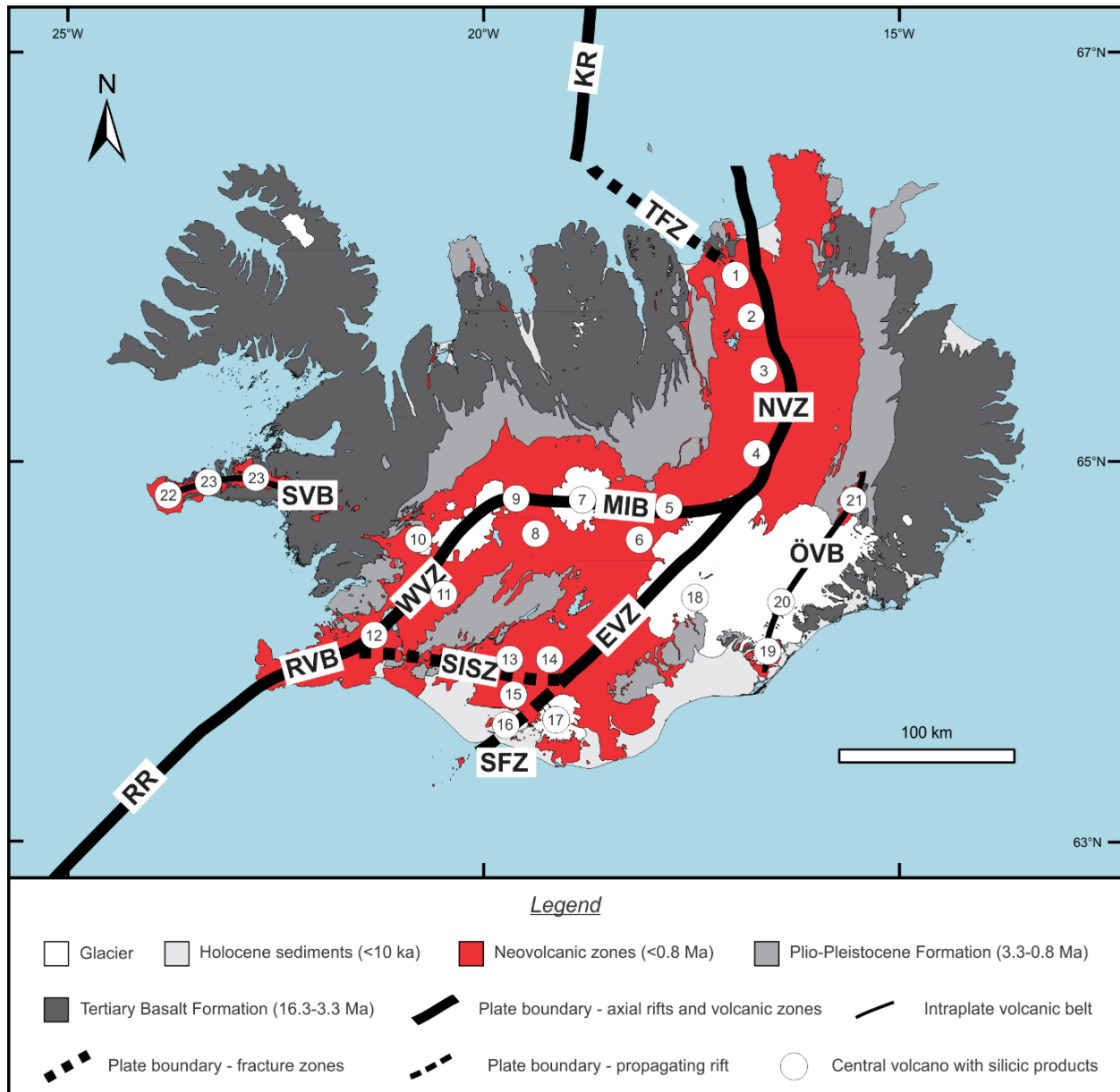
Figure 1.1. Map of Iceland showing the main elements of its geology and tectonics, including the neovolcanic zones and plate boundary. Major volcanic or tectonic features are labelled as follows: (RR) Reykjanes Ridge, (RVB) Reykjanes Volcanic Belt, (WVZ) West Volcanic Zone, (SISZ) South Iceland Seismic Zone, (SFZ) Southern Flank Zone, (EVZ) East Volcanic Zone, (MIB) Mid-Iceland Belt, (NVZ) North Volcanic Zone, (ÖVB) Öræfi Volcanic Belt, (SVB) Snæfellsnes Volcanic Belt, (TFZ) Tjörnes Fracture Zone, (KR) Kolbeinsey Ridge. Central volcanoes in the neovolcanic zones that have produced silicic products are labelled after Jónasson (2007): (1) Þeistareykir, (2) Krafla, (3) Fremri Námur, (4) Askja, (5) Vonarskarð, (6) Hágöng, (7) Hofsjökull, (8) Kerlingarfjöll, (9) Þjófadalir, (10) Prestahnúkur, (11) Geysir, (12) Hengill, (13) Hekla, (14) Torfajökull, (15) Tindfjallajökull, (16) Eyjafjallajökull, (17) Katla, (18) Þórðarhyrna, (19) Öræfajökull, (20) Esjufjöll, (21) Snæfell, (22) Snæfellsjökull, (23) Lýsuskarð, (24) Ljósufjöll. Map modified after Jóhannesson and Sæmundsson (1998) and Thordarson and Larsen (2007).

7
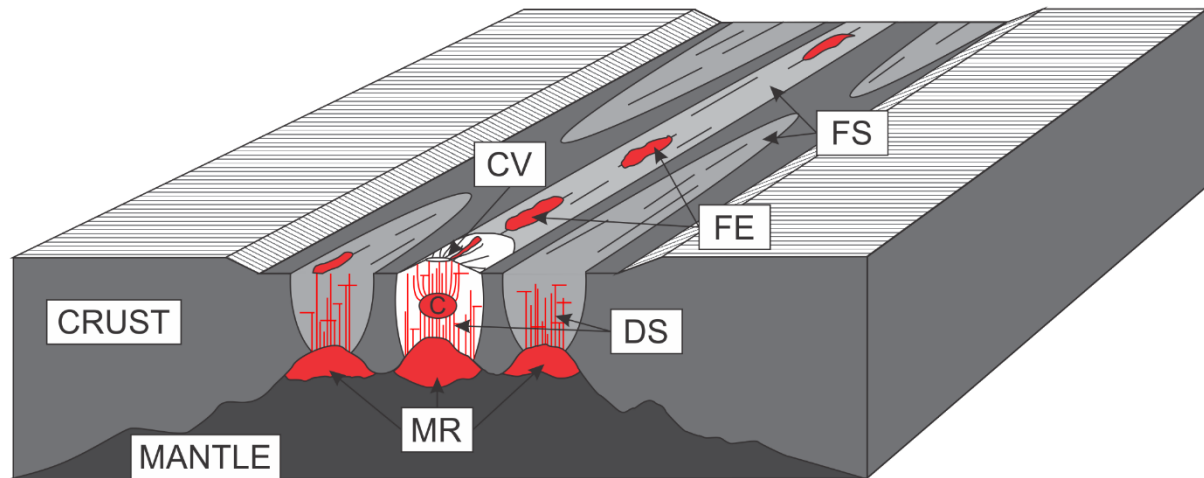
Figure 1.2. Schematic diagram showing key structures of Icelandic volcanic systems. MR = deep magma reservoir; DS = dike swarm; CV = central volcano; C = shallow crustal magma chamber; FS = fissure swarm; FE = fissure eruption. Adapted from Gudmundsson (1995) and Thordarson and Larsen (2007).

1.3.2. Icelandic Volcanism

With ≥20 eruptions per century and magma output rates of ≥5 km^3 per century, Iceland is one of the most active and productive regions of subaerial volcanism on Earth (Thordarson and Höskuldsson, 2008). Icelandic volcanism is notable for its extreme diversities in style and composition, encompassing almost all of the common terrestrial magma types and eruption styles (e.g., Thordarson and Larsen, 2007; Thordarson and Höskuldsson, 2008). Mafic compositions are dominant, representing 91% of the total postglacial output, while intermediate and silicic products comprise 6% and 3%, respectively (Thordarson and Höskuldsson, 2008).

Volcanism in Iceland is divided among so-called "volcanic systems" (Fig. 1.2), some 30 of which are considered active (Jóhannesson and Sæmundsson, 1998; Thordarson and Larsen, 2007; Thordarson and Höskuldsson, 2008). Each system is defined based on spatial groupings of eruption sites that are active within a geologically short window of time (typically 0.5-1 M.y.;

Gudmundsson, 2000) and linked by common tectonic, petrographic and geochemical characteristics (Sæmundsson, 1978, 1979; Jakobsson, 1979). Individual systems may consist of a fissure swarm, a central volcano, or both (Fig. 1.2). Fissure swarms are elongate zones of normal faults, open fissures and crater rows oriented perpendicular to the direction of crustal spreading. Individual fissure swarms are 5-20 km wide and up to >100 km in length (Gudmundsson, 1995; Einarsson, 2008). Magmatism along the fissure swarms is almost exclusively basaltic, and commonly fed laterally from the central volcanoes (e.g., Jakobsson, 1979; Björnsson et al., 1977). Central volcanoes form where magmatism becomes focused over time, forming an area of locally high topography and volcanic output (Jakobsson, 1979; Imsland, 1983). The central volcanoes usually host an active magma reservoir or reservoirs and high-temperature hydrothermal systems in the shallow crust (e.g., Gudmundsson, 1995; Kelley and Barton, 2008), and many have central collapse calderas (Sæmundsson, 1982; Gudmundsson, 1988, 1995, 2000). Significant volumes of silicic magmas are commonly produced by the central volcanoes (e.g., Walker, 1966). Gudmundsson (1995, 2000) provides thorough reviews of the development and architecture of the volcanic systems.

1.4. RHYOLITIC MAGMATISM AND VOLCANISM IN ICELAND

1.4.1. Distribution of Icelandic Rhyolites

Despite its oceanic setting and the dominance of basaltic compositions, silicic rocks, including dacites, trachytes, rhyolites, and silicic intrusive rocks, form up to 15% of the Icelandic crust (e.g., Walker, 1966; Jakobsson, 1972; Sæmundsson, 1979; Jónasson, 2007). The silicic volcanic rocks are dominantly rhyolitic in composition and include both effusive (lavas and domes) and explosive

(tephra layers, welded tuffs and ignimbrites) products (e.g., Walker, 1966; Jónasson, 2007), many of which were erupted subglacially (e.g., McGarvie, 2009, and references therein).

Icelandic rhyolites in both the rift and flank zones occur almost exclusively in and around the central volcanoes, where the flux of basaltic magma from depth is highest (Fig. 1.1; see Jónasson, 2007, for a comprehensive overview). In most systems they are a minor component, subordinate to basalt; an exception is Torfajökull, where rhyolites comprise >90% of the surface outcrop (McGarvie, 1984, 1985). Compositions of Icelandic rhyolites range from metaluminous to peralkaline, with the alkalic types found only in the flank zones, and low-alkali rhyolites occurring mostly within the rift zones (Jakobsson, 1972, 1979; Jónasson, 2007).

1.4.2. Silicic Eruptions in Iceland

Silicic eruptions involving dacitic, rhyolitic and trachytic magmas (grouped here for convenience because of their similar eruptive styles) have occurred throughout the geologic history of Iceland and span a range of sizes and styles. The largest explosive events ($\geq$ several cubic kilometres of magma) form voluminous ignimbrite deposits, which are common in the Tertiary volcanic pile (Dearnley, 1954; Tryggvason and White, 1955; Walker, 1962, 1963, 1966; Blake, 1969; Schmincke et al., 1982). Young ignimbrites, however, are rare. Only three Quaternary examples are known: 1) the ca. 110-115 ka Halarauður ignimbrite at Krafla (reconstructed volume 7 ± 6 km^3 dense rock equivalent [DRE]; Rooyakkers et al., 2020; Chapter 2 of this thesis; ^{40}Ar/^{39}Ar age from Sæmundsson and Pringle, 2000), 2) the ca. 55.6 ± 2.4 ka Þórsmörk ignimbrite (preserved volume 1.5-2 km^3 DRE; Thórarinsson, 1969; ^{40}Ar/^{39}Ar age from Guillou et al., 2019), originally attributed to the Tindfjallajökull system (Jørgensen, 1980, 1981) but now thought to derive from Torfajökull

(Moles et al., 2019), coeval with extrusion of a voluminous ring of rhyolite tuyas (~18 km^3 DRE; McGarvie, 2009), and, most recently, 3) the 11,980 B.P. Sólheimar ignimbrite from the Katla system ($\geq$6-7 km^3 DRE; Lacasse et al., 1995, 2007; Tomlinson et al., 2012). Both the Þórsmörk and Sólheimar ignimbrites are correlated with widespread offshore tephra layers in the north Atlantic and in Greenland ice cores (e.g., Grönvold et al., 1995; Lacasse et al., 1995; Lacasse and Garbe-Schönberg, 2001; Austin et al., 2004; Tomlinson et al., 2010). The apparent scarcity of Quaternary ignimbrites is likely an erosional artefact resulting from Quaternary glaciations (Gudmundsson et al., 2008), and is not reflected by any corresponding break in regional tephra records. Offshore tephra layers provide evidence for at least 19 additional major silicic (mostly rhyolitic) eruptions from Icelandic rift and flank zone volcanoes in the last 2 Ma that dispersed tephra across much the North Atlantic (Lacasse and Garbe-Schönberg, 2001). One of these events, dated at 201 ka, was suggested to correlate with the Halarauður event from Krafla (Lacasse and Garbe-Schönberg, 2001), although this age is not consistent with ^{40}Ar/^{39}Ar dating of Halarauður products by Sæmundsson and Pringle (2000), or with other stratigraphic constraints (K. Sæmundsson, pers. commun., 2016). None of the other Quaternary tephras have been reliably correlated with onshore deposits, although in some cases the source volcanic systems have been suggested based on their distinct geochemical signatures (Lacasse and Garbe-Schönberg, 2001). Based on these offshore tephra data, Thordarson and Höskuldsson (2008) suggest a recurrence frequency of approximately one event every 100,000 years for major explosive silicic eruptions >2.5 km^3 DRE in volume.

Smaller explosive silicic eruptions (volumes 0.25-2.5 km^3 DRE) occur approximately every 1000 years in Iceland, while explosive events <0.25 km^3 have frequencies of approximately one eruption every 200-300 years (Thordarson and Höskuldsson, 2008). Approximately 58

explosive silicic eruptions are known from the Holocene (e.g., Larsen and Eiríksson, 2007). Effusive events are comparatively rare and of small volume (<0.2 km^3; Thordarson and Höskuldsson, 2008). Explosive silicic eruptions since settlement of Iceland have posed a major hazard to local populations, and also had impacts further afield. Significant events have occurred from the Hekla, Öræfajökull, Eyjafjallajökull, Torfajökull and Askja systems (Larsen et al., 1999), including three of rhyolitic composition: the 1104 C.E. H1 eruption of Hekla (~0.9 km^3; Thorarinsson, 1967a; Larsen and Thorarinsson, 1977; Larsen et al., 1999; Janebo et al., 2016), the 1362 C.E. eruption of Öræfajökull (~1.2 km^3 DRE; Thorarinsson, 1958; Selbekk and Trønnes, 2007; Sharma et al., 2008), Iceland's largest explosive eruption since settlement, and the 1875 C.E. eruption of Askja (~0.3 km^3 DRE; Sparks et al., 1981; Carey et al., 2010). All three rhyolitic events involved Plinian phases and dispersed ash as far as mainland Europe (e.g., Thorarinsson, 1981; Larsen, et al., 1999; Wastegård and Davies, 2009). Major fatalities are suspected for the 1362 eruption, and the effects of the 1104 eruption have been linked with famine in Iceland (Gudmundsson et al., 2008). Similar future silicic Icelandic eruptions of volcanic explosivity index (VEI) >4 are very likely to produce ashfall that reaches northern Europe (Watson et al., 2017), and pose a major risk to human lives and infrastructure in Iceland (e.g., Gudmundsson et al., 2008; Barsotti et al., 2018).

1.4.3 Petrogenesis of Icelandic Rhyolites

The origin of Icelandic rhyolites (and other silicic rocks) has intrigued petrologists and geochemists for more than 60 years. Central to this intrigue is their occurrence in an oceanic environment, where silicic magmas are typically rare. Consequently, much debate has centred around whether the processes that form silicic rocks in Iceland are an analogue for the formation

of early continental crust (Martin et al., 2008; Willbold et al., 2009; Reimink et al., 2010; Bindeman et al., 2012; Carley et al., 2014). Despite decades of research, many aspects of rhyolite generation in Iceland remain poorly understood, but major progress has been made in recent years using novel petrologic methods.

The first modern studies concerned with the origin of Icelandic rhyolites focused on tholeiitic rocks from Tertiary centres in eastern Iceland, and considered two possible processes: 1) partial or complete melting of sialic (i.e., continental) crust (Walker, 1963), or 2) extensive crystal fractionation from a basaltic parental melt (Carmichael, 1964). The former hypothesis was quickly abandoned by most workers after Sr and Pb isotopic compositions of the rhyolites were found to be inconsistent with such an origin (Moorbath and Walker, 1965; Welke et al., 1968). However, proponents of the crystal fractionation model struggled to demonstrate evidence for significant volumes of intermediate magmas or mafic cumulates that would be produced during extensive fractionation from a basaltic parent (Walker, 1966; Thorarinsson, 1967b; Grönvold, 1972). Additional complexity was realised with the discovery of alkaline rhyolites during studies in western and southern Iceland (Sigurdsson, 1970, 1971; Grönvold, 1972), and a further challenge to the fractionation model came with recognition that the $\delta^{18}O$ and $^{87}Sr/^{86}Sr$ isotopic compositions of Icelandic rhyolites are commonly distinct from nearby basalts, thus precluding a simple co-genetic relationship (Muehlenbachs, 1973; O'Nions and Grönvold, 1973). Consequently, alternative models for rhyolite petrogenesis involving partial melting of the mantle (Walker, 1966), partial remelting of basaltic crust (Gibson, 1969; Grönvold, 1972; Muehlenbachs, 1973; O'Nions and Grönvold, 1973; Sigvaldason, 1974; Jóhannesson, 1975), or partial melting of silicic differentiates in the mid-crust (Sigurdsson, 1977) gained traction, though others continued to favour a closed-system fractional crystallisation origin (Wood, 1978).

Through the 1980's and 1990's, opinion on the origin of Icelandic rhyolites was fiercely divided. Many workers, often comparing simple least squares or Rayleigh fractionation calculations with whole-rock data, continued to favour closed-system fractional crystallisation from parental basalts (e.g., Macdonald et al., 1990; Furman et al., 1992a). Where such models were unable to fully account for the compositional trends or low $\delta^{18}O$ isotopic compositions, assimilation of altered (low $\delta^{18}O$) crustal rocks and/or mixing with mafic magmas were suggested to play a subordinate role alongside fractional crystallisation (Sigurdsson and Sparks, 1981; Macdonald et al., 1987; Nicholson et al., 1991). On the other hand, many workers cited isotopic compositions (particularly low $\delta^{18}O$ and/or $^{230}Th/^{232}Th$) as evidence for generation of Icelandic rhyolites by partial melting of basaltic crust (± subsequent fractional crystallisation), with low $\delta^{18}O$ reflecting high-temperature hydrothermal alteration of the source rock by isotopically light meteoric water (e.g., Hattori and Muehlenbachs, 1982; Óskarsson et al., 1982, 1985; Condomines et al., 1983; Steinthórsson et al., 1987; Marsh et al., 1991; Sigmarsson et al., 1991, 1992; Hemond et al., 1993; Jónasson, 1994; Gunnarsson et al., 1998). Melting experiments on basalts and metabasalts provided strong support for the partial melting models, with Thy et al. (1990) demonstrating a close similarity between the compositions of Icelandic rhyolites and water-undersaturated silicic melts produced by dehydration melting of amphibolite at P_{H_2O} <1 kbar.

More recent studies have attempted to resolve the controversial origin of Icelandic rhyolites with an integrated model linking the mode of petrogenesis to the local geodynamic environment. Martin and Sigmarsson (2007, 2010) suggested that variation in the geothermal gradient across Iceland, related to proximity to the mantle plume and rift systems, plays a strong role in determining the dominant process. In their conceptual model, partial melting of altered basaltic crust by intruding basalts is enabled by the high geothermal gradient in the rift zones, forming low-

$\delta^{18}O$ silicic melts that may undergo subsequent crystal fractionation and/or assimilation. In contrast, away from the rift zones or plume centre the flux of basaltic inputs is lower and the crust is hence cooler and unlikely to cross its solidus; this favours extensive fractional crystallization of basaltic intrusions over crustal melting or assimilation, thus forming silicic melts with normal or only slightly depleted $\delta^{18}O$. Noting the O-Sr-Nd-Pb isotopic similarities between basalts and rhyolites at Öræfajökull and many other flank systems (cf. Sigmarsson et al., 1992; Hards et al., 2000), Selbekk and Trønnes (2007) reached a similar conclusion, suggesting that the thicker, cooler and stronger crust in the flank zones limits anatexis, while absence of hydrothermal systems limits hydration and alteration of the crust, thus favouring fractional crystallization over melting. More recent studies lend support to these ideas. Schattel et al. (2014) proposed a correlation among tectonic setting, isotopic composition, H_2O content, fO_2 and P-T storage conditions based on petrologic studies of rhyolites from on-rift (Askja) and off-rift systems (Öræfajökull, Hekla): hotter (935-1008°C), drier (<2.7 wt% H_2O) and oxidised ($fO_2 \sim$ QFM + 1.4) low $\delta^{18}O$ (<2‰) rhyolites at Askja were suggested to reflect extensive assimilation of hydrothermally altered crust at shallow depths ($\geq$1.8 km) in the rift zone, whereas cooler (874-902°C), wetter (4-6.3 wt% H_2O) and more reducing ($fO_2 \sim$ FMQ to FMQ - 1) rhyolites from the off-rift centres, with normal to only slightly lowered $\delta^{18}O$ (5.2-6‰), experienced little to no assimilation of altered crust. A recent comprehensive survey of zircon $\delta^{18}O$ compositions from across Iceland by Carley et al. (2020) provides strong support for a greater contribution of altered crust in the petrogenesis of on-rift silicic magmas relative to those in the flank zones. Melting of altered crust is now generally accepted to play an important role in petrogenesis of low $\delta^{18}O$ rhyolites, but whether this occurs principally by anatexis (e.g., Jónasson, 2007; Pope et al., 2013; Zierenberg et al., 2013) or by assimilation of low $\delta^{18}O$ crust into pre-existing magma bodies (e.g., Elders et al., 2011), and

whether fractional crystallisation also plays a role in the rift setting (e.g., Charreteur et al., 2013), remain controversial. Additional complexities may occur in propagating rift settings, where isotopic data imply highly variable contributions of altered crust and an important role for fractional crystallisation of mantle melts in producing rhyolites (Banik et al., 2018; Carley et al., 2020).

Aside from advancing understanding of the links between tectonic setting and petrogenesis, recent studies applying modern petrologic methods have made other important advances in understanding Icelandic rhyolites. One major area of progress is in constraining volatile contents. Icelandic rhyolites were traditionally assumed to be relatively dry due to an absence of hydrous phenocrysts (e.g., Sigurdsson and Sparks, 1981; Jónasson, 2007). Contrary to this assumption, recent melt inclusions studies (Portnyagin et al., 2012; Owen et al., 2013a, b; Schattel et al., 2014; Lucic et al., 2016) and analyses of quenched glass sampled directly from rhyolite magma in the IDDP-1 well at Krafla (Elders et al., 2011; Zierenberg et al., 2013) have shown evidence for variable and often high (up to 6.3 wt%) magmatic H_2O contents, which may correlate with local tectonic setting (Schattel et al., 2014) and can exert a major influence on eruptive style (Owen et al., 2013a). Portnyagin et al. (2012) proposed that the absence of hydrous mineral phases may relate to the low fO_2 of Icelandic rhyolites rather than low aH_2O, but this hypothesis has yet to be tested experimentally. Other volatiles, including CO_2, S, Cl and F, have received little attention, and few data are available (e.g., Elders et al., 2011; Zierenberg et al., 2013; Clay et al., 2015; Lucic et al., 2016). Further, it is largely unknown at what stage in their evolution Icelandic rhyolites reach volatile saturation, but the results of Lucic et al. (2016) suggest that some may be undersaturated until they erupt. Hence, further work is needed to constrain the volatile budgets of Icelandic rhyolites.

A second area of progress is in understanding the longevity and tempo of rhyolitic magmatism within individual systems through application of modern isotopic dating methods. $^{40}Ar/^{39}Ar$ dating studies have revealed a protracted history of silicic volcanism at the active Krafla, Ljósufjöll, Kerlingarfjöll and Torfajökull systems, with eruption ages spanning several hundred thousand years (Sæmundsson and Pringle, 2000; Flude et al., 2008, 2010; Clay et al., 2015). Zircon dating studies suggest even longer timescales of silicic magmatism in now-extinct Tertiary systems, with zircon U-Pb ages implying remarkably long lifespans of >2.8 M.y. for the Tertiary Breiðuvík and Kækjuskörð systems in east Iceland (Carley et al., 2017), and ca. 1.5 M.y. for the Hafnarfjall-Skarðsheiði system in west Iceland (Banik et al., 2018). Durations of silicic magmatism thus appear to be commensurate with the lifespans of individual volcanic systems. Both $^{40}Ar/^{39}Ar$ and zircon U-Pb dating methods have great potential for tracing the evolution of rhyolitic volcanism at individual centres through time, but further studies are needed to better understand the factors that control the tempo of silicic magmatism, including possible links with glacial-interglacial cycles (Sigvaldason, 2002; Flude et al., 2008).

A final key area of progress is in isotopic analysis (O, Hf and U-series) and dating of individual minerals or mineral separates, particularly *in situ* methods applied to zircon, to constrain the processes and timescales over which individual rhyolite batches are generated, assembled and stored. In one of the first such studies, Zellmer et al. (2008) applied U-series methods to whole-rock samples and mineral separates from two young Torfajökull rhyolites to suggest that both magmas were derived from remelting of a hydrothermally altered mafic protolith ≤60 ka in age, and that crystals in both rhyolites grew ≤3.2 k.y. before eruption. More recent studies have revealed diverse trace element and isotopic compositions among zircon grains from individual eruptions and U-Th disequilibria ages spanning a range of >10 k.y. prior to eruption ages, suggesting either

1) entrainment of zircons with diverse crystallization histories from disaggregating mush or partially molten source rock into silicic melts distinct from those in which they crystallised (Carley et al., 2011), or 2) mixing of isotopically diverse zircon-bearing magmas generated by partial melting of compositionally heterogeneous and variably altered crust (Bindeman et al., 2012; Gurenko et al., 2015; Padilla et al., 2016). In either case, isotopic disequilibrium between zircons and their host melt implies that the final erupted magmas are assembled faster than the $\sim 10^3$-10^4 year timescales of zircon isotopic re-equilibration (Bindeman et al., 2012). Although the emerging picture is one of mixing of compositionally and isotopically distinct melts and crystals followed by relatively short (k.y.) pre-eruptive residence times, further work is needed to understand whether similar processes apply in all settings, and the potential differences in processes and timescales involved in assembling large versus small rhyolite bodies.

1.5. THE KRAFLA VOLCANIC SYSTEM

1.5.1. Overview

Krafla is one of seven volcanic systems in Iceland's North Volcanic Zone (NVZ), a N-S striking segment of the axial rift zone extending ~200 km from central Iceland to the offshore Tjörnes Fracture Zone and active since ca. 4 Ma (Sæmundsson, 1974; Einarsson, 2008; Hjartardóttir et al., 2016; Fig. 1.1). Deformation across the NVZ is almost purely divergent (Einarsson, 2008). The Krafla system consists of two components: the Krafla central
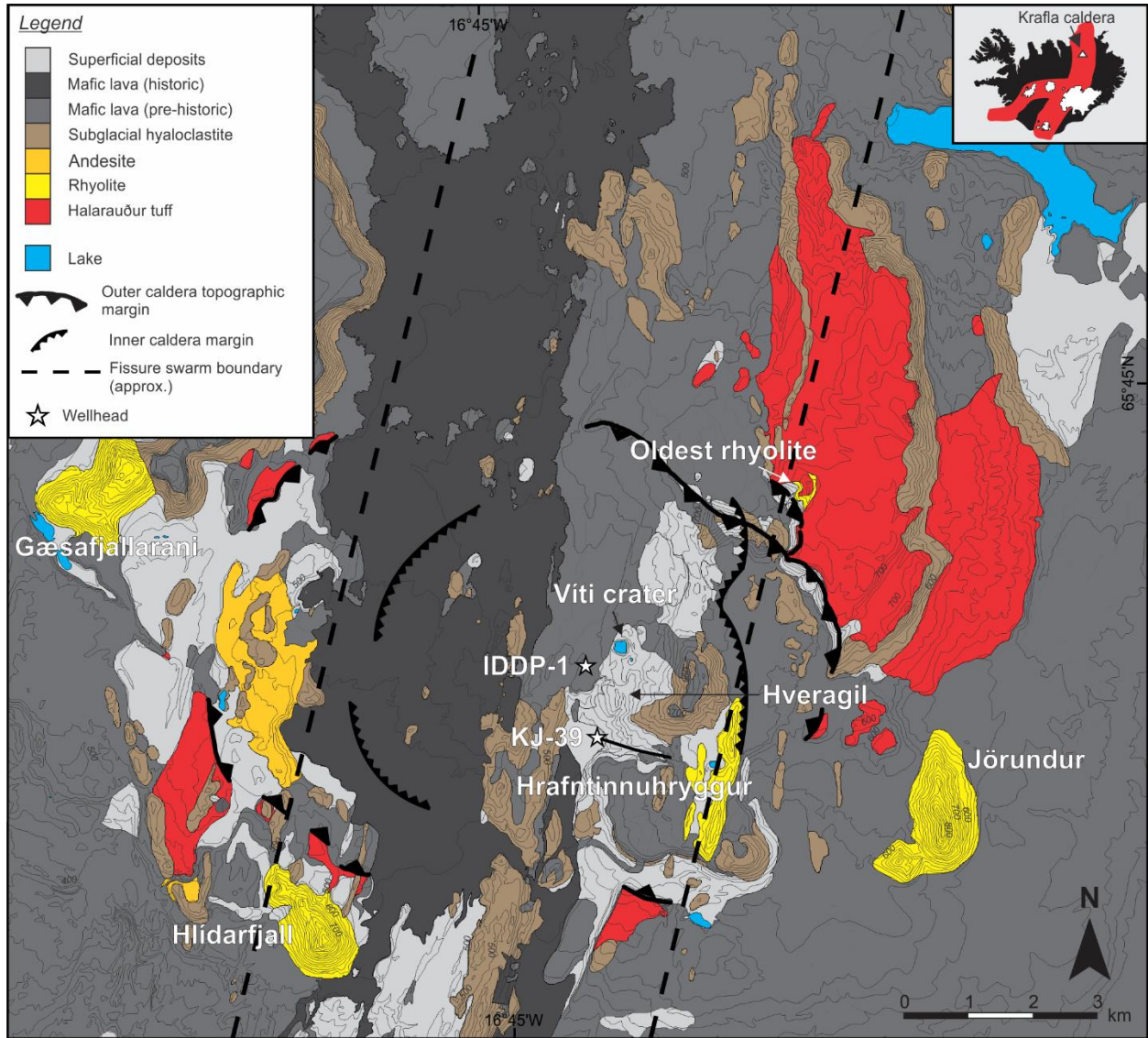
Figure 1.3. Simplified geological map of the Krafla caldera and surroundings, adapted from Sæmundsson et al. (2012). Rhyolitic units or their source vent areas are labelled, as well as the IDDP-1 and KJ-39 boreholes where rhyolitic magma or melt bodies were recently intercepted. The tail extending from the KJ-39 wellhead shows the direction of the slanted well path; IDDP-1 was drilled vertically. The inner caldera margin is from Árnason et al. (2009) and Árnason (2020) (see text). Inset shows the location of the Krafla central volcano within the neovolcanic zone (red).

volcano (Fig. 1.3), a broad (~21 x 17 km) shield with a central ~8 x 10 km collapse caldera, and the Krafla fissure swarm, a 100 km-long and up to 10 km-wide, NNE-SSW-oriented zone of subparallel fissures and normal faults that transects the caldera perpendicular to the plate spreading vector (Sæmundsson, 1991; Hjartardóttir et al., 2012). Two high-temperature geothermal fields

19

are associated with the system: the intracaldera Krafla-Leirhnjúkur geothermal field, harnessed by the 60 MW$_e$ Krafla power plant since 1977 (Ármannsson et al., 1987), and the Námafjall field, ~5 km south of the caldera. Whole-rock chemical analyses of Krafla rocks range from olivine tholeiites to rhyolites (Nicholson, 1990; Nicholson et al., 1991; Jónasson, 1994). Basaltic rocks are dominant (>90%), but subordinate rhyolite is present in and around the caldera (Jónasson, 1994). Intermediate compositions are rare, and all show evidence for hybridisation of mafic and silicic endmembers (Jónasson, 1994). Removal of hybrid compositions from whole-rock compositional plots reveals a clear Daly gap between 55-69 wt% SiO_2 (Jónasson, 1994).

The most intense volcanism and geothermal activity in the Krafla system are focused within the caldera. Seismic studies suggest a crustal thickness of ~19-21 km beneath the caldera region (Brandsdóttir et al., 1997; Staples et al., 1997; Darbyshire et al., 2000), with a broad high-velocity dome, interpreted as gabbroic cumulates, ascending from the lower crust (Brandsdóttir and Menke, 1992, 2008; Brandsdóttir et al., 1997). Previous studies have linked formation of the caldera with a composite welded tuff sheet around its margins, variably referred to as the Krafla Welded Layer (Calderone et al., 1990) or Halarauður welded tuff (Guðmundsson et al., 1983; Sæmundsson, 1991, 2008; Sæmundsson et al., 2012), and interpreted as the product of a major explosive mixed basalt-rhyolite eruption at ca. 110-115 ka ($^{40}Ar/^{39}Ar$ age from Sæmundsson and Pringle, 2000). The caldera has been almost entirely infilled since the Halarauður event, and its present-day expression consists of a broad and relatively flat area, ~300-500 m in elevation, dotted with occasional ridges of subglacially-erupted basaltic hyaloclastites or rhyolitic tuffs and lavas reaching elevations of up to 900 m. The presence of a younger "inner" caldera nested within the main structure was recently proposed based on gravity data (Árnason et al., 2009; Árnason, 2020),

but its origin is poorly understood. The subsurface geology sampled by intracaldera boreholes is dominated by intercalated hyaloclastites and basaltic lavas to a depth of ~1-2 km, with gabbros and occasional intermediate to felsic intrusives at deeper levels (e.g., Ármannsson et al., 1987; Weisenberger et al., 2015).

Geophysical studies in the caldera region have provided useful insights into the architecture of the shallow magmatic and hydrothermal systems, although many aspects remain poorly resolved. The presence of a shallow basaltic magma chamber was first proposed by Einarsson (1978) based on two S-wave shadow zones imaged in the central caldera region, each with a top at ~3 km depth and base at <7 km. Numerous subsequent geodetic, magnetotelluric and seismologic studies found similar evidence for a large shallow magma storage zone with a top at ~2.5-3 km depth (see Kelley and Barton, 2008, and references therein), conceptualised as either a unitary magma chamber or a network of dikes and sills (Kennedy et al., 2018; Árnason, 2020). The most recent magnetotelluric data reveal a large, low resistivity zone beneath the central caldera region, doming up to a depth of ~1.6 km and partially overlapping with the S-wave shadow zones (Lee et al., 2020). The base of the IDDP-1 well where rhyolite magma was encountered occurs near the upper edge of this feature, but the cause of anomalous resistivity is not well constrained: partial melt, aqueous fluids or chlorite and epidote dehydration are all possibilities (Lee et al., 2020). Seismic studies also show anomalies near the base of the IDDP-1 and KJ-39 wells; a low V_p/V_s seismic anomaly imaged by Schuler et al. (2015) near the bottom of both wells was interpreted as a superheated steam zone above shallow magma, while large amplitude seismic reflections near the base of these wells have also been linked with the presence of magma (Kim et al., 2017, 2020). Because of the limited spatial resolution of these techniques, it remains unclear

21

whether the IDDP-1 and KJ-39 wells intercepted the same magma body, or separate small pockets of silicic magma.

Tephrochronological and mapping studies (Thorarinsson, 1951; Thorarinsson, 1979) have recognised two distinct phases of postglacial activity at Krafla, separated by a ~3 k.y. hiatus: the Ludent phase (older than the ~6 ka Hekla H_5 tephra) and the Hverfjall phase (younger than the ~2.9 ka Hekla H_3 tephra). A total of 35 postglacial eruptions are known: 20 within the caldera and its immediate surroundings, and the remainder focused in the Námafjall area of the fissure swarm, south of the caldera (Björnsson et al., 1977; Sæmundsson, 1991). These eruptions are thought to be concurrent with major rifting events (Sæmundsson, 1991), and two have produced rhyolitic products: the ca. 9000 B.P. Hveragil tephra, and the 1724 C.E. Víti pumice (Jónasson, 1994). Two major historical volcano-tectonic episodes have occurred: the Mývatn Fires (1724-1729 C.E.) and Krafla Fires (1975-1984 C.E.). Both events were characterised by episodic rifting, intense earthquake activity, and effusive basaltic eruptions along the fissure swarm (e.g., Grönvold, 1984; Einarsson, 1991b).

The progression of the Krafla Fires rifting episode is well-documented in the literature. Most of the episode was characterised by uplift and earthquake activity focused within the caldera, as magma ascended from depth and accumulated within a shallow storage region. This long-term trend of uplift within the caldera was punctuated by short (hours to at most a few months) episodes of subsidence, rifting, and intense seismicity, as the walls of the shallow storage zone were breached and magma flowed into the fissure system, feeding dikes that propagated laterally away from the reservoir (Björnsson et al., 1977, 1979; Brandsdóttir and Einarsson, 1979; Einarsson and Brandsdóttir, 1980; Tryggvason, 1980, 1994; Marquart and Jacoby, 1985; Buck et al., 2006). A total of 21 dikes were injected into the fissure swarm over the entire episode, nine of which fed

eruptions. S-wave shadow zones (Einarsson, 1978) and modelling of deformation data (Björnsson et al., 1979; Tryggvason, 1984; Ewart et al., 1991; Árnadóttir et al., 1998) suggest a depth to the top of the shallow reservoir of ~2.5-3 km, with larger reservoirs also detected at deeper crustal levels (Tryggvason, 1986; Árnadóttir et al., 1998; de Zeeuw-van Dalfsen et al., 2004, 2006). A total volume of 1.1-2.1 km^3 of magma was added to the upper crust during the entire episode, of which only ~0.2-0.4 km^3 was erupted (Hollingsworth et al., 2013). A total horizontal extension of ~8-10 m (mostly accommodated by rift-bounding normal faults; Hollingsworth et al., 2012) occurred near the caldera, decreasing to 3-4 m near the northern coastline and approaching zero approximately 15-20 km south of the caldera (Tryggvason, 1984; Wendt et al., 1985; Árnadóttir et al., 1998; Hollingsworth et al., 2012). The average opening of ~4.3 m over the ~80 km zone of rifting is equivalent to ~250 years of constant plate divergence at the average spreading rate of ~2 cm yr^{-1} (Tryggvason, 1994; Hjartardóttir et al., 2012; Hollingsworth et al., 2012), demonstrating that extension along the plate boundary is not spatially or temporally continuous, but instead occurs as discrete, short-lived events at localised segments of the rift (Björnsson et al., 1977; Björnsson, 1985; Wright et al., 2012).

1.5.2. Rhyolitic Magmatism and Volcanism at Krafla

Eight eruptions involving rhyolite are known from the Krafla system. The first, linked by Jónasson (1994) with the Halarauður eruption (see below) but later recognised as a separate event, involved emplacement of a small (<0.05 km^3; Jónasson, 1994) un-named rhyolite dome near the northeastern margin of the present-day caldera at ca. 190 ka (Fig. 1.4a) (^{40}Ar/^{39}Ar age from Sæmundsson and Pringle, 2000). Exposure of this dome is poor due to burial by younger Halarauður deposits.
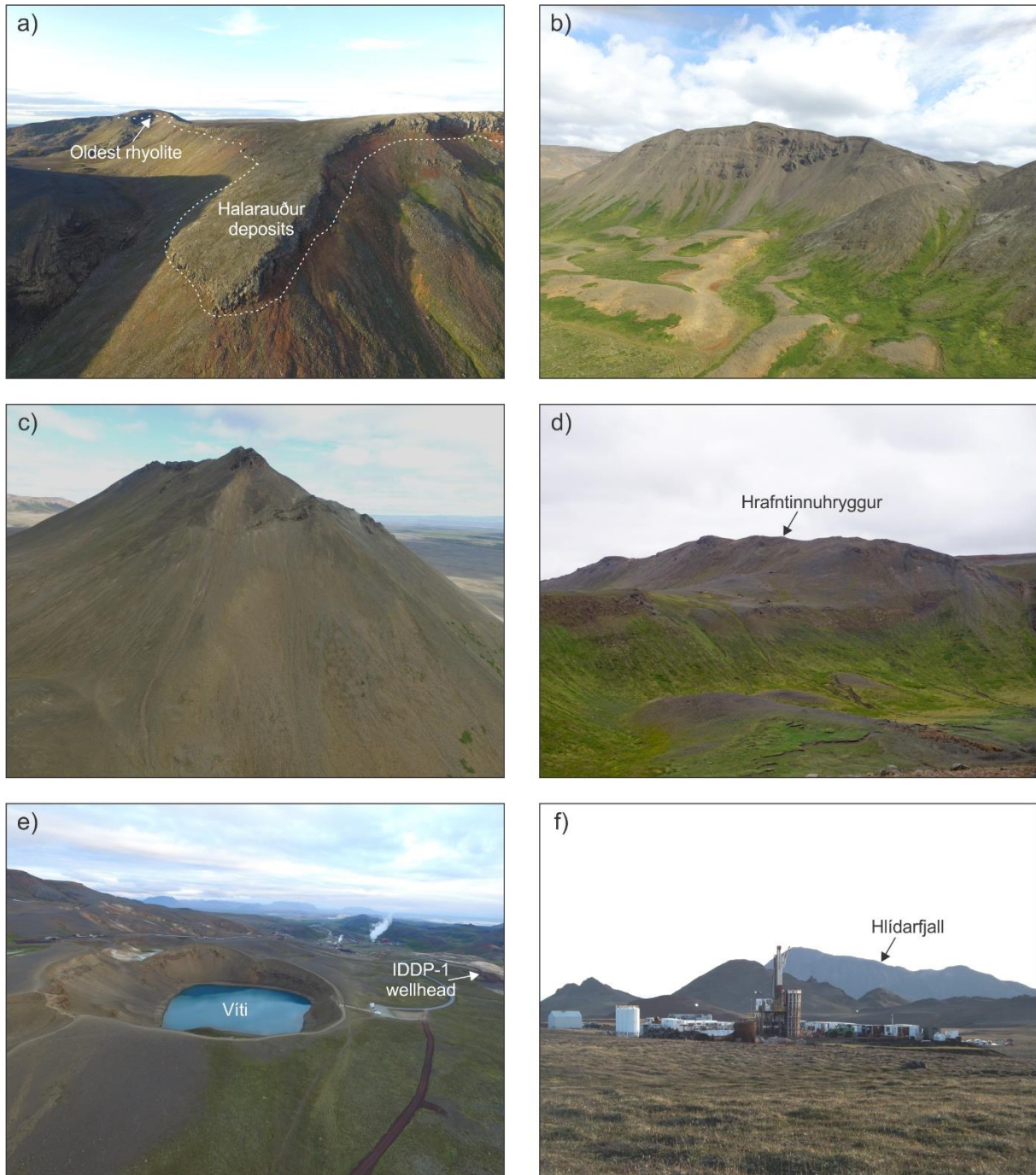
Figure 1.4. Selected features associated with rhyolite at Krafla. a) Oldest (un-named) Krafla rhyolite viewed from the northeast caldera margin (looking north), overlain by deposits of the mixed basalt-rhyolite Halarauður eruption. b) Northwestern face of the subglacially-erupted Gæsafjallarani ridge (view to the southeast) showing stacked rhyolite lavas. c) View of Jörundur from the southwest. Occasional microcrystalline lava lobes near the top of the ridge project through sparsely exposed fragmental deposits and thick talus cover. d) Southern end of the Hrafntinnuhryggur ridge (viewed from the southwest) cutting through basaltic hyaloclastites in the foreground. e) Víti crater, looking south towards the Krafla power station (distant steam plume). f) IDDP-1 drill rig viewed from near Víti (looking southwest), with Hlídarfjall in the distance.

The second and largest event, the mixed basalt-rhyolite Halarauður eruption at ca. 110-115 ka (^{40}Ar/^{39}Ar; Sæmundsson and Pringle, 2000), has widely been linked with formation of the Krafla caldera (Björnsson et al., 1977; Calderone et al., 1990; Sæmundsson, 1991). Deposits from this event occur around the caldera up to a distance of ~7 km, and were interpreted by early workers as 'a welded dacitic tuff sheet of airfall origin' (Björnsson et al., 1977). Calderone et al. (1990) presented the first detailed study of the deposits (which they referred to as the "Krafla Welded Layer"), dividing them into five units (A-E). Unit A was described as a basal fine-grained Plinian rhyolitic fall deposit, overlain by unit B, a Plinian basaltic scoria fall deposit. Mingled intermediate compositions were described above these basal layers, with unit C, a thin black vitrophyre, overlain by unit D, a thick, densely welded unit of incompletely mixed basaltic and rhyolitic pyroclasts interpreted as a welded fall deposit. The uppermost unit, E, was described as a densely welded lava-like rheomorphic tuff, also interpreted as welded tephra fall. Calderone et al. (1990) calculated a total volume for the extracaldera deposits of 2.4 km^3 DRE, which they suggested to account for 50-55 m of subsidence of the 45 km^2 caldera floor. The eruption was inferred to have been triggered by injection of the basaltic component into the rhyolite.

Rhyolitic activity after the Halarauður eruption resumed at ca. 65 ka (U-Th zircon ages from Hampton et al., in prep), when three ridges, Jörundur, Hlídarfjall and Gæsafjallarani, were erupted subglacially around the caldera margin (each ~0.15 km^3; cf. Agustsdóttir et al., 2010). Each ridge rises ~250-300 m above its immediate surrounds (Fig. 1.4b, c). Sparse outcrops of radiating columns and phreatomagmatic tephra beneath scree-covered slopes attest to subglacial emplacement (McGarvie, 2009). Jónasson (1994) suggested that the similar shape, composition and age of the ridges reflect a distinct and short-lived phase of rhyolitic volcanism at Krafla, possibly associated with the emplacement of a ring-dike.

Subsequent rhyolitic eruptions have been small-volume events within the caldera. The first occurred late during the last glacial at ca. 24 ka (^{40}Ar/^{39}Ar; Sæmundsson and Pringle, 2000), when Hrafntinnuhryggur (0.02 km^3), a 2.5 km-long ridge of aphyric rhyolite with abundant obsidian (Fig. 1.4d), was emplaced beneath thin ice (Wright, 1915; Jónasson, 1994; Tuffen and Castro, 2009; Agustsdóttir et al., 2010). The eruption was fed by a dike striking parallel to the regional tectonic trend, exposed at the southern end of the ridge (Tuffen and Castro, 2009). Two post-glacial rhyolitic eruptions followed: the ca. 9000 B.P. Hveragil tephra, and the 1724 C.E. Víti pumice. Both postglacial rhyolites show textural evidence for mixing with basaltic magma (Grönvold, 1984; Sæmundsson, 1991). The Víti eruption, which marked the beginning of the 1724-1729 Mývatn Fires rifting episode, formed a small maar crater (Fig. 1.4e), ejecting hydrothermally altered country rock and felsite xenoliths (Sigurdsson, 1968) along with very minor volumes of juvenile rhyolitic pumice and basaltic scoria (Grönvold, 1984; Jónasson, 1994).

The origin of silicic magma at Krafla remains controversial. Although ^{87}Sr/^{86}Sr and ^{143}Nd/^{144}Nd ratios are similar for Krafla mafic and silicic rocks (Condomines et al., 1983), ^{230}Th/^{232}Th and δ^{18}O values are distinctly lower in the rhyolites, precluding their generation by simple fractional crystallisation of basalt (Sigmarsson et al., 1991; Nicholson et al., 1991; Jónasson, 1994; Pope et al., 2013). Oxygen exchange between rocks and meteoric water in high-temperature geothermal systems is known to readily lower the δ^{18}O of crustal rocks, with values as low as -10‰ measured in hydrothermally altered basalts from Krafla boreholes (Muehlenbachs et al., 1974; Hattori and Muehlenbachs, 1982; Gautason and Muehlenbachs, 1998). Nicholson et al. (1991) therefore argued that decreasing δ^{18}O and ^{230}Th/^{232}Th with decreasing MgO in Krafla rocks reflects an assimilation fractional-crystallisation (AFC) process, whereby mantle-derived mafic magmas fractionate and assimilate low-δ^{18}O, low-^{230}Th/^{232}Th hydrothermally altered

basaltic crust to produce rhyolites. Jónasson (1994, 2007) presented a contrasting argument for near-solidus fractionation, proposing that the rhyolites are minimum melts of hydrothermally altered basalts equilibrated at low water pressures (<1 kbar), high temperatures (850-950°C), and relatively reducing conditions ($fO_2 \leq FMQ$) around the margins of basaltic magma chambers or intrusions, and extracted crystal-free during crustal deformation. Experiments generating melts similar to Krafla rhyolites by equilibrium melting of tholeiitic basalts under similar conditions (e.g. Spulber and Rutherford, 1983; Thy et al., 1990) were cited as supporting evidence. A close compositional similarity between silicic glass cuttings recovered from the KJ-39 well and partial melts of metapelites described from hornfels facies zones adjacent to intrusions was cited by Mortensen et al. (2010) as evidence for a similar partial melting process. Zierenberg et al. (2013) and Pope et al. (2013) also proposed a partial melting model for generation of the IDDP-1 rhyolite, based on its low $\delta^{18}O$ values (+3.2 ± 0.2‰), and δD values (-121 ± 2‰) that overlap with the measured range for hydrothermal epidote in the Krafla geothermal system. However, based on comparison with MELTS models, Charreteur et al. (2013) argued that the very low Mg# of some Krafla rhyolites reflects protracted fractional crystallisation (± minor assimilation) under reducing conditions ($fO_2 \sim FMQ$-1), whereas the higher Mg# and presence of disequilibrium phenocrysts in other rhyolites were consistent with AFC under more oxidising conditions ($fO_2 \sim FMQ$) and possible mixing with basalt. In summary, although it is universally accepted that the low $\delta^{18}O$ of Krafla rhyolites requires input of altered crust, whether this occurs by a purely anatectic process or involves assimilation into pre-existing magma, and whether fractional crystallisation also plays a role in rhyolite petrogenesis, remain controversial.

2. Emplacement of Unusual Rhyolitic to Basaltic Ignimbrites During Collapse of a Basalt-Dominated Caldera: The Halarauður Eruption, Krafla (Iceland)

The original research component of the thesis begins here with a comprehensive field study of products of the ca. 110 ka mixed basalt-rhyolite Halarauður eruption, linked by previous workers with formation of the Krafla caldera. Shane Rooyakkers planned the study with input from John Stix and Kim Berlo, and performed all fieldwork and data collection, excluding XRF analyses, which were performed by Simon Barker. All authors discussed the findings, and Shane Rooyakkers wrote the chapter, published as Rooyakkers et al. (2020), with editorial input from John Stix, Kim Berlo and Simon Barker.

2.1. ABSTRACT

Deposits of the ca. 110 ka Halarauður eruption of Krafla caldera (reconstructed volume 7 ± 6 km^3 dense rock equivalent) include the only spatter-rich ignimbrite known in Iceland, and an exceptionally rare lava-like basaltic ignimbrite. We present a revised stratigraphy and new whole-rock major-element data set for products of this unusual event, one of only three Quaternary ignimbrite eruptions identified in Iceland. Compositions of Halarauður products span a broad range (50.0-74.6 wt% SiO$_2$), reflecting mixing of rhyolite with underplating basalt. Small-volume, valley-ponded basal pumice- and spatter-bearing lithic breccias and ignimbrite (rhyolite to andesite) reflect rapid column collapse during early opening of ring fault vents. A transition to voluminous, regionally-dispersed spatter agglomerates (dacite to basaltic andesite) marks an abrupt eruptive intensification, as gas-poor magma was squeezed into a developing ring fault system by the subsiding chamber roof. Spatial heterogeneities in ascent rates and outgassing

through this variably dilated fault system caused coeval formation of collapsing plumes and spatter fountains at separate vents. Spatter was entrained into flows from the more explosive vents, which deposited proximal spatter agglomerates and more distal spatter-bearing ignimbrite. Overlying lava-like ignimbrite deposits (basaltic andesite to basalt) reflect a final opening of vents, as mafic magma from deep levels of the chamber was squeezed through a dilated ring fault system by the subsiding roof block and erupted at uncharacteristically high mass flux. Development of a mature ring fault conduit system during early tapping of silicic magma appears to be a prerequisite for the emplacement of welded basaltic ignimbrites, and should be considered as a possible eruption scenario in basalt-dominated systems where silicic magma has been known to also accumulate. Poor preservation of the Halarauður deposits exemplifies the challenges of studying ignimbrite eruptions in frequently glaciated regions like Iceland, where they may be more common than the geological record suggests.

2.2. INTRODUCTION

The most destructive volcanic eruptions are those that form ignimbrites, which are voluminous deposits laid down by hot pyroclastic density currents that devastate vast areas (Freundt et al., 2000). Moderate to large ignimbrite-forming eruptions with magma volumes exceeding several cubic kilometres (in extreme cases up to thousands of cubic kilometres) generally occur at systems dominated by silicic magmas (i.e., dacite to rhyolite) and are usually accompanied by large-scale caldera collapse (e.g., Smith and Bailey, 1966; Wilson and Hildreth, 1997; Simmons et al., 2017). Ignimbrites are commonly also associated with caldera-forming events in systems dominated by intermediate or evolved alkaline magmas (e.g., Mahood and Hildreth, 1986; Sigurdsson and Carey, 1989; Rosi et al., 1996). In contrast, calderas dominated by mafic magmas (i.e., basalt to basaltic

andesite) often lack ignimbrite deposits. These calderas are thought to form not by catastrophic collapse during large explosive events, but instead by the cumulative effect of many small-volume eruptions and subsurface magma drainage (e.g., Michon et al., 2011; Swanson et al., 2014; Gudmundsson et al., 2016), and/or passive and protracted subsidence driven by sinking of dense cumulates or deformation of altered rocks (Walker, 1988; Merle et al., 2010).

Because of their relative scarcity, ignimbrites associated with mafic calderas have received little attention compared with their silicic counterparts (e.g., Williams, 1983; Robin et al., 1994, 1995; Freundt and Schmincke, 1995; Allen, 2005; Burgisser, 2005; Lohmar et al., 2005, 2007; Giordano et al., 2006; Pérez and Freundt, 2006; Larsen et al., 2007; Silva Parejas et al., 2010; Caulfield et al., 2011; Firth et al., 2015). Consequently, the styles and dynamics of these events, and the factors that enable mafic magmas to erupt in an uncharacteristically explosive style more typical of silicic compositions, are poorly understood. This is especially apparent in Iceland, where basalt-dominated calderas are abundant (Sæmundsson, 1982), but only two associated Quaternary ignimbrites are known (plus a third from the rhyolite-dominated Torfajökull system; Gudmundsson et al., 2008; Tomlinson et al., 2012; Moles et al., 2019). Ignimbrites are common in Iceland's Tertiary volcanic pile (Dearnley, 1954; Tryggvason and White, 1955; Walker, 1962, 1966; Blake, 1969; Schmincke et al., 1982), however, and this apparent scarcity of young ignimbrites is likely an erosional artefact from Quaternary glaciations (Gudmundsson et al., 2008). The risk associated with ignimbrite-forming events in Iceland may hence be underestimated, and studies of Iceland's ignimbrites are thus essential to understand the dynamics of the most destructive Icelandic eruptions and their associated hazards.

This chapter presents a detailed field study of deposits from the c. 110 ka Halarauður eruption, a mixed basalt-rhyolite event linked with collapse of the basalt-dominated Krafla caldera

in northeastern Iceland (^{40}Ar/^{39}Ar age from Sæmundsson and Pringle, 2000). We provide a revised eruptive stratigraphy coupled with new, stratigraphically-constrained whole-rock major element analyses of juvenile products, and offer new insights into the nature of the Halarauður event. Several uncommon features, including spatter-rich ignimbrite facies that have not previously been described in Iceland, as well as a welded basaltic ignimbrite unit that has only one known equivalent globally, are identified. Many welded facies of the Halarauður deposits superficially resemble proximal lava fountain deposits or lava flows, and other similar ignimbrite deposits in Iceland and elsewhere may have been misinterpreted as such. We discuss the features that distinguish the Halarauður ignimbrites from these more common products of mafic volcanism and also from high grade silicic ignimbrites, and identify an uncommon but critical combination of factors that led to this unusual eruption style and allowed basaltic ignimbrite to weld. Similar events should be considered as an extreme eruption scenario at basalt-dominated calderas in Iceland and elsewhere where silicic magmas are known to also accumulate.

2.3. GEOLOGICAL BACKGROUND

2.3.1. Krafla Volcanic System

Krafla is one of five en-echelon volcanic systems in the Northern volcanic zone, a segment of the axial rift zone marking the locus of the divergent Eurasian-North American plate boundary through Iceland (Sæmundsson, 1979). The Krafla system is composed of a central volcano, consisting of a broad shield of ~25 km diameter with an ~8 x 10 km caldera at its center, transected by a 100 km-long, 5-8 km-wide fissure swarm (Fig. 2.1; Sæmundsson, 1991; Hjartardóttir et al., 2012).
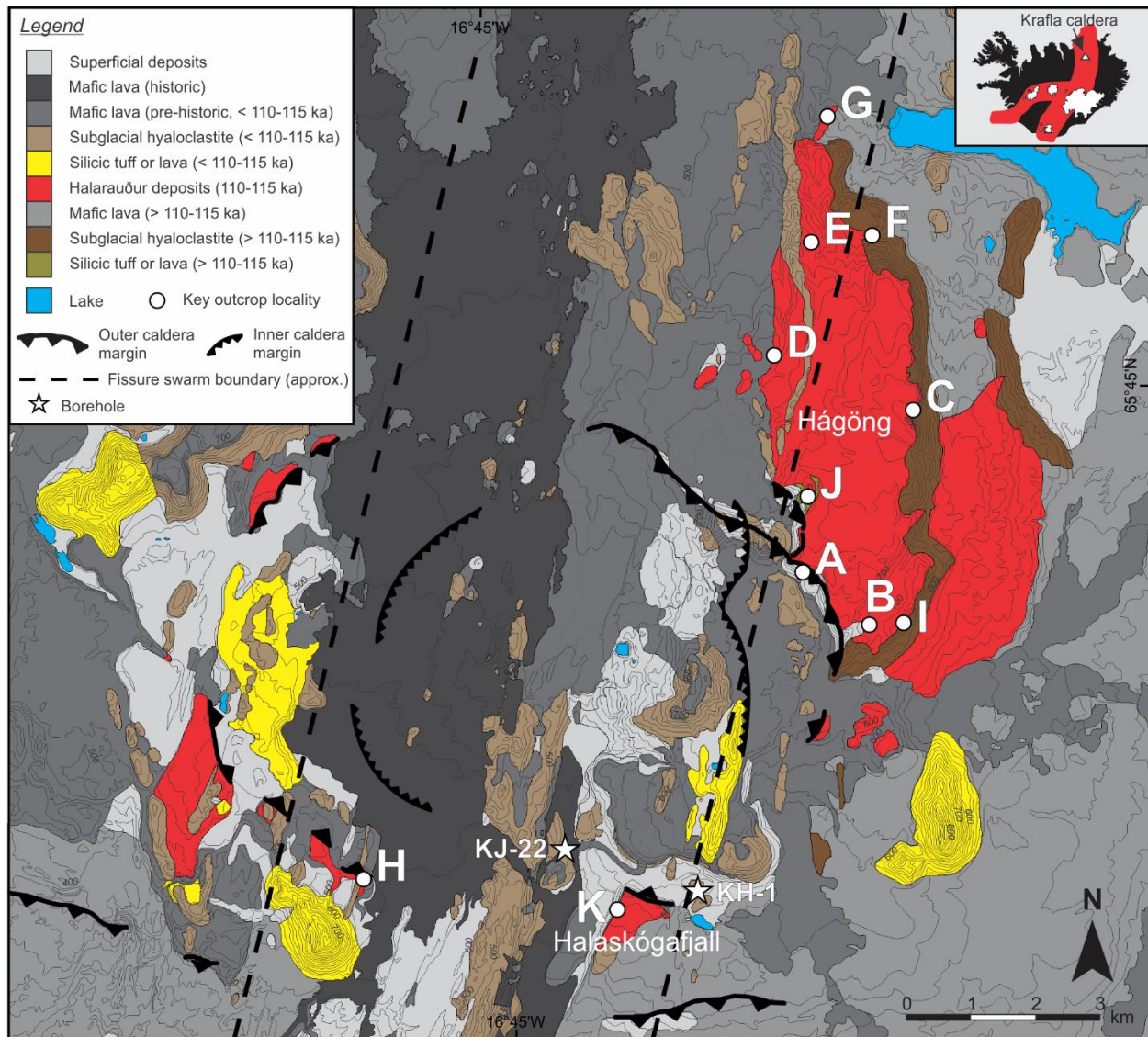
Figure 2.1. Simplified geological map of the Krafla caldera and surroundings. Key sites referred to in the text are labelled. Inset shows the location of the caldera within Iceland's neovolcanic zone (red). Adapted from Sæmundsson et al. (2012), with inner caldera margin from Árnason et al. (2009).

Volcanism and geothermal activity are most intense within and around the caldera, which is now almost completely infilled by basaltic lavas and hyaloclastites (Ármannsson et al., 1987). A region of low and steeply-bounded Bouguer gravity anomalies within the central part of the caldera was recently inferred by Árnason et al. (2009) to reflect a younger, completely buried inner caldera nested within the main structure (Fig. 2.1).

Krafla has been active since at least 300 ka (Sæmundsson, 1991). Erupted products are compositionally bimodal, with basaltic lavas and subglacial hyaloclastites dominant (> 90%), and subordinate low-δ^{18}O rhyolite erupted within and around the caldera (Jónasson, 1994). Postglacial activity has been dominated by basaltic fissure eruptions within and near the caldera, and along the fissure swarm to the south near Námafjall (Thorarinsson, 1979; Sæmundsson, 1991). Interplay between regional tectonics and volcanism has characterised recent activity, with long (c. 300-1000 yr) periods of tectonic and volcanic quiescence interrupted by short (<10 yr) rifting events (Hjartardóttir et al., 2016). Two major historical events, the Mývatn Fires (A.D. 1724-1729) and Krafla Fires (1975-1984), have occurred, each characterised by episodic rifting of the fissure swarm, intense seismicity, and basaltic fissure eruptions (e.g., Hollingsworth et al., 2012). A zone of shear-wave attenuation at ~3-7 km depth in the central caldera region is inferred to reflect a shallow basaltic magma chamber (Einarsson, 1978) or storage zone comprising a network of dikes and sills (Kennedy et al., 2018). A body of molten rhyolite presently overlies this zone at ~2 km depth (Elders et al., 2011; Zierenberg et al., 2013), but its extent and dimensions are poorly constrained (see Schuler et al., 2015).

2.3.2. The Halarauður Eruption

The deposits of what we here call the Halarauður eruption have previously been linked with formation of the Krafla caldera during the last interglacial (Björnsson et al., 1977; Calderone et al., 1990; Sæmundsson, 1991). They occur in patchy exposures around the caldera, up to ~7 km from its margin, and have also been identified in two intra-caldera boreholes, KH-1 and KJ-22 (Fig. 2.1; Guðmundsson et al., 1983). The deposits were first described by Björnsson et al. (1977) as a dacitic welded airfall tuff. Subsequent work by Calderone et al. (1990) identified a range of

compositions from basalt to rhyolite, which they attributed to magma mixing during basaltic recharge of a rhyolitic chamber. Based on $^{40}Ar/^{39}Ar$ dating, Sæmundsson and Pringle (2000) suggest an eruption age of 110-115 ka. A 201 ka age has also been proposed based on correlation of glass compositions with a marine tephra layer northeast of Iceland (Lacasse and Garbe-Schönberg, 2001), but appears to be inconsistent with field relationships between the deposits and other dated units (K. Sæmundsson, pers. comm., 2016).

The name "Halarauður" was coined by Kristján Sæmundsson during mapping of Krafla in the 1970's, and derives from "Halaskógafjall", a mountain on the southern boundary of the caldera where the deposits are easily accessed, and "rauð" (Icelandic for red), in reference to their distinctive colour (Á. Guðmundsson, pers. comm., 2019). The name appeared in Sæmundsson's overview of the Krafla system and a recent map of the Northern volcanic zone (Sæmundsson, 1991; Sæmundsson et al., 2012); however, in the only detailed study of the deposits to date, Calderone et al. (1990) referred to them simply as the "Krafla welded layer". Here we revert to Sæmundsson's original Icelandic name.

Calderone et al. (1990) divided the Halarauður deposits into five units (A-E, from base to top), which were all interpreted as fall deposits. Their conceptual model for the eruption involved a progression from Plinian phases erupting rhyolite (unit A), basalt (unit B) and then hybrid intermediate compositions (unit C), to lava fountaining of hybrid intermediate to basaltic compositions emplacing widespread welded fall deposits (the volumetrically dominant units D and E, respectively). We have revised this original stratigraphy and here offer a different interpretation in light of new field observations and data presented below.

2.4. METHODS AND TERMINOLOGY

2.4.1. Methods

We studied the Halarauður deposits over three consecutive field expeditions in the summers of 2016-2018. Deposit characteristics, including the preserved thickness, depositional and/or welding textures, and the component abundance and size of juvenile and lithic clasts were recorded at >100 sites around the caldera. We recognised three distinct stratigraphic units, H1-H3, based on lithofacies and dispersal characteristics. Dispersal patterns for H2 and H3 were characterised by constructing approximate isopach maps, but patchy dispersal and poor exposure prevented isopach mapping of H1.

Stratigraphic logging was performed at widely-spaced sites where the deposits are well-preserved. We studied deposits at these sites in detail using standard field and laboratory techniques, including grain size and componentry analysis of non-welded facies, density and vesicularity (φ)

TABLE 2.1. WELDING SCHEME FOR HALARAUÐUR DEPOSITS

Welding intensity	Description	Approximate density (g cm^{-3})
Non-welded	Loose, unconsolidated and undeformed. Can be disaggregated by hand. Individual clasts are easily extracted.	N.D.*
Incipiently welded	Some fragments loosely stuck together (sintered) at point contacts, but voids are present between clasts and clast edges are clearly recognizable. Clasts are easily extracted with a hammer.	N.D.*
Moderately welded	Clasts welded together with some flattening, but clastic texture is still apparent, and edges of individual clasts are mostly recognizable. Some void space between clasts is retained. Clasts cannot be extracted without fracturing the deposit. Weak welding fabric, spatter is commonly contorted and folded.	1.65 - 2.40 [1.66, 1.78, 1.78, 1.85, 2.00, 2.05, 2.07, 2.37]
Strongly welded	Clasts flattened and aligned with no void space between them. Matrix texture not recognizable but outlines of large (dm- to m-scale) juvenile clasts are often clear. Strong fabric defined by flattening of relict clasts and some vesicles, but no lineation. Banding may occur locally.	1.60 - 2.60 [1.61, 1.70, 1.80, 1.86, 1.88, 1.94, 1.95, 1.96, 2.06, 2.14, 2.22, 2.23, 2.27, 2.27, 2.43, 2.46, 2.47, 2.49, 2.60]
Very strongly welded	Almost no relict pyroclastic texture. Original clastic nature is only apparent from occasional clustering of vesicles, or faint "ghost" outlines of large clasts.	2.60 - 2.90 [2.59, 2.71, 2.71, 2.87]

Note: Measured densities are listed in square brackets.
*N.D. = not determined.

measurements of juvenile clasts, componentry analysis of lithic types, and major element analysis of juvenile products by X-ray fluorescence spectroscopy (XRF). Full details are in Appendix 1. Considerable breakage of large clasts occurred during grain size sampling, so these data are skewed towards finer sizes.

2.4.2. Terminology and Lithofacies Classification

We use 'spatter' as a purely descriptive term, to denote bomb-sized (>64 mm; Fisher, 1961) juvenile clasts with a fluidal form. 'Ignimbrite' refers to deposits containing variable proportions of juvenile clasts (pumice, scoria or spatter), ash and lithics that were deposited by pyroclastic density currents (Freundt et al., 2000). 'Welding' denotes the sintering together of hot clasts, either during or after deposition, to form a coherent 'welded' deposit.

Traditional quantitative measures, such as bulk density or clast aspect ratios, are poor proxies for welding intensity in the Halarauður deposits due to their high lithic content, common post-welding vesiculation, and local zones of noncoaxial shear. We thus describe welding intensities using a mostly qualitative scheme (Table 2.1). Lithofacies are described following the non-genetic scheme in Table 2.2.

2.5. ERUPTIVE STRATIGRAPHY

The most extensive Halarauður exposures are at Hágöng, a plateau of hyaloclastites and lavas steeply bounded on its eastern side and truncated by caldera faults to the southwest (Fig. 2.1). The deposits form a sheet across the plateau, locally thickening into small paleovalleys (landscape-

TABLE 2.2. LITHOFACIES SCHEME FOR HALARAUÐUR DEPOSITS

Lithofacies	Code	Description
Massive pumice-rich lithic breccia	mplBr	Massive, non-welded, poorly to very poorly sorted lithic breccia. Valley ponded, pinching out laterally over a few tens of metres. Lapilli-dominated matrix, ranging from ash-rich to ash-poor, with subequal proportions of angular to subangular pumice and lithics. Matrix supports ~20-30 vol% angular to rounded dm-scale lithic blocks, occasionally with concentrically cracked margins. Scarce outsized blocks up to ~1 m.
Pumice- and spatter-rich lithic breccia	pSplBr	Like mplBr, with matrix supporting up to ~20 vol% dm-scale black spatter bombs. Spatter is commonly imbricated.
Welded pumice- and spatter-rich lithic breccia	wpSplBr	Welded equivalent of pSplBr. Spatter are flattened/sheared.
Massive ash	mA	Massive, non-welded ash with minor lapilli.
Massive lithic-rich ash	mlA	Massive, non-welded ash with minor lapilli. Very lithic rich.
Spatter-rich agglomerate	SpAg	Non-welded. Massive to crudely bedded. Coarse, poorly sorted, matrix- to clast-supported mix of spatter bombs, lithic blocks and lapilli, with minor ash. >40-50 vol% dm-sized spatter. Moderate lithic content, typically ~5-10 vol%. Common dm-scale angular to rounded lithic blocks, occasionally with concentrically cracked margins.
Incipiently welded spatter-rich agglomerate	iwSpAg	Like SpAg, with pervasive incipient welding.
Heterogeneously welded spatter-rich agglomerate	hwSpAg	Heterogeneously welded equivalent of SpAg. Lithics commonly clustered in m- to dm-scale irregular or pod-like concentrations, where local lithic abundance reaches ~20-30 vol%. Lithic concentrations of ~2-5 vol% are typical elsewhere. Welding intensities are locally heterogeneous at the dm- to m-scale, typically with moderate welding around lithic concentrations, and higher intensities elsewhere. Welding intensities are often highest (strong to very strong) around large spatter bombs.
Eutaxitic spatter-rich agglomerate	eSpAg	Strongly welded SpAg. Outlines of only the largest spatter clasts are visible and highly flattened. Red and black flow banding is often well-developed locally.
Vitrophyre	Vit	m-scale lenses of black vitrophyre, dissociating into ~10 cm-thick moderately welded zones around the margins. Heterogeneously vesicular at the dm-scale, with outlines of relict clasts faintly visible locally.
Spatter-bearing lapilli tuff	SpLT	Non-welded. Massive or crudely bedded. Poorly sorted, lapilli-dominated matrix with minor to moderate ash, supporting up to ~30 vol% spatter bombs. Minor (<2-3 vol%) lithic blocks. Spatter commonly imbricated.
Welded spatter-bearing lapilli tuff	wSpLT	Welded equivalent of SpLT.
Pumice-rich spatter-bearing lapilli tuff	pSpLT	Like SpLT, with pumice-rich matrix.
Massive lava-like tuff	lava-like	Massive, very strongly welded throughout, resembling a lava flow. Very dense and vesicle-poor (ϕ <~2 vol%). Minor to moderate lithics (typically <10 vol%).
Lava-like tuff with fabric	lava-like-f	Vesicular equivalent of lava-like tuff (ϕ up to ~20%). Moderate to strong fabric defined by highly flattened vesicles and cm-scale partings. Lithic-poor (2 vol%).

burying; Brown and Andrews, 2015), and can be traced in near-continuous exposure along the plateau margins. Additional good exposures occur in incised gullies draining Hágöng to the north, and near the southeast and southwest caldera margins.

We divide the Halarauður deposits into three major stratigraphic units, H1-H3 from base to top, based on characteristic differences in lithofacies and dispersal (summarised in Table 2.3; Figs. 2.2, 2.3). H2 and H3 are further divided into subunits at proximal sites on the northeast caldera margin (and some more distally for H3) based on vertical changes in overall welding intensity and other lithofacies characteristics detailed below. Juvenile clast compositions span a continuous range from basalt to rhyolite, and correlations between all elements are highly linear (Fig. 2.4). Compositions are more mafic on average up-section, but successive stratigraphic units show some overlap. All units are very crystal poor (<1 modal% plagioclase + clinopyroxene). Here we outline the features of each unit and our interpretations. Detailed logs of key sites, where not included in this chapter, are in Appendix 2.

TABLE 2.3. CHARACTERISTICS OF HALARAUÐUR UNITS

Unit	Preserved volume (km^3)	Dispersal	wt% SiO_2	Major lithofacies	Minor lithofacies
H1	Poorly constrained, <0.01	Sporadic, valley-ponded lenses. Preserved up to ~7 km from caldera	60-9 - 74.6 (Andesite to rhyolite)	mplBr pSplBr	wpSplBr pSpLT iwSpAg mA mlA Vit
H2	~0.1	Landscape-burying sheet. Preserved up to ~7 km from caldera	54.5 - 69.4 (Basaltic andesite to dacite)	SpAg hwSpAg	SpLT wSpLT eSpAg
H3	~0.04	Landscape burying sheet. Preserved up to ~4 km from caldera	50.0 - 54.6 (Basalt to basaltic andesite)	lava-like lava-like-f	SpLT wSpLT

Figure 2.2. a, b) Approximate isopach maps for a) H2 and b) H3. True thickness measurements (in metres) are labelled in bold italics; all other thicknesses are minima. c) Median of the average dimension ([longest axis + shortest axis]/2) of the five largest lithics at H2 and H3 outcrops vs. distance from the caldera margin. The digital elevation model is from Porter et al. (2018).

2.5.1. H1

2.5.1.1. Dispersal and Characteristics

H1 comprises small-volume, poorly exposed pumice-bearing lithic breccias (± spatter; mplBr, pSplBr and wpSplBr; Table 2.2), and distally equivalent pumice- and spatter-rich lapilli tuffs and agglomerates (pSpLT and iwSpAg). The deposits occur sporadically as topographically-ponded lenses up to ~5 m thick (typically 1-2 m), pinching out laterally over a few tens of metres. An ~6

Figure 2.3. Scaled stratigraphic logs of Halarauður deposits, showing correlations between key sites (labelled in Fig. 2.1).
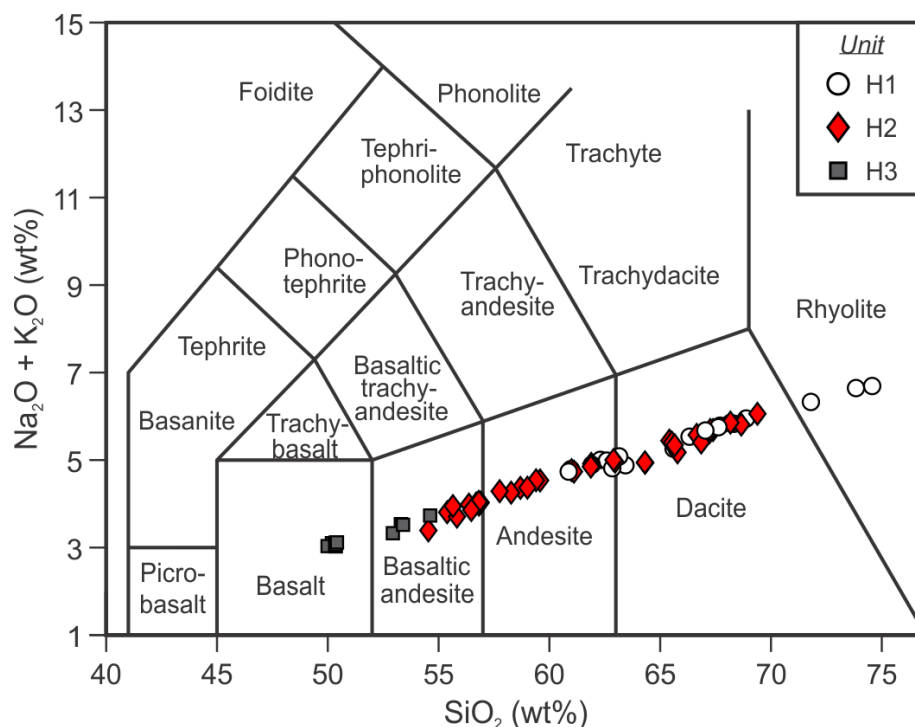
Figure 2.4. Total alkali vs. silica (TAS) diagram for Halarauður juvenile products. Analytical uncertainties are smaller than the symbols.

m section of H1 mplBr was also observed in core from the KH-1 borehole near the southeast caldera margin. H1 deposits are absent at almost all sites where the base of the Halarauður sequence is exposed and consequently their distribution is not mappable. Volume constraint is poor, but considering their absence at most sites and low average thickness relative to H2 and H3, we estimate H1 deposits comprise <5% of the total preserved volume. Basal contacts are sharp and unconformable with hyaloclastites and lavas.

H1 juvenile clast compositions range from andesite to rhyolite (60.9 – 74.6 wt% SiO_2; Fig. 2.4), and magma mixing textures are ubiquitous. Fluidal streaks or filaments of contrasting melt composition are typical of spatter (most easily seen in thin section), while red or purple mafic enclaves up to ~1 cm in size are a minor matrix component. Small enclaves (<3 mm) are also

ubiquitous as inclusions in pumice clasts (comprising ~1-2 vol%), and are interpreted as juvenile products based on their crenulate margins and microcrystalline quench textures (cf. Bacon, 1986).

H1 lithic breccias are best-exposed at sites C and H (Figs. 2.3, 2.5a-d, A2.1, A2.2), where they show an upward transition from massive and spatter-free (mplBr) in their lower 20-30%, to spatter-bearing, with crude bedding defined by weak alignment of spatter long axes (pSplBr). The breccia becomes incipiently welded at the very top (wpSplBr) before grading into H2 over ~30 cm. At site C, a ~10 cm basal layer of massive, lithic-rich ash (mlA) with minor pumice lapilli grades up into the breccia over ~3 cm. At both sites the breccia is coarse and poorly sorted (e.g., Md_ϕ = -4.8 and σ_ϕ = 2.6 at site C). Approximately 20 vol% angular to rounded lithic blocks up to ~60 cm (plus rare outsized blocks >1 m) are supported in a lapilli-dominated matrix comprising sub-equal proportions of angular to sub-angular lithics and white to grey pumice, with minor ash. White pumices are moderately to extremely vesicular (e.g., φ = 59-84% at site C, mean = 75%), while slightly lower vesicularities occur in the grey variety (φ = 50-73% at site C, mean = 72%). Spatter clasts are black and poorly to non-vesicular (φ <20%), reaching a maximum of ~60 cm in length. Breadcrusted spatter margins and non-vesicular quenched rinds up to ~1 cm thick are common at site C.

H1 breccias at sites D and E have yellowish interstitial ash and sharp contacts with overlying deposits (Figs. 2.6, A2.3). At E, a ~10 cm-thick bed of consolidated, yellow, lithic-free ash (mA) with occasional aggregates overlies the breccia (Fig. 2.5e, f). The layer is dominated by fine ash (37 wt% <63 µm), and its top has been eroded during subsequent emplacement of H2, forming rip-ups in the lower few centimetres of H2 (Fig. 2.5f).

Figure 2.5. Representative photographs of H1 lithofacies. a) Lens of ponded H1 breccia at site C, gradational with overlying H2. Arrow points to ~1.5 m outsized lithic clast. Insets b) and c) show mplBr and pSplBr facies, respectively. Note imbrication of spatter in c). d) Lithified pSplBr at site H. Spatter are partially glassy and commonly flattened. Note imbrication of some clasts (arrowed). e) Thin mA layer overlying mplBr at site E. Close-up of the layer f) shows cm-sized rip ups at the top of the layer (arrowed). Interstices are filled by orange-brown H2 ash.

The most distal H1 outcrops are at sites F and G. At F, a > 2 m-thick basal pumice-rich and spatter-bearing lapilli tuff (pSpLT) transitions up-section to incipiently welded spatter agglomerate

(iwSpAg) with metre-scale vitrophyre lenses (Vit), which grades up into H2 (Figs. 2.7, 2.8). White (φ = 56-76%, mean = 69%) to grey (φ = 46-81%, mean = 66%) pumice dominate the lapilli-rich matrix in the pSpLT and grade out in the agglomerate, where less vesicular black clasts dominate (φ = 34-70%, mean = 56%). Lithic abundance is 5-10 vol%. At G, H1 overlies fluvial gravels in sharp contact. A thin ($\leq$3 cm), laterally discontinuous and poorly sorted basal layer of fine white ash, pumice and lithic lapilli partially infills the relief of the contact. This layer is truncated by a ~2 m-thick deposit of incipiently welded spatter agglomerate (iwSpAg) with local lenses of moderate welding, which we correlate with the iwSpAg and Vit at site F.

H1 lithic assemblages are dominated by mafic lavas, but site-specific variations in their overall proportion (57-89% of clasts) and petrography (e.g., dominance of crystal-rich vs. crystal-poor types) are considerable. Plutonic lithics are exclusively mafic, and relative abundances also vary greatly between sites (0-43%). Hyaloclastites and altered lithics are minor to absent (each $\leq$9%).

2.5.1.2. Lithofacies Interpretation

The local, ponded distribution of H1 implies deposition from topographically-confined flows. Lateral emplacement is also supported by the very poor sorting, a lack of hydraulic equivalence among pumice lapilli, spatter bombs and large lithic blocks, an absence of ballistic impact-sags, and imbrication of spatter.

We interpret mplBr, pSplBr and wpSplBr as co-ignimbrite breccias associated with vent-opening and the possible onset of caldera collapse (Druitt and Sparks, 1982; Walker, 1985; Branney and Kokelaar, 2002). The fines-poor matrix at most sites is typical of co-ignimbrite

Figure 2.6. Stratigraphic log of site D, showing vertical variations in lithofacies, bulk composition and lithic componentry.

Figure 2.7. a) Outcrop at site F. Ponded H1 pSpLT grades into iwSpAg, overlain by H2. b) Close-up of iwSpAg, dominated by black spatter and lapilli. c) Close-up of pSpLT, showing ~50 cm black tapered spatter bomb in matrix of white to grey pumice.

breccias , implying substantial elutriation of ash during transport and/or fluid escape during deposition from a concentrated lower flow boundary. The thin basal mlA layer at site C is interpreted to reflect percolation of fine-grained (mostly dense lithic) material between large clasts in the concentrated basal part of the flow (Branney and Kokelaar, 2002).

Figure 2.8. Stratigraphic log of site F, showing vertical variations in lithofacies, bulk composition and lithic componentry.

We interpret the ~10 cm mA layer overlying the breccia at site E as co-ignimbrite ash deposited during a break in flow passage at this site. Occasional ash aggregates in this layer and the presence of rip-ups at the top of the layer, which requires cohesion between grains, both suggest that the ash was deposited wet. Although this could suggest a phreatomagmatic origin, we found no blocky shards indicative of magma-water interaction; instead, the ash was probably flushed from the co-ignimbrite plume by a local shower. Restriction of this facies to site E only implies that the corresponding break in flow passage was a local feature and does not reflect an eruptive pause. The sharp contact between H1 and H2 at site D may reflect a similar short local depositional break, or local erosion of the top of H1 by a sustained flow in which the lower flow boundary temporarily became erosive. Gradational contacts between H1 and H2 at sites C and H and upward increases in spatter abundance indicate the deposit aggraded progressively from a sustained flow (Branney and Kokelaar, 1992, 2002) that received an increased supply of spatter over time. Reverse coarse-tail grading of spatter could also reflect an increase in current competence, but this seems unlikely given that lithics are not similarly graded.

The H1 deposits at sites F and G are interpreted as fines-poor, spatter-rich ignimbrite. They were likely deposited from the same sustained current(s) that deposited the proximal lithic breccias. The lower H1 deposits at site F mainly consist of low density pumice that was able to bypass the depositional lower flow boundary at proximal sites where dense lithics were preferentially deposited. The upward-increasing abundance of spatter at site F correlates with similar increases upward through H1 breccias at sites C and H, implying deposition by progressive aggradation with an increased supply of spatter to the current over time. This increased proportion of spatter relative to lithics increased heat retention, allowing upper parts of H1 to incipiently weld at sites G and F. We interpret the vitrophyre lenses at site F to reflect agglomerations of spatter

clustered around outsized clasts that effectively retained heat and kept temperatures hot enough to weld locally.

2.5.2. H2

2.5.2.1. Dispersal and Characteristics

H2 is the most widely dispersed and volumetrically dominant unit, with a preserved volume of ~0.1 km^3. The unit is composed of variably welded spatter-rich agglomerates (SpAg, hwSpAg, and eSpAg; Table 2.2, Fig. 2.9), which transition laterally to spatter-bearing lapilli tuffs (SpLT and wSpLT; preserved only at the most distal site, G). The deposits are thickest near the caldera margins (~16 m at site A; Fig. 2.10) and gradually thin outwards, locally thickening into small paleovalleys and thinning across paleo-highs (Figs. 2.2, 2.11). Maximum lithic sizes also decrease outward from the caldera (Fig. 2.2c). An anomalously thick exposure of ~15 m occurs at the most distal site (G), where overlying volcaniclastic deposits have protected the unit from glacial erosion (Figs. 2.9g, A2.4). Elsewhere, where not overlain by H3, the tops of H2 outcrops are erosional and form the modern landscape surface (± soil cover). Where H1 is absent (most sites), basal H2 contacts are sharp and unconformable with hyaloclastites and lavas.

H2 juvenile compositions span a continuous range from basaltic andesite to rhyodacite (54.5-69.4 wt% SiO_2; Fig. 2.4), becoming more mafic on average up-section (e.g., Figs. 2.6, 2.10). Fluidal magma mixing textures are common, with light grey- to cream-coloured silicic blebs and filaments up to several centimetres in length comprising up to 5 vol% of the unit (Fig. 2.9f). The deposits are grey-black where non-oxidised, but red oxidation is typical. Vertical gradation between lower oxidised and upper non-oxidised H2 deposits occurs at some sections (e.g., site C;
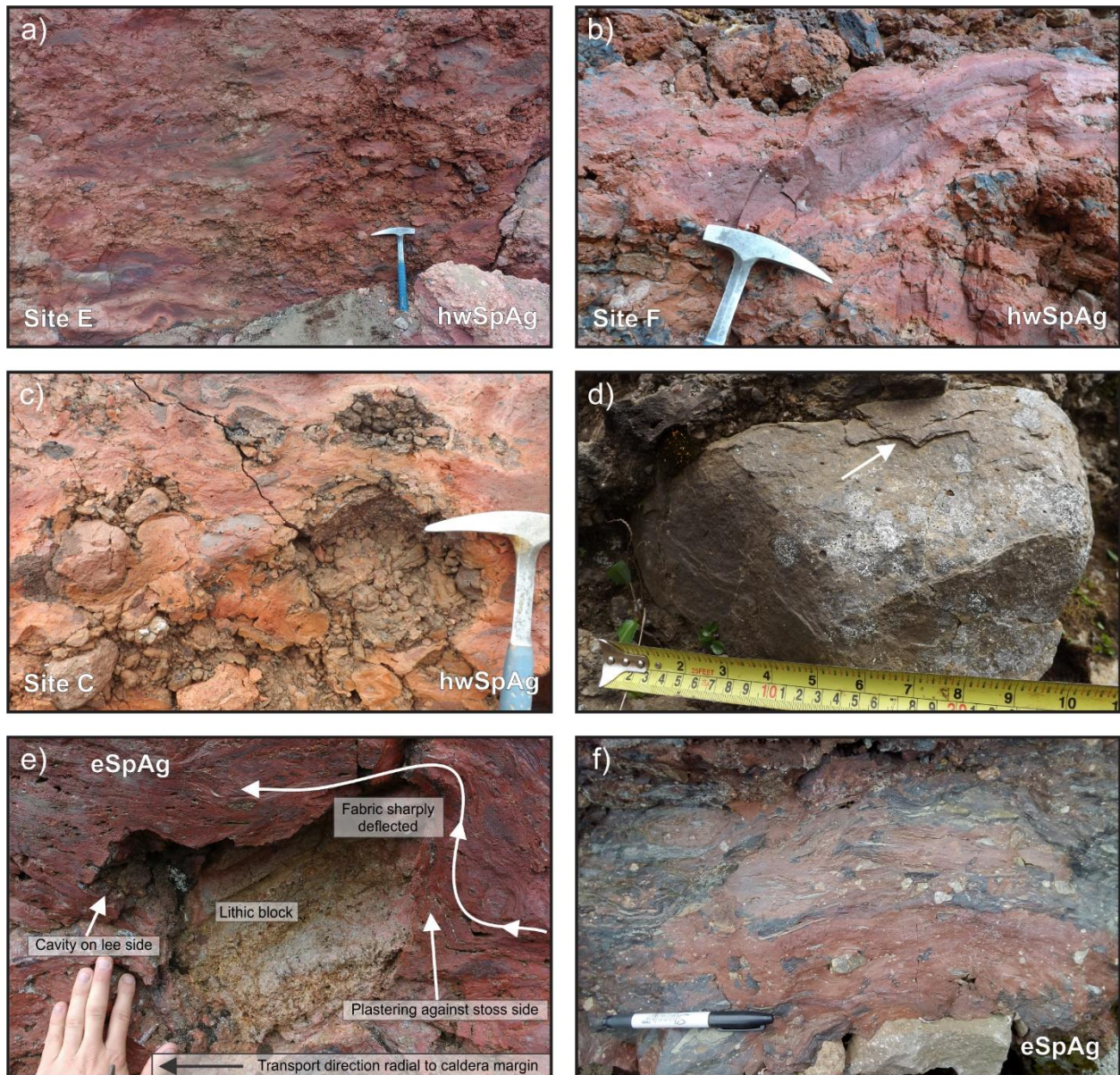
Figure 2.9. Representative photographs of H2 lithofacies. a) Lithofacies hwSpAg at site E. Note pervasive oxidation and heterogeneous welding. b) ~50 cm tapered spatter bomb at site F, with halo of high welding intensity around the margin. c) Lithofacies hwSpAg at site C. Note the lower welding intensities locally around lithic concentrations. d) Flaky, concentric cracks on sub-rounded lithic clast hosted in hwSpAg. e) Plastering of material against a lithic block near site H. f) Lithofacies eSpAg at site A. Pale grey streaks are silicic material, indicative of magma mixing. (Continues over page).
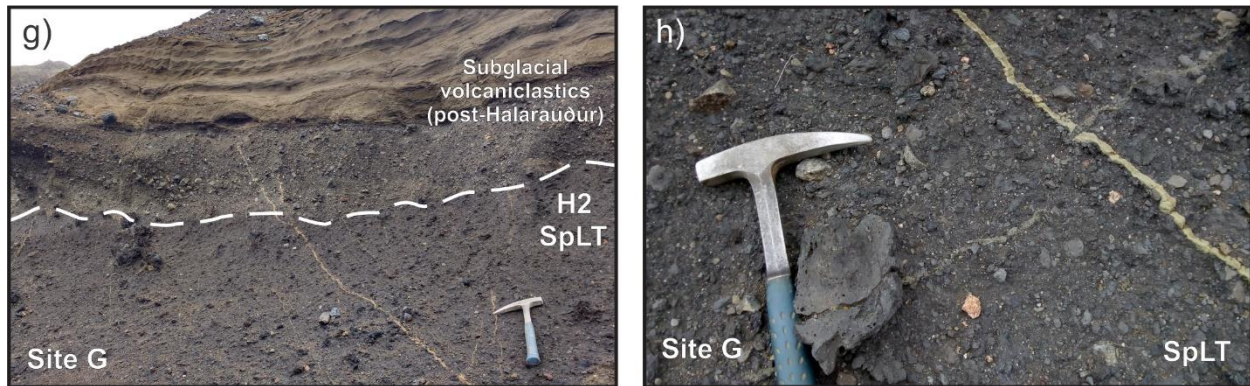
Figure 2.9. (Continued) g, h) Non-oxidised lithofacies SpLT at site G, overlain by post-Halarauður subglacial volcaniclastic deposits sourced from a nearby hyaloclastite ridge to the west. Cross-cutting clastic dikes (pale yellow) penetrate the volcaniclastics, so are post-Halarauður features.

Fig. A2.1). Sharp lateral transitions between pervasively oxidised and non-oxidised H2 deposits also occur, but do not correspond with changes in facies or thickness.

Spatter agglomerates consisting of $\geq$40-50 vol% decimetre-scale spatter clasts (SpAg and welded equivalents) dominate H2 at all but the most distal site (Figs. 2.3, 2.9). Non-welded facies are coarse and very poorly sorted (Md_φ = -4.5 to -5.3, σ_φ = 2.3 – 3), plotting within the lag breccia field on the σ_φ vs. Md_φ diagram of Walker (1985). Juvenile clast vesicularities show a broad range (φ = 5-69%), with site-specific averages of 32% (A), 33% (J) and 52% (F). Maximum spatter lengths are ~50-100 cm at most sites, with occasional outsized bombs up to ~4 m in length near the caldera margin. Minor deformation and contortion of individual spatter clasts are typical, but strong horizontal shearing is rare and occurs only locally. Clast aspect ratios rarely exceed 10:1, and a pervasive rheomorphic lineation is absent. Flow banding is common in individual spatter clasts, but the limited deformation of the clasts themselves implies that it formed during shearing in the conduit prior to fragmentation rather than during syn- or post-depositional rheomorphism. Individual spatter clasts host up to ~5 vol% inclusions of ash- to lapilli-sized lithics (<2 cm), with
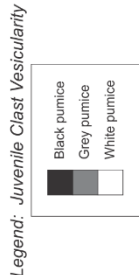
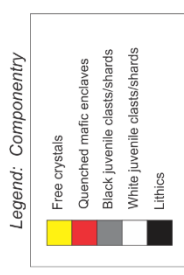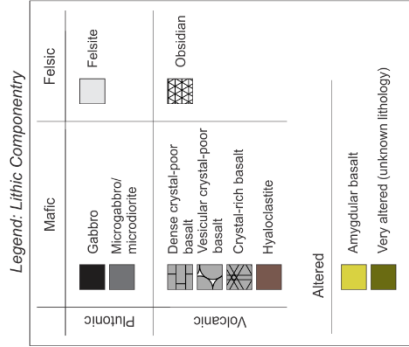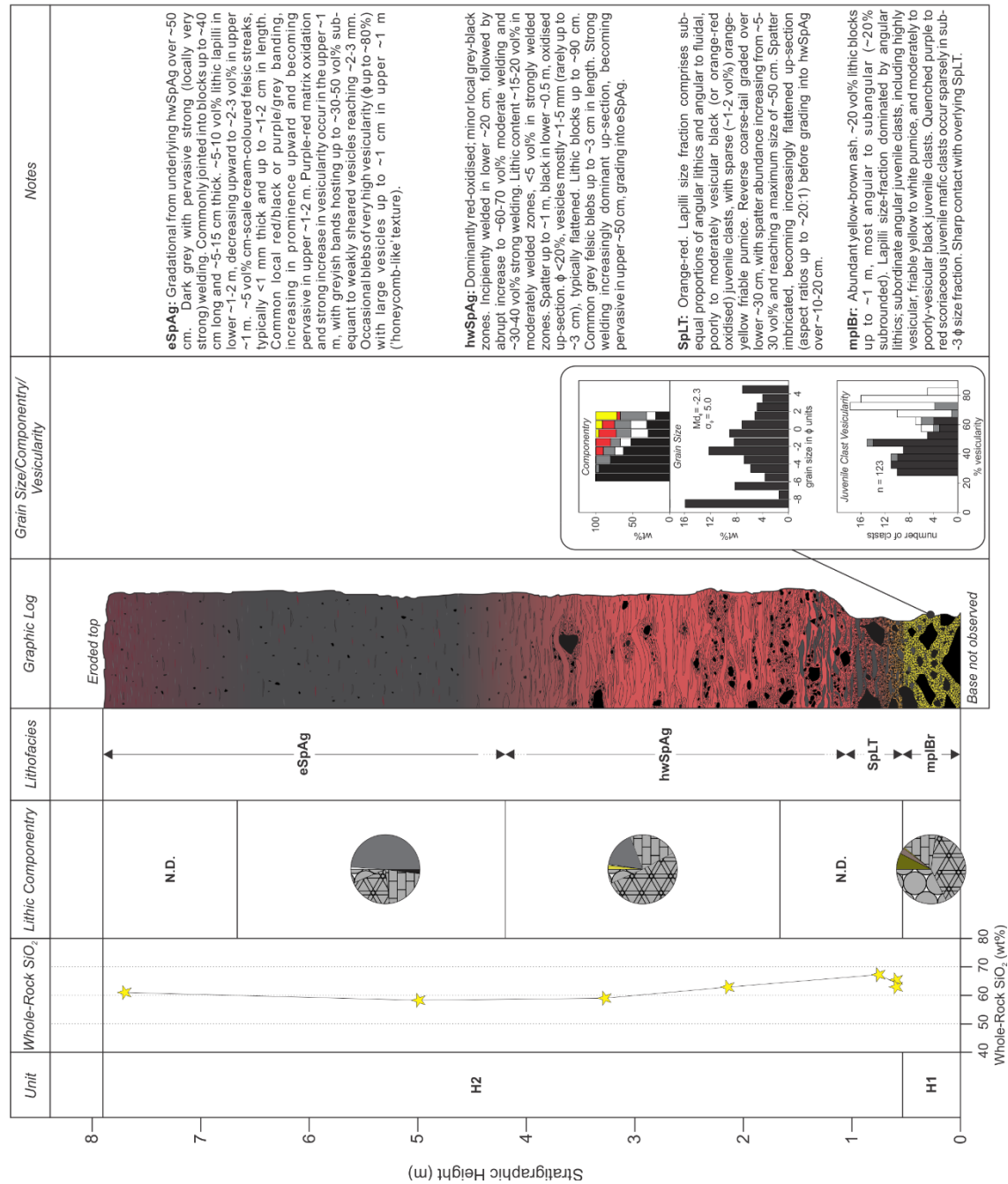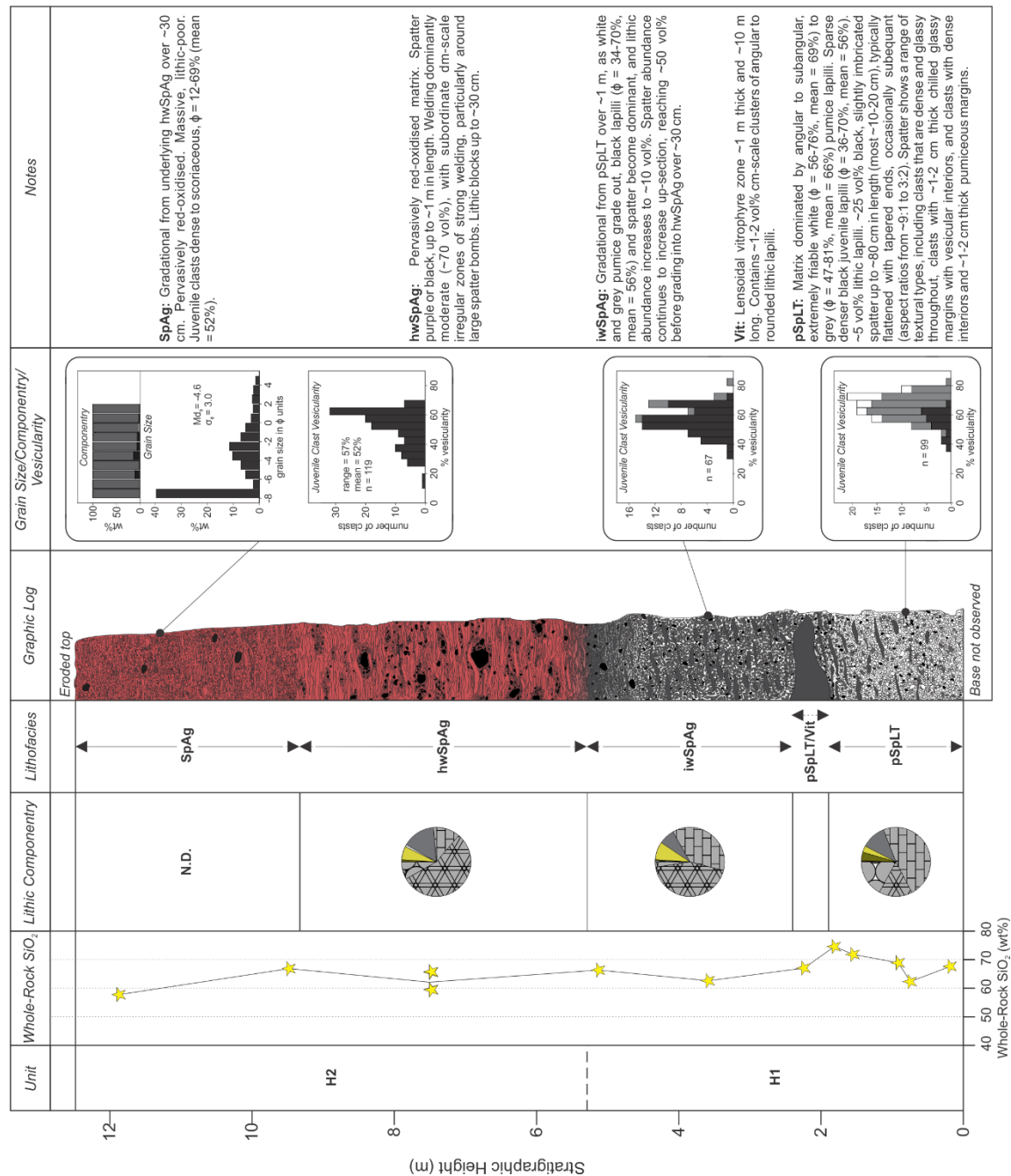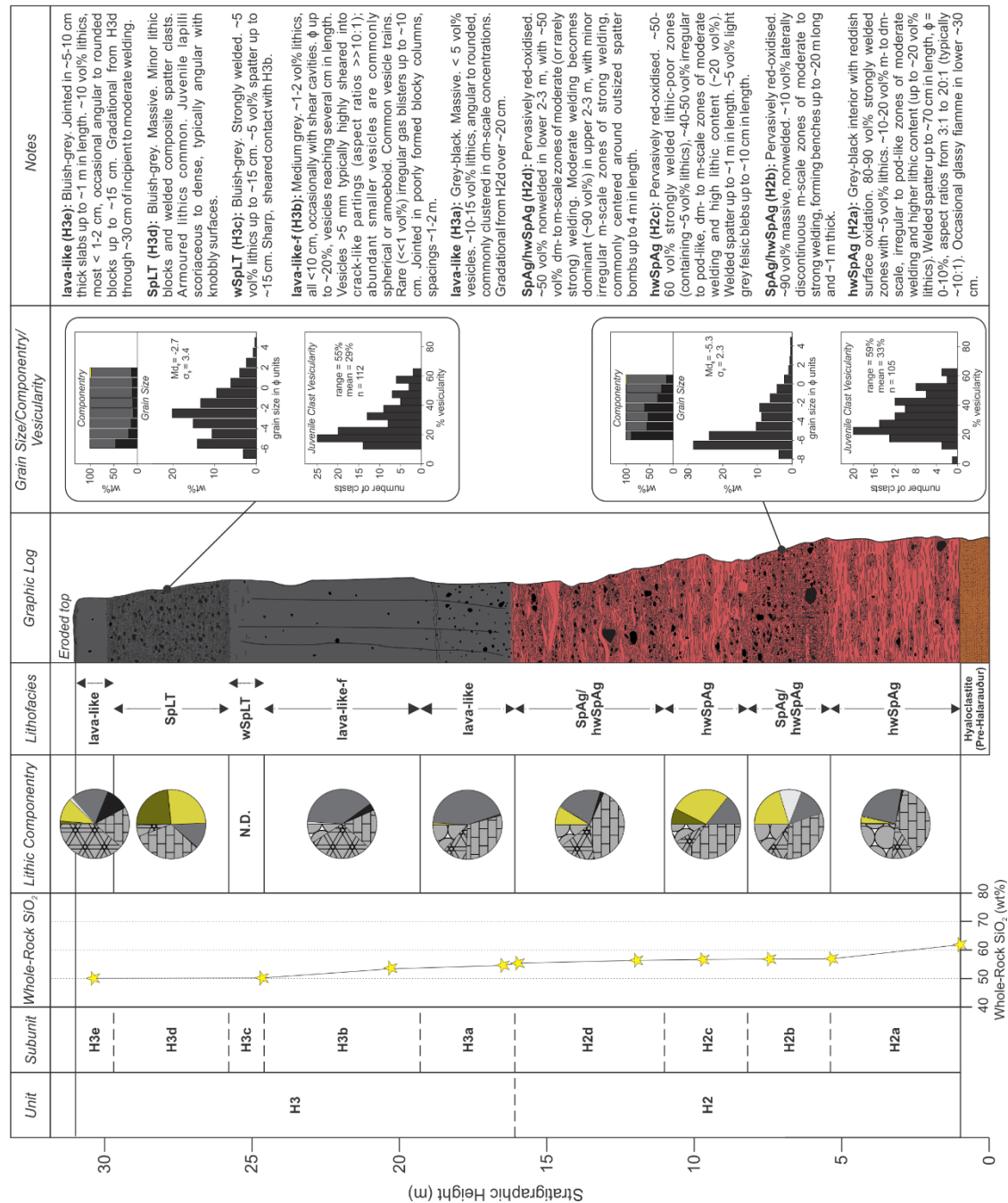**Figure 2.10.** Stratigraphic log of site A, showing vertical varia0tions in lithofacies, bulk composition and lithic componentry.

diverse lithologies often present in a single clast. Spatter surfaces are typically ropy where not overprinted by welding (i.e., incipient to moderate welding; Table 2.1), but occasional breadcrust textures also occur. At the most distal site, G (Fig. A2.4), poorly-sorted lapilli tuffs with ~5 vol% spatter (SpLT and wSpLT; $Md_\varphi = -0.9$, $\sigma_\varphi = 3.1$) are correlated with H2 based on bulk composition and interpreted as distal equivalents of the agglomerates (Fig. 2.9g, h). Juvenile clast vesicularities are similar to those in SpAg ($\varphi = 0$-71%, means of 35% and 46%).

Lithic fragments comprise an average of ~5-10 vol% of H2 at a given site. Most are ash- to lapilli-sized, but decimetre-scale blocks are common, and rare outsized blocks reach up to 2 m in size. Many blocks have flaky, concentrically-cracked margins (Fig. 2.9d), and at least 50% are sub-rounded to rounded. In welded facies, lithic distribution is strongly clustered at the decimetre- to metre-scale, with many lithics concentrated in irregular or pod-like zones where their abundance reaches ~20-30 vol% (Fig. 2.8f, g). Abundances of <5 vol% are typical outside these zones. Lithic assemblages are dominated by mafic lavas (60-79% at a given site), but like H1 the proportions of different petrographic types vary greatly between sites. Plutonic lithics are mostly mafic and comprise 5-37% (typically ~10-20%). Altered lithics comprise 1-19%, but hydrothermally altered types are rare ($\leq$2%). Significant vertical changes in lithic componentry, including the relative abundance of plutonic and/or altered clasts, are typical through all H2 (e.g., Figs. 2.6, 2.10), but do not show systematic trends between sites.

2.5.2.2. Welding

Welded facies (hwSpAg ± eSpAg) dominate H2 at all but the most distal outcrop (site G). The
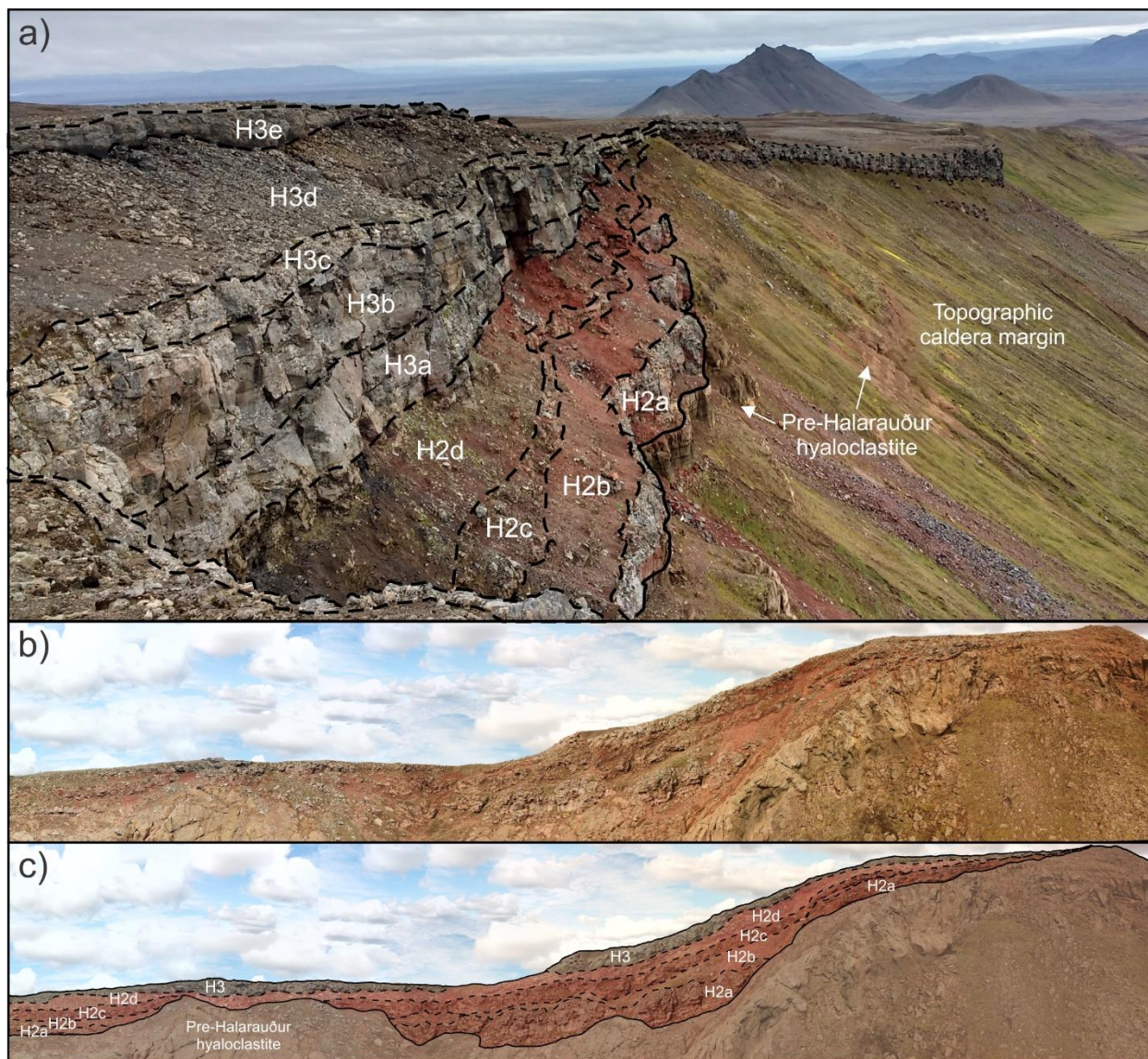
Figure 2.11. a) Halarauður deposits overlying hyaloclastites at site A. View is facing southeast, along the caldera fault scarp. H2 and H3 subunits are demarcated. The entire sequence is ~30 m thick. b, c) Halarauður deposits overlying hyaloclastite at site I (maximum thickness is ~20 m) on the eastern margin of Hágöng. Interpretation of subunits are shown in c); note the progressive infilling of topography by subsequent subunits.

dominant facies, hwSpAg, is characterised by marked vertical and lateral variations in local welding intensity, with irregular to pod-like, metre- to decimetre-scale zones of moderate welding commonly centered around lithic concentrations (Fig. 2.9c), and haloes of strong to very strong

welding around the margins of large spatter clasts (Fig.2.9b). Eutaxitic facies with homogeneous

strong welding throughout (eSpAg; Fig. 2.9e, f) are minor. At outcrop scale, the overall 'average'

welding intensity of H2 (analogous to the 'regional welding' of Carey et al., 2008a) is laterally

invariant, but vertical gradients are common. These gradients are not easily correlated between

sites, and show no relationship with either the deposit thickness or distance from the caldera. An

exception is near the northeast caldera margin (e.g., sites A and J), where vertical transitions in

average welding intensity are traceable over several kilometres, allowing recognition of four

proximal subunits (H2a-H2d, from base to top; Figs. 2.10, A2.5), which progressively fill the

paleotopography (Fig. 2.11).

2.5.2.3. Lithofacies Interpretation

The fluidal forms of H2 spatter clasts indicate deposition in a hot and plastic state. H2 spatter-rich

agglomerates superficially resemble vent-proximal deposits of Hawaiian or Strombolian eruptions

(e.g., Wolff and Sumner, 2000), and were interpreted as welded Strombolian fallout by Calderone

et al. (1990; their unit D). However, many features of these deposits are inconsistent with fall

deposition, and instead imply that emplacement was lateral (i.e., by flow). Evidence for deposition

after significant lateral transport includes: 1) wide dispersal of spatter-rich facies (cf. Brown et al.,

2014); 2) ponding in paleovalleys and onlapping against paleo-highs (Fig. 2.11); 3) very poor

sorting of non-welded facies, and grain size parameters that plot within the lag breccia field of

Walker (1985); 4) little change in grain size or facies with distance from the caldera; 5) plastering

of juvenile material on the stoss side of lithic blocks (Fig. 2.9e; cf. Valentine et al., 2000); 6)

absence of bomb sags or impact structures; 7) spalled margins of lithic blocks, indicative of hot

emplacement (Fig. 2.9d; Branney and Kokelaar, 2002); 8) welding at distances greater than several

kilometres from vent (cf. Thomas and Sparks, 1992; Capaccioni and Cuccoli, 2005); 9) common imbrication of spatter clasts; and 10) local intergradation with H1 lithic breccias. The presence of H2 across paleo-highs as well as in valleys and absence of basal autobreccias or pervasive rheomorphic structures indicate that coherent post-depositional flow was not significant for H2 and rule out an origin as a fountain-fed lava (cf. Sumner, 1998). We thus interpret H2 agglomerates (SpAg and welded equivalents) as coarse proximal ignimbrite deposited rapidly by progressive aggradation from the relatively concentrated flow boundary zones of energetic, density-stratified, spatter-rich pyroclastic density currents (Branney and Kokelaar, 1992, 2002; Valentine et al., 2000). SpLT and welded equivalents at site G are interpreted as their more distal equivalents, comprised of mostly finer-grained material that bypassed the depositional lower parts of the flow at proximal sites where coarse spatter was preferentially deposited. The origin of these currents and their implications for the eruptive dynamics are addressed in the discussion below.

The absence of any systematic relationship between overall 'average' welding intensity and deposit thickness in H2 implies that welding was not strongly influenced by load compaction, but instead governed by syn-depositional agglutination of very hot low-viscosity particles (Branney and Kokelaar, 1992). High emplacement temperatures and agglutination were enhanced by the abundance of coarse spatter, which effectively retains heat during transport due to its low surface area relative to volume (Thomas and Sparks, 1992; Capaccioni and Cuccoli, 2005). We interpret local variations in welding intensities at the centimetre to decimetre-scale (hwSpAg) to reflect diverse local cooling rates in the heterogeneous deposit. Faster cooling around concentrations of cold lithic clasts produced zones of less intense welding (Eichelberger and Koch, 1979) and prevented total coalescence of spatter clasts, while slower cooling around large hot

spatter bombs intensified welding locally (Carey et al., 2008b) and allowed some particles to coalesce.

2.5.3. H3

2.5.3.1. Dispersal and Characteristics

The uppermost unit, H3, is preserved only at sites within ~4 km of the caldera, mainly east of the fissure swarm (Fig. 2.2; preserved volume ~0.04 km^3). Preservation is typically poor and the top is eroded in all exposures, forming the modern landscape surface (± soil cover). The unit comprises a lower sequence of lava-like welded tuff facies (lava-like, lava-like-f; Unit E of Calderone et al., 1990), overlain by non-welded to welded spatter-bearing lapilli tuffs (SpLT and wSpLT; Fig. 2.12). Juvenile clast compositions range from basalt to basaltic andesite (50.0-54.6 wt% SiO$_2$; Fig. 2.4) and are increasingly mafic up-section (e.g., Fig. 2.10). Like H2, the unit is thickest near the caldera (maximum of ~18 m at site A) and thins outward as a sheet. Local thickening into paleovalleys is typically subtle due to prior infilling by H2; rare exposures without basal H2 pond in valleys (Fig. 2.12g). Lower contacts with H2 are usually gradational over ~10-20 cm (Fig. 2.12a), but are sharp at some of the most distal outcrops.

We recognise five distinct H3 subunits (H3a-e, from base to top) based on vertical lithofacies transitions at sites near the northeast caldera margin, all of which are traceable over several kilometres across Hágöng (e.g., between sites A and J; Figs. 2.10, A2.5). H3a and H3b can also be traced east of Hágöng and near the southeast caldera margin at Halaskógafjall (site K; Fig. A2.6), where H3b is cut by an erosional surface.
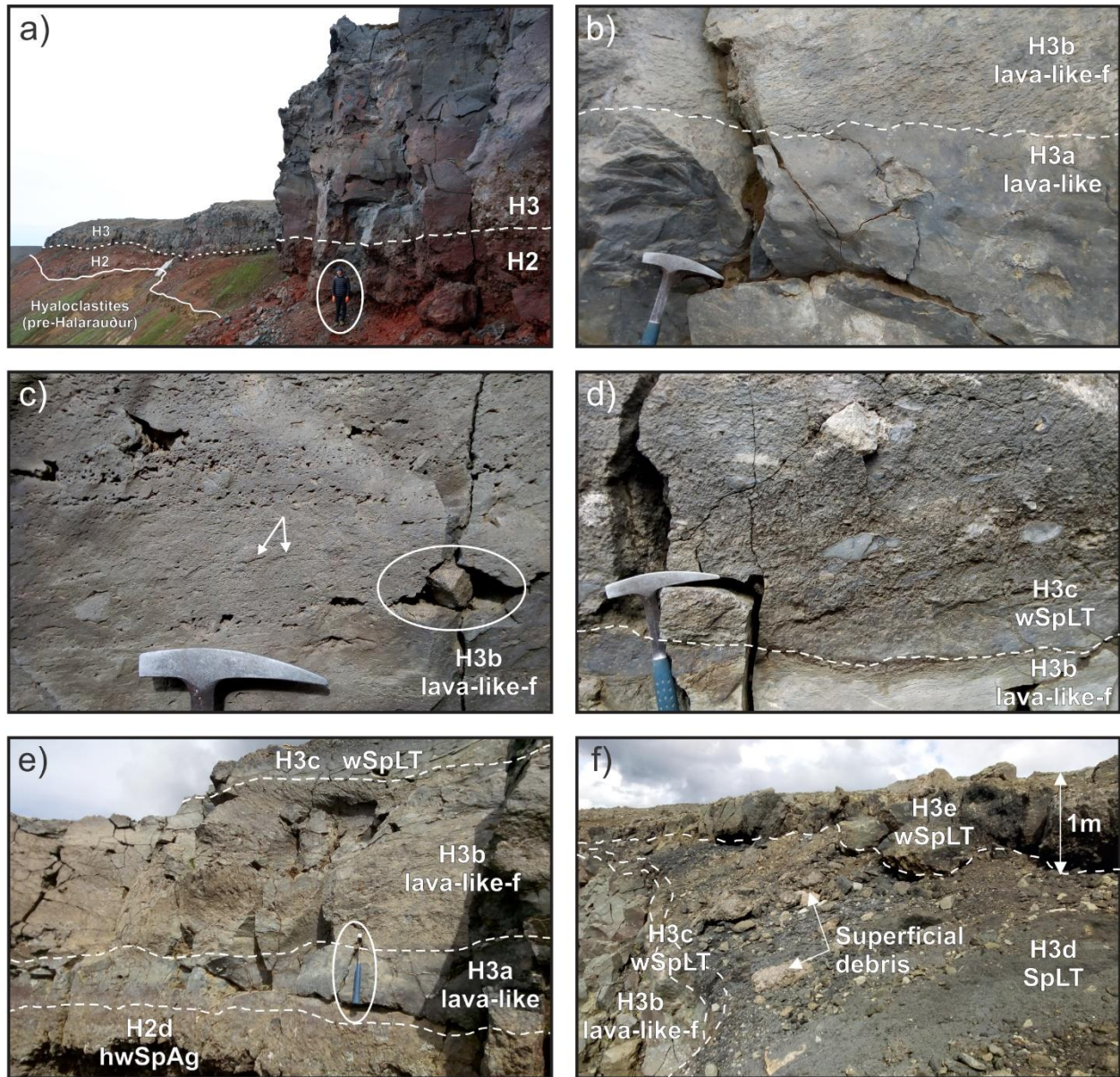
Figure 2.12. Representative photographs of H3 lithofacies. a) Gradational contact between H2 and H3 near site A on the northeast caldera margin. Person (circled) for scale. b) Sharp contact between H3a and H3b near site A. Note the moderate lithic content of H3a and their absence in H3b. c) H3b, near site A. Note the strain shadow around the lithic clast (circled), the fabric defined by flattened vesicles and partings (arrowed), and the abundance of unflattened (late stage) vesicles. d) Contact between H3b and strongly welded H3c near site A. e) Lower H3 subunits at site J. Hammer (circled) for scale. f) Upper H3 subunits at site J truncated by erosional surface. (Continues over page).
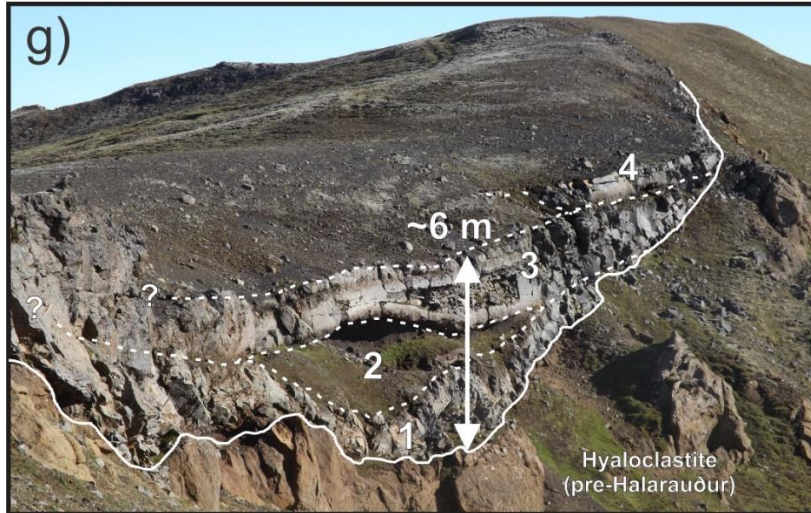
Figure 2.12. (Continued) g) Ponded H3 at site B (interpreted as upper H3 sequence). Complex lensoidal welding relations reflect onlapping 'packages' deposited from a sequence of at least four flow pulses (numbered), with channeling of earlier deposits by later flows.

H3a is a grey-black, massive lava-like tuff (lava-like; Fig. 2.12b) with moderate lithic content (~10 vol%) and low vesicularity (φ <2%). The contact with overlying H2b is typically sharp and often demarcated by a ~10 cm zone of sub-horizontal joints. H3b (lava-like-f; Fig. 2.12c) is distinguished by an increase in vesicularity (φ ~20%) and decrease in lithic content (~1-2 vol%), as well as a moderate to strong fabric defined by sheared vesicles and centimetre-scale crack-like partings (Fig. 2.12c). Cavities around rotated lithics and minor local (decimetre-scale) contortion of the H3b fabric are common. Blocky jointing is typical of both lava-like facies, with crudely formed columns defined by ~1-2 m-spaced sub-vertical joints cutting across both subunits in outcrops along the caldera rim.

At Hágöng, where not truncated by erosion, the lava-like subunits are overlain by a sequence of bluish-grey, variably welded spatter-bearing lapilli tuffs (SpLT and wSpLT; the latter is locally lava-like at site A). Non-welded facies are coarse and poorly sorted (Md_ϕ = -3.0 to -0.4, σ_ϕ = 3.1 – 3.3), and juvenile clast vesicularities vary widely (φ = 1-67%; site averages are 29-33%). Lithic clasts coated with a rind of dense juvenile material are common. Subunits H3c-e are

defined at sites on the caldera margin, where a central non-welded layer up to 4 m thick (SpLT; H3d) grades between upper and lower strongly welded layers (wSpLT or lava-like; H3c and e; Figs. 2.10, 2.11). Several interbedded SpLT and wSpLT layers, each ranging from decimetres to several metres in thickness, are also exposed in gullies draining Hágöng to the west, and at site B where complex lensoidal welding patterns allow at least four depositional 'packages' to be identified (Fig. 2.12g). These are interpreted as part of upper H3, but much of the unit has likely been eroded, and correlations between sites and with subunits H3c-e are tenuous.

At sites where both units are preserved, the H2-H3 transition coincides with a marked increase in the relative abundance of plutonic lithics (Figs. 2.10, A2.6), which comprise 29-33% of the total H3 lithic assemblage at each site. Mafic lavas remain the dominant component, however, comprising 52-60% of clasts. Altered lithics comprise 10-15% of H3 lithics, but are particularly abundant in H3d where they comprise 50% (Fig. 2.10).

2.5.3.2. Lithofacies Interpretation

Despite the absence of clastic textures, the lava-like subunits H3a and b grade both upward and downward into demonstrably pyroclastic deposits, thicken into paleovalleys but also cover paleo-highs, and lack both the upper and basal autobreccias typical of lava flows. We thus interpret them as lava-like ignimbrite, deposited from extremely hot currents in which clast viscosities were sufficiently low to allow complete coalescence upon deposition (extremely high-grade ignimbrite sensu Branney and Kokelaar, 1992). Gradational contacts with underlying H2 imply that deposition was by progressive aggradation. The fabric of H3b and rotated lithics are inferred to reflect minor ductile shearing (rheomorphism) of the aggrading deposit by the overriding current,

which stretched out small vesicles to form the crack-like partings but was not strong enough to develop a pervasive lineation or flow banding (cf. Pioli and Rosi, 2005).

The upper H3 deposits are also interpreted as ignimbrite based on their interactions with paleotopography and the grain size characteristics of non-welded facies, which plot within the lag breccia or ignimbrite fields of Walker (1985). Less intense welding in the upper subunits indicates lower emplacement temperatures, which prevented complete particle coalescence (wSpLT; H3c and e) and were temporarily low enough to inhibit welding altogether (SpLT; H3d). The complex lensoidal welding relationships at site B imply alternations between erosion and deposition of onlapping ignimbrite 'packages' from multiple flow pulses, which each cooled semi-independently. We observed intervening fall deposits between only one set of packages (a ~3 cm ash bed between packages 3 and 4; Fig. 2.12g), implying that any local breaks in flow passage were short.

2.6. DISCUSSION

The Halarauður deposits include the first spatter-rich ignimbrites identified in Iceland, and one of only two welded basaltic ignimbrites ever described. They thus reflect a style of eruption previously unknown in Iceland and with few analogs globally. Here we explore the magnitude and nature of this event, and address the critical question: what factors gave rise to such atypical deposits?

2.6.1. Volume Considerations: A 'Caldera-Forming' Eruption?

The modest volume of the Halarauður outflow deposits preserved in outcrop (~0.14 km^3) appears inconsistent with any link to a large caldera-forming event. However, any estimate of the total erupted volume must also account for 1) material eroded during glaciation or covered by younger units, 2) the volume of intra-caldera deposits, and 3) the volume of co-ignimbrite ash.

Erosion has significantly affected preservation of the Halarauður deposits, as indicated by the eroded tops of almost all outcrops. The c. 110-115 ka eruption age of Sæmundsson and Pringle (2000) places the Halarauður event at the marine oxygen isotope stage (MIS) 5e and 5d boundary, broadly corresponding with the onset of the Weichselian glaciation in which Iceland was almost fully ice-covered (Geirsdóttir et al., 2007, and references therein). Sedimentary records suggest full glacial conditions were reached in the Northern volcanic zone by 80-90 ka (MIS 5b; Van Vliet-Lanoë et al., 2005, 2010) and persisted until ~13-15 ka (Geirsdóttir et al., 2009; Ingólfsson et al., 2010). The Halarauður deposits have thus been subjected to a minimum of 65 kyr of glaciation. We suggest that present-day outcrops reflect only the most proximal deposits, which were thick enough to survive full removal by glacial erosion. Further, substantial burial by younger units has limited exposure of the remaining deposits (Fig. 2.1), which is biased towards elevated areas such as Hágöng where burial by lavas was impeded. We thus infer that the modest volume of ~0.14 km^3 now exposed in outcrop represents only a small fraction of the total material erupted.

The original volume of Halarauður outflow deposits can be estimated to a first order by assuming a glacial erosion rate and then reconstructing their original distribution. Uncertainties in these estimates are large and highlight the inherent difficulties in reconstructing eruption histories and magnitude-frequency relationships from pyroclastic deposits in Iceland and other frequently glaciated areas. Based on cosmogenic exposure dating, erosion rates of 1-10 and 1-25 cm kyr^{-1} have been proposed for the Fennoscandian and Laurentide ice sheets, respectively, during the last

glacial cycle (Colgan et al., 2002; Stroeven et al., 2016), equivalent to removal of 0.7 – 16 m of material in 65 kyr. These rates apply to hard bedrock, and we infer that poorly consolidated pyroclastic material would erode more rapidly. We suggest 5 m as a conservative minimum estimate for the thickness of eroded Halarauður material, and 15 m as a maximum estimate (equivalent to rates of 7.7-23.1 cm kyr^{-1}). A total thickness difference of >12 m between deposits at site G (~17 m thick), where cover by subglacial volcaniclastics prevented subsequent erosion, and nearby eroded outcrops (<5 m thick; Fig. 2.2) suggests that these estimates are reasonable. For each erosion rate, we performed two reconstructions: one conservative, assuming an asymmetric dispersal in lobes centered around known outcrops, and one less conservative, assuming a more symmetric radial dispersal (Fig. A2.7). For the latter, the gently undulating paleotopography in areas of present-day exposure was assumed to be representative of the whole dispersal area. Post-eruptive crustal spreading was corrected for prior to reconstruction by closing the fissure swarm across its central axis, assuming axisymmetric spreading at 2 cm yr^{-1} over 110 kyr (Hjartardóttir et al., 2012). Our most and least conservative reconstructions yielded original outflow bulk volume estimates of 0.5 and 6.9 km^3, respectively.

Constraining the volume of intracaldera ignimbrite is even more challenging, although drill hole data provide some limited insight. As of 2015, 46 wells had been drilled inside the caldera for geothermal exploration or production, mostly in its central region (Weisenberger et al., 2015). The Halarauður deposits have been identified in only two of these: in cuttings from well KJ-22 (275-290 m depth; Guðmundsson et al., 1983), and in core from well KH-1 (36-55 m depth; authors' observations), both near the southern caldera margin (Fig. 2.1). We calculate a first-order volume estimate for the intracaldera ignimbrite of 0.6-0.8 km^3 by extrapolating these thicknesses across the original 40 km^2 area of the caldera floor. Accounting for an additional 5-15 m of material

removed during glaciation (see above) increases this range to 0.8-1.4 km^3. However, if caldera subsidence began early in the eruption, as suggested by the presence of basal lithic breccias, the thickness and volume of ponded intracaldera ignimbrite should exceed that of outflow deposits (cf. Willcock et al., 2013). The relatively thin deposits in the KJ-22 and KH-1 wells, and their particularly shallow depth in KH-1, imply that only minor subsidence occurred on peripheral faults near the outer caldera margin. Indeed, we suggest that the buried 'inner caldera' identified by Árnason et al. (2009; Fig. 2.1) may in fact comprise the main structural caldera from the Halarauður event, while the 'outer caldera' is the present topographic rim formed by minor peripheral subsidence and mass-wasting (Lipman, 1997). The apparent absence of ignimbrite within the central caldera region, however, is puzzling. This absence could reflect non-deposition or complete erosion in this area (a paleo-high?), or possible misidentification of very strongly welded (lava-like) and/or strongly altered proximal facies in sparse drill cutting samples; intense alteration is particularly likely in the inner regions of the caldera, where geothermal activity is concentrated. Intermediate and silicic products have been identified in many of the intracaldera wells (Weisenberger et al., 2015), and we suggest that these should be re-examined for a possible link to the Halarauður event.

We have no direct constraint on the volume of co-ignimbrite ash deposits associated with the Halarauður eruption. However, the volumes of outflow, intracaldera deposits and co-ignimbrite ash from other caldera-forming eruptions are commonly subequal (Lipman, 1984). Hence, taking together our minimum outflow and intracaldera volume estimates (0.5 and 0.8 km^3, respectively) and conservatively assuming 0.2 km^3 of co-ignimbrite ash, we suggest a minimum original volume for the Halarauður deposits of 1.5 km^3 (~1 km^3 dense rock equivalent [DRE]). Taking our maximum outflow volume of 6.9 km^3 and assuming subequal volumes of intracaldera deposits and

co-ignimbrite ash (Lipman, 1984) yields a maximum volume estimate of ~20 km^3 (~13 km^3 DRE). We thus propose a total erupted volume of 7 ± 6 km^3 DRE, equivalent to a volcanic explosivity index (VEI) 5-6 event (Newhall and Self, 1982) and comparable to large effusive basaltic eruptions such as Laki in 1783 (15 km^3 DRE; Thordarson and Self, 1993) and the recent 2014-2015 Bárðarbunga-Holuhraun event (1.4 km^3 DRE; Dirscherl and Rossi, 2018). Eruptions of similar magnitudes have recurrence times in Iceland of 100-1000 years (Gudmundsson et al., 2008).

While our volume estimates are consistent with an event involving caldera collapse, we caution against linking all caldera subsidence at Krafla with the Halarauður eruption. As recent events at Bárðarbunga demonstrate (Gudmundsson et al., 2016), calderas in the Icelandic rift zones are composite structures that form incrementally, and lateral drainage of magma during effusive events can cause further subsidence of pre-existing structures.

2.6.2. Eruption Sequence

The prominent transitions in lithofacies and dispersal between units H1-H3 each correspond with a major shift in eruptive style and dynamics. Here we synthesise our field, compositional and textural data to discuss the progression of the eruption and the dynamics of each phase.

2.6.2.1. Phase 1

The onset of the Halarauður eruption is recorded by H1 lithic breccias and distally-equivalent spatter-bearing ignimbrite. Juvenile clast compositions include the most evolved of the eruptive sequence (i.e., rhyolite), reflecting tapping from the upper levels of a compositionally

heterogeneous, density-stratified reservoir (Fig. 2.13a). Fall deposits are absent at the base of H1, implying that column collapse occurred almost immediately. This likely reflects choking of the column with large volumes of cold, dense lithic debris (Shea et al., 2011), which was subsequently fed into energetic pyroclastic density currents and emplaced proximally as H1 lithic breccias. Although we cannot rule out the complete erosion of thin basal fall deposits by phase 1 flows, it seems unlikely that this would occur at all sites. The patchy dispersal and topographic ponding of H1 deposits suggest that early flows were small-volume and channeled along paleovalleys.

The presence of basal lithic breccias, as well as large differences in H1 lithic componentry between sites, is inconsistent with activity confined to a central vent, and instead implies that opening of a fissure or multiple vents occurred at the onset of the eruption (Fig. 2.13a). Deep-derived plutonic lithics occur in most H1 deposits, and are in some cases abundant (e.g., site H), suggesting early vent excavation to deep levels. Lithic breccias associated with ignimbrite are commonly interpreted to mark extensive vent erosion at the onset of caldera collapse (e.g., Brown and Branney, 2004). We thus interpret H1 basal breccias as recording the initial opening of ring fault vents and possible incipient caldera collapse (cf. Branney et al., 1992; Willcock et al., 2013). Early collapse during ignimbrite eruptions is favored by a low aspect ratio of the chamber roof (R = thickness/width), vertical zoning of the chamber volatile content, and extensional tectonics (e.g., Martí et al., 2000; Roche and Druitt, 2001; Gudmundsson and Nilsen, 2006), consistent with evidence for shallow magma storage at Krafla (e.g., Einarsson, 1978), the transition from vesicular felsic pumice-rich deposits to more mafic and poorly vesicular spatter-rich deposits, and the extensional tectonic setting, respectively. Lateral subsurface drainage of magma from a shallow chamber is also common during rift zone eruptions in Iceland (e.g., during the Krafla Fires; Buck
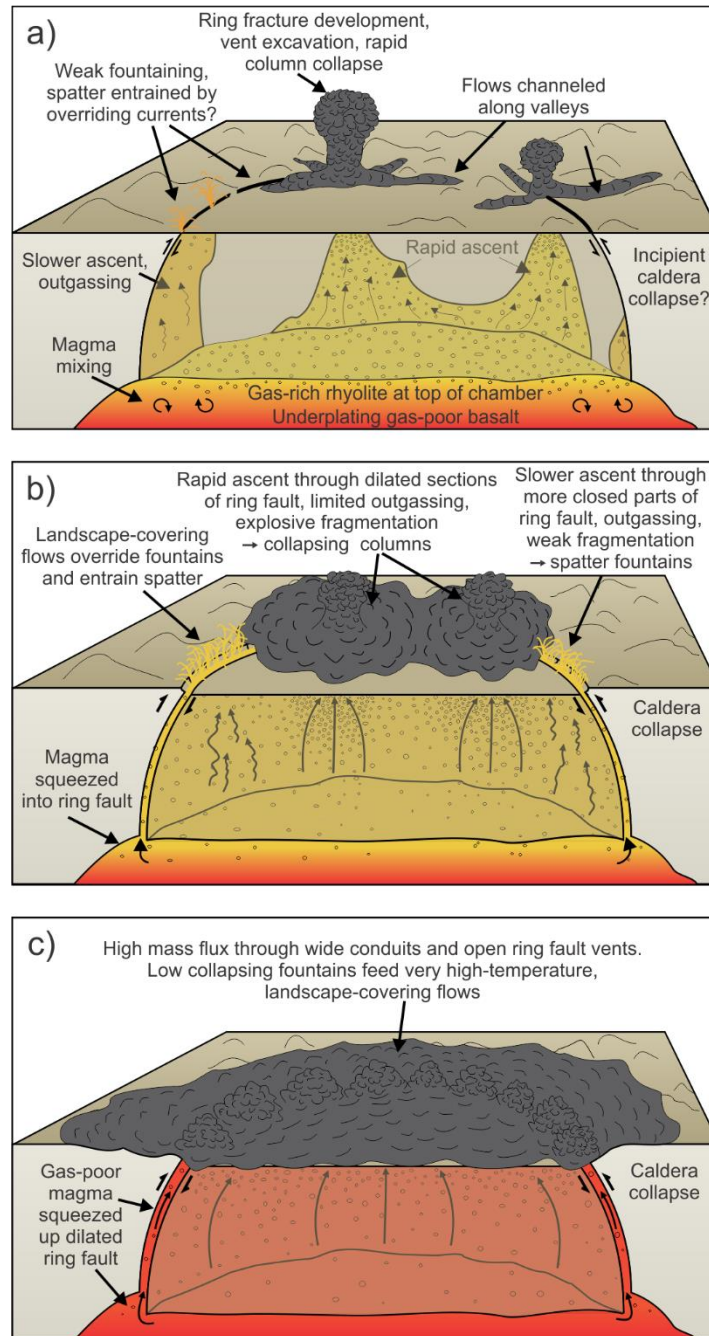
Figure 2.13. Schematic diagrams showing key aspects of the eruptive sequence. a) Phase 1: Immediate column collapse and topographic channeling of flows that emplace H1 during opening of ring fault vents. Possible incipient caldera collapse. b) Phase 2: Gas-poor hybrid magma from deeper levels is squeezed through a developing ring fault by the subsiding chamber roof. Heterogeneities in ascent rates and outgassing around the ring fault cause co-eruption of collapsing plumes and spatter fountains from discrete vents. Spatter-rich pyroclastic density currents form as currents from explosive vents override the spatter fountains, and emplace H2. c) Gas-poor basaltic magma from the deepest levels is squeezed up open ring fault conduits and erupted with very high mass-flux, forming low collapsing fountains and very high temperature flows that emplace H3.

et al., 2006), and may have allowed a chamber underpressure sufficient for collapse to develop after only small volumes had vented.

The dominance of highly vesicular silicic pumice and the small range of vesicularities in the juvenile component of lower H1 are consistent with dry magmatic fragmentation of highly viscous melt (Houghton and Wilson, 1989; Barker et al., 2012), reflecting explosive venting of the most evolved and gas-rich (and therefore lowest density) magma concentrated at the top of the chamber. The appearance of coarse, poorly vesicular dacitic to andesitic spatter at higher levels of H1 and its increasing abundance upward marks the onset of a gradual shift from generation of pumice to the spatter-dominated regime of phase 2. We interpret the initial arrival of spatter to reflect venting of less evolved, gas-poorer (and therefore denser) hybrid magma drawn from deeper levels of the chamber, where rhyolite was mixed with underplating basalt. The co-eruption of spatter and pumice in phase 1 implies that multiple fragmentation mechanisms were operating simultaneously, and could reflect either mixing of spatter from a weak eruptive fountain into an overriding pyroclastic current originating from a different vent (Rosi et al., 1996; Martin et al., 2018), or co-eruption of heterogeneously degassed magma from a single vent (or vents) simultaneously producing both spatter and pumice (Bear et al., 2009).

2.6.2.2. Phase 2

The transition from patchy dispersal of small-volume, pumice-bearing H1, to regional dispersal of landscape-burying, voluminous H2 deposits in which spatter dominates and pumice is absent reflects a marked intensification of the eruption and a major shift in its style. This occurred after only a small fraction (<~5%) of the total erupted volume had vented, and narrow gradational

contacts between H1 and H2 (<30 cm at sites C and F) imply that the transition was abrupt (minutes to tens of minutes?).

The prevalence of coarse, poorly vesicular spatter agglomerates (SpAg and welded equivalents) in almost all H2 outcrops and the absence of pumice are unusual. Most ignimbrites are pumiceous and dominated by fines-rich facies (e.g., Sparks, 1976; Branney and Kokelaar, 2002), reflecting the efficient fragmentation of highly vesiculated magma and subsequent transfer of energy and momentum from a collapsing convective plume or fountain into vigorous pyroclastic density currents. In contrast, coarse spatter-rich deposits are typical of weak (Hawaiian or Strombolian) eruptions in which fragmentation is inefficient (Kueppers et al., 2006; Mueller et al., 2019), tephra dispersal is limited, and pyroclastic density currents do not form. The abundance and wide dispersal of spatter throughout H2 thus presents a paradox.

Since first identified by Trigila and Walker (1986) at Latera caldera (Italy), a plethora of mechanisms have been suggested to explain the generation of spatter-rich pyroclastic density currents. These include: 1) explosive disruption of a degassed lava lake or gas-poor magma triggered by ingress of water (Mellors and Sparks, 1991; Valentine et al., 2000; Kokelaar et al., 2007); 2) entrainment of spatter from lava fountains into an overriding current(s) sourced from a different vent(s) (Rosi et al., 1996; Allen, 2005; Larsen et al., 2007; Martin et al., 2018); 3) deep fragmentation of gas-poor magma triggered by a drop in lithostatic pressure during chamber roof collapse (Perrotta and Scarpati, 1994); 4) collapse of rapidly-accumulated, over-steepened spatter cones during large Strombolian events (Valentine et al., 2000; Behncke, 2009); 5) interaction of gas-poor magma with a hydrothermal system (Druitt et al., 1989; Mellors and Sparks 1991; Kokelaar et al., 2007); 6) co-eruption of heterogeneously degassed magma from a single vent or fissure (Bear et al., 2009); 7) fragmentation of poorly vesicular magma following a drop in magma

pressure after partial emptying of the chamber (Palladino and Simei, 2005); and 8) fluidization of a rapidly accumulating fountain-fed dispersion, which deposits spatter proximally as fallout but distally propagates as a spatter-rich current (Turbeville, 1992; Allen, 2005). Although minor local magma-water interaction may have occurred transiently during phase 2 (see below), the prevalence of welded facies, which require high emplacement temperatures, and the absence of chilled margins or normal joints on most spatter clasts argue against this as a major mechanism of spatter generation. We also consider that collapse of vent-proximal spatter piles is an unlikely source for the Halarauður spatter-rich pyroclastic density currents; known examples of this mechanism formed very small-volume deposits with limited runout (even compared with the present-day eroded extent of H2; e.g., Behncke, 2009), and it seems unlikely that much larger piles could build up and then collapse outward in all directions to generate the radial dispersal of H2. Although repeated collapse of small spatter accumulations might produce a similar dispersal, deposition in this case would be punctuated, and evidence for depositional breaks should be apparent in the deposits. The lack of evidence for depositional pauses, wide dispersal of spatter throughout H2, and large differences in lithic componentry between sites imply that spatter generation during phase 2 was vigorous, sustained, and occurred at multiple vents. Consequently, we favor a mechanism that is intrinsically tied to the overall eruptive dynamics and operating at a regional scale.

We suggest that the spatter-rich H2 deposits reflect interplay between the eruptive dynamics and sustained caldera collapse. We propose a conceptual model in which less gas-rich hybrid magma from deeper levels of the chamber, generated by mixing of resident rhyolitic magma with underplating basalt, was squeezed into the developing caldera fault system (and/or faults cross-cutting the caldera floor) by the pressure exerted by the subsiding block(s) following initial

roof failure in phase 1 (Rosi et al., 1996; Gudmundsson, 2015) (Fig. 2.13b). We envisage hydraulic ascent of this magma through a complex caldera fault system, along which the extent of collapse, openness of the fault and magma ascent rates were locally variable. Rapid ascent could occur through more dilated segments of the fault system, limiting outgassing and driving explosive fragmentation and local formation of collapsing eruptive plumes, while slower ascent through more closed or tortuous fault segments led to outgassing, weak inertia-driven fragmentation of poorly vesicular degassed magma (Namiki and Manga, 2008), and formation of low spatter fountains. Activity at multiple vents is consistent with large differences in H2 lithic componentry between sites. During ascent through the still-developing ring fault system, lithic material could be incorporated into the magma at depth (i.e., before final fragmentation) by minor explosive interactions with groundwater (Allen, 2005; Kokelaar, 2007) or partial breakup of the subsiding roof block(s), explaining the origin of lithic inclusions with diverse lithologies inside individual H2 spatter clasts. We suggest that energetic pyroclastic density currents formed from collapsing convective plumes overrode the weak fountains at surrounding vents, entraining spatter that was then transported laterally in these currents and deposited as ignimbrite. Our proposed vent geometry bears similarity to that of the 1886 basaltic eruption of Tarawera, in which Plinian columns were fed by four discrete vents along a 17 km-long fissure, while vents along the rest of the fissure displayed weak Strombolian activity (Sable et al., 2006).

The dominance of coarse clasts and modest ash content of almost all H2 deposits (SpAg and welded equivalents) are difficult to reconcile with the above model, in which large volumes of fine material should be produced by the more explosive vents. This relative scarcity of ash also appears at odds with the transport of large spatter and lithic clasts, which cannot be supported by fluid turbulence alone and require momentum transfer from fine particles in a dusty gas (Dufek et

al., 2009). We thus interpret H2 agglomerates as a coarse proximal facies, analogous to lithic breccias (cf. Druitt et al., 1989), of what was originally a more extensive ignimbrite sheet. Fine material was effectively elutriated by gas escape during proximal deposition of coarse lithic and spatter clasts from a concentrated lower flow boundary zone (Branney and Kokelaar, 2002; Kokelaar et al., 2007), and deposited more distally as fines-rich ignimbrite or lofted into co-ignimbrite plumes (Sparks and Walker, 1977). Similar lateral transitions have been described in other spatter-rich ignimbrites (e.g., Palladino and Simei, 2005; Kokelaar et al., 2007). Proximal sedimentation of coarse spatter was likely enhanced by agglutination or coalescence of sticky low-viscosity spatter clasts upon segregation to the more concentrated lower parts of the flow, limiting the occurrence of agglomerate facies to within ~5 km from vent (Freundt, 1998). We infer that preservation of the Halarauður deposits was biased towards these thick proximal deposits, and that almost all record of any thinner and more distal fines-rich facies (plus co-ignimbrite fallout) has been removed by erosion (see discussion above). Welding of proximal deposits, enhanced by the abundance of coarse spatter clasts that effectively retained heat during transport due to their low surface areas relative to volumes (Thomas and Sparks, 1992; Capaccioni and Cuccoli, 2005) also favored their preservation over non-welded distal equivalents. Fines-rich H2 deposits are now preserved only at site G, where cover by volcaniclastic deposits prevented extensive erosion. Vertical fluctuations in average welding intensity between the proximal H2 subunits could be attributed to either 1) stacking of deposits from multiple discrete pyroclastic density currents (i.e., flow units) emplaced at different temperatures, which cooled semi-independently (Smith, 1960), or 2) progressive aggradation from a single sustained but unsteady pyroclastic density current, with fluctuations in emplacement temperature and therefore welding intensity (Branney and Kokelaar, 1992). We prefer the latter mechanism, as transitions between the subunits are gradational, and no

evidence for any sustained breaks in ignimbrite deposition, such as interbedded fall deposits, were observed. Fluctuations in emplacement temperature from a sustained flow could relate to variable admixing of air during unsteady discharge, and/or the cooling effect of temporary magma-water interactions. An increase in the relative abundance of altered lithics in H2b and c at site A (Fig. 2.10) as well as abundant poorly vesicular blocky ash shards in non-welded H2b, suggests transient interactions with a hydrothermal system at this stage. The restriction of correlatable H2 subunits to only the most proximal sites could reflect either 1) periods of restricted flow runout, forming proximal subunits that do not have distal equivalents, or 2) erosion of upper subunits from distal sites. Compared with upper subunits H2b-d at site A, the relatively evolved compositions of H2 at sites beyond the range of proximal subunits (e.g., sites C, D, E, F) are more consistent with the latter, implying that later-vented subunits tapped from deeper, more mafic parts of the chamber have been eroded at these more distal sites.

2.6.2.3. Phase 3

The H2 to H3 transition is marked by the appearance of lava-like facies, indicating flow emplacement at temperatures well above the minimum welding temperature and sufficiently high to allow complete particle coalescence upon deposition (Branney and Kokelaar, 1992). Similar lava-like facies are well-documented in silicic and peralkaline ignimbrites (e.g., Henry and Wolff, 1992; Sumner and Branney, 2002). However, the rapid kinetics of crystallisation in low-viscosity basaltic melts usually allows substantial crystallisation to occur prior to emplacement of basaltic ignimbrites, thus inhibiting welding (Giordano et al., 2005). Welded basaltic ignimbrites thus require extremely high emplacement temperatures (likely near liquidus) and are exceptionally rare.

We are aware of only one previously-described example: the basaltic ignimbrite P1 on Gran Canaria (Freundt and Schmincke, 1995).

The strong increase in welding intensity between H2 and H3 does not coincide with a sharp change in composition (Fig. 2.10), implying that the shift toward extremely high emplacement temperatures for lower H3 deposits was not triggered by an influx of new high-temperature magma, but instead related to changing source conditions at vent. The transition coincides with a marked increase in the relative abundance of deep-derived plutonic lithics, followed by a sharp reduction in total lithic content in H3b (Figs. 2.10, A2.6), suggesting a major opening of the vent system and deepening of the fragmentation level. At most sites the H2-H3 contact is narrow but gradational (over ~10 – 30 cm), indicating that this occurred rapidly (minutes to tens of minutes?). Sharp contacts at some more distal H3 sites may reflect local breaks in flow passage, but the absence of intervening fall deposits suggests that any such pauses were short.

We interpret the lava-like facies of H3 to reflect unusually high mass-flux effusion and magmatic fragmentation of basaltic magma from the deepest and hottest levels of the chamber, which was squeezed through a highly dilated vent system as the sinking roof block(s) neared the chamber floor (Fig. 2.13c). Final vent adjustment/widening is recorded by the relatively lithic-rich H3a subunit, after which steady open vent conditions prevailed and lithic-poor H3b was emplaced. Very high mass-flux venting of gas-poor basaltic magma was enabled by the wide vent system, forming low collapsing 'boil-over' columns that entrained little air or lithic material and fed extremely high-temperature flows (Sparks et al., 1978). These high temperatures prevented rapid crystallisation of the low viscosity particles, which fully coalesced upon deposition.

Large effusive basaltic eruptions involving up to several tens of km^3 of magma are relatively common in Iceland (e.g., Laki 1783-1784, 15 km^3 DRE; Thordarson and Self, 1993),

but explosive basaltic eruptions are almost exclusively small phreatomagmatic events (Gudmundsson et al., 2008). We suggest that early venting of silicic magma and opening of a ring-fault vent system in the Halarauður eruption provided the "push" needed to erupt a comparatively large volume of basaltic magma explosively, and were the key factors that distinguished the event from a more normal effusive outpouring of voluminous basaltic lavas. A similar argument was made by Freundt and Schmincke (1995) to explain welding of basaltic ignimbrite P1 on Gran Canaria. In their conceptual model, basaltic magma injected into a large shallow chamber during explosive venting of silicic magmas utilised a wide and open, already well-developed caldera vent system to erupt at an uncharacteristically high discharge rate.

Hence, we suggest that emplacement of welded basaltic ignimbrites requires a very specific set of conditions that are rarely fully met, including 1) early explosive venting of silicic magmas, and 2) early onset of caldera collapse leading to 3) development of a mature and highly dilated conduit system, and 4) late-stage expulsion of gas-poor basaltic magma from deep levels, driven from the chamber by the pressure exerted by a subsiding roof block or blocks. Non-welded basaltic ignimbrites reflect the more common scenario where these criteria are not all met (e.g., Williams, 1983; Robin et al., 1995; Giordano et al., 2006; Pérez and Freundt, 2006). The common presence of rhyolite as a minor component in Iceland's basalt-dominated systems (e.g., Jónasson, 1994) may increase the likelihood of explosive ignimbrite eruptions and formation of welded basaltic ignimbrites relative to basalt-dominated systems elsewhere.

Gradations between welded and non-welded facies (wSpLT and SpLT) in upper H3 (including subunits H3c-e) imply fluctuating emplacement temperatures, which were consistently low enough to inhibit particle coalescence (excluding for H3e at some proximal sites, which is locally lava-like). A major spike in the abundance of altered lithics in H3d and an abundance of

blocky, poorly vesicular ash suggest short-lived interaction with a hydrothermal system at this stage, which caused sufficient cooling to suppress welding. Welding reversals may also reflect an unsteady mass eruption rate, with greater admixing of air and cooling of the eruptive fountain during periods of waning discharge. Oscillations in mass eruption rate are also consistent with evidence for pulsatory deposition of onlapping ignimbrite 'packages' in upper H3 at site B. Although finer-grained than H2 agglomerates, the grain size parameters of non-welded H3 facies fall within the lag breccia and fines-depleted ignimbrite fields of Walker (1985). We infer they were emplaced by a similar mechanism to H2, involving rapid progressive aggradation from a relatively concentrated lower flow boundary dominated by fluid escape, which effectively elutriated the ash component.

2.6.3. Comparisons with High-Grade Silicic Ignimbrites

Like the H2 and H3 welded deposits, high-grade (lava-like) silicic ignimbrites are inferred to form from hot, low-viscosity pyroclasts that are transported and deposited by pyroclastic density currents (e.g., Branney and Kokelaar, 1992). During emplacement, these low viscosity clasts are thought to undergo pervasive noncoaxial shearing in a vertically migrating shear zone at the lower flow boundary (e.g., Branney et al., 1992; Pioli and Rosi, 2005), forming intensely welded rheomorphic ignimbrite. Strain heating associated with this syn-depositional rheomorphism may be a key factor in retaining high temperatures and enabling intense welding to occur (Robert et al., 2013).

A rigorous comparison of these more common high-grade silicic deposits with the lava-like H3 basaltic ignimbrite is limited by poor preservation of welded H3, although the relatively

minor rheomorphic structures in H3 suggest that shearing was of secondary importance here in allowing very strong welding. Contrasts between high-grade silicic ignimbrites and H2 spatter agglomerates are more striking, and we infer that the much coarser grain size (cf. Branney et al., 2008) and scarcity of rheomorphic structures in welded H2 imply a fundamentally different transport and depositional system for phase 2 spatter-rich pyroclastic density currents. We infer that the coarse grain size and high density (low vesicularity) of H2 spatter favored its rapid segregation to relatively concentrated basal regions of the current(s), where agglutination and deposition of these coarse particles, accompanied by upward displacement of interstitial fluid and fines (fluid-escape-dominated flow boundary; Branney and Kokelaar, 2002), limited deposition of spatter agglomerates to within a few kilometres from vent (Freundt, 1998). We suggest that gas escape suppressed traction across this relatively concentrated basal region (Branney and Kokelaar, 2002), preventing the development of widespread rheomorphic textures as the deposit aggraded, while the coarse spatter effectively retained the heat required for welding. In contrast, the finer grain size of many or most high-grade silicic ignimbrites (Branney et al., 2008) may limit the formation of fluid-escape-dominated flow boundaries, instead allowing greater shearing of the aggrading deposit and widespread syn-depositional rheomorphism (Branney et al., 1992; Pioli and Rosi, 2005). Further studies aimed at linking the transport and depositional systems and thermal budgets of pyroclastic density currents with the grain size/density characteristics of their constituent particles will be useful in advancing understanding of both kinds of deposits.

2.7. CONCLUSIONS

Deposits of the c. 110-115 ka Halarauður eruption include the first spatter-rich ignimbrite facies identified in Iceland, and one of only two welded basaltic ignimbrites ever described. Although

previously interpreted as fall deposits, multiple lines of evidence indicate lateral emplacement, including interactions with paleotopography, the presence of lithic concentration zones, and welding at distances up to 7 km from the caldera. We conclude that these atypical deposits reflect interplay between caldera collapse and eruption style during venting of a compositionally heterogeneous magma chamber, in which basalt underplated and mixed with rhyolite. Early caldera collapse and opening of ring fault vents during initial tapping of gas-rich silicic magma were likely favored by a low aspect ratio of the chamber roof, vertical zoning of magmatic volatile content, and the extensional tectonic setting. During collapse, less-evolved gas-poor magma from deeper levels was squeezed out along a still-developing ring fault system by the sinking chamber roof. Spatial heterogeneities in ascent rates and outgassing through the ring fault system caused coeval eruption of collapsing ash-rich plumes and weak spatter fountains at different vents around the ring fracture(s), forming spatter-rich pyroclastic density currents as energetic currents from explosive vents overrode the spatter fountains. Proximal spatter agglomerates were deposited from these flows in a similar manner to lithic breccias. Emplacement of welded (mostly lava-like) basaltic ignimbrites in the final stages of the Halarauður event reflects the unusually vigorous venting of gas-poor basaltic magma that was driven through a mature, highly dilated caldera fault system by the subsiding chamber roof. A similar mechanism was proposed by Freundt and Schmincke (1995) for a welded basaltic ignimbrite on Gran Canaria. We conclude that early venting of silicic magmas and the development of a mature caldera vent system during collapse are likely required for the emplacement of welded basaltic ignimbrites. The preserved ~0.14 km^3 volume of the Halarauður outflow deposits reflect only a small fraction of the 1.5-20 km^3 (7 ± 6 km^3 DRE) original deposit that remains after extensive glacial erosion. The poor preservation of the deposits and large uncertainties in our volume estimates exemplify the challenges of

constraining the frequency, magnitude and dynamics of ignimbrite-forming events in Iceland. While the style of the Halarauður eruption appears to be unusual, a similar event should be considered as an extreme scenario for hazard assessments at basalt-dominated calderas where bodies of silicic magma are known to accumulate.

3. Generation, Assembly and Eruption of Krafla Rhyolites: Insights from Petrology

The Halarauður ignimbrite eruption explored in Chapter 2 demonstrates the potentially devasting consequences of rhyolitic magmatism in Iceland, and underlines the importance of effective monitoring and hazard mitigation at Krafla and similar systems. Such an endeavour, however, requires detailed knowledge of the inner workings of these magmatic systems and the processes by which Icelandic rhyolites are generated, assembled, and mobilised for eruption. Petrologic studies of erupted products from past rhyolitic events have potential to offer important insights on these processes that can inform monitoring efforts. This chapter presents one such study. Work presented here was carried out in collaboration with Maurizio Petrelli (University of Perugia, Italy), who assisted with LA-ICP-MS, Simon Barker (Victoria University of Wellington, New Zealand), who performed the XRF analyses, and Rachel Hampton (University of Oregon, USA), who offered useful insights from a parallel zircon and oxygen isotope study of Krafla rhyolites. Shane Rooyakkers planned the study, conducted all sampling, prepared samples for whole-rock analyses, performed EPMA, Raman and LA-ICP-MS analyses, and wrote the chapter in consultation with, and with editorial input from, John Stix and Kim Berlo (McGill University).

3.1. ABSTRACT

We present a detailed petrologic study of rhyolites from seven eruptions spanning the full (~190 k.y.) history of rhyolitic volcanism at Krafla volcano, northeast Iceland. The eruptions vary widely in size and style, but all rhyolites have high-silica compositions (73.7-75.8 wt% SiO_2) and similar trace element systematics. Macrocrysts ($\leq$6 modal%: plagioclase $\pm$ augite $\pm$ pigeonite $\pm$

orthopyroxene ± fayalite ± titanomagnetite) and melt inclusions principally record crystal growth from evolved melts. Melt inclusions are exclusively rhyolitic and most crystal core compositions are appropriate for equilibrium with melts equivalent in composition to their respective whole-rock, although a significant number derive from less evolved intermediate or silicic magmas. Complex zoning patterns and internal resorption surfaces are common in macrocrysts, but compositional variations are slight (e.g., typically <10 mol% An for plagioclase, Mg# <10 for pyroxene), and zoning is consistent with an overall trend of cooling and differentiation by fractional crystallisation. Evidence for interaction with mafic recharge magmas (e.g., coupled increases in An and Fe in plagioclase) is absent in most crystals. Rhyolite storage and fractionation thus occurred largely in isolation from the underlying mafic system, and crystal resorption and zoning instead reflect closed-system processes and/or remelting of sub-solidus felsic intrusions without mafic-felsic mixing. Our lines of evidence for late-stage fractional crystallisation from mineral compositions and zoning patterns are not consistent with generation of Krafla high-silica rhyolites in a single step by partial melting of hydrothermally altered basalts. Additionally, comparisons with experimental work reveal difficulties in producing high-silica rhyolite compositions by partial melting alone, and trace element models for basalt partial melting provide a poor fit to the observed compositions. Instead, MELTS trace element models suggest a dominant role for assimilation-fractional crystallisation (AFC) in generating Krafla rhyolites. We thus propose that the absence of intermediate erupted compositions reflects the presence of uneruptible intermediate mush bodies at depth. Silicic melts are extracted from these mush bodies, and may then undergo further fractional crystallisation; crystals in the rhyolites predominantly record this last phase of differentiation. Parallel REE patterns among the ca. 110 ka Halarauður rhyolite associated with major caldera collapse and all younger units imply that the overall processes that

produce Krafla rhyolites have been similar across much of the system's lifespan. The ca. 190 ka oldest (un-named) rhyolite is distinct from all younger units with respect to both REE patterns and incompatible element ratios, implying a distinct source and possibly deeper crustal melting prior to development of a large and long-lived shallow mafic system. Similar chemistries and crystal populations reveal a common parentage for three rhyolite ridges (each ~0.15 km^3) erupted subglacially around the caldera margins at ca. 65 ka, which reflect a distinct phase of post-caldera rhyolitic volcanism possibly resulting from basaltic recharge of the shallow system after caldera collapse. Rhyolitic eruptions since ca. 24 ka have been focused in the central-eastern region of the caldera and were small in volume (each $\leq$0.02 km^3). Products from this period are either aphyric, reflecting possible superheating by adjacent basalt, or show textual evidence for basalt-rhyolite interaction, implying a triggering role for basalt in recent rhyolitic eruptions. Basalt-rhyolite interactions in the C.E. 1724 Víti eruption, which formed a small maar crater in the central caldera region, were syn-eruptive and too rapid for crystals to record. Compositional overlap between Víti products and quenched rhyolite magma recently sampled from ~2.1 km depth in the IDDP-1 well suggests that this well encountered either the same magma body tapped by the Víti event, or a younger body derived from the same source. Rapid basalt triggering of the Víti eruption raises the possibility that the IDDP-1 body could produce a similar explosive event if intercepted by ascending basalt. This study highlights the wealth of insights that detailed microanalysis can offer on the dynamics of rhyolitic magmatism in Iceland. Similar studies of other Icelandic systems have great potential to help resolve the controversial origin of Icelandic rhyolites and constrain the dynamics and timescales of their assembly and mobilisation.

3.2. INTRODUCTION

Silicic rocks, predominantly rhyolites, form approximately 10% of the volcanic pile in Iceland (e.g., Walker, 1966; Jónasson, 2007). This abundance of rhyolite in oceanic crust, where silicic rocks are usually rare, has intrigued petrologists since the 19th century (Bunsen, 1851) and spawned much debate over its origin and possible similarities with Earth's early continental crust (e.g., Martin et al., 2008; Bindeman et al., 2012; Carley et al., 2014). Traditionally, most workers have favoured one of two end-member models for the petrogenesis of Icelandic rhyolites: 1) a near-liquidus origin involving extensive fractional crystallisation of basaltic melts (e.g., Carmichael, 1964; Macdonald et al., 1990; Furman et al., 1992a), possibly with minor assimilation of altered wallrock and/or mixing with mafic magmas (Sigurdsson and Sparks, 1981; Macdonald et al., 1987; McGarvie et al., 1990; Nicholson et al., 1991), or 2) an origin from near-solidus processes involving partial melting of hydrated and hydrothermally altered basaltic crust (e.g., Óskarsson et al., 1982, 1985; Condomines et al., 1983; Thy et al., 1990; Sigmarsson et al., 1991, 1992; Jónasson, 1994) and/or silicic differentiates (Sigurdsson, 1977; Marsh et al., 1991; Gunnarsson et al., 1998). Several recent studies have attempted to reconcile these differences using the concept that the local tectonic setting determines the dominant petrogenetic process. In this conceptual model, low $\delta^{18}O$ tholeiitic rhyolites are suggested to form by near-solidus melting of altered crust (and possible subsequent crystal fractionation) in mature rift zones with high heat flow, whereas rhyolites in immature rifts or off-rift settings, which typically have normal to only slightly low $\delta^{18}O$, form predominantly by fractional crystallisation in thicker, cooler and stronger crust with less input of crustal melt (Martin and Sigmarsson, 2007, 2010; Selbekk and Trønnes, 2007; Schattel et al., 2014; Banik et al., 2018; Carley et al., 2020). While these ideas have gone some way toward resolving the controversial origin of Icelandic rhyolites, debate persists even for individual volcanic systems

(e.g., Hekla: Oswald et al., 2007; Sverrisdóttir, 2007; Portnyagin et al., 2012; Lucic et al., 2016; Bergþórsdóttir, 2018).

One likely reason for this controversy is that most petrologic studies have focused exclusively or almost exclusively on whole-rock chemistries. Petrogenetic models have mainly compared the major and trace element and/or isotopic (typically Sr-Nd-O-Th) compositions of rhyolites and co-existing basaltic to intermediate suites from a single system or small group of systems, often using mass balance calculations for fractional crystallisation and/or assimilation to model liquid lines of descent (e.g., O'Nions and Grönvold, 1973; Macdonald et al., 1987; Nicholson et al., 1991; Furman et al., 1992a; Hemond et al., 1993; Hards et al., 2000). Although such models can provide important insights on the over-arching processes of magmatic evolution, whole-rock compositions are an average of the rock-forming components (minerals ± glass), each of which may have distinct origins and/or record different processes, timescales and physicochemical conditions during the assembly of the erupted magma (e.g., Ginibre et al., 2007; Cooper, 2017). The fine-scale heterogeneities that may be preserved in crystal zoning patterns and/or matrix glass and melt inclusion compositions are not reflected by whole-rock data, which may obscure many of the subtleties of magmatic processes when considered in isolation.

A deeper understanding of magmatic evolution can be afforded by detailed microanalytical studies of mineral populations, matrix glasses and/or melt inclusions in erupted products. Although phenocryst compositions are commonly reported in petrologic studies of Icelandic rhyolites, very few workers have examined these crystal cargoes and their zoning patterns in detail (e.g., Gunnarsson et al., 1998; Weber and Castro, 2017). Recent studies have revealed a marked diversity in age, trace element and isotopic compositions of the zircon cargoes in Icelandic rhyolites or felsic xenoliths from a single eruption, suggesting that these magmas comprise a mixture of melts and

crystals derived from chemically and isotopically distinct sources (Carley et al., 2011; Bindeman et al., 2012; Gurenko et al., 2015; Banik et al., 2018). However, these data are limited to a handful of eruptions from a small number of volcanic systems. Similarly, relatively few studies have investigated the primary volatile contents of Icelandic rhyolites, but available data suggest widely variable magmatic H_2O contents (Elders et al., 2011; Portnyagin et al., 2012; Owen et al., 2013a, 2013b; Zierenberg et al., 2013; Schattel et al., 2014; Lucic et al., 2016). More detailed microanalytical studies of Icelandic rhyolites are needed to reconcile the controversies surrounding their origin and provide a more complete understanding of how these magmas are assembled, stored and primed for eruption.

The direct sampling of quenched glasses and crystals from magma at two sites beneath the Krafla caldera (northeast Iceland) during recent geothermal drilling projects (Mortensen et al., 2010; Elders et al., 2010; Zierenberg et al., 2013) offers a unique opportunity to compare the chemistries of active rhyolite bodies at depth with the quenched eruptive products of similar magmas or melts. Towards this objective, we have conducted a detailed petrologic study of erupted products from past rhyolitic eruptions from the Krafla system, expanding on previous work by Nicholson (1990), Nicholson et al. (1991) and Jónasson (1994). Here we present and discuss a comprehensive petrologic dataset, including major and trace element compositions of whole-rock samples, minerals, matrix glasses and melt inclusions, as well as H_2O contents of melt inclusions, and compare these data with published analyses of quenched rhyolite glass and crystals recently sampled from active magma or melt bodies at depth (Mortensen et al., 2010; Elders et al., 2011; Zierenberg et al., 2013; Masotta et al., 2018). We focus especially on *in-situ* mineral and glass compositional data, emphasising the insights they can provide on the processes by which Icelandic rhyolites are generated and assembled.
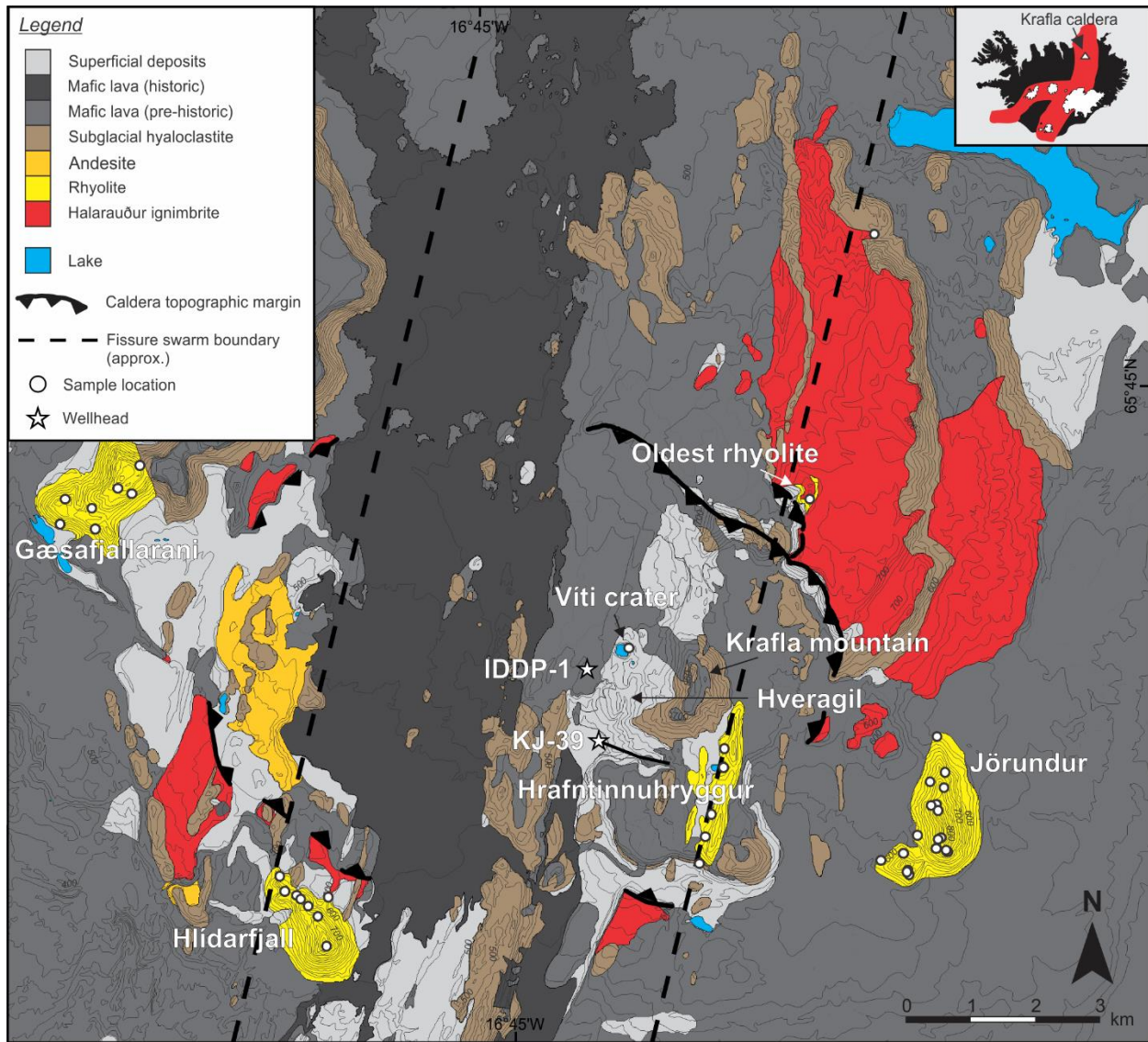
Figure 3.1. Simplified geological map of the Krafla caldera and surroundings, adapted from Sæmundsson et al. (2012). Sampling locations for whole-rock XRF analyses are marked, as well as the IDDP-1 and KJ-39 boreholes where rhyolitic magma or melt bodies were recently intercepted. The tail extending from the KJ-39 wellhead shows the path of the slanted well. IDDP-1 was drilled vertically.

3.3. GEOLOGICAL BACKGROUND AND PREVIOUS WORK

3.3.1. Krafla Volcanic System

Krafla is one of five en-echelon volcanic systems located in the Northern Volcanic Zone (NVZ) of Iceland, a segment of the axial rift zone associated with the divergent Eurasian-North American

TABLE 3.1. OVERVIEW OF KRAFLA RHYOLITE UNITS

Unit	Age	Volume (km^3)	Description
Oldest rhyolite (un-named)	ca. 190 ka[a]	<0.05[d]	Small dome NE of the present caldera margin, poorly exposed beneath Halarauður ignimbrite
Halarauður ignimbrite	110-115 ka[a]	7 ± 6[e]	Ignimbrite sheet related to caldera collapse event. Mixed basalt-rhyolite eruption. Rhyolite pumice common in basal deposits, later-erupted material mostly hybrid compositions[d]
Jörundur	66.9 ± 7.9 ka[b]	~0.15	Subglacially-erupted ridge, rising ~250-300 m above surrounds[d,g]
Gæsafjallarani	67.4 ± 8.4 ka[b]	~0.15	Subglacially-erupted ridge, rising ~250-300 m above surrounds[d,g]
Hlídarfjall	65.8 ± 7.8 ka[b]	0.14[f]	Subglacially-erupted ridge, rising ~250-300 m above surrounds[d,g]
Hrafntinnuhryggur	ca. 24 ka[a]	0.02[f]	Dike erupted beneath thin ice, lobes of microcrystalline rhyolite and obsidian[g]
Hveragil tephra	ca. 9000 B.P.[c]	n.q.	Small explosive mixed basalt-rhyolite eruption from the Víti area, dispersed pumice across the central and sothern caldera region[c,d]
Víti	1724 A.D.[c]	n.q.	Rhyolitic pumice co-erupted with small volumes of basaltic scoria and partially melted granophyric xenoliths in a phreatomagmatic event during the opening phase of the Mývatn Fires, forming the maar crater Víti[b,c]

[a]Sæmundsson and Pringle (2000)

[b]Hampton et al. (in prep.)

[c]Sæmundsson (1991)

[d]Jónasson (1994)

[e]Rooyakkers et al. (2020; Chapter 2)

[f]Agustdottir et al. (2010)

[g]McGarvie (2009)

[h]Tuffen and Castro (2009)

n.q. = not quantified, but estimated as <<0.0.1 km^3 based on published accounts of dispersal

plate boundary (Sæmundsson, 1979). The system comprises the Krafla central volcano, a broad shield of ~25 km diameter with an ~8 x 10 km caldera at its centre, and a 100 km-long, 5-8 km-wide fissure swarm that transects the central volcano from northeast to southwest (Fig. 3.1; Sæmundsson, 1991; Hjartardóttir et al., 2012). Volcanism and geothermal activity are mainly concentrated in and around the caldera, which is thought to have largely formed during a major ignimbrite eruption at ca. 110 ka (Rooyakkers et al., 2020; Chapter 2; eruption age from Sæmundsson and Pringle, 2000).

The Krafla system has been active since at least 300 ka (Sæmundsson, 1991). Erupted products are compositionally bimodal; basaltic lavas and subglacial hyaloclastites are dominant

(>90% by volume), while subordinate rhyolite has erupted in and around the caldera (Nicholson et al., 1991; Sæmundsson, 1991; Jónasson, 1994). All rhyolites have low $\delta^{18}O$ compositions (whole-rock values are +1.0 to +3.3‰, compared with typical mid-ocean ridge basalt [MORB] values of +5.5 to +5.9; Nicholson et al., 1991; Eiler, 2001; Pope et al., 2013). Intermediate products are rare, and those erupted within the caldera show clear evidence for a hybrid origin by mixing of basalt and rhyolite (Jónasson, 1994; Rooyakkers et al., 2020; Chapters 2 and 4). Postglacial activity has been dominated by basaltic fissure eruptions within and near the caldera, and along the fissure swarm to the south near Námafjall (Thorarinsson, 1979; Sæmundsson, 1991). Interplay between regional tectonics and volcanism has characterized recent activity, with long (ca. 300-1000 year) periods of tectonic and volcanic quiescence interrupted by short (<10 year) rifting events and accompanying eruptions (Hjartardóttir et al., 2016), most recently in the 1975-1984 Krafla Fires episode (e.g., Hollingsworth et al., 2012). A zone of shear-wave attenuation at ~3-7 km depth in the central caldera region is inferred to reflect a shallow basaltic magma chamber (Einarsson, 1978) or network of dikes and sills (Kennedy et al., 2018). Extensive drilling associated with geothermal exploration has provided a reasonably clear outline of the subsurface geology in the central caldera region. Basaltic lavas and hyaloclastites dominate the upper ~1-2 km and are underlain by intrusive complex of basaltic dikes and gabbroic rocks, with sporadic intermediate and felsic intrusions (Ármannsson et al., 1987; Weisenberger et al., 2015).

3.3.2. Rhyolitic Magmatism and Volcanism at Krafla

Eight eruptions involving rhyolitic magma (hereafter "units", for convenience) are known from the Krafla system (summarised in Table 3.1; locations marked on Fig. 3.1). For convenience, Jónasson (1994) grouped these events into three phases of activity: 1) extrusion of a small unnamed

dome (hereafter 'oldest rhyolite') at the edge of the Hágöng plateau, followed by the mixed basalt-rhyolite Halarauður eruption associated with major caldera collapse; 2) subglacial emplacement of the ridges Jörundur, Hlídarfjall and Gæsafjallarani (hereafter the 'extra-caldera ridges') around the margins of the caldera during the last glacial, possibly associated with intrusion of a ring-dike; and 3) small-volume intra-caldera eruptions, including emplacement of the Hrafntinnuhryggur ridge late in the last glacial period, and two post-glacial eruptions: the ca. 9000 B.P. Hveragil tephra and 1724 C.E. Víti pumice. The latter occurred during the opening phase of the Mývatn Fires volcanotectonic episode and formed the small maar crater Víti (Grönvold, 1984; Sæmundsson, 1991). Products of the Víti eruption consist mainly of altered country rock, but small volumes of juvenile rhyolitic pumice and basaltic scoria were also ejected along with partially melted xenoliths of felsite and granophyre (Sigurdsson, 1968; Grönvold, 1984).

In 2008, quenched glass ranging in composition from dacite to high-silica rhyolite was identified in cuttings from the bottom of well KJ-39 (~2.6 km total vertical depth) in the central region of the caldera, indicating that a silicic magma body or zone of partial melt had been pierced during drilling (Fig. 3.1) (Mortensen et al., 2010). The glass comprised up to 30% of the cuttings from the base of the well, with the remainder consisting of fresh holocrystalline basalt (Mortensen et al., 2010). The following year, a high-silica rhyolite magma body, hosted in a felsite intrusion undergoing partial melting, was unexpectedly intercepted at ~2.1 km depth in the IDDP-1 well, drilled ~1 km north of the KJ-39 wellhead (Fig. 3.1) (Elders et al., 2011; Zierenberg et al., 2013; Schiffman et al., 2014). Partially melted felsite fragments were recovered in cuttings from directly above the magma body, and quenched glass fragments hosting sparse crystals, and distinct in composition from the KJ-39 glasses, were sampled directly from the magma. A low V_p/V_s seismic anomaly imaged by Schuler et al. (2015) near the bottom of both wells was interpreted as a

superheated steam zone above shallow magma, while large amplitude seismic reflections near the base of these wells have also been linked with the presence of magma (Kim et al., 2017, 2020). Because of the limited spatial resolution of these techniques, it remains unclear whether the IDDP-1 and KJ-39 wells intercepted the same magma body, or separate small pockets of silicic magma.

The origin of rhyolite at Krafla has been controversial. Although $^{87}Sr/^{86}Sr$ and $^{143}Nd/^{144}Nd$ ratios are similar for mafic and silicic rocks (Condomines et al., 1983), $^{230}Th/^{232}Th$ and $\delta^{18}O$ values are distinctly lower in the rhyolites, precluding their generation by simple fractional crystallisation of basalt parental melts (Sigmarsson et al., 1991; Nicholson et al., 1991; Jónasson, 1994; Pope et al., 2013). The $\delta^{18}O$ of crustal rocks can be lowered by oxygen exchange between rocks and meteoric water in high-temperature geothermal systems, and values as low as -10‰ have been measured in hydrothermally altered basalts from Krafla boreholes (Muehlenbachs et al., 1974; Hattori and Muehlenbachs, 1982). Nicholson et al. (1991) thus argued that decreasing $\delta^{18}O$ and $^{230}Th/^{232}Th$ with decreasing MgO in Krafla rocks reflects a near-liquidus process of assimilation-fractional-crystallisation (AFC), whereby crystallising basalts assimilate low-$\delta^{18}O$, low-$^{230}Th/^{232}Th$ hydrothermally altered basaltic crust to produce rhyolites. In contrast, Jónasson (1994, 2007) argued that Krafla rhyolites form by near-solidus melting of hydrothermally altered basalts around the margins of basaltic magma chambers or intrusions at low P_{H_2O} (<1 kbar), temperatures of 850-950°C, and relatively reducing conditions (fO$_2$ on or below the fayalite-magnetite-quartz [FMQ] buffer), and are extracted crystal-free from these source regions by crustal deformation. Both assimilation of partially melted altered basalts into mantle-derived basaltic magma (Elders et al., 2011) and partial melting of altered basaltic crust without any implied assimilation into existing magma (Zierenberg et al., 2013; Pope et al., 2013) have been proposed to explain the origin of the IDDP-1 rhyolite, while the KJ-39 rhyolite was suggested to reflect the initial stages of partial

melting of altered basalt (Mortensen et al., 2010). However, based on comparison with MELTS models, Charreteur et al. (2013) recently argued that the very low Mg# of some Krafla rhyolites reflects protracted fractional crystallisation (with minor assimilation) under reducing conditions (fO_2 ~ FMQ-1), whereas the higher Mg# and presence of disequilibrium phenocrysts in others were consistent with AFC under more oxidising conditions (fO_2 ~ FMQ) and possible mixing between basalt and rhyolite. In summary, although it is universally accepted that the low $\delta^{18}O$ of Krafla rhyolites requires input of altered crust, the extent of melting and importance of fractional crystallisation remain controversial.

3.4. METHODS

Rhyolite samples were collected for petrologic and chemical analysis during field campaigns in 2015-2017 (sample locations are marked on Fig. 3.1). We sampled fresh obsidian and/or microcrystalline rhyolite from subglacially-erupted lava lobes across each of the extra-caldera ridges (Jörundur, Hlídarfjall and Gæsafjallarani) and the intra-caldera ridge Hrafntinnuhryggur, as well as occasional large pumice clasts from Jörundur and Hlídarfjall. Widely spaced outcrops were sampled to assess any possible chemical variability across each ridge and to ensure representative sampling. Exposures of the oldest rhyolite are scarce and altered, so only a single, slightly altered microcrystalline sample was collected from this unit. Víti samples comprise fresh pumice collected inside Víti crater. The Halarauður ignimbrite spans a continuous compositional range from basalt to rhyolite and shows abundant textural evidence for magma mixing (Rooyakkers et al., 2020; Chapter 2). A detailed petrologic study of all Halarauður products will be presented in Chapter 4. For comparison with the other rhyolites, we here report the bulk composition of a pumice sample collected from the basal ignimbrite unit (H1) ~5 km northeast of the caldera, which is the most

evolved Halarauður sample that we analysed and is considered to represent the rhyolitic mixing endmember.

Analytical methods and data quality are detailed in Appendix 3 and briefly summarised here. Whole-rock samples were crushed and powdered in an alumina ceramic (n = 38) or tungsten carbide (n = 11) mill and analysed for major element contents by X-ray fluorescence spectroscopy (XRF) in New Zealand at either the University of Waikato or the University of Auckland. Individual pumice samples from Víti and the Halarauður ignimbrite were too small for XRF analysis, so whole-rock analyses for these units each comprise several clasts. Analytical precision determined by repeat analyses of standard reference materials is $\leq$3% relative (2σ) for all elements (usually <1% relative), and mean values are accurate to within 5% (usually within 1-2%) of accepted values. Loss on ignition (LOI) was $\leq$2.1 wt%.

A subset of 22 whole-rock samples, selected to cover the full range of major element compositions for each eruption, were analysed for trace element content by Actlabs (Ancaster, Canada). Sample powders were fused with a lithium metaborate/tetraborate flux to form molten beads, which were then digested in weak HNO_3. The resulting solutions were analysed by inductively-coupled plasma mass spectrometry (ICP-MS). Estimates of 2σ analytical precision based on replicate analyses of RGM-1 standard reference material are <10% relative (usually <5%) for all elements. Mean values measured for RGM-1 and GSP-2 are accurate to within 10% (usually within 5%) of accepted values, excluding Tb, Dy, Er, Tl and Cu (all within $\leq$18%), and Pb (within 30%).

Mineral and glass major- and minor-element compositions were determined by electron probe microanalysis (EPMA) at McGill University (Montreal, Canada). For each unit, EPMA analyses were performed on crystals and glasses selected at random from multiple bulk samples

spanning a range of whole-rock compositions and sampling locations, and are thus considered representative. Minerals were analysed by wavelength dispersive spectroscopy (WDS) with a JEOL 8900 electron microprobe, using an accelerating voltage of 15 kV (plagioclase, pyroxene) or 20 kV (Fe-Ti oxides), beam current of 20 nA (plagioclase) or 30 nA (pyroxene, Fe-Ti oxides), and beam diameters of 5 μm (plagioclase and pyroxene) or 1 μm (olivine and Fe-Ti oxides). Plagioclase Fe measurements were corrected for fluorescence of the surrounding glass following Sugawara (2001); all corrections were <0.04 wt%. Glasses were analysed by WDS with a Cameca SX Five FE electron microprobe using a 15 kV accelerating voltage and 10 μm beam diameter. For glass analyses we first used a 2 nA beam current to analyse major elements, followed by 10 nA for minor elements (P, Cl, S and Ti), and a zero-time correction was applied for Na, K and Si to correct for any possible Na loss. Analytical precision (2σ) estimated from repeat analyses of standard reference materials is <3% relative for elements with concentrations >10 wt%, and <5% relative for elements comprising 1-10 wt% (excluding Na_2O and K_2O and FeO* in glass; <12% and <9%, respectively). Mean values are accurate to within 1% of reference values for elements comprising >1 wt%, excluding Na_2O, Al_2O_3, K_2O and FeO* in glass (within 4.5%, 4%, 2.5% and 7.5%, respectively).

In-situ mineral and glass trace element analyses were performed by laser-ablation inductively-coupled plasma mass spectrometry (LA-ICP-MS) at the University of Perugia (Italy), using a Teledyne/Photon Machine G2 laser system coupled with a Thermo Scientific iCAP-Q quadrupole mass spectrometer (Petrelli et al., 2016). NIST 610 glass was used as the calibration standard. For most analyses we used a 30 μm circular beam pulsed for 40 s at 10 Hz with a fluence of 4.72 J cm^{-2}. Where higher spatial resolution was required to analyse narrow mineral growth zones, a 10 μm beam was rastered across the sample surface for ~75 s at a scan speed of 2 μm s^{-1}.

Data were processed with Iolite (Hellstrom et al., 2008), using ^{42}Ca as an internal standard for plagioclase and pyroxene, ^{29}Si for fayalite and glass, and ^{47}Ti for Fe-Ti oxides. Estimates of analytical precision (2σ) based on repeat analyses of BCR-2G are better than 10-15% relative for most elements, and most measured values are accurate to within 10% of reference values.

H_2O contents of glassy plagioclase- and augite-hosted melt inclusions were analysed by Raman spectroscopy at McGill University following methods similar to Di Genova et al. (2017). Spectra were acquired at a depth of 5 μm below the surface of polished, epoxy-mounted samples using a Reinshaw InVia confocal micro-Raman spectrometer equipped with a 532 nm wavelength laser and optical microscope, calibrated daily with a silicon standard. Instrumental settings consisted of a 1200 grooves mm^{-1} grating density, 25 μm slit diameter, 1.5 mW laser power and 100x objective lens, with an exposure time of 60 s for 5 accumulations. Details of the calibration procedure and data treatment are in Appendix 3. Despite the highly confocal instrumental configuration, high fluorescence associated with the mounting epoxy, which has a strong Raman signal, caused contamination of most spectra with some epoxy signal. Spectra were therefore also collected from inside the epoxy beneath each crystal and subtracted from the melt inclusion spectra until no spectral peaks associated with epoxy were observed. This procedure lowered the precision of our data relative to the capabilities of the method under optimal conditions. From replicate analyses, we estimate a 2σ analytical precision of ± 1 wt%, comparable to H_2O determinations from EPMA by difference (i.e., the difference between raw EPMA totals and 100%). We find good agreement between our H_2O determinations by Raman and EPMA by difference (see below), and thus present both as semi-quantitative measures of melt inclusion H_2O contents.

3.5. RESULTS

3.5.1. Petrography

For the purposes of this chapter, crystals larger than the groundmass are defined as "macrocrysts" (>0.05 mm for titanomagnetite, and >0.1 mm for other phases). All Krafla rhyolites studied by us are crystal-poor, with <6 modal% macrocrysts hosted in a glassy to devitrified spherulitic groundmass. Hrafntinnuhryggur samples are aphyric, while Halarauður rhyolite pumice contains only very sparse (<1-2 modal%) macrocrysts of plagioclase and augite, most of which were inherited during mixing with basaltic magmas. The Halarauður crystals and associated mixing processes will be considered in Chapter 4.

Plagioclase is the dominant macrocryst in all phyric samples, comprising up to 5 modal% (Table 3.2). In all samples it occurs as euhedral, tabular to prismatic crystals reaching up to ~4 mm in the extra-caldera rhyolites and ~2 mm in Víti pumices, as well as occasional glomerocrysts (± pyroxene, fayalite and/or titanomagnetite). Complex optical zoning and inclusions of melt, zircon (absent in Víti and oldest rhyolite) and apatite are common. Green, subhedral to anhedral (rarely skeletal) augite up to ~1 mm is a ubiquitous minor phase, comprising up to 0.6 modal% (Table 3.2). Fine exsolution lamellae of pigeonite are common in Víti augites,

TABLE 3.2. REPRESENTATIVE MODES FOR KRAFLA RHYOLITES

Sample Number	Unit	Plagioclase	Augite	Pigeonite + Orthopyroxene	Titanomagnetite	Fayalite	Granophyric clots	Zircon	Apatite
KR-6-a	Víti	4.5	-	<0.1	0.2	-	0.5	-	Trace
KR-6-l	Víti	1.9	-	<0.1	0.1	-	0.5	-	Trace
KR-153-e	Víti	2.7	0.3	<0.1	0.0	-	-	-	Trace
KR-40	Hlídarfjall	1.8	0.2	<0.1	<0.1	-	-	Trace	Trace
KR-123	Jörundur	4.3	0.4	0.1	0.2	-	-	Trace	Trace
KR-128	Jörundur	2.7	0.2	0.0	0.2	0.1	-	Trace	Trace
KR-129	Jörundur	4.1	0.3	0.1	0.2	0.4	-	Trace	Trace
KR-150	Gæsafjallarani	-	-	<0.1	0.1	0.3	-	Trace	Trace
KR-147	Gæsafjallarani	4.2	0.6	<0.1	0.3	0.2	-	Trace	Trace
KR-106	Oldest rhyolite	1.1	0.1	-	0.1	-	-	-	Trace

Note: Modal compositions (in %, normalised void-free) for selected Krafla samples, determined from image analysis of high-resolution scans or BSE maps of polished thin sections using ImageJ (https://imagej.nih.gov).

but rare in those from the extra-caldera ridges. Around 50% of augites occur as glomerocrysts with plagioclase and/or titanomagnetite, in some cases with minor interstitial glass. Small (<50 μm) inclusions of glass, apatite and/or Fe-Ti oxides are common. Pigeonite and orthopyroxene are minor phases (together $\leq$0.1 modal%) in all but the oldest rhyolite. For Víti, both phases occur as rare, discrete euhedral to subhedral grains up to ~0.5 mm, often with augite exsolution lamellae, but are more common in composite grains where they overgrow or are overgrown by augite. In the three extra-caldera ridges, pigeonite and orthopyroxene occur only as rare cores mantled by augite. Euhedral to subhedral prismatic titanomagnetite up to ~0.3 mm (typically <0.1 mm) occurs in all units (up to 0.3 modal%), both as inclusions in plagioclase and mafic minerals and as a discrete phase. Fayalite was identified in Jörundur and Gæsafjallarani samples only, as anhedral crystals up to ~1 mm. Zircon (Hlídarfjall, Jörundur and Gæsafjallarani only) and apatite are common accessory phases, occurring both as discrete grains and as inclusions in other minerals. Occasional irregular clots of granophyric material (intergrown quartz and K-feldspar) up to ~0.5 mm occur in Víti pumices; quartz is otherwise absent.

The petrographies of erupted Krafla rhyolites are similar to the rhyolitic magma recently intercepted in the IDDP-1 well. Silicic glass cuttings from IDDP-1, described in detail by Zierenberg et al. (2013) and Masotta et al. (2018), host $\leq$3-5 modal% crystals (up to ~1 mm), with an assemblage of euhedral plagioclase, euhedral to subhedral pigeonite and augite, subhedral titanomagnetite, accessory apatite and trace pyrrhotite. Both pigeonite and augite commonly host exsolution lamellae of the alternate phase, and intergrowths of the two pyroxenes also occur. Some pigeonites have augite overgrowths. Resorbed glomerocrysts of quartz, plagioclase, augite and magnetite (± heavily resorbed alkali feldspar), resembling the felsite body surrounding rhyolite magma, were also identified in some cuttings and interpreted as material assimilated from the

margins of the intrusion. Anhedral plagioclase, clinopyroxene and oxides were also identified in silicic glass cuttings from the KJ-39 well by Mortensen et al. (2010), but a detailed petrography was not presented.

3.5.2. Whole-Rock Chemistry

Krafla rhyolites are metaluminous, with 2.5-2.9 wt% K_2O and 73.7-75.8 wt% SiO_2 (normalised anhydrous). Major element compositions from each unit define discrete compositional fields with minor scatter (Fig. 3.2), as noted by Jónasson (1994). Within each unit, $Fe_2O_3^T$, MnO, MgO, and CaO show broad negative correlations with SiO_2, while trends for TiO_2 and P_2O_5 are flat, and Al_2O_3 and Na_2O are generally more scattered. K_2O is positively correlated with SiO_2 for most units, excluding Gæsafjallarani and Hlídarfjall which show greater scatter. Minor compositional scatter within each unit is readily accounted for by small differences in crystal content and phase proportions. For example, least squares mass balance calculations using representative phase compositions (see below) imply that the most evolved Jörundur composition (KR-142) can be derived from the least evolved Jörundur composition (KR-96) by removal of 2.7 wt% crystals (80% plagioclase, 4% titanomagnetite and 16% fayalite; Table 3.3). Minor variations in phase abundance and proportions are supported by the modal data in Table 3.2.

Whole-rock compositions for the extra-caldera ridge Hlídarfjall are the most evolved of the suite, with the lowest $Fe_2O_3^T$, MnO and MgO, and highest SiO_2 contents (excluding KR-148 from Gæsafjallarani, which has anomalously high SiO_2 and low Na_2O and Al_2O_3; Fig. 3.2). Compositions of the other extra-caldera ridges, Gæsafjallarani and Jörundur, are similar to each other but distinct from Hlídarfjall within analytical error for all major elements except Al_2O_3 and
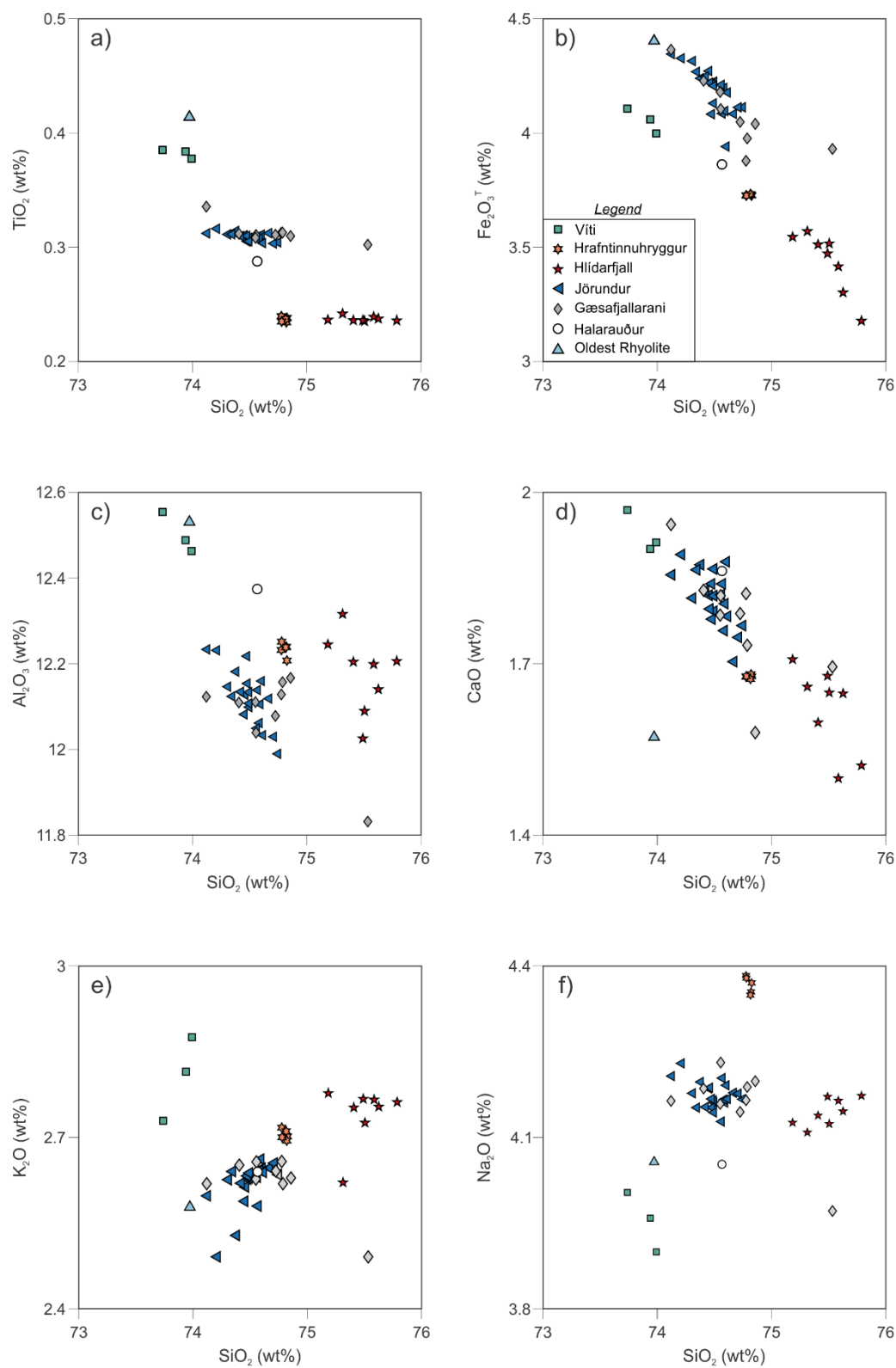
Figure 3.2. Selected whole-rock major element plots (data normalised volatile-free), analysed by XRF. Estimated 2σ analytical uncertainties are smaller than the symbols.

TABLE 3.3. LEAST SQUARES MASS BALANCE CALCULATIONS FOR JÖRUNDUR WHOLE-ROCK COMPOSITIONS

| | Starting Composition | Final Composition | Phases Fractionated | | | | Results | | | |
	KR-96 (Jörundur)	KR-142 (Jörundur)	Augite (Mg# 30)	Plagioclase (An$_{40}$)	Titanomagnetite (Usp$_{58}$)	Fayalite (Fo$_{13}$)	Bulk Composition Fractionated	Observed Difference Between Magmas	Calculated Difference Between Magmas	Residuals (r)
SiO$_2$	74.49	75.09	48.86	58.86	-	30.52	52.20	0.60	0.58	0.01
TiO$_2$	0.31	0.31	0.33	-	19.98	0.01	0.85	-0.01	-0.01	0.01
Al$_2$O$_3$	12.29	12.04	0.71	25.95	1.55	0.01	22.25	-0.25	-0.26	0.01
FeO*	3.93	3.72	25.43	0.56	77.35	61.77	12.51	-0.21	-0.22	0.01
MnO	0.10	0.09	0.92	-	0.73	1.94	0.29	-0.01	-0.01	0.00
MgO	0.17	0.15	6.10	-	0.39	5.38	0.50	-0.03	-0.01	-0.02
CaO	1.86	1.77	17.44	8.06	-	0.38	5.77	-0.09	-0.10	0.01
Na$_2$O	4.23	4.19	0.19	6.25	-	-	5.34	-0.04	-0.03	-0.01
K$_2$O	2.61	2.65	0.01	0.33	-	-	0.28	0.04	0.06	-0.02
Total	100	100	100	100	100	100				
		wt% of Fractionated Assemblage	0.0	80.2	4.1	15.7			∑(r^2)	0.00
									wt% Fractionated Solids	2.73

Note: Calculated with PetroGraph (Petrelli et al., 2005) using the least squares algorithm of Stormer and Nicholls (1978).

99

Na$_2$O, which almost completely overlap. Víti pumices and the oldest rhyolite have the least evolved compositions (e.g., lower SiO$_2$ and higher TiO$_2$, Al$_2$O$_3$, MgO and Fe$_2$O$_3^T$ than the rest of the suite) with overlap for many elements, but are clearly distinguished by the much higher CaO and K$_2$O and lower Fe$_2$O$_3^T$ and Na$_2$O of the Víti samples. Hrafntinnuhryggur rhyolites form a tight cluster with respect to all major elements and are distinguished by the highest Na$_2$O and total alkali contents of the suite (Na$_2$O + K$_2$O ~ 7.1 wt%), while the single pumice sample from the Halarauður ignimbrite plots near the middle of the full rhyolite suite for all major elements.

The patterns of major element compositions are largely confirmed by our trace element data, which similarly define discrete compositional fields for each unit with minor scatter (Fig. 3.3). All units show similar trace element systematics, with very large negative Sr, P and Ti anomalies, and small negative Nb and positive Zr anomalies (Fig. 3.3a). In particular, the close chemical affinity of the extra-caldera subglacial ridges is highlighted; Gæsafjallarani and Jörundur show near-complete overlap for all trace elements, while Hlídarfjall is distinguished only by lower Zr (Fig. 3.3c) and a trend towards higher (but partially overlapping) Ba (not shown). Hrafntinnuhryggur is distinguished by slightly higher LREE contents and high Ba/Rb, but otherwise largely overlaps with the three extra-caldera ridges and has similar incompatible element ratios (e.g., Th/Ta, Th/Nb and Nb/Y; Fig. 3.3d- f). The Víti, Halarauður and oldest rhyolites are distinct and show only limited compositional overlap with each other and the other rhyolites.

Incompatible element ratios for the Halarauður rhyolite are similar to the extra-caldera ridges, but most ratios are distinct for Víti and the oldest rhyolite (Fig. 3.3d-f). Chondrite-normalised REE patterns for all units show strong LREE enrichment ([La/Yb]$_N$ = 3.28 – 4.54), steep LREE-MREE trends ([La/Sm]$_N$ = 2.27 – 2.74), negative Eu anomalies (Eu/Eu* = 0.56 – 0.71) and relatively flat MREE-HREE trends ([Dy/Lu]$_N$ = 0.95 – 1.09) (Fig 3.3b). The overall
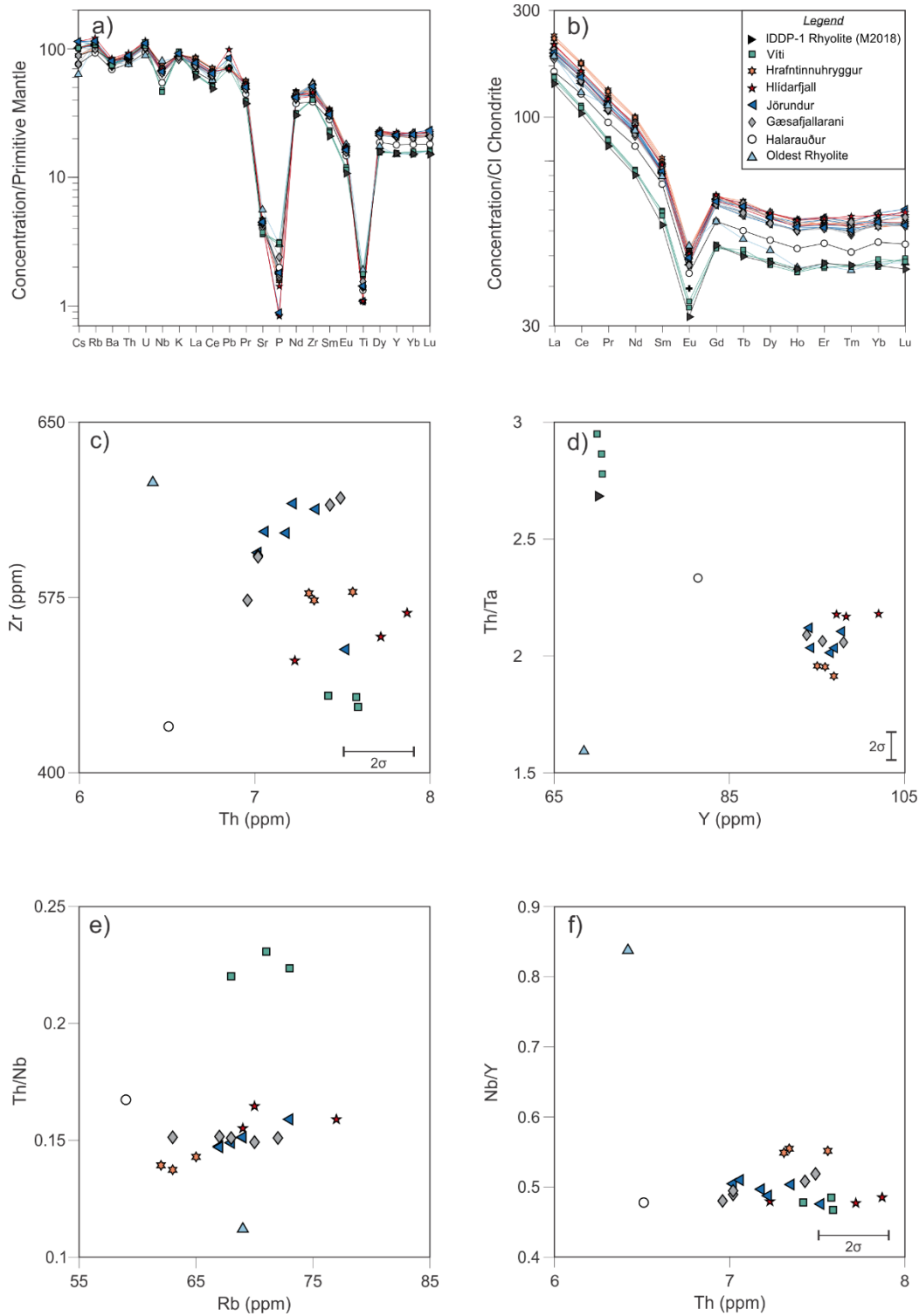
Figure 3.3. Selected whole-rock trace element plots (analysed by ICP-MS). Data in a) and b) are normalised to the primitive mantle and chondrite values of Sun and McDonough (1989) and McDonough and Sun (1995), respectively. Estimated 2σ analytical uncertainties based on duplicate analyses are smaller than the symbols except where shown with error bars. M2018 = Masotta et al. (2018). Note that Masotta et al. (2018) did not report Nb or Y data for the IDDP-1 rhyolite.

101

shape of the REE patterns are essentially indistinguishable for all but the oldest rhyolite, which has notably higher LREE/HREE, a steeper MREE trend from Gd to Ho, and a shallower Eu anomaly. Bulk analyses of selected trace elements in the IDDP-1 rhyolite (Masotta et al., 2018) overlap with Víti for most elements within analytical uncertainty (Fig. 3.3a, b).

3.5.3. Mineral Chemistry

3.5.3.1. Plagioclase

Plagioclase macrocrysts within each rhyolite show moderate compositional scatter. Core compositions from each unit span a range of ~20-25 mol% An, approximating a normal distribution for all units except Víti which has a prominent mode centred at ~An_{48-49} and a second, less well-defined mode at ~An_{55-59} (Fig 3.4a). The latter approaches the most calcic compositions measured in Krafla rhyolites. Rim compositions for all units are unimodal and span a range of ~15 mol% An (5 mol% for the oldest rhyolite), each approximating a normal distribution (Fig. 3.4b). Both core and rim An distributions for the three extra-caldera ridges are essentially identical (Fig. 3.4a, b), although Hlídarfjall rims are shifted towards slightly more calcic compositions on average (Fig. 3.4c, d). Jörundur and Gæsafjallarani plagioclase trace element contents overlap within uncertainty and are distinguished from Hlídarfjall only by slightly higher Mg (Fig. 3.4f) and higher average (but largely overlapping) Ti contents. Trace element compositions from Víti and the oldest rhyolite are more distinct; both have higher Mg and lower Eu than the extra-caldera ridges (Fig. 3.4g, h), while Sr contents for the oldest rhyolite are the highest of the suite (up to 634 ppm), and Víti has the lowest Sr at a given An content (Fig. 3.4i). Plagioclase from the IDDP-1 rhyolite is similar to Víti, with overlap between the core (An_{48-52}) and rim (An_{42-45}) compositions reported by
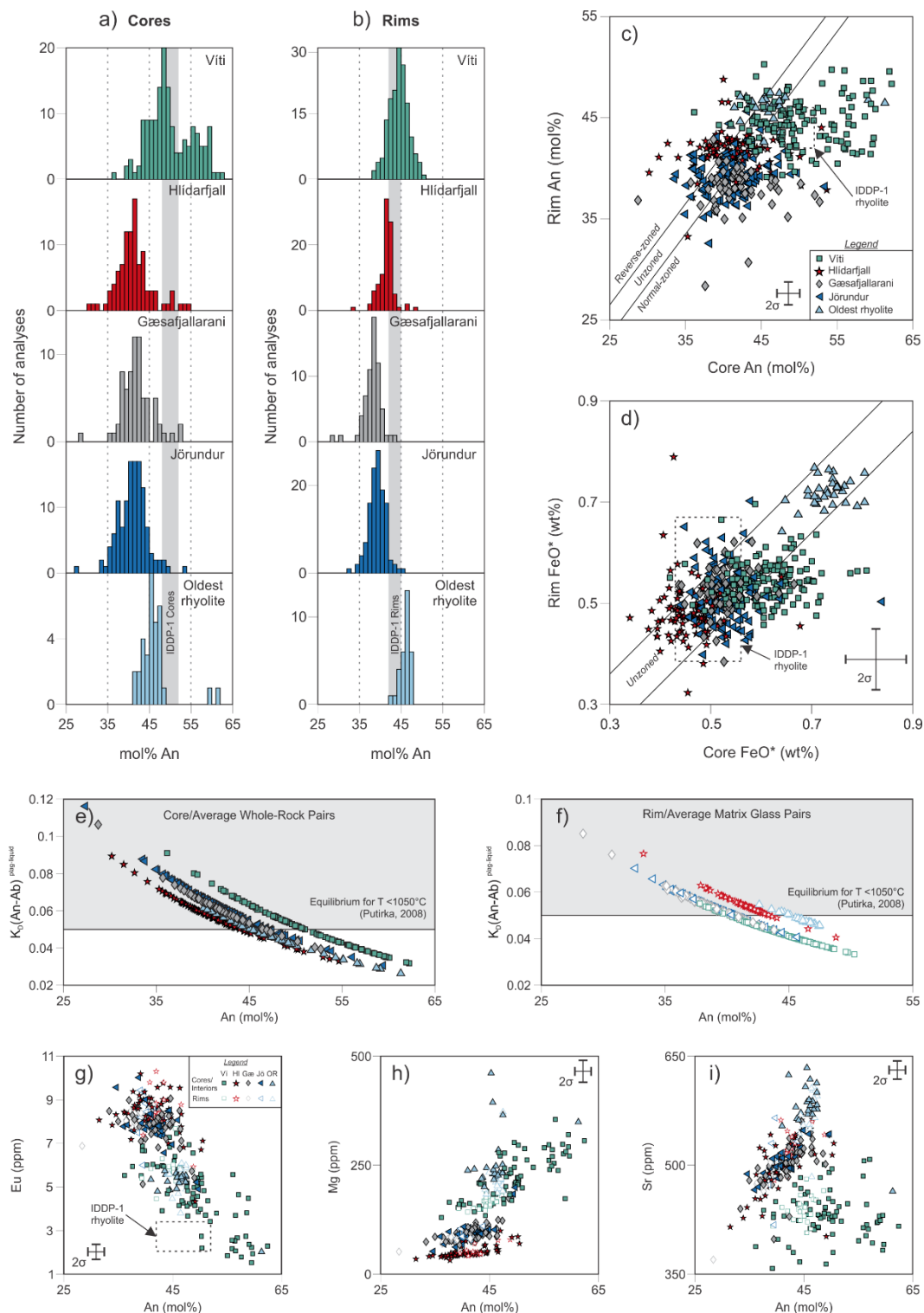
Figure 3.4. Selected plagioclase compositional plots. Major elements and FeO* were analysed by EPMA, and trace elements by LA-ICP-MS. Estimated 2σ analytical uncertainties for EPMA and LA-ICP-MS were determined from repeat analyses of NMNH 115900 plagioclase and BCR-2G glass standards, respectively. Grey bars or boxes denote the ranges of core (n = 14) and rim (n = 15) analyses from Masotta et al. (2018) for plagioclase in IDDP-1 rhyolite cuttings (Mg and Sr not reported).

103

Masotta et al. (2018) and the corresponding modes for Víti compositions (Fig. 3.4a, b).

We tested cores and rims from each unit for equilibrium with average whole-rock and matrix glass compositions, respectively, using the criterion $K_D(An\text{-}Ab)^{plag\text{-}liq} = 0.10 \pm 0.05$ at equilibrium for T <1050°C (Putirka, 2008). Matrix glass compositions are not available for the oldest rhyolite or Gæsafjallarani due to pervasive devitrification; rims from the oldest rhyolite were therefore paired with the whole-rock composition, which closely approximates the carrier liquid due to the unit's very low crystal content, whereas Gæsafjallarani rims, which are indistinguishable from Jörundur rims within analytical uncertainty (see below), were paired with the average Jörundur glass composition. Most cores have compositions appropriate for equilibrium with a melt equivalent in composition to their respective whole-rock, although a significant number from each unit are too calcic for equilibrium (Fig. 3.4e). Similarly, rims from the extra-caldera ridges are mostly in or near equilibrium with their host melt, but most rims from Víti and the oldest rhyolite are apparently too calcic for equilibrium (Fig. 4f). The latter result is surprising given the euhedral forms of all Víti plagioclase crystals and the relatively narrow and unimodal distribution of rim compositions, which both suggest an approach to equilibrium. However, testing for equilibrium with K_D values is limited by their sensitivity to temperature, P_{H_2O} and X_{An}, and values lower than 0.05 may in some cases be appropriate for silicic melts (Humphreys et al., 2016).

Net (i.e., core to rim) zoning is subtle, rarely exceeding 10 mol% An and 0.2 wt% FeO* (Fig. 3.4c, d). All erupted units contain both normal- and reverse-zoned plagioclase, though normal zoning is more common (especially prominent for Víti; 75% of crystals). Many crystals show no net major or trace element zoning within 2σ analytical uncertainty; notable exceptions are minor rim enrichments in Sr relative to cores (up to 110 ppm, usually <50 ppm) for some Hlídarfjall and Víti crystals (70% and 57%, respectively), as well as relative rim enrichments in Eu and depletions

in Mg for Víti crystals with the most calcic cores (Fig. 3.4e, f). IDDP-1 plagioclases analysed by Masotta et al. (2018) all show minor normal zoning ($\leq$10 mol% An; Fig. 3.4c).

Despite only minor core-rim zoning, the internal zoning patterns of individual crystals are often complex. We recognise eight texturally distinct zoning types, summarised in Table 3.4. All rhyolites host at least seven of these types (Fig. 3.5). A minimum of 25% of crystals from each unit contain one or more internal resorption surface (dark resorbed core, multiple resorption, patchy and some bright cores types; Fig. 3.5). Internal resorption textures are particularly prominent in Víti crystals (~75%). However, intra-crystal chemical variations in all units are usually minor. Most resorption surfaces are overgrown by more calcic compositions (brighter in back-scattered electron [BSE] images), but compositional differences across them are rarely >10 mol% An (often <5 mol%), and only 12% show a coupled increase in An and FeO*. Total intra-crystal An zoning is rarely >10 mol% and never >20 mol%. Intra-crystal FeO* variations reach a maximum of 0.36 wt% but exceed the 2σ analytical uncertainty (0.12 wt%) in only 15% of crystals. Minor intra-crystal Sr variations (~30-60 ppm) are common (40% of crystals), although only 6% of crystals show variations comparable to the 100-150 ppm range of rim compositions present in each unit. Similarly, Ba zonation is <50 ppm in 51% of crystals analysed, while variations of 100-200 ppm, comparable to the total range of rim Ba contents in each unit, occur in only 14% of crystals. Hence, within each unit, inter-crystal differences in plagioclase trace element compositions outweigh those within individual crystals.

3.5.3.2. Pyroxene

Augite is the dominant pyroxene in both the extra-caldera ridges and Víti, occurring as a discrete

TABLE 3.4. PLAGIOCLASE ZONING TYPES

Schematic	Zoning Type	Description	Sr Zoning (ppm)	Ba Zoning (ppm)
	Unzoned	No discernible zoning	<30	<50
	Smooth normal	Gradational zoning from more calcic (BSE brighter) core to more sodic (BSE darker) rim. No reversals or sharp compositional boundaries. Intra-grain An variations usually <5-10 mol%, rarely up to 15 mol%	<30 - 33 (median = 28)	<50 -60 (median = 51)
	Subtle oscillatory	Fine-scale concentric oscillations, most zones <20 μm thick. Adjacent zones vary by ~1-3 mol% An. Total intra-grain variations are <10 mol% An, rarely exceeding 5 mol%	<30 - 47 (median = 6)	<50 (median = 17)
	Prominent oscillatory	Broad concentric oscillatory zones, commonly >50-100 μm thick. Contacts between zones range from sharp to gradational. Adjacent zones vary by up to 7 mol% An. Total intra-grain variations reach up to ~20 mol% An, but rarely exceed 10 mol%	<30 - 104 (median = 29)	<50 - 169 (median = 55)
	Dark resorbed core	BSE dark, rounded/resorbed core mantled by a smooth normal or oscillatory over-growth. Cores may show minor internal normal or oscillatory zoning. Intra-grain An variations typically <5-10 mol%, occasionally up to 15-20 mol%	<30 - 114 (median = 38)	<50 - 190 (median = 47)
	Bright core	Large, homogeneous or subtly zoned BSE bright core in sharp contact with darker overgrowth. May have an oscillatory mantle. Intra-grain An variations typically ~5-10 mol%, occasionally up to ~15 mol%	<30 - 125 (median = 67)	55 - 169 (median = 105)
	Multiple resorptions	Resorbed inner core overgrown by oscillatory mantle with one or more resorption surfaces. Intra-grain An variations typically <5-10 mol%, occasionally up to 15 mol%	<30 - 77 (median = 60)	<50 - 146 (median = 69)
	Patchy	Heavily resorbed core with complex, patchy zoning. Intra-grain An variations are usually <5 mol%, occasionally up to 15 mol%	<30 - 158 (median = 53)	<50 - 99 (median = 40)
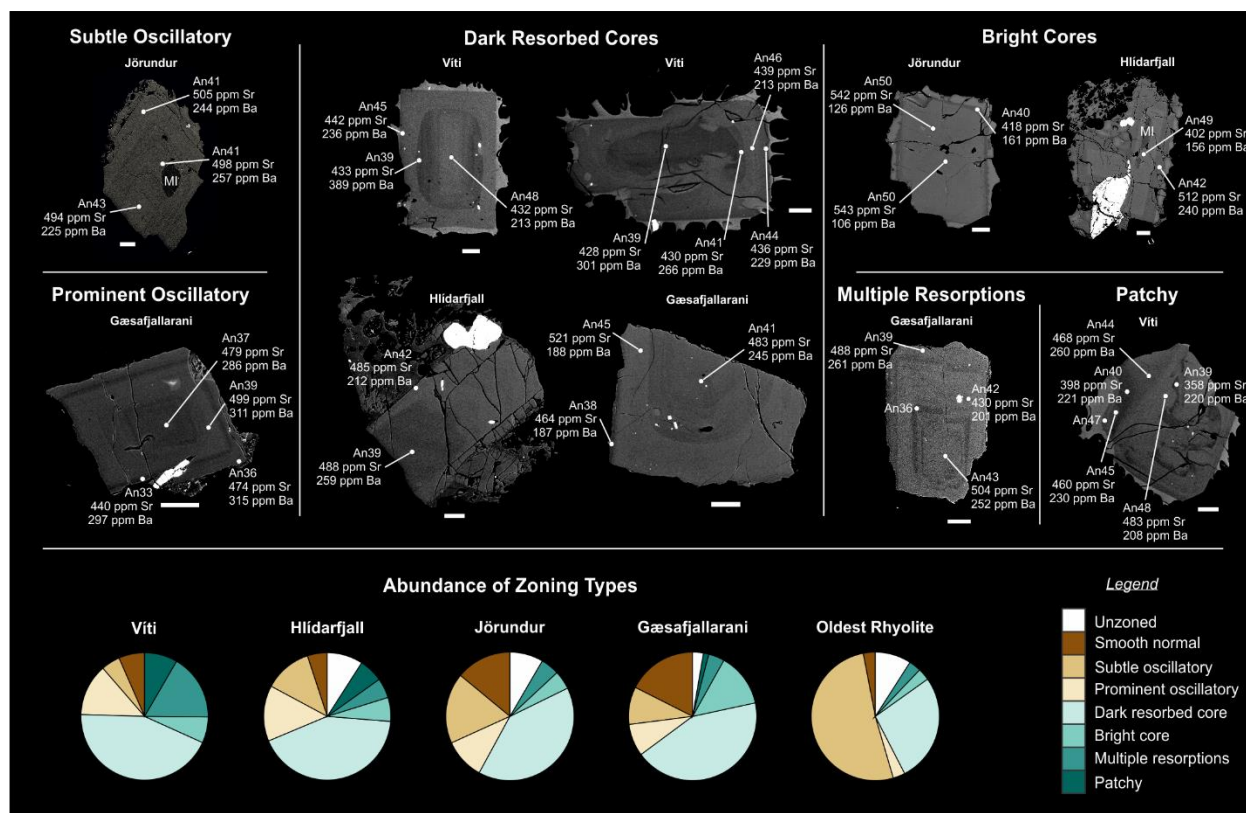
Figure 3.5. Labelled back-scattered electron (BSE) images of selected plagioclase crystals, highlighting zoning types and associated variations in An, Sr and Ba content. Pie charts show the relative proportion of each zoning type within each unit. Melt inclusions are labelled 'MI'. Scale bars are 100 μm.

phase and as overgrowths on pigeonite and orthopyroxene, as well as intergrowths with pigeonite in Víti samples. Compositions for the extra-caldera ridges are predominantly Fe-rich: cores from Jörundur and Gæsafjallarani cluster between Mg# 22-35 ($En_{14-21}Fs_{40-50}Wo_{36-39}$), with several more magnesian outliers extending up to Mg# 72 ($En_{42}Fs_{16.5}Wo_{41.5}$) (Fig. 3.6a, d), while rim compositions approximate a tight normal distribution centred around a mode of Mg# 25-26 ($En_{14-15}Fs_{45-46}Wo_{40}$) for both ridges (Fig. 3.6c, e). Augite trace element compositions for these units show near total overlap, and Cr contents are below detection limit (<2-3 ppm) for all except two high-Mg# cores from Gæsafjallarani with ~130-150 ppm. Hlídarfjall cores are slightly more Fe-rich on average than the other extra-caldera ridges, ranging between Mg# 9-41 with a prominent mode centred around Mg# 17-18 ($En_{10}Fs_{49}Wo_{41}$), while rims range from Mg# 11-27 with a mode at Mg# 15-16 ($En_9Fs_{49}Wo_{42}$). Hlídarfjall trace element compositions partially overlap with the other extra-caldera ridges, but extend to higher Sc, Sr, Zr, Hf and Ti and lower Co, Y, and HREE contents. Víti core compositions are more magnesian and less clustered than the other rhyolites, ranging between Mg# 35-71 ($En_{21-41}Fs_{18-41}Wo_{38-41}$), while rims cluster around a prominent mode at Mg# 41-42 ($En_{25-26}Fs_{37-38}Wo_{41-42}$). Modes for Víti core and rim compositions both overlap with the range of Mg# 41-53 reported for augites from the IDDP-1 rhyolite (Fig. 3.6d, e; Zierenberg et al., 2013; Masotta et al., 2018). Trace element compositions for Víti largely overlap with the range for the extra-caldera ridges, but the highest Mg# cores are enriched in compatible transition metals (Co, Cr, Ni, Cr and V; Fig. 3.6g). Cr contents are mostly <10 ppm, reaching up to ~80 ppm (excluding one outlier with 450 ppm) for a subgroup of the most magnesian grains (Mg# >50).

The K_D for Fe-Mg exchange between clinopyroxene and liquid is commonly used as a test for equilibrium. Putirka (2008) proposes an equilibrium value of $K_D(Fe\text{-}Mg)^{aug\text{-}liq} = 0.28 \pm 0.08$. However, the experimental data from which this value was derived are mainly from more
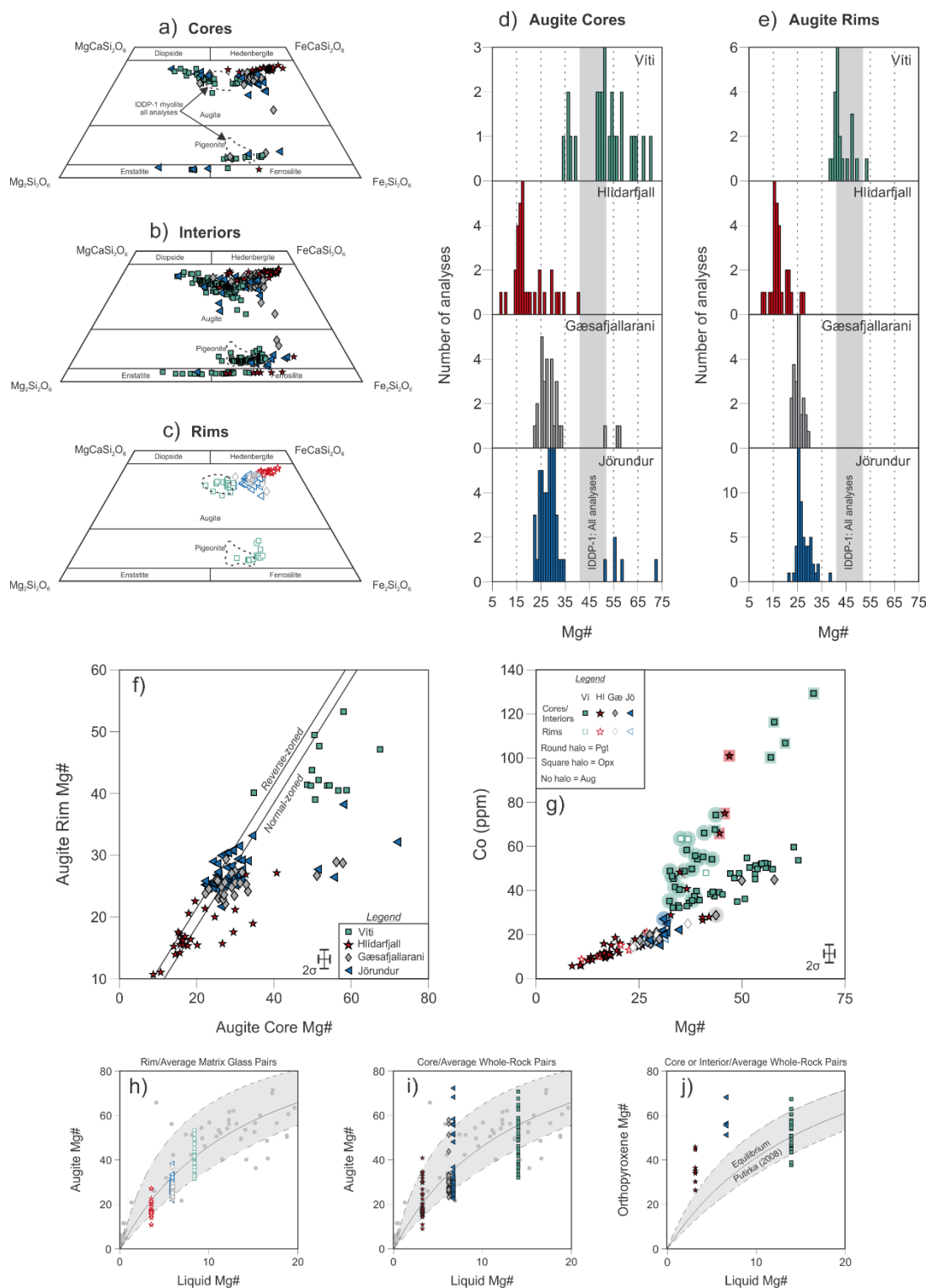
Figure 3.6. Selected compositional plots for pyroxenes. Major and trace elements were determined by EPMA and LA-ICP-MS, respectively. Analytical uncertainties (2σ) were determined from replicate analyses of Taylor Diopside (EPMA) and BCR-2G glass (LA-ICP-MS) standards. Experimental values for augite are from Almeev et al. (2012), Gardner et al. (2014), Bolte et al. (2015), Iacovino et al. (2015), and Brugman and Till (2019).

mafic compositions. To determine whether this value is applicable to evolved melts and Fe-rich augites, we calculated K_D values for each of the crystal-liquid pairs used to calibrate the Brugman and Till (2019) clinopyroxene-liquid thermometer, specifically designed for use on silicic compositions. The K_D values (n = 64, from 5 experimental studies) show a roughly symmetrical, unimodal distribution with a mean of 0.13 and standard deviation of 0.07. Hence, we infer that Putirka's (2008) value is too high for evolved melts, and we test against the value of 0.13 ± 0.07. Most cores are in or near equilibrium with melts equal in composition to their respective average whole-rock, and almost all rims are in equilibrium with the average groundmass glass (as before, pairing Gæsafjallarani rims with Jörundur glass).

Pigeonite is a minor phase in the Víti rhyolite. Cores and interiors range from $En_{28-43}Fs_{47-64}Wo_{8-10}$ (Mg# 31-48; Fig. 3.6a, b), mainly overlapping with compositions reported from the IDDP-1 rhyolite ($En_{33-40}Fs_{52-59}Wo_8$, Mg# 37-44; Zierenberg et al., 2013; Masotta et al., 2018). Most Víti pigeonites are overgrown by augite, but a minority have rims of more Fe-rich pigeonite, and pigeonite rims of $En_{27-33}Fs_{59-63}Wo_{8-10}$ (Mg# 31-37) also occasionally mantle Víti augite cores. In the extra-caldera ridges, pigeonite occurs as rare cores and/or interiors of $En_{18-39}Fs_{52-72}Wo_{8-10}$ (Mg# 20-44) (Fig. 3.6a, b), mantled by augite.

Orthopyroxene is rare in Krafla rhyolites, but cores and/or interiors overgrown by either augite or pigeonite were observed in occasional grains from Hlídarfjall ($En_{25-44}Fs_{53-73}Wo_{3-4}$; Mg# 26-46), Jörundur ($En_{49-65}Fs_{31-48}Wo_{3-4}$; Mg# 51-68) and Víti ($En_{36-64}Fs_{32-61}Wo_{3-4}$; Mg# 38-67) (Fig. 3.6a, b). Additionally, a single discrete subhedral grain of orthopyroxene ($En_{36-47}Fs_{50-61}Wo_{3-4}$; Mg# 38-49) was identified in hand-picked mineral separates from a crushed Víti pumice. We test for equilibrium using the K_D formulation of Putrika (2008), which estimates the equilibrium K_D as a

TABLE 3.5. AUGITE ZONING TYPES

Schematic	Zoning Type	Description
	Unzoned	No discernible zoning
	Smooth normal	Gradational normal zoning from BSE darker core to brighter rim. No reversals or sharp compositional boundaries. Inta-grain Mg# variations are usually <5-10, rarely reaching up to 25
	Smooth reverse	Gradational reverse zoning from BSE brigher core to darker rim. No reversals or sharp compositional boundaries. Intra-grain Mg# variations are <5
	Concentric	Concentric zones. Internal boundaries may show evidence for minor resorption, but growth zones do not cross-cut. Intra-grain Mg# zoning is usually <5-10 and occasionally up to 15
	Dark resorbed core	BSE dark, rounded and resorbed core mantled by a smooth normal or oscillatory overgrowth (sharp or narrow diffuse contact <50 μm). Large intra-grain Mg# variations, usually 20-30
	Patchy	Heavily resorbed core/interior with complex, patchy zoning. Intra-grain Mg# variability is usually <5-10, but can be large (maximum of 35)
	Pigeonite or orthopyroxene core	Partially resorbed core of orthopyroxene (BSE dark) or pigeonite (BSE bright), overgrown with augite. Occasionally, orthopyroxene cores are mantled by pigeonite with an augite rim. Augite overgrowths may show normal or patchy zoning, with variations in Mg# up to 20
	Pigeonite overgrowth	High Mg# (50-70) augite core overgrown with less magnesian, normally-zoned pigeonite (Mg#30-45). Cores range from faceted to resorbed and may show complex internal zoning
	Augite-pigeonite intrgrowths	Intergrowths of pigeonite and augite, often with complex boundaries. Both pigeonite and augite may host thin (<1 μm) exsolution lamellae of the other phase. High Mg# orthopyroxene occasionally occurs as cores within pigeonite. Intra-grain Mg# variations in augite range from <10 up to 25; pigeonite Mg# varies by <10

function of X_{Si} of the melt; melts equivalent to the average Krafla whole-rock compositions for each unit yield equilibrium $K_D(Fe\text{-}Mg)^{opx\text{-}liq}$ values of 0.16 ± 0.06. Assuming this value, almost all Víti core and interior compositions are appropriate for equilibrium with a melt equivalent in composition to the average Víti whole-rock (Fig. 4j). Compositions from Jörundur and Hlídarfjall fall outside of the equilibrium range, but many are close and have compositions appropriate for equilibrium with silicic melts similar to the Víti rhyolite (i.e., Mg# $\leq$15).

Like plagioclase, compositional zoning in augites from Krafla rhyolites is usually subtle. Normal core-rim zoning is common (57% of crystals), but rarely exceeds Mg# 10, while reverse zoning is scarce (13% of crystals) and limited to Mg# $\leq$5 (Fig 3.6f). Intra-crystal zoning exceeds Mg# 10 in only one third of crystals. Nonetheless, like plagioclase, internal zoning patterns in individual crystals can be complex. We recognise 9 distinct zoning types, summarised in Table 3.5

and Fig. 3.7. Each unit hosts 5-7 of these types. Large-magnitude intracrystal zoning (Mg# variations >20; 12% of crystals) occurs almost exclusively in crystals with prominent resorption surfaces (dark resorbed core and patchy types; Table 3.5, Fig 3.7), and occasionally in Víti augites intergrown with or overgrown by pigeonite. Intracrystal trace element variations largely mirror the major elements; decreases in Mg# usually correspond with lower V, Ni and Co and higher Sc, Y and REE contents, but compositional shifts are often slight (e.g., 85% of intra-crystal Co zoning is <10 ppm, 90% of V zoning is <30 ppm).
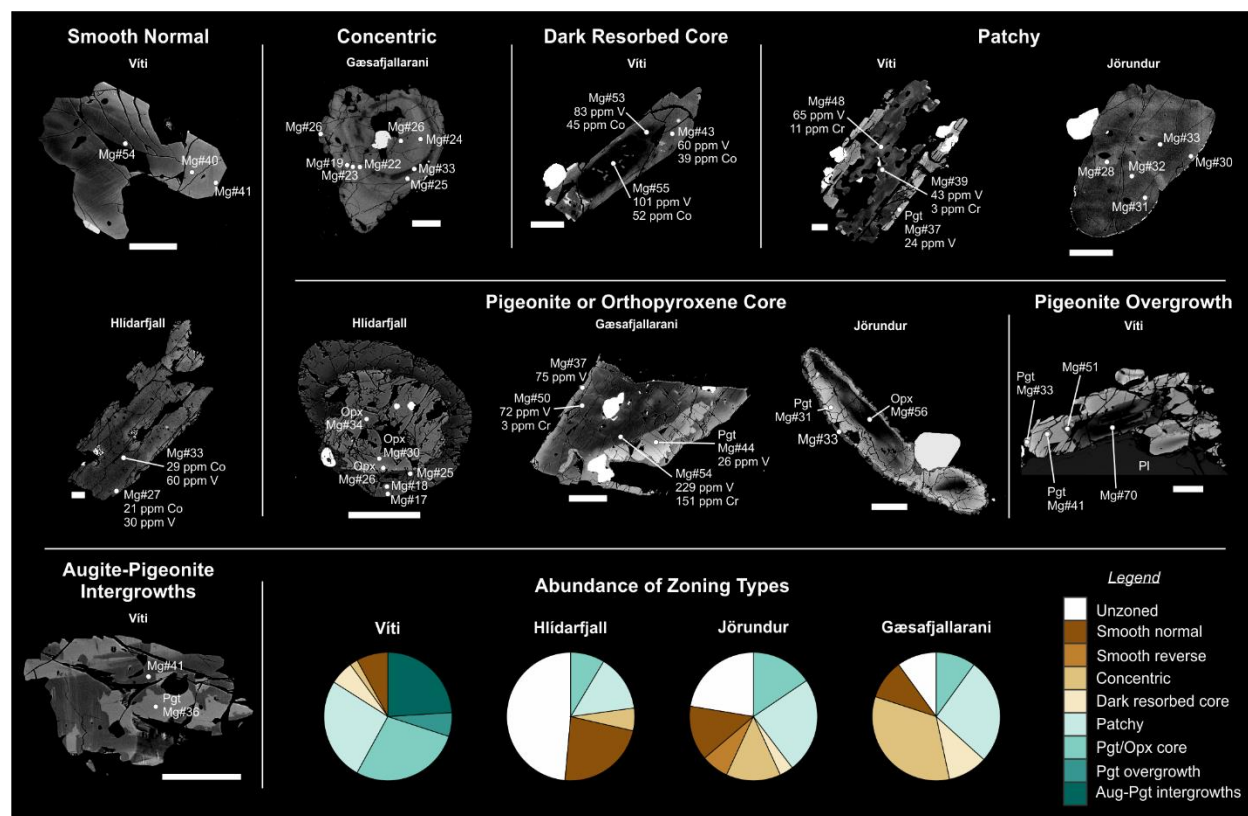
Figure 3.7. Labelled BSE images of selected augite crystals (± pigeonite and/or orthopyroxene), highlighting different zoning types. Pie charts show the relative proportion of each zoning type within each unit. All analyses are augite unless specified: Pgt = pigeonite; Opx = orthopyroxene; Pl = plagioclase. Scale bars are 100 μm.

3.5.3.3. Fayalite

Fayalite (Fo_{11-17}) occurs sparsely in the Jörundur and Gæsafjallarani rhyolites (Table 3.2). All crystals are anhedral and unzoned, with 35-43 ppm Co and 5-9 ppm Ni. Major and trace element compositions for the two ridges are indistinguishable within 2σ analytical uncertainty.

3.5.3.4. Fe-Ti Oxides

Homogeneous grains of titanomagnetite are ubiquitous in the crystal-bearing rhyolites. Occasional trellis-type grains with ilmenite lamellae also occur in some Jörundur, Gæsafjallarani and oldest rhyolite samples. These exsolved grains are inferred to reflect oxidation-exsolution during post-eruptive cooling (Haggerty, 1991) and are not considered further. Ilmenite is otherwise absent in all Krafla rhyolites except Hlídarfjall, where we identified a single euhedral grain (Ilm_{95}).

Titanomagnetite compositions from Jörundur, Gæsafjallarani and Hlídarfjall are tightly clustered, with ranges comparable to the 2σ analytical uncertainty for most elements [Fig. 3.8; Fe and totals recalculated after Carmichael (1967); mol% Usp calculated after Stormer (1983)]. Excluding one outlier (Usp_{30}), Jörundur and Gæsafjallarani compositions are indistinguishable within error (Usp_{51-61}). Hlídarfjall extends to more Ti-rich compositions (Usp_{58-68}), and is also distinguished by lower MgO and Co, and a slight enrichment in some trace elements (e.g., REEs). Compositions for the oldest rhyolite (Usp_{45-60}) mostly fall within or near the range for Jörundur and Gæsafjallarani, but low recalculated totals (95.9 – 98.8 wt%) are consistent with textural evidence for minor alteration. Víti titanomagnetites (Usp_{52-66}, excluding two outliers with ~Usp_{35}) are the most Mg-rich of the suite and extend to higher V and Cr contents (Fig. 3.8b, c).
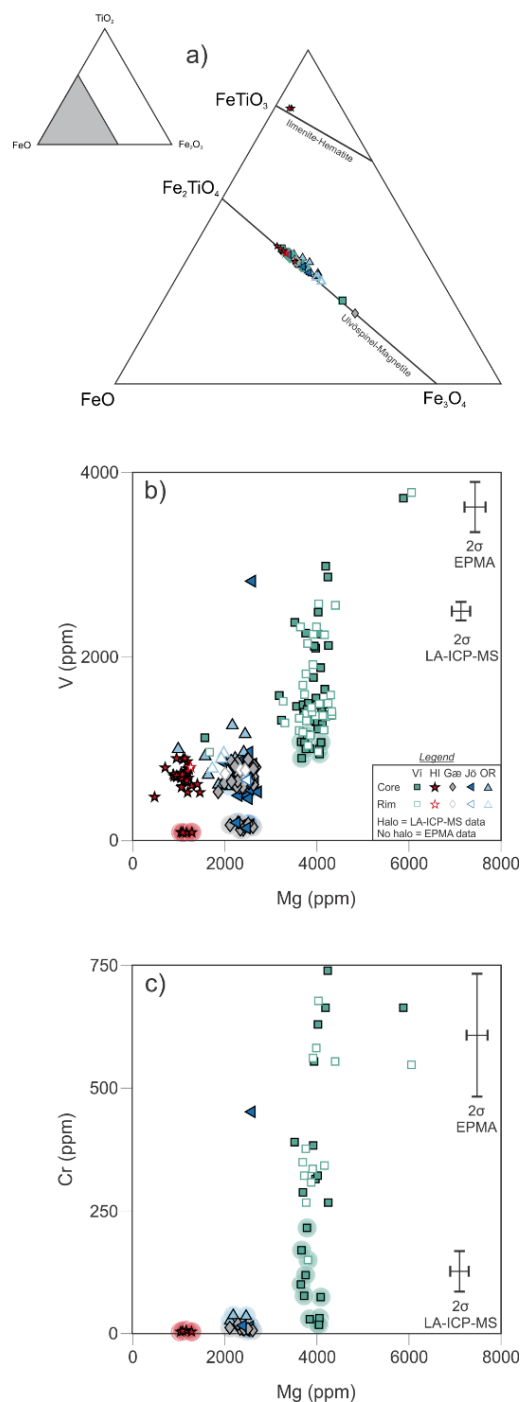
Figure 3.8. Selected compositional plots for Fe-Ti oxides. a) Enlargement of part of the FeO-Fe₂O₃-TiO₂ ternary (shaded in inset). EPMA analyses recalculated after Carmichael (1967). b, c) Concentrations of selected minor elements determined by both LA-ICP-MS (circular halo) and EPMA (no halo). Error bars (2σ) for EPMA analyses were determined from replicate analyses of the NMNH 96189 ilmenite standard. Errors for LA-ICP-MS analyses are estimated were estimated based on relative errors for replicate analyses of BCR-2G glass.

Titanomagnetites from the IDDP-1 rhyolite are more Fe-rich and Ti-poor than most grains in the erupted rhyolites (Usp$_{31-53}$; Masotta et al., 2018).

3.5.4. Glass Chemistry

3.5.4.1. Matrix Glass

Matrix glasses from Jörundur, Hlídarfjall, Hrafntinnuhryggur and Víti are high-silica rhyolite (>74.5 wt% SiO$_2$, normalised anhydrous). The major element compositional fields for each unit overlap within analytical uncertainty, but mean compositions are distinct within $\pm$ 2 σ_M (where σ_M is the standard error of the mean) (Fig. 3.9). Hrafntinnuhryggur matrix glass is the least evolved of the suite, with the lowest average SiO$_2$ and K$_2$O contents, but the highest Na$_2$O, whereas Víti glasses have the highest average SiO$_2$ and K$_2$O contents (Fig. 3.9c), but also the highest MgO, TiO$_2$ and Co (not shown) , and lowest REE (Fig. 3.10a), Y (Fig. 3.10c), Nb, Ta and Ga (not shown). Jörundur and Hlídarfjall glasses display near-total compositional overlap for many major and most trace elements, but Hlídarfjall is distinguished by lower average FeO*, MgO and TiO$_2$, higher average Al$_2$O$_3$, and lower Sc and Zr. Chondrite-normalised REE patterns for each unit are essentially parallel and mirror the whole-rock patterns, with steep LREE-MREE and flat MREE-HREE trends, and negative Eu anomalies (Eu/Eu* = 0.47-0.61; Fig. 3.10a). Due to extensive groundmass devitrification, we were unable to obtain reliable matrix glass analyses for Gæsafjallarani or the oldest rhyolite.

Published glass compositions for the IDDP-1 rhyolite (normalised anhydrous) (Elders et al., 2011; Zierenberg et al., 2013; Masotta et al., 2018) show strong overlap with matrix glasses from Jörundur, Hlídarfjall and Víti (Figs. 3.9, 3.10). An exception is the Na$_2$O data of Masotta et
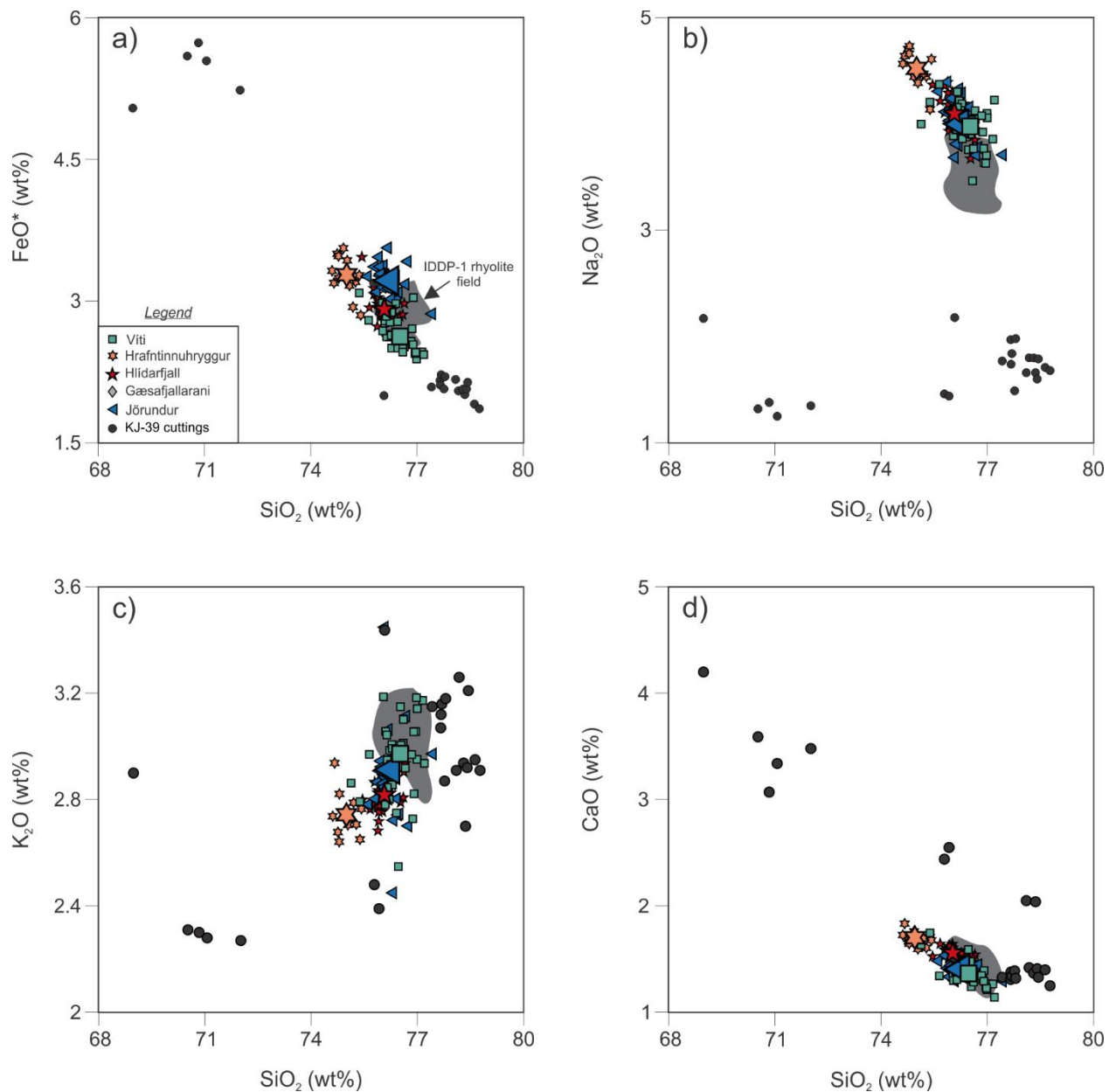
Figure 3.9. Selected major element compositional plots (determined by EPMA) for matrix glasses, normalised anhydrous. Large symbols show the mean for each unit; ± 2 σ_M error bars are smaller than these symbols. Grey field shows the range of published glass analyses for drill cutting samples of the IDDP-1 rhyolite from Zierenberg et al. (2013) and Masotta et al. (2018). KJ-39 drill cutting data are from Mortensen et al. (2010).

al. (2018), which are systematically lower than those of the other authors, likely reflecting minor

Na$_2$O loss during their EPMA analyses. On the other hand, glasses from the KJ-39 cuttings span a

wide compositional range from dacite to rhyolite (Mortensen et al., 2010; Fig. 3.9). KJ-39 rhyolitic

compositions are distinct from both the IDDP-1 and erupted rhyolites, with lower FeO* and Na_2O

and higher CaO and Al_2O_3 at a given SiO_2 content.
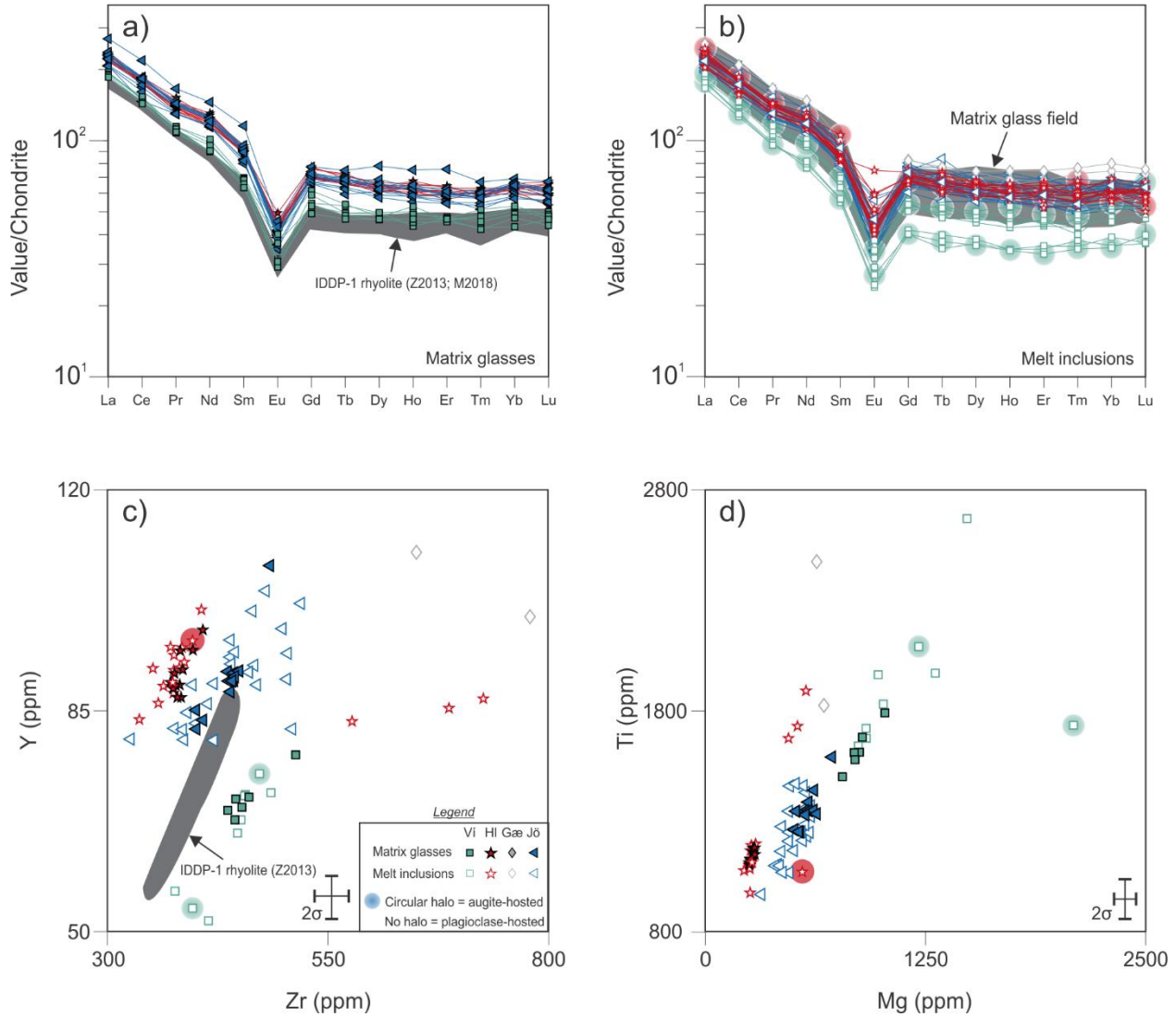
Figure 3.10. Selected trace element compositional plots (determined by LA-ICP-MS) for matrix glasses and melt inclusions. a) and b) show matrix glasses and melt inclusions, respectively, normalised to the chondrite value of McDonough and Sun (1995). Analytical uncertainties (2σ) were estimated based on relative errors for replicate analyses of BCR-2G. Z2013 = Zierenberg et al. (2013); M2018 = Masotta et al. (2018).

3.5.4.2. Melt Inclusions

Melt inclusion compositions from each erupted unit are exclusively rhyolitic and mainly cluster inside the field of matrix glasses. Almost all analyses from Hlídarfjall, Jörundur and Víti are within 2σ analytical error of their respective mean matrix glass major element composition (Fig. 3.11), excluding two slightly more primitive augite-hosted inclusions from Víti and three plagioclase-hosted inclusions from Hlídarfjall that extend to lower SiO_2 and higher Al_2O_3, FeO*, CaO, P_2O_5, MgO and/or TiO_2. The three primitive Hlídarfjall inclusions are also enriched in Zr (Fig. 3.10c), Hf, Sc and Eu relative to matrix glasses and all or most other Hlídarfjall inclusions. Trace element compositions of most other inclusions overlap almost completely with their corresponding matrix glasses for most elements; notable exceptions are a subset of inclusions from Hlídarfjall and Jörundur and a single inclusion from Víti with shallower Eu anomalies ($Eu/Eu^* = 0.65 - 0.95$; Fig. 3.10b), three Víti inclusions near the middle of the SiO_2 range with low REE and Y contents (Fig. 3.10b, c), and an additional two Víti inclusions with high Mg and/or Ti (Fig. 3.10d).

The analytical precision of our melt inclusion H_2O Raman analyses is relatively poor due to the interfering effects of the mounting epoxy, which had to be removed by subtracting the epoxy background from the spectrum for each glass (see methods section). Nonetheless, we observe a good linear correlation between our epoxy-corrected Raman data and estimates of H_2O from EPMA analyses (by difference), which cluster around the 1:1 line (Fig. 3.12). We thus consider our Raman and EPMA by difference H_2O data to provide first-order estimates of glass H_2O contents, with an error of approximately ±1 wt%. Víti melt inclusions, along with several outliers from Hlídarfjall, Jörundur, and a single glassy inclusion from Gæsafjallarani, mainly cluster between ~2-4 wt% H_2O (Fig. 3.12). Other analyses for Hlídarfjall and Jörundur cluster between
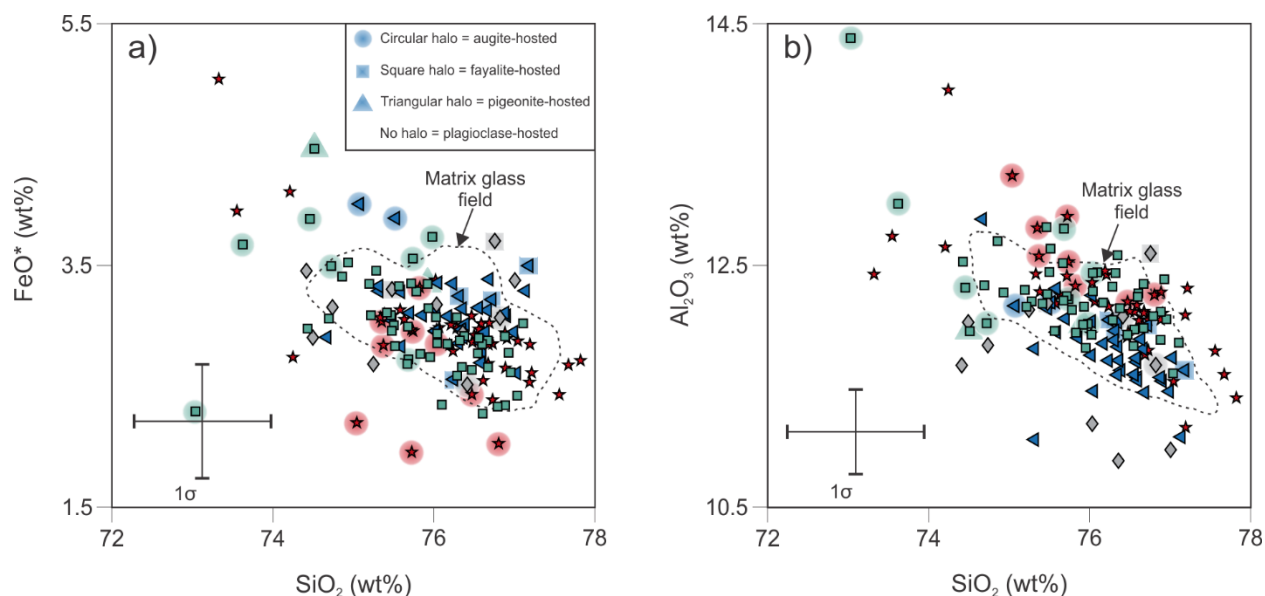
Figure 3.11. Selected melt inclusion major element compositional plots (determined by EPMA). The dashed field encloses all matrix glass analyses from erupted Krafla rhyolites.
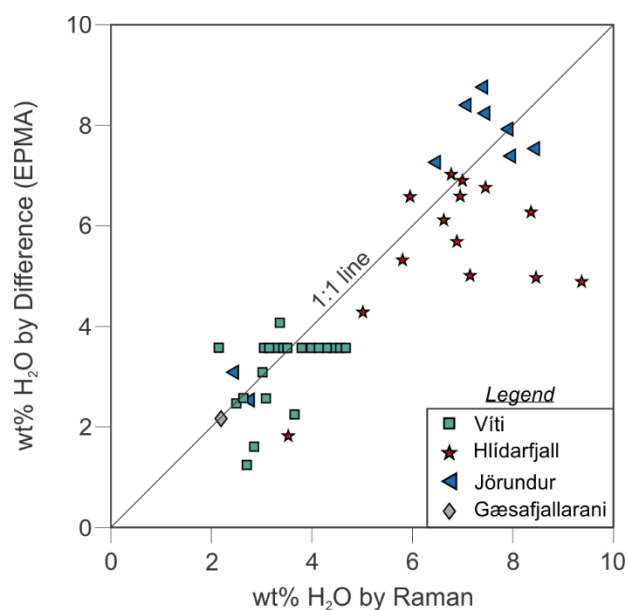
Figure 3.12. Glass H_2O from EPMA by difference (i.e., difference between the raw analytical total and 100%) vs. H_2O by Raman.

~4-7 and ~7-9 wt% H_2O, respectively (Fig. 3.12). Cracks connecting these more H_2O-rich inclusions with the crystal rims are usually visible in the plane of section, and we thus interpret their high H_2O contents to reflect secondary (post-eruptive) glass hydration. The lower H_2O

inclusions from these ridges and Víti do not show textual evidence for hydration or post-entrapment crystallisation, so we infer that these inclusions record magmatic H_2O contents of approximately 2-4 wt%. These values are in good agreement with the 2.9 wt% primary H_2O content calculated for the IDDP-1 rhyolite prior to ascent and degassing, and its present (partially degassed) H_2O content of 1.77 ± 0.15 wt% (Zierenberg et al., 2013). The middle of our proposed range also agrees well with the 2.7 wt% H_2O content of the compositionally similar 1875 C.E. rhyolite from the nearby Askja system determined from melt inclusion analyses (Schattel et al., 2014).

3.5.5. Geothermometry and Geohygrometry

Magmatic temperature estimates for the crystal-bearing rhyolites were derived from equilibrium crystal rim/carrier melt pairs using the plagioclase-melt thermometers of Putirka (2008) and Waters and Lange (2015), and the clinopyroxene-melt thermometer of Brugman and Till (2019). Matrix glass compositions are not available for the oldest rhyolite or Gæsafjallarani due to pervasive devitrification; hence, as above, rims from the oldest rhyolite were paired with the whole-rock composition, which approximates the carrier melt due to its low crystal content, and Gæsafjallarani rims were paired with the average Jörundur matrix glass. We also calculated temperature estimates for Víti using paired augite-pigeonite rim compositions from individual crystal aggregates using QUILF (Andersen et al., 1993), and zircon saturation temperatures for all units using the model of Boehnke et al. (2013). Both plagioclase-liquid thermometers require pressure and magmatic H_2O estimates as inputs, so we calculated a range of temperatures for each equilibrium pair using H_2O contents of 2 and 4 wt% (from Raman analyses; see above) and pressures of 0.5 and 1 kbar. Our minimum pressure estimate corresponds with the approximate
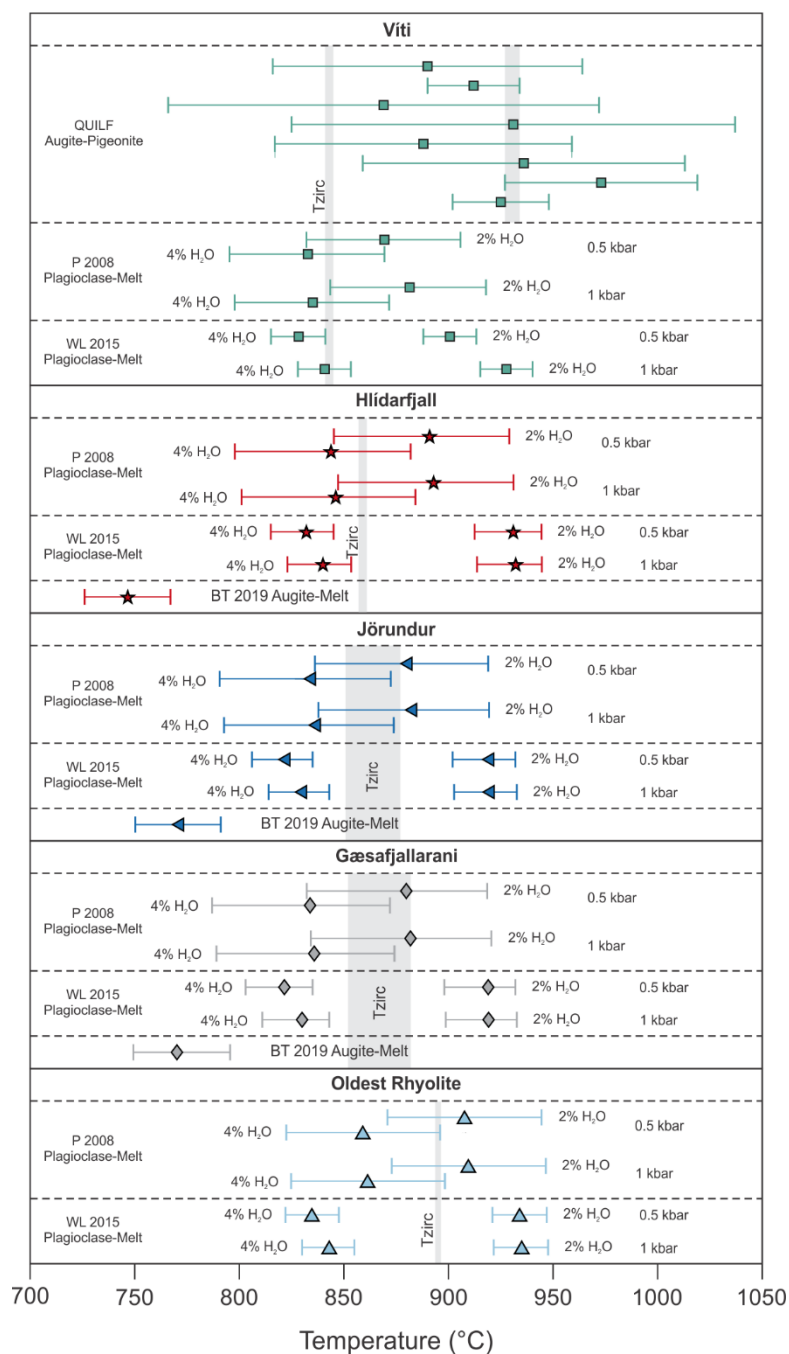
Figure 3.13. Geothermometry results. P 2008 = Putirka (2008); WL 2015 = Waters and Lange (2015); BT 2019 = Brugman and Till (2019). QUILF temperatures are from individual augite-pigeonite pairs; vertical grey bar highlights the temperature range at which all pairs overlap within error. Symbols for other thermometers show the median temperature calculated for each unit and error bars denote the full calculated temperature range, including the standard error of estimate associated with each thermometer. Vertical grey bars labelled Tzirc are zircon saturation temperatures after Boehnke et al. (2013).

120

depth of the IDDP-1 rhyolite at ~2 km, and the maximum matches the approximate depth of the shallow basaltic magma system around which rhyolites are thought to form (Jónasson, 1994; Pope et al., 2013). Although we cannot rule out storage at higher pressures, both thermometers are relatively insensitive to pressure inputs (see below), so any errors resulting from incorrect pressure estimates are unlikely to be larger than the calibration errors of the thermometers.

The Putirka (2008) and Waters and Lange (2015) thermometers yield results that are within error for each set of inputs. Both calibrations are highly sensitive to melt H_2O content. Estimates range from ~800-940°C for Víti and Hlídarfjall, ~790-930°C for Jörundur and Gæsafjallarani, and ~820-950°C for the oldest rhyolite, with the highest temperatures corresponding with the driest melts (Fig. 3.13). For Víti, the higher temperatures, corresponding with 2 wt% H_2O, are in reasonably good agreement with the augite-pigeonite temperatures from QUILF; individual estimates have large errors, but most cluster between ~880-950°C, and all QUILF temperatures overlap within uncertainty over a narrow range at ~930°C. Plagioclase-melt temperatures for Hlídarfjall, however, are uniformly higher than the ~725-770°C range predicted by the Brugman and Till (2019) clinopyroxene-melt thermometer, while the lowest plagioclase-melt temperatures for Jörundur and Gæsafjallarani are just within error of the ~750-800°C predicted by the Brugman and Till model (Fig. 3.13). Although this could suggest that our melt H_2O estimates for plagioclase-melt thermometry are too low, these temperatures are difficult to reconcile with the low crystallinity of these units. To investigate this further, we ran isobaric equilibrium crystallisation models with rhyoliteMELTS (Gualda et al., 2012) using a representative Jörundur whole-rock composition (KR-128) with H_2O contents of 2 and 4 wt% as the starting melt, pressures of 0.5 and 1 kbar, and oxygen fugacities of FMQ and FMQ+1. For all models, rhyoliteMELTS predicts a total crystallinity of at least 34% by mass for temperatures below 800°C,

well above the observed crystal content (cf. Table 3.2). Models with lower pressure and/or lower H_2O inputs predict higher crystal contents, usually well above 50%. Achieving crystal contents approaching those observed in the Krafla rhyolites at <800°C requires unreasonably high pressure and/or H_2O inputs. We thus conclude that the low temperatures returned by the Brugman and Till (2019) model are in error. This may be a consequence of the Fe contents of these rhyolites, which are high compared with most melts used to calibrate the thermometer and may thus stabilise Fe-rich pyroxenes at higher temperatures than typical for silicic melts. We suggest caution in applying this thermometer to Fe-rich Icelandic rhyolites.

Comparison with our calculated zircon saturation temperatures provides an additional constraint on our temperature estimates, and hence also on melt H_2O contents. For the zircon-bearing extra-caldera ridge magmas, zircon saturation temperatures suggest a maximum magmatic temperature of ~850°C. Using the average zircon saturation temperature for each ridge as a temperature input for the Waters and Lange (2015) model suggests minimum melt H_2O contents (median ± standard error of estimate) of 3.6 ± 0.4 wt% for Hlídarfjall, 3.1 ± 0.4 wt% for Jörundur, and 3.0 ± 0.4 wt% for Gæsafjallarani. The Boehnke et al. (2013) model provides minimum magmatic temperature estimates for the zircon undersaturated units, suggesting T ≥841°C for Víti and ≥895°C for the oldest rhyolite. These minimum temperatures correspond with maximum melt H_2O contents of 3.9 ± 0.4 wt% and 2.8 ± 0.4 wt%, respectively. We thus conclude that the extra-caldera ridge rhyolites were cooler, and possibly more hydrous, than the Víti and oldest rhyolites.

3.6. DISCUSSION

Previous studies of Krafla rhyolites have mainly focused on distinguishing between two endmember petrogenetic processes: 1) fractional crystallisation of basaltic parental melts with minor assimilation of hydrothermally altered basaltic wall rock (Nicholson et al., 1991; Charreteur et al., 2013), and 2) low-degree partial melting (anatexis) of hydrothermally altered basaltic crust around the margins of intrusions, followed by extraction of this rhyolitic melt by crustal deformation (Jónasson, 1994, 2007). These opposing models are largely based on differing interpretations of whole-rock chemical and isotopic data. Here, we first consider the different perspective that detailed microanalysis offers on the processes by which Krafla rhyolites assemble and evolve. We then integrate this perspective with insights from published experimental work on partial melting of altered basalts and new petrologic modeling, and present a revised conceptual model for rhyolite petrogenesis at Krafla. Lastly, we examine the dynamics of rhyolitic magmatism at Krafla through time.

3.6.1. Generation and Assembly of Krafla Rhyolites

3.6.1.1. Origin of the Crystal Populations

Macrocryst compositions in Krafla rhyolites are mainly consistent with growth from rhyolitic melts similar to, or only slightly more primitive than, their carrier melt. Most plagioclase cores and interiors, for instance, have compositions appropriate for equilibrium with a melt equivalent in composition to the average whole-rock analysis for their respective unit (Fig. 3.4e). The majority that do not meet the equilibrium criterion come close; of the 10% of plagioclase cores from the extra-caldera ridges that fail the equilibrium test, three quarters have compositions appropriate for equilibrium with a slightly less evolved rhyolite, similar to the Víti composition. Similarly, most

augite and orthopyroxene cores and interiors are appropriate for equilibrium with their respective whole-rock compositions, or with melts only slightly less evolved (Fig. 3.6i, j). Cr contents are almost always below detection limit (<2-3 ppm) for augites and orthopyroxenes with Mg# <50, and commonly also for Mg# >50, implying that most pyroxenes derive from fractionated melts depleted in highly compatible elements. Growth of most macrocrysts from melts similar to their host is also supported by the overlap of most melt inclusions with matrix glass compositions of their respective unit (Figs. 3.10, 3.11).

A minority of macrocryst compositions, however, are too primitive for equilibrium with high-silica rhyolite melt. For example, 12% of all plagioclase cores are too calcic for equilibrium with the least evolved (Víti) rhyolite bulk composition (cf. Fig. 3.4e). These crystals, however, are more sodic (<~60 mol% An) than the most evolved plagioclase reported from Krafla basalts (cf. Nicholson, 1990; Cooper et al., 2016), and we thus infer that they derive from intermediate or less evolved silicic melts (i.e., dacite or low-silica rhyolite). Scarce augite and orthopyroxene cores and interiors from Jörundur and Víti with Mg# >60 could derive from mafic or intermediate melts, but could also be in equilibrium with relatively evolved liquids similar to the Víti rhyolite (Fig. 3.6i, j). High concentrations of highly compatible trace elements in some of the most primitive augites and orthopyroxenes (e.g., 134 and 151 ppm Cr in two analyses from Gæsafjallarani with Mg# 58 and 54; 453 ppm Cr in one analysis from Víti with Mg# 63), however, imply growth from mafic melts not yet depleted in strongly compatible elements. We thus conclude that the rhyolite crystal populations mainly comprise true phenocrysts genetic to their host melt, but a minority of cores and interiors are derived from less evolved melts. The source of these foreign crystals is explored further below.

3.6.1.2. Crystal Zoning as a Record of Late-Stage Magma Assembly and Evolution

The abundance of normal core-rim zoning among plagioclase and augite populations (Figs. 3.4, 3.6) and rim-ward decreases in compatible element concentrations (e.g., Co, V and Cr in pyroxenes; Fig. 3.7) are consistent with a general trend of crystal growth in a progressively evolving melt. Occasional melt inclusions with compositions more primitive than matrix glasses (Fig. 3.10), and enriched in elements compatible in the observed mineral assemblages (e.g., Sc, Zr, Hf, Ti, Mg and Eu; Fig. 3.11), also imply progressive melt evolution during crystal growth. We interpret these features as further evidence for late-stage fractional crystallisation, which drove the cooling melt to high-silica rhyolite compositions. This is consistent with recent findings of Hampton et al. (in prep.), who identified trends of decreasing Hf/Yb with increasing Th/U in zircons from the extra-caldera ridges that are well-modelled by 20-30% fractional crystallisation.

Although mineral compositions and core-rim zoning patterns are consistent with an overall trend of cooling and differentiation, complex internal zoning patterns in many plagioclase and pyroxene crystals allude to oscillating physical and/or chemical conditions within the magma body or bodies and periods of disequilibrium between crystals and melt. For plagioclase, the fine-scale oscillatory zoning with small chemical oscillations (<2-3 mol%) shown by the "subtle oscillatory" type (Table 3.4) can be attributed to kinetic effects in a local boundary layer between the growing crystal and melt, but larger abrupt compositional shifts and internal resorption surfaces require a different process or processes (e.g., Ginibre et al., 2002a). For melt of a given composition, the An content of crystallising plagioclase is positively correlated with both temperature and P_{H_2O} (e.g., Waters and Lange, 2015). Hence, in a magma body closed to recharge, fluctuations in plagioclase An content can relate to 1) temperature variations related to thermal convection (Couch et al.,

2001), or 2) multiple stages of ascent and decompression, possibly with resultant degassing of H_2O (e.g., Humphreys et al., 2006).

Alternatively, open system processes involving magma mixing and/or thermal rejuvenation of near- or sub-solidus intrusions by hot recharge magma can cause abrupt changes in An content. Usually, intruding recharge magmas are compositionally distinct from the resident magma, although rejuvenation of sub-solidus felsite intrusions by rhyolite melt of almost identical composition was likely involved in assembling the IDDP-1 rhyolite body (see Masotta et al., 2018). In the more usual case where recharge magmas are compositionally distinct, Fe concentrations provide a useful means to identify open system processes because Fe incorporation into plagioclase primarily depends on melt composition (e.g., Ginibre et al., 2002b; Lundgaard and Tegner, 2004). Small differences in Fe partitioning can result from slight changes in fO_2 during closed-system differentiation and degassing, but large and correlated Fe-An shifts imply mixing between compositionally distinct magmas (e.g., Ruprecht and Wörner, 2007).

Compositional contrasts in An content and FeO* across major plagioclase resorption surfaces are plotted in Fig. 3.14. The majority of resorption events, corresponding mainly with "dark resorbed core" or "multiple resorption" type zoning patterns (Table 3.4), show An increases of <10 mol% and no resolvable change in Fe within 2σ uncertainty. A smaller number (9%), including "patchy-", "bright core-" and "multiple resorption-" type crystals show decreases in An content, which are usually decoupled from any detectable change in Fe. We interpret these resorption events with no corresponding change in Fe as a likely consequence of closed-system processes, involving either thermal oscillations in a convecting magma body, or changes in P_{H_2O} related to ascent. Alternatively, some such resorption events may reflect incorporation of crystals from sub-solidus felsite intrusions into compositionally similar rhyolitic melt, as proposed by

Masotta et al. (2018) for the IDDP-1 crystals. The considerable diversity in major and especially trace element compositions of Víti crystals imply mixing of crystals from several sources (discussed further below), consistent with the latter process. On the other hand, normal zoning across resorption surfaces in the absence of Fe changes, such as the "bright core-" type crystals, may be a consequence of plagioclase resorption during ascent of a water-undersaturated melt (e.g., Holtz et al., 2001), followed by water exsolution and overgrowth of more sodic compositions once saturation is achieved at shallower depths (Humphreys et al., 2006). Only 12% of resorption surfaces show a coupled increase in Fe and An ($>2\sigma$ analytical uncertainty) consistent with incorporation into a more mafic melt. We thus infer that the late-stage evolution of the Krafla rhyolites occurred largely in isolation from the underlying mafic system, and most crystals did not experience compositional mixing with mafic recharge magmas.
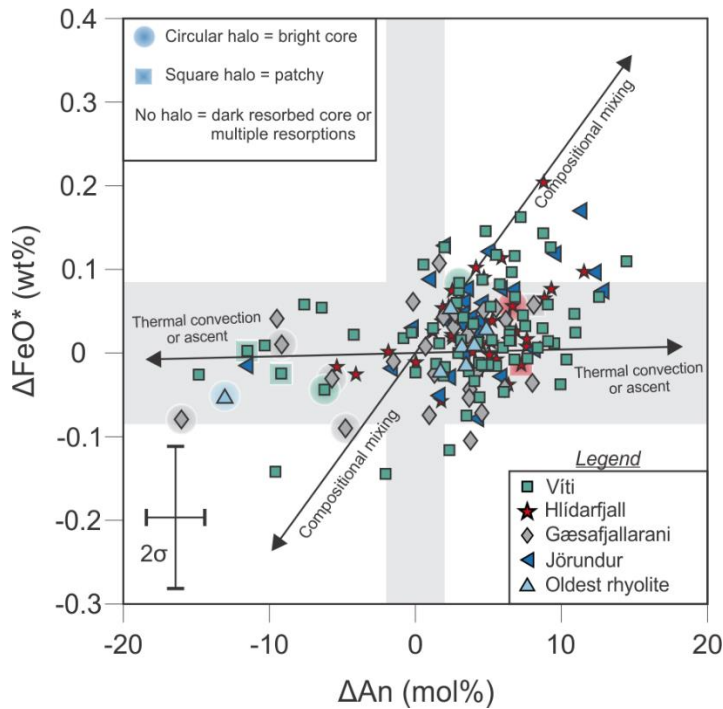
Figure 3.14. Compositional changes across plagioclase internal resorption surfaces. ΔAn = change in plagioclase An (mol%; outer zone – inner zone). ΔFeO* = change in total Fe expressed as FeO (wt%; outer zone – inner zone). Compositional mixing and thermal convection or ascent vectors after Ruprecht and Wörner (2007). Compositional changes plotting within the grey fields are less than the 2σ analytical uncertainty.

Like plagioclase, augite zoning is consistent with differentiation of silicic magma that was largely closed to mafic input. Major resorption surfaces or sharp compositional boundaries corresponding with large and coupled increases in Mg# (>10) and compatible element concentrations (e.g., Sc, V, Cr, Co), indicative of mixing with mafic recharge magma (e.g., Astbury et al., 2018; Ubide and Kamber, 2018), are absent. Those crystals that do show textural evidence for large and abrupt compositional shifts (Mg# >10) or major resorption events ("dark resorbed core-", "patchy-" and some "concentric" types) are normally zoned across these boundaries. The small number of dark-resorbed cores with Mg# >60 (in equilibrium with basaltic melts) could perceivably derive from intruding basaltic magmas, but the lack of evidence for such recharge events in the other crystals implies that they more likely reflect minor assimilation of basaltic restite or wallrock.

3.6.1.3. Petrogenesis of Krafla Rhyolites

The mineral compositions and zoning patterns discussed above, and occasional melt inclusions less evolved than their corresponding matrix glass, are inconsistent with Jónasson's (1994, 2007) model for the generation of Krafla rhyolites in a single step by melting of hydrothermally altered basalts, and require at least some degree of fractional crystallisation (FC hereafter). Two scenarios are possible: 1) the partial melting process envisioned by Jónasson (1994, 2007) produces an intermediate or less evolved silicic melt (e.g., a low-silica rhyolite or dacite), which is extracted from its source region and then evolves to high-silica rhyolite by FC (± assimilation) (Sigmarsson et al., 1991, 1992; Martin and Sigmarsson, 2010), or 2) the minerals record the final stages of a protracted AFC process from a mafic parent (sensu Nicholson et al., 1991), but most or all crystals that have cores in equilibrium with mafic melts from the earliest stages of differentiation have been

completely separated from the final magma. Here we combine evidence from melting experiments on altered basalts with new major and trace element modeling to explore these alternatives.

3.6.1.3.1. Experimental Perspectives on Rhyolite Petrogenesis

Central to Jónasson's (1994, 2007) argument are the Fe-rich and Al- and Ca-poor compositions of Krafla rhyolites, which he noted resemble low-degree partial melts of hydrated basalts or metabasalts produced experimentally at P_{H_2O} <1 kbar and P_{total} = 1-3 kbar (Spulber and Rutherford, 1983; Thy et al., 1990; Beard and Lofgren, 1989, 1991). Jónasson (1994, 2007) also argued for melting at $fO_2 \leq$ FMQ, but we note that only the Spulber and Rutherford (1983) experiments were run at these reducing conditions. More recent low-pressure melting experiments on altered basaltic or gabbroic rocks have produced melts similar to Icelandic rhyolites at relatively oxidizing conditions more appropriate for hydrothermally altered materials (fO_2 on or above the nickel-nickel oxide [NNO] buffer; Koepke et al., 2004; France et al., 2010; Erdman et al., 2015), and we suggest that the fO_2 constraint can be relaxed. Nonetheless, because of its strong effect on plagioclase stability, low P_{H_2O} is especially important in Jónasson's model. Due to the greater stability of plagioclase relative to mafic phases in the source, melting at low P_{H_2O} forms silicic melts that are rich in Fe and poor in Al and Ca, similar to Icelandic rhyolites (Spulber and Rutherford, 1983; Beard and Lofgren, 1989, 1991; Thy et al., 1990).

Despite their compositional similarities, we note the following problems in Jónasson's (1994, 2007) comparison of Krafla rhyolites with experimental melts. First, because of the breakdown of hydrous alteration minerals and the relatively low solubility of H_2O in silicic melts at low pressure, experimental melts of hydrothermally altered basaltic rocks at low pressure (1-2

kbar) may in some cases reach water saturation regardless of whether excess water is added to the experimental charge or not (e.g., France et al., 2010). Thus, at low pressure, even pure dehydration melting of altered basaltic rocks, where only structural water in hydrous minerals is available for melting reactions, can destabilize plagioclase and produce melts in equilibrium with a water-rich fluid (i.e., $P_{H_2O} \sim P_{total}$, aH_2O close to 1), which have higher Al contents than Icelandic rhyolites. Second, the experimental results reveal difficulties in producing high-silica rhyolite compositions; the required melt fractions are low (generally <10%) and restricted to a narrow temperature window (<~50°C) near the solidus, and some experiments failed to produce high-silica rhyolite at all (Fig. 3.15). Although melting at a eutectic could produce low degrees of evolved melt at constant temperature, field evidence of partial melting around the roofs of exhumed shallow mid ocean ridge magma chambers suggests that large heterogeneities in degree of melting and melt composition develop locally, and that segregation of silicic partial melts from their source region is relatively inefficient (Gillis and Coogan, 2002). Hence, even though the bulk melt composition produced by low-degree partial melting of altered basalts is undoubtedly silicic, we infer that significant volumes of high-silica rhyolite are unlikely to be generated by this melting process alone, and, as suggested by our petrologic data, at least some degree of fractional crystallization is required.

3.6.1.3.2. Modeling of Rhyolite Petrogenesis

To test the possibility that Krafla rhyolites derive from a two-stage process involving partial melting of altered basalts followed by FC, we first calculate the parental melt compositions for Krafla rhyolites prior to varying degrees of FC of their observed mineral assemblages (i.e.,
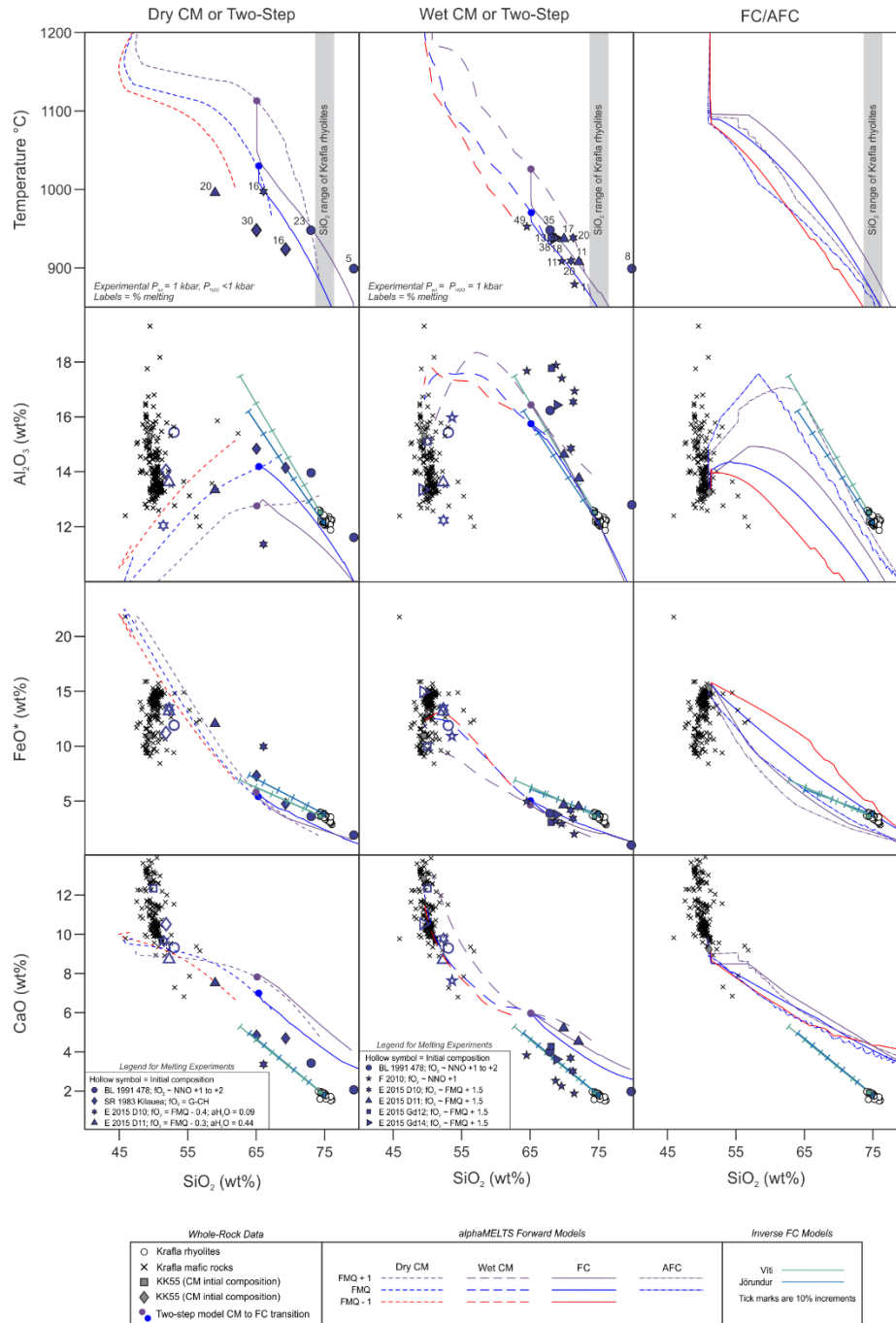
Figure 3.15 Selected major element models for rhyolite petrogenesis by nominally dry (initial H_2O = 0.1 wt%; left column) or wet (initial H_2O = 3 wt%; central column) continuous melting, a two-step process involving melting followed by FC (left and central columns), and pure FC or AFC (right column). Details of conditions and starting compositions are in the text. Compositions of experimental partial melts produced from hydrated or altered basalts and metabasalts are shown for water-undersaturated (left column) or water-saturated (middle column) conditions and 1 kbar total pressure. Data for Krafla mafic rocks are from Grönvold and Mäkipää (1978), Nicholson (1990), Hemond et al. (1993), Jónasson (1994) and Cooper et al. (2016). SR 1983 = Spulber and Rutherford (1983); BL 1991 = Beard and Lofgren (1991); F 2010 = France et al. (2010); E 2015 = Erdman et al. (2015).

inverse FC, by mass balance), and compare them with the experimental melts produced at 1 kbar (approximately equivalent to the upper parts of basaltic magma chamber or storage zone at Krafla at ~3-4 km depth; e.g., Einarsson, 1978). Calculations were performed for representative whole-rock compositions from Víti and Jörundur, using average measured mineral core compositions and representative modal proportions (Tables A4.1, A4.2). The calculated compositions trend towards the majority of experimental melts, including both water-saturated and water-undersaturated experiments (Fig.3.15), suggesting that the major element compositions of the Krafla rhyolites could be consistent with generation by FC of silicic partial melts generated from altered basalts at $P_{H_2O} \leq 1$ kbar; approximately 10-20% fractionation of the observed mineral assemblage is required to produce the observed compositions from a low-silica rhyolite, and ~20-50% fractionation is required from a dacite. Where reported, trace elements compositions of altered basalts from the experimental literature differ from the relatively enriched Krafla basalts, precluding a direct comparison for trace elements.

To further explore the above two-step model for rhyolite petrogenesis (partial melting followed by FC), and the alternative of protracted AFC from a basaltic parent, we forward-modelled both scenarios using alphaMELTS version 1.9 (Smith and Asimow, 2005), implementing the MELTS algorithm of Ghiorso and Sack (1995). Additionally, parental melt trace elements compositions were calculated with inverse FC models using mineral-melt partition coefficients calculated from the average rim and matrix glass compositions (determined by LA-ICP-MS, including only rims that passed the major element K_D test for equilibrium), and compared with silicic partial melts produced by the forward models. The apparent partition coefficients are in or near the range of published values for most elements and show the expected parabolic trends on Onuma plots (values and plots are in the electronic appendix), hence we infer that they provide

a better estimate of element partitioning in this system than values chosen arbitrarily from the literature. Partition coefficients for most elements are generally lower in less evolved melts, so extrapolating our apparent coefficient coefficients back to dacitic compositions provides a maximum estimate for most elements.

Our ability to forward model a partial melting scenario is limited by a lack of quantitative petrologic data from altered Krafla (or similar Icelandic) basalts (e.g., bulk trace element compositions, compositions and modal proportions of igneous and alteration minerals). Hence, these models are presented with the caveat that MELTS is unable to model hydrous alteration phases. Despite this limitation, the MELTS models reproduce the general major element trends of the above experimental studies and predict the residual phases relatively well, so we infer that they provide a reasonable approximation of the partial melting scenario. Large ion lithophile elements (Rb, Sr, Ba), and in some cases LREE, are mobile during even low-grade alteration (e.g., Wood et al., 1976; Gibson et al., 1982), so their concentrations in altered Krafla basalts may be poorly approximated by the fresh starting composition used. We therefore focus discussion on the high field strength elements (Zr, Nb, Hf, Ta,), Y, Th, and MREE-HREE, which are immobile even under greenschist conditions (Pearce and Cann, 1973).

Forward models for equilibrium and continuous melting (i.e., continual melt extraction from the system to retain a specified melt fraction, in this case 5 vol%) were generated for sample KK55 from Nicholson (1990), a representative Krafla basalt that falls near the middle of the observed range for most major and trace elements. Results for equilibrium and continuous melting were similar, so we present and discuss only the continuous melting models. For ease of comparison with the melting experiments, pressure was set at 1 kbar, and aH_2O was fixed at 1 by adding 3 wt% H_2O to simulate hydration from hydrothermal alteration. Nominally dry models

were also run with 0.1 wt% H_2O to constrain the effect of low P_{H_2O} on melting. To test the viability of the two-step process, FC after partial melting was forward-modelled for all partial melts that reached 65 wt% SiO_2. Minor differences in the initial melt composition produced by partial melting are not expected to have a large affect on the trends for subsequent FC, hence we consider these models to be broadly representative of the two-step process.

We also computed isenthalpic (i.e., heat-balanced) forward AFC models with alphaMELTS, using the same fO_2 and pressure inputs. To minimise the difference between the starting and target (rhyolitic) composition, a relatively evolved basaltic starting composition (KR-257, from the uppermost part of the Halarauður ignimbrite) was chosen, and we assumed 1 wt% H_2O, a typical value for the most evolved Icelandic basalts (Nichols et al., 2002; Guilbaud et al., 2007). KK55 with an assumed 3 wt% H_2O was used as the assimilant, with an assumed temperature of 600°C. For comparison, pure FC models (i.e., without assimilation) were also run. All MELTS models used composition- and temperature-dependent partition coefficients for plagioclase and clinopyroxene calculated after Blundy and Wood (1994) and Wood and Blundy (1997), respectively.

As expected, the nominally dry melting models produce depletions in Na_2O and Al_2O_3 relative to melting at $aH_2O = 1$, because of the greater stability of plagioclase at lower aH_2O (Fig. 3.15). However, except under the most oxidising conditions (FMQ + 1), they fail to produce rhyolitic melt even at very low melt fractions; initial melts are rhyodacitic at fO_2 = FMQ, and andesitic-dacitic at FMQ-1. In the most oxidising case, rhyolite is produced only at melt fractions <4%. These results are in good agreement with melting experiments, and further emphasise the above-mentioned difficulties in producing rhyolite by partial melting alone. Even more indicative are the trace elements, which are a poor match for the natural rhyolites (Fig. 3.16). The worst fit
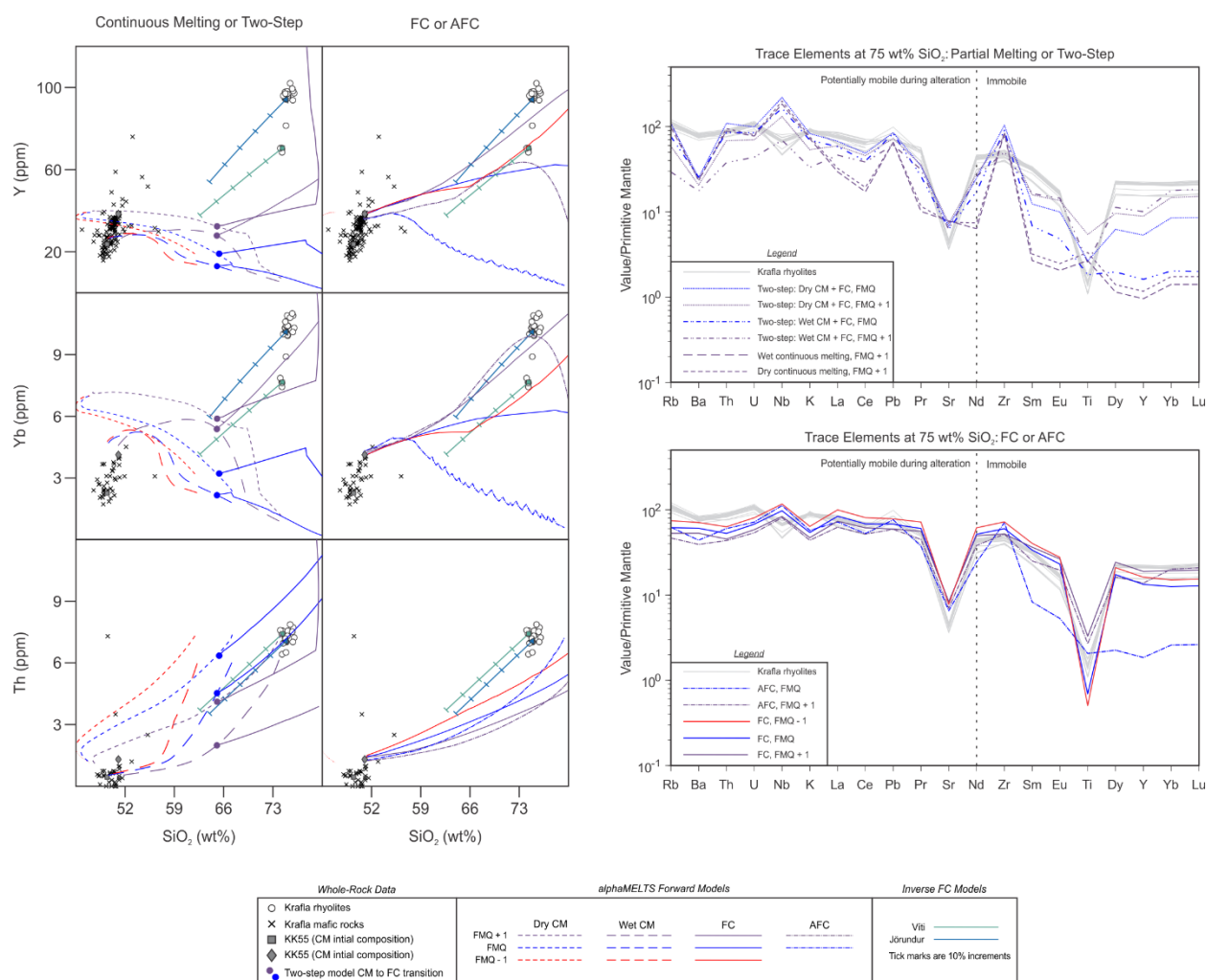
Figure 3.16 Selected trace element models for rhyolite petrogenesis by nominally dry (Dry CM) or wet (wet CM) continuous melting, a two-step process involving continuous melting followed by FC, and pure FC or AFC (details are in the text). Spider diagram normalised to primitive mantle values of Sun and McDonough (1989). Elements to the left of the dashed vertical line may be mobile during hydrothermal alteration, so should be viewed with caution for partial melting and AFC models. Inverse FC model calculations and partition coefficients are in the electronic appendix.

is for the REE, especially the MREE-HREE (plus Y), for which the normalised concentrations at 75 wt% SiO_2 are more than an order of magnitude lower than those observed. The two-step forward models provide a better fit for most trace elements at the most oxidising conditions (fO_2 = FMQ + 1), approximating the trends of the reverse FC models for some elements, but the overall fit is still

TABLE 3.6. SUMMARY OF FC, AFC AND TWO-STEP MODELS

Model	Starting Composition	fO₂ Buffer	Assimilant	R (Mass assmilated/mass of cumulates) at 75 wt% SiO₂	Temperature (°C) at 75 wt% SiO₂	Assemblage at 75 wt% SiO₂
FC	KR-257, 1 wt% H_2O	FMQ+1	-	-	894	70% plag, 9.1% aug, 7.6% opx, 5.9% ilm, 3.7% Ti-mt, 3.4% ap
FC	KR-257, 1 wt% H_2O	FMQ	-	-	867	68% plag, 9.5% aug, 8.6% pgt, 11.2% Ti-mt, 2.6% ap
FC	KR-257, 1 wt% H_2O	FMQ-1	-	-	826	84.7% plag, 12.5% Ti-mt, 2.8% ap (fayalite also stable at slightly lower T)
AFC	KR-257, 1 wt% H_2O	FMQ+1	KK55, 3 wt% H_2O, 600°C	0.68	865	57.2% plag, 23.8% aug, 12% opx, 4.7% Ti-mt, 1.3% ilm and 0.9% ap
AFC	KR-257, 1 wt% H_2O	FMQ	KK55, 3 wt% H_2O, 600°C	0.78	858	49.5% aug, 47.5% plag and 3% ilm
Two-Step	KK55, 3 wt% H_2O, followed by FC from dacitic partial melt with 65 wt% SiO₂	FMQ+1	-	-	869	81.1% plag, 10.5% opx, 2.6% Ti-mt, 3.5% ilm, 2.3% apatite
Two-Step	KK55, 3 wt% H_2O, followed by FC from dacitic partial melt with 65 wt% SiO₂	FMQ	-	-	846	80.9% plag, 12.1% aug, 3.1% Ti-mt, 2.3% ilm, 1.7% apatite
Two-Step	KK55, 0.1 wt% H_2O, followed by FC from dacitic partial melt with 65 wt% SiO₂	FMQ+1	-	-	924	60% plag, 22.8% aug, 1.3% Ti-mt, 10.5% ilm, 5.3% apatite
Two-Step	KK55, 0.1 wt% H_2O, followed by FC from dacitic partial melt with 65 wt% SiO₂	FMQ	-	-	869	70.6% plag, 18% aug, 7.3% Ti-mt, 3,9% ilm

Note: plag = plagioclase, aug = augite, pgt = pigeonite, opx = orthopyroxene, Ti-mt = titanomagnetite, ilm = ilmenite, ap = apatite

poor for many elements (e.g., Th). Two-step models at more reducing conditions give similar results to pure partial melting.

Except AFC at FMQ-1, which retained a basaltic composition (not shown), the FC and AFC forward models more accurately match the compositions of the natural rhyolites. Rhyolitic compositions produced by pure FC models are low in Al_2O_3 due to extensive plagioclase fractionation, so the AFC models are the better fit for major elements (Fig. 3.15). Reasonably good fits to the observed trace element compositions are produced by all three FC models, as well as the most oxidising AFC model, predicting large negative Sr and Ti anomalies and REE + Y concentrations similar to the natural samples (Fig. 3.16). The strong discrepancy in behaviour of the REE between the melting and crystallization models reflects high crystal-melt partition coefficients for rhyolitic melts. Because partition coefficients are lower for mafic melts, FC along a liquid line of descent from basalt produces greater REE enrichments than small degrees of partial melting, where melt compositions are always silicic and thus partition coefficients are higher throughout the process. Brophy (2009) has previously used this dichotomy in REE behaviour to argue for the importance of fractional crystallisation in generating Icelandic rhyolites. For all

crystallisation models, the predicted temperatures at 75 wt% SiO$_2$ agree fairly well with those from thermometry. Predicted mineral assemblages at 75 wt% SiO$_2$ for the FC models are in reasonable agreement with observed assemblages (Table 3.6; cf. Table 3.2), whereas those for AFC are comparatively low in plagioclase. None of the models predict quartz or alkali feldspar until near the solidus (if at all), supporting our use of the original MELTS algorithm rather than rhyoliteMELTS, which places quartz in the assemblage at high temperatures for these compositions.

3.6.1.3.3. Synthesis

In detail, the process that ultimately produces rhyolites is undoubtedly more complex than any of those considered here, likely involving some combination of FC, assimilation or partial melting, mixing of distinct silicic magma batches and/or remobilisation of felsic intrusions. Unsurprisingly, none of our models capture all of the features of the Krafla rhyolites, but we suggest that their general trends provide strong indications of the dominant process.

Both published experiments and our models imply that producing highly silicic melts by partial melting is difficult, and the models predict compositions far from the Krafla rhyolites. One possibility that we cannot exclude is disequilibrium melting, where melting occurs faster than the minerals can equilibrate by diffusion. In the most extreme case, disequilibrium melting produces trace element concentrations in the melt that are determined simply by their weighted concentration in the melting assemblage (Allègre and Minster, 1978), resulting in a much greater enrichment in incompatible elements than the equilibrium process. Because of the lack of mineral trace element compositions and modal proportions for altered Icelandic basalts, we did not attempt

to model disequilibrium melting. Although trace element compositions of partial melts observed around the upper margins of exhumed mid ocean ridge magma chambers have been suggested to reflect some degree of disequilibrium during melting, melt segregation from these zones appears to be inefficient, and the bulk melt compositions are considerably less silicic than the Krafla rhyolites (Gillis and Coogan, 2002). Thus, although we suggest that the melting behaviour of altered Icelandic basalts warrants further investigation, we conclude that an origin for Krafla rhyolites by a process dominated by partial melting appears unlikely.

The mineral compositions and zoning patterns of the Krafla rhyolites indicate that some degree of FC has occurred in their evolution to high-silica rhyolite. Our inverse FC models trend towards the experimental and modeled partial melt compositions, broadly consistent with the possibility that this FC occurred from silicic melts that were produced by partial melting of altered basalts. Forward models of this two-step process, however, produce relatively poor fits to the observed trace element compositions. Instead, the good fit of our MELTS models for pure FC to the observed trace element compositions points towards a more dominant role for FC, with some assimilation of altered basaltic crust required to lower the $\delta^{18}O$ and buffer certain elements (notably Al_2O_3, which is depleted by extensive plagioclase fractionation). The AFC model for $fO_2 = FMQ + 1$ provides a good fit for most elements, but such oxidising conditions are unrealistic for Krafla basalts; they could, however, be approached later in the AFC process given that the basaltic crust is likely to be oxidised during alteration. We thus suggest that FC from basalt with moderate assimilation of altered and oxidised crust is the dominant process by which Krafla rhyolites are produced, and that fO_2 likely increases throughout the process as relatively oxidised altered crust is assimilated.

The dearth of intermediate compositions (excluding basalt-rhyolite hybrids) at Krafla and similar Icelandic systems has previously been used as evidence against AFC from a basaltic parent (Jónasson, 1994). However, it is now recognised that such compositional gaps do not necessarily reflect a paucity of intermediate magmas at depth. After crystallising sufficiently to reach intermediate bulk compositions, magma bodies commonly reach a state of rheological lockup (Bachmann and Bergantz, 2004); efficient extraction of interstitial silicic melt from the resultant mush may then feed silicic eruptions, but the intermediate mushes themselves are too crystalline to erupt (e.g., Dufek and Bachmann, 2010). We suggest that the absence of intermediate magmas at Krafla reflects such a process, and that the Krafla rhyolites derive from silicic liquids extracted from intermediate or silicic mush bodies formed from AFC. Most crystals derived from more mafic melts are left behind in the mush, forming cumulates at depth, while the extracted silicic melts ascend and then undergo further cooling and FC at shallower levels; the majority of crystals in the Krafla rhyolites record this latest stage of evolution. Ultimately, the rhyolite bodies either freeze to form felsite, or erupt. Wholesale remobilisation and recycling of small subsolidus felsite bodies may occur in the shallow crust (Masotta et al., 2018), but the chemistries of the resultant magmas mainly reflect the earlier AFC process.

3.6.2. Rhyolitic Magmatism at Krafla Through Time

Having considered general aspects of rhyolite petrogenesis, we now examine distinct periods of rhyolitic magmatism at Krafla. We first focus briefly on the oldest and Halarauður rhyolites, the latter of which is discussed further in Chapter 4. Post-Halarauður rhyolites are then discussed in

detail. Finally, we turn to the present state of the system, and examine the similarities (or lack thereof) between erupted rhyolites and the magmas or melts recently sampled during drilling.

3.6.2.1. Pre- and Syn-Caldera Rhyolitic Magmatism: The Oldest and Halarauður Rhyolites

Although Jónasson (1994) implied that the oldest and Halarauður rhyolites were erupted in the same event, subsequent dating (Sæmundsson and Pringle, 2000) and the petrologic data presented herein clearly demonstrate a lack of any temporal or genetic link between the two. Indeed, ratios of highly incompatible elements (e.g., Th/Ta, Th/Nb, Nb/Y; Fig. 3.3e, f), which are immobile during alteration and not significantly fractionated during crystallisation or melting, distinguish the oldest rhyolite from all younger units and imply generation from a chemically distinct source. REE patterns for the oldest rhyolite also differ from all younger units (Fig. 3.3b), implying that the oldest rhyolite was generated from a compositionally distinct source and/or under different P-T conditions than the younger rhyolites . In contrast, parallel REE patterns among the Halarauður rhyolite and younger units (Fig. 3.3b) imply that these younger magmas were generated by similar processes, and similar highly incompatible element ratios imply a common or chemically similar source region for the Halarauður magma and most younger rhyolites (excluding Víti; Fig. 3.3e, f) .

The reason for the distinct trace element systematics of the ca. 190 ka oldest rhyolite are not clear, but may reflect the mobility of the LREE during the slight alteration of this sample (Wood et al., 1976). Alternatively, higher LREE/HREE and a shallower Eu anomaly for the oldest rhyolite relative to later units are consistent with greater fractionation of pyroxene relative to plagioclase, perhaps reflecting differentiation at higher pressure and P_{H_2O} in the relatively young

a)

Oldest rhyolite

First Krafla rhyolite produced as shallow basaltic system becomes established

Immature shallow basaltic system

ca. 190 ka

b)

Large rhyolite body assembled

Large shallow basaltic system established

ca. 190-110 ka

c)

Halarauður ignimbrite

Major caldera collapse in Halarauður eruption

Rhyolite body completely vented

Basaltic chamber depleted

ca. 110 ka

d)

Extra-caldera ridges originate from common magma body

Heat from replenished mafic system drives formation of new rhyolite body

Shallow basaltic system recharged after Halarauður eruption

ca. 65 ka

e)

Hrafntinnuhryggur

Superheating by adjacent basalt?

Small rhyolite batches

Shallow basaltic system waning?

ca. 24 ka

f)

Víti

Basaltic dike intercepts rhyolite body at onset of Mývatn Fires

Small rhyolite batches

Freezing/remelting of small rhyolite/felsite bodies

1724 C.E.

g)

KJ-39   IDDP-1

IDDP-1 intercepts residual or rejuvenated Víti magma

KJ-39 intercepts heterogeneous silicic partial melt zone adjacent to mafic heat source

Present

Figure 3.17 . Schematic diagrams showing key aspects of the evolution of rhyolitic magmatism at Krafla through time. a) Subglacial emplacement of the oldest rhyolite at ca. 190 ka. Deeper melting around the immature shallow basaltic storage zone produces the distinct REE pattern of this unit. b) Large shallow basaltic storage zone is established by ca. 110 ka, and a large rhyolite body forms above it. c) Large rhyolite body is completely evacuated (continues over page)

141

(caption continues) during the ca. 110 ka Halarauður eruption, together with a significant portion of the shallow basaltic system. d) Decompression of the magmatic system associated with the Halarauður event triggers post-caldera basaltic recharge. Major basaltic influx into the shallow system provides heat to generate a second large rhyolite body, which forms over the next ca. 30-40 k.y. above the replenished shallow basaltic system. The rhyolite is emplaced as a cone sheet or circumferential dike at ca. 65 ka, erupting at three points around the outer caldera margins to form the extra-caldera ridges. e) The focus of rhyolitic magmatism in late- and post-glacial time shifts towards production of small rhyolite batches in the central-eastern caldera region, possibly reflecting waning mafic input into the shallow system after the extra-caldera ridge phase. The first (aphyric) batch, possibly superheated by an adjacent basaltic body, erupts beneath shallow ice at ca. 24 ka, emplacing the Hrafntinnuhryggur ridge. f) Generation of small rhyolite bodies continues over the next ca. 24 k.y., most of which freeze at shallow depths to form felsite intrusions. Remelting and recycling of felsite intrusions is favoured by their small volume. A small volume of eruptible rhyolite forms prior to 1724 C.E., erupting at the onset of the Mývatn Fires when intercepted by ascending basalt. g) The KJ-39 well intercepts a heterogeneous zone of silicic partial melt veins or pods near the margins of a mafic body at ~2.6 km depth in 2008. The following year, the IDDP-1 well intercepts magma residual from the Víti eruption, or derived from remelting of the same source, at 2.1 km depth.

Krafla system at 190 ka, prior to establishment of the mature shallow basaltic storage zone beneath the present-day caldera (Einarsson, 1978; Kennedy et al., 2018). Future detailed studies of Krafla basalt chemistries through time will likely prove useful in testing this hypothesis and tracing the establishment and evolution of the shallow mafic system.

3.6.2.2. The Extra-Caldera Ridges: A Discrete Phase of Post-Caldera Rhyolitic Magmatism

Noting similarities in their chemistry, apparent age (last glacial) and distribution around the caldera margin, Jónasson (1994) concluded that the extra-caldera ridges reflected a discrete phase of silicic volcanism at Krafla, likely associated with intrusion of a ring dike. Our significantly larger compositional dataset confirms a strong petrogenetic relationship between the three ridges, and offers further insights to their magmatic history.

A striking feature of our larger dataset is the almost total overlap of Jörundur and Gæsafjallarani whole-rock and mineral compositions (Figs. 3.2, 3.3, 3.4, 3.6 and 3.8). Core and

rim compositional histograms for both plagioclase and augite show essentially identical populations (Figs. 3.4, 3.6). Both ridges are also petrographically indistinguishable, and are the only Krafla units that contain fayalite (Table 3.2). These similarities are consistent with statistically indistinguishable zircon U-Th ages and mineral $\delta^{18}O$ compositions for the two ridges (Hampton et al., in prep). We conclude that these chemical and petrographic similarities reflect venting of the same magma batch, likely coevally or near-coevally, on opposite sides of the caldera. These ridges line up along a WNW-ESE trending low gravity anomaly identified by Árnason et al. (2009) and Árnason (2020), inferred to reflect a graben structure that cuts across the caldera. The Jörundur/Gæsafjallarani magma may have exploited this structure during ascent.

Slightly more evolved whole-rock compositions, an absence of fayalite, and subtle differences in mineral compositions and zoning patterns distinguish Hlídarfjall from the other two ridges. The compositional differences, however, are minor, implying a close petrogenetic relationship among all three ridges. The distribution of plagioclase core An compositions for Hlídarfjall and the other ridges are essentially identical, and most trace elements show near total overlap for both cores and interiors from all three ridges; the only exception is Mg, which is lower in Hlídarfjall plagioclase (Fig. 3.4h), likely reflecting rapid equilibration of fast-diffusing Mg with the more evolved Hlídarfjall melt (e.g., Coote and Shane, 2016; Andersen et al., 2018). We interpret these features to reflect a predominantly shared magmatic history for the plagioclase populations of all three ridges, after which the Hlídarfjall magma was separated from the Jörundur/Gæsafjallarani magma and continued to differentiate. This interpretation is consistent with recent findings of Hampton et al. (in prep), who observe a slightly younger average zircon U-Th age (Table 3.1) and subtle differences in mineral $\delta^{18}O$ compositions for Hlídarfjall. Two mechanisms for separation of the Hlídarfjall magma are possible: 1) the Hlídarfjall magma

segregated from the common magma body and became physically disconnected, evolving in isolation from the common ridge magma body in its final stage of differentiation, or 2) Jörundur and Gæsafjallarani were erupted first from the same magma body, which then continued to differentiate and was later tapped again to form Hlídarfjall.

Plagioclase rim compositions for Hlídarfjall are similar to the other ridges, but the distribution is shifted to slightly higher An contents, possibly reflecting lower pressure and/or higher melt H_2O content during rim growth. Similarities among the plagioclase populations of Hlídarfjall and the other ridges, however, are not shared by augite or titanomagnetite. Hlídarfjall augite cores and rims both cluster at more Fe-rich compositions than the other ridges (Fig. 3.6). This difference is also reflected in Hlídarfjall zoning patterns, which show a much greater abundance of unzoned and smooth normally zoned crystals relative to the other ridges (Fig. 3.7). We attribute these differences to an episode of augite crystallisation in the Hlídarfjall magma after it separated from the common ridge magma body. Higher Fe contents are consistent with crystallisation from a more evolved (and likely cooler) melt (Carmichael, 1967; Warshaw and Smith, 1986). The comparatively Ti-rich compositions (higher Usp) of most Hlídarfjall titanomagnetites are also consistent with lower temperatures (e.g., Mollo et al., 2013). Lower Sc and Co in most Hlídarfjall augites and a trend of decreasing concentration with decreasing Mg#, as well as lower Mg and Co in Hlídarfjall titanomagnetites, indicate extreme depletion of these compatible elements in the highly fractionated melt.

Overall, we suggest that differences between Hlídarfjall and the other ridge rhyolites reflect further cooling and differentiation of the Hlídarfjall magma by fractional crystallisation of plagioclase + augite + titanomagnetite (+ accessory zircon and apatite) after separation from the Jörundur/Gæsafjallarani magma. A least squares solution to mass balance calculations using

144

representative measured mineral compositions implies that only 2.7% fractionation of an assemblage comprising 49% plagioclase, 25% augite and 26% titanomagnetite is required to differentiate from KR-128, a typical Jörundur composition, to KR-116, near the middle of the compositional range for Hlídarfjall ($\sum[r^2]$ = 0.02; Table 3.7). Expected whole-rock trace element compositions (calculated with the fractional crystallisation equation and our apparent partition coefficients for Jörundur; see electronic appendix), are essentially unchanged by such a small degree of FC, consistent with the indistinguishable trace element compositions of all three ridges (excluding lower Zr for Hlídarfjall, which is readily explained by fractionating accessory zircon).

The total ~0.5 km^3 volume of the three extra-caldera ridges is large compared with subsequent rhyolite bodies produced at Krafla. Our chemical evidence for a genetic relationship among all three ridges, as well statistically equivalent zircon U-Th ages and similar O isotopic compositions (Hampton et al., in prep), support Jónasson's (1994) suggestion that the ridges reflect a distinct "pulse" of rhyolitic magmatism at Krafla. Despite the larger magma volumes produced during this phase, however, virtually parallel REE patterns between the extra-caldera ridges and younger small-volume rhyolites (Hrafntinnuhryggur, Víti and IDDP-1; Fig. 3.3b) imply that the overall petrogenetic processes that produced them were similar. We suggest that the extra-caldera ridge "phase" reflects a high flux of deep-derived basaltic magma into the Krafla system after major caldera collapse during the Halarauður event, which recharged the shallow basaltic storage zone and provided sufficient heat to drive production of a new large rhyolite body (Fig. 3.17b c). Rapid recharge after large caldera-forming events is common, and often attributed to the major crustal decompression associated with removal of large magma volumes during the caldera-forming event (e.g., Kennedy et al., 2012; Barker et al., 2014, 2015; Mucek et al., 2017). In Iceland, it is also well-established that decompression associated with glacial unloading drives

TABLE 3.7. LEAST SQUARES FRACTIONAL CRYSTALLISATION MODEL FOR HLÍÐARFJALL

	Starting Composition	Final Composition	Phases Fractionated				Results		
	KR-128 (Jörundur)	KR-116 (Hlíðarfjall)	Augite (Mg# 16)	Plagioclase (An$_{40}$)	Titanomagnetite (Usp$_{64}$)	Bulk Composition Fractionated	Observed Difference Between Magmas	Calculated Difference Between Magmas	Residuals (r)
SiO$_2$	74.84	75.79	47.96	58.82	-	40.73	0.94	0.93	0.01
TiO$_2$	0.31	0.24	0.40	-	22.30	5.93	-0.07	-0.15	0.08
Al$_2$O$_3$	12.15	12.13	0.85	26.01	1.34	13.25	-0.02	-0.03	0.01
FeO*	3.82	3.18	28.04	0.52	75.40	26.99	-0.64	-0.63	-0.01
MnO	0.09	0.07	0.89	-	0.77	0.42	-0.02	-0.01	-0.01
MgO	0.16	0.06	2.93	-	0.19	0.79	-0.09	-0.02	-0.07
CaO	1.80	1.66	18.74	8.18	-	8.70	-0.15	-0.19	0.04
Na$_2$O	4.18	4.14	0.18	6.18	-	3.06	-0.04	0.03	-0.07
K$_2$O	2.64	2.74	-	0.29	-	0.14	0.09	0.07	0.02
Total	100	100	100	100	100				
wt% of Fractionated Assemblage			25.1	48.8	26.1			$\Sigma(r^2)$	0.02
								wt% Fractionated Solids	2.66

Note: Calculated with PetroGraph (Petrelli et al., 2005) using the least squares algorithm of Stormer and Nicholls (1978).

enhanced melting of the shallow mantle beneath the rift zones, increasing crustal magma fluxes and surface volcanism in the early postglacial period (Jull and McKenzie, 1996; Slater et al., 1998; Maclennan et al., 2002). Decompression associated with removal of a large magma volume during the Halarauður event may have had a similar (albeit more localized) effect on the mantle beneath Krafla, resulting in a short period of greater melt input into the Krafla system that drove enhanced rhyolite production. If this hypothesis is correct, the time gap of ~30-40 k.y. between the Halarauður event and extrusion of the extra-caldera ridges, which is long compared with the ~1-3 k.y. lag between deglaciation and enhanced early Holocene volcanism in the NVZ (Slater et al., 1998; Maclennan et al., 2002), reflects the gestation time required to produce this comparatively large rhyolite body by AFC or partial melting and subsequent crystal fractionation. We infer that the ring-like distribution of the ridges around the caldera margins is a consequence of the local stress field after caldera collapse, which favoured formation of a cone sheet or circumferential dike that erupted outside the caldera margins (Gaete et al., 2019).

3.6.2.3. Late- and Post-Glacial Rhyolitic Magmatism

Since emplacement of the extra-caldera ridges, rhyolitic eruptions at Krafla have been small (volumes <0.02 km^3; Table 3.1) and have occurred exclusively inside the caldera, focused in the area around Krafla mountain. This region overlies one of two S-wave shadow zones seismically imaged beneath the caldera, each inferred to represent a shallow lobe of magma at ~3 km depth, underlain by a large unified basaltic chamber or active intrusive complex extending to ~7 km depth (Einarsson, 1978; Kennedy et al., 2018). The spatial clustering of late- and post-glacial eruptions above this zone implies that this shallow basaltic lobe has underlain the central-eastern region of the caldera since at least late glacial times, and provided the heat needed to produce small batches

of rhyolite in the overlying crust (Fig. 3.17e, f). If the volumes of rhyolitic eruptions at Krafla are proportional to the volumes of rhyolite produced at depth, the comparatively small rhyolite volumes erupted over this time may reflect waning of basaltic input into the shallow magmatic system and consequent reduction in rhyolite production after the extra-caldera ridge phase. A short-lived (<2 k.y.) phase of enhanced basaltic magmatism in the early postglacial period triggered by glacial unloading (Maclennan et al., 2002), however, does not appear to have triggered a corresponding phase of enhanced silicic volcanism. Rates of rhyolite generation and eruption may thus be decoupled to some degree from basaltic magma flux, and/or from one another, and links between rates of rhyolite genesis, eruption, and the state of the basaltic system warrant further investigation.

Highly incompatible element ratios (e.g., Ta/Th, Th/Nb, Nb/Y; Fig. 3.3e, f) for the two eruptions from this period studied by us (Hrafntinnuhryggur and Víti) are distinct from one another, and usually also from the older and more voluminous rhyolites, implying compositionally different source regions for these magmas. We suggest that these differences are primarily a function of volume. Although the size of recent eruptions are not necessarily proportional to the size of their source magma bodies, we infer that the volumes of the recent rhyolite bodies are likely to be somewhat smaller than the relatively large rhyolite bodies tapped in the Halarauður and extra-caldera ridge eruptions. If this assumption is correct, the distinct incompatible element ratios of the recent rhyolites (Hrafntinnuhryggur and Víti) could be explained by local spatial heterogeneities in the compositions of basaltic inputs and/or crustal assimilants. In contrast, generation of larger batches (the Halarauður and extra-caldera ridge rhyolites) likely involved mixing of melts produced over a wider source region, which thus averaged out any local heterogeneities to produce similar incompatible element ratios in the final assembled magmas.

Despite these differences, chondrite-normalised REE patterns for the young, small-volume units are parallel to the more voluminous older Halarauður and extra-caldera ridge rhyolites (Fig. 3.3b), and $\delta^{18}O$ values of their minerals and groundmasses are comparable and low (Hampton et al., in prep.). We thus infer that the overall processes that produce Krafla rhyolites have been similar at least since generation of the Halarauður rhyolite, but operated over varying spatial scales.

Two of the three eruptions involving rhyolite from the late/post-glacial period show direct evidence for basalt-rhyolite interaction: the ca. 9000 B.P. Hveragil tephra (not studied by us; see Sæmundsson, 1991) and the 1724 C.E. Víti pumice. Hence, although differentiation of Krafla rhyolites largely occurs in isolation from the underlying mafic system (see above), interaction with ascending mafic magmas shortly before eruption has been common in recent times. The role of basaltic recharge in mobilising the Víti rhyolite is discussed further below. Although the Hrafntinnuhryggur rhyolite does not show direct evidence for interaction with basalt, we suggest that absence of macrocrysts in this unit likely reflects close proximity to a mafic heat source that heated the rhyolite and caused dissolution of any resident crystals.

An interesting feature of our mineral trace element data for Víti is the poor correlation between plagioclase Sr and An content (Fig. 3.4i). Because Sr partitioning in plagioclase is strongly influenced by anorthite content (Blundy and Wood, 1991), plagioclase grown from a single closed magma batch should show correlation between Sr and An, as observed for the extra-caldera ridge plagioclases (Fig. 3.4i). The highly scattered relationship between Sr and An for Víti implies that differences in melt composition, not the composition of plagioclase itself, were the main control on Sr partitioning. In other words, plagioclase with similar An contents crystallised from melts with different Sr contents. Mixing of crystals from several distinct sources is also consistent with considerable scatter for other trace elements in plagioclase (e.g., Mg; Fig. 3.4h)

and titanomagnetite (Fig. 3.8b, c). We suggest two possible explanations: 1) the Víti magma was assembled from several physically and compositionally discrete rhyolite bodies that were mixed together shortly before eruption, similar to the mechanism proposed elsewhere to explain the chemically and isotopically diverse zircon cargoes of some Icelandic rhyolites (Carley et al., 2014), or 2) a large component of the Víti crystal population was assimilated from compositionally diverse felsic wallrock. Masotta et al. (2018) recently proposed that crystals in the IDDP-1 rhyolite were ingested from a previously solidified felsite intrusion almost identical in composition to the rhyolite. Given the close chemical and geographic similarities between the Víti and IDDP-1 rhyolites (discussed further below), a similar scenario involving ingestion of crystals from several felsite bodies of subtly distinct composition could explain the diverse origins of the Víti crystal cargo. The presence of abundant small felsic intrusive bodies in the shallow crust of the central caldera region (Weisenberger et al., 2015), support this conceptual model, as does the abundance of internal resorption surfaces in Víti crystals relative to older units. We thus concur with Masotta et al. (2018) that rejuvenation of previously solidified felsite intrusions has been important in assembling recent melt-dominant rhyolite magma bodies at Krafla. We suggest that the recent importance of this process reflects a shift towards generation of smaller rhyolite batches, which can rapidly freeze after emplacement in the cooler upper crust but are easily remobilised by mafic intrusions or fresh batches of hot silicic magma ascending from depth (Simakin and Bindeman, 2012).

3.6.2.4. *Present State of the Silicic System: The KJ-39 and IDDP-1 Rhyolites*

The rhyolite magmas or melts recently sampled during drilling occur in the same region of the caldera as the most recent rhyolitic eruptions. However, as noted by Mortensen et al. (2010), the

KJ-39 rhyolite does not resemble any rhyolites erupted at Krafla or elsewhere in Iceland. Heterogeneous compositions, with >10 wt% variation in SiO_2, are in strong contrast with the homogeneous melt sampled in the IDDP-1 well (excluding local heterogeneities within ingested, partially remelted felsite fragments; Elders et al., 2011; Zierenberg et al., 2013; Masotta et al., 2018). We suggest that the marked compositional heterogeneities in the KJ-39 glasses likely reflect intersection of small (centimetre- to decimetre-scale) melt pockets or veins in a heterogeneous melting zone around a shallow intrusion, similar to melting zones above the roofs of exhumed mid-ocean ridge magma chambers (e.g., Gillis and Coogan, 2002). The presence of only ~30% glass among the cuttings from the bottom of the well, the rest of which comprised holocrystalline basalt (Mortensen et al., 2010), is consistent with this scenario, implying that both partial melt and wallrock were sampled. Mortensen et al. (2010) reached a similar conclusion by noting compositional similarities between the KJ-39 glasses and small patches of anatectic melt in contact-metamorphosed (hornfels facies) metapelites, and also partial melts produced experimentally from biotite schist at 10 kbar. We suggest that low pressure partial melts of hydrated or hydrothermally altered basaltic rocks, which are more representative of the shallow crust beneath Krafla, are a more appropriate comparison. Low degree partial melts produced experimentally from such protoliths at 1 kbar (Spulber and Rutherford 1983, Beard and Lofgren 1991, France et al. 2010; Erdman et al., 2015; Fig. 3.15) are broadly similar to the KJ-39 melts, but low sodium contents comparable with the <2 wt% Na_2O observed in the KJ-39 melts (cf. Fig. 3.9b) have not been produced in any such experiments. The Na_2O and K_2O contents of the experimental melts primarily reflect their concentrations in the source (Thy et al., 1990; Beard and Lofgren, 1991). Hence, we suggest that the low Na_2O contents of the KJ-39 melts may reflect a protolith that has suffered intense leaching of highly mobile Na_2O during shallow hydrothermal

alteration, as described elsewhere at Krafla (cf. Kristmannsdottir, 1979). The limited compositional overlap between the KJ-39 glass and other Krafla rhyolites (and others in Iceland) implies that this process of local partial melting of the KJ-39 source is not representative of the complete process that produces eruptible rhyolite magmas at Krafla or elsewhere in Iceland. Instead, we suggest that the KJ-39 melts may be an example of the incipient stage of this process. The possibility that the two-stage petrogenetic process proposed above may ultimately form a small melt-dominant rhyolite magma body, similar in composition to the previously erupted rhyolites, by extraction of the KJ-39 melts from their source region, pooling, homogenisation and fractional crystallisation at higher crustal levels, warrants further investigation.

On the other hand, comparison of our new petrologic data with published glass and mineral analyses reveals a close compositional affinity between the IDDP-1 magma body and the 1724 C.E. Víti rhyolite. Published plagioclase and augite compositions from IDDP-1 (Zierenberg et al., 2013; Masotta et al., 2018) span a narrower range than the other Krafla rhyolites, likely reflecting the smaller number of analyses compared with our larger datasets. However, compositional modes for Víti plagioclase and augite cores and rims overlap with IDDP-1 compositions (Figs 4a-b, 6d-e), while pigeonite compositions fall within or very near to the range for IDDP-1 (Fig. 6a-c). Glass compositions for IDDP-1 and Víti also largely overlap with respect to both major and trace elements (Figs 9, 10), and whole-rock ratios of highly incompatible elements overlap within error and are distinct from other units (e.g., Ta/Th ~9.5, compared with >12.5 for all other Krafla rhyolites; IDDP-1 data from Masotta et al., 2018). Together, these similarities, as well as the proximity of Víti crater and the IDDP-1 well (Fig. 1), imply a common source region and similar magmatic histories for both rhyolites. Although titanomagnetite compositions for the two magmas are distinct, the very short timescales over which this phase re-equilibrates in response to changes

in temperature or fO_2 (at most several months for grains <100 µm; Venezky and Rutherford, 1999) do not preclude a common origin. Given the compositional similarities outlined above, we suggest that the Víti rhyolite magma either 1) erupted from the same magma body that was sampled by IDDP-1, which has remained in a largely molten state in the shallow crust since then, or 2) reflects earlier remelting and mobilisation of the same felsite intrusion, which has since been remelted again to form the IDDP-1 body (cf. Masotta et al., 2018). The former scenario bears similarities to recent processes at Eyjafjallajökull, where a shallow body of rhyolitic magma residual from its 1821 eruption interacted with intruding basalt in 2010 (Sigmarsson et al., 2011).

3.6.3. Triggering of Rhyolitic Eruptions at Krafla

Mafic recharge of silicic magma bodies is commonly evoked as a trigger of explosive silicic eruptions, either by generating overpressure in an existing melt-dominant magma body through the addition of mass and volatiles (e.g., Sparks et al., 1977; Leonard et al., 2002), or by thermally rejuvenating and mobilising near- or sub-solidus silicic intrusions (e.g., Cooper and Kent, 2014). Interactions between mafic and silicic magmas are especially common in the compositionally bimodal central volcanoes of Iceland, where upper crustal silicic magma bodies often lie in the path of propagating mafic dikes (e.g., Blake, 1984; McGarvie, 1984; McGarvie et al., 1990; Sigmarsson et al., 2011; Laeger et al., 2017). Mafic triggering has been proposed for several explosive silicic eruptions in Iceland, including the historic 1875 C.E. Plinian eruption of Askja (Sparks et al., 1977; Sigurdsson and Sparks, 1981) and large Holocene eruptions of Hekla (Sverisdottir, 2007). An important question arises: does mafic recharge play a role in triggering rhyolitic eruptions at Krafla?

Two rhyolitic eruptions at Krafla studied by us show textural evidence for basalt-rhyolite interactions: the ca. 110 ka Halarauður ignimbrite and the 1724 C.E. Víti pumice. Evidence for rapid mafic triggering of the Halarauður eruption will be presented in Chapter 4. In the Víti pumice, black and white streaky mingling textures and rinds or inclusions of quenched basalt are common. Basalt-rhyolite interactions are not, however, recorded by the crystals within Víti pumice clasts. Plagioclase crystals are exclusively euhedral, predominantly unzoned or normally zoned, and show no signs of the reaction or re-equilibration with hotter and/or with more mafic melt that would be expected from prolonged interactions with hot mafic recharge magma, such as partial dissolution or Ca- or Fe-rich overgrowths (Fig. 3.4). Similarly, up-temperature signals such as outer rim resorption or magnesian rim compositions are absent for Víti pyroxenes. We thus infer that the timescales of interaction between the Víti rhyolite body and intruding basalt were too short for crystals in the rhyolite to record. Crystals in other Icelandic rhyolites that interacted with basalt over short timescales (several months or less) are commonly resorbed due to superheating of their host melt by the hotter intruding basalt (e.g., the 1875 C.E. Askja rhyolite; Sparks et al., 1977; Sigurdsson and Sparks, 1981). Elsewhere, intimate interactions between rhyolitic and more mafic magmas that are not recorded by crystal resorption or reaction have been regarded as syn-eruptive (e.g., Singer et al., 2016).

The absence of reverse zoning or resorption textures at the rims of Víti crystals rule out thermal remobilisation of the Víti rhyolite from a highly crystalline state, instead implying that it was a dominantly liquid magma body when it encountered the basalt. We thus suggest that the very rapid (essentially syn-eruptive) timescale of basalt-rhyolite interaction and the minor volume of rhyolite erupted from Víti reflect interception of a near-liquidus rhyolite body by an ascending basaltic dike associated with the Mývatn Fires rifting event, which then provided a pathway for

the rhyolite to rapidly ascend and erupt with the basalt (Fig. 3.17f). Interaction between the two magmas likely occurred mainly in the dike during ascent (Koyaguchi, 1985; Snyder et al., 1997).

The very short timescales of basalt-rhyolite interactions prior to the Víti eruption would offer little warning of an imminent explosive event, particularly if the intruding basalt ascended rapidly from depth. Recent evidence from the NVZ for ascent of primitive magma from the Moho to surface (~24 km) in as little as ten days (~0.02 ms^{-1}; Mutch et al., 2019) thus has implications not only for the short warning times that might be expected for effusive mafic eruptions at Krafla, but also for possible rapid triggering of explosive silicic ones. At similar ascent rates, and assuming basalt-rhyolite mixing occurs mainly during ascent, a mafic dike ascending from the shallow storage region beneath Krafla (~3-4 km depth) could trigger the explosive eruption of a silicic magma body in the overlying crust in ~1-2 days. At the faster rates of 0.1-0.3 m s^{-1} determined for ascent in the upper crust during the recent Bárðarbunga-Holuhraun event (Hartley et al., 2018), this timescale reduces to as little as ~3 hours. These very short warning times are of even greater concern given the difficulties in detecting small to moderate-sized silicic magma bodies with geophysical methods, as recently demonstrated by the unexpected discovery of the IDDP-1 rhyolite body. Other similar silicic magma bodies may exist undetected in the shallow crust beneath Krafla and similar Icelandic systems, and could pose a similar eruption hazard if intercepted by ascending basalt.

Textural evidence for mafic-silicic interactions, such as mafic enclaves or filaments, were not observed in any outcrops of the oldest rhyolite, extra-caldera ridges or Hrafntinnuhryggur. This absence implies a different triggering mechanism for these eruptions. Several scenarios are possible, including 1) internal triggering due to late-stage volatile saturation (e.g., Stock et al., 2016), 2) volatile fluxing from the underlying mafic system (e.g., Andersen et al., 2018), or 3)

155

destabilization of the magma body by seismicity or faulting (e.g., Manga and Brodsky, 2006), such as during a rifting episode. Although we cannot discern between these possibilities with our petrologic data, all such mechanisms would also offer little warning of an imminent eruption.

3.7. CONCLUSIONS

The petrologic dataset presented and discussed here offers new and important insights on rhyolitic magmatism at Krafla. We conclude the following:

1. Fractional crystallisation, accompanied by assimilation of hydrothermally altered basaltic crust (i.e., AFC), plays a central role in the petrogenesis of Krafla rhyolites. A significant proportion of mineral grains derive from less evolved intermediate or silicic magmas, which differentiated to high-silica rhyolite by crystal fractionation. Generation of high-silica rhyolites in a single step by very small degrees (<10%) of near-solidus partial melting is difficult and inconsistent with evidence for FC in crystal zoning patterns. Instead, the major and trace element compositions of Krafla rhyolites are consistent with a petrogenesis dominated by AFC processes.

2. Parallel REE patterns among the ca. 110 ka Halarauður rhyolite and all younger units imply that the overall processes that produce Krafla rhyolites have been similar during much of the system's lifespan. Distinct highly incompatible element ratios for Hrafntinnuhryggur and Víti relative to each other and the older units reflect local spatial heterogeneities in the compositions of basaltic melts and/or assimilated crust from which these small magma batches were produced, whereas similar ratios for the larger volume Halarauður and extra-caldera ridge rhyolites reflect fractional crystallisation and assimilation over larger regions,

with smoothed out local heterogeneities in parental melt and assimilant compositions. The ca. 190 ka oldest rhyolite is distinct from all younger rhyolites with respect to both REE patterns and incompatible element ratios, implying a distinct source and possibly reflecting deeper fractionation prior to development of a large and long-lived shallow mafic system.

3. Cryptic evidence for mafic recharge of the silicic system is lacking in the zoning patterns of most crystals. Storage and fractionation of silicic magma bodies at Krafla occurs largely in isolation from the underlying mafic system.

4. The extra-caldera ridge rhyolites share a common parentage. Gæsafjallarani and Jörundur are compositionally and petrographically identical and were tapped from the same magma batch, which vented on opposite sides of the caldera. Hlídarfjall also derives from this common magma body, but underwent a small amount (~3%) of additional fractional crystallisation to reach a slightly more evolved composition. The ridges reflect a distinct phase of post-caldera rhyolitic volcanism that likely resulted from major mafic recharge of the shallow magma system after caldera collapse in the Halarauður event. Above-average rates of rhyolite generation may thus occur immediately after, as well as before, large caldera collapse events in similar systems.

5. Focusing of late- and post-glacial rhyolite eruptions within the central-eastern region of the caldera implies that the shallow basaltic magma body imaged beneath this region is a long-lived feature. Rhyolitic eruptions over this period have been small in volume (≤ 0.02 km^3), possibly reflecting waning of basaltic magma flux into the shallow system and a resultant decrease in rates of rhyolite genesis after the intra-caldera ridge phase. Remelting

and recycling of small near- or sub-solidus felsite intrusions have been important in assembling recently erupted rhyolites.

6. Products of both postglacial rhyolitic eruptions show direct evidence for mixing of basalt and rhyolite (Hveragil tephra and Víti pumice), while the late-glacial Hrafntinnuhryggur rhyolite lacks such evidence but may have been superheated by proximity to basalt. Although Krafla rhyolites mainly evolve in isolation from the underlying mafic system, they are commonly mobilised for eruption by ascending basalt.

7. Basalt-rhyolite interactions prior to the explosive formation of Víti crater (1724 C.E.) were essentially syn-eruptive and too rapid for crystals in the rhyolite to record. Interception of melt-dominant rhyolite bodies in the shallow crust by ascending mafic dikes can have explosive consequences. Rapid triggering timescales and difficulties in detecting rhyolite melt bodies with geophysical methods make such events difficult to forecast.

8. The active IDDP-1 magma body represents either 1) the same magma body tapped in the Víti eruption, which has remained molten since then, or 2) remelting of the same felsite intrusion that was previously melted in a separate event to produce the Víti magma (cf. Masotta et al., 2018). Mobilisation of the IDDP-1 rhyolite in an explosive basalt-triggered event should be considered a possible hazard scenario if unrest in the underlying mafic system is detected.

4. Unravelling Pre- and Syn-Eruptive Processes in a Large Mixed Basalt-Rhyolite Eruption: A Petrologic Study of the Halarauður Ignimbrite

Chapter 3 demonstrated the wealth of insights that petrologic studies, including detailed microanalysis of minerals and glasses, can offer for understanding the processes and dynamics of rhyolitic magmatism at Krafla. We now apply a similar approach to products of the mixed basalt-rhyolite Halarauður eruption, discussed at length in Chapter 2, to constrain the nature and timing of the subvolcanic processes that occurred in the build-up to, and during, this large event. Work presented here was performed in collaboration with Simon Barker and Bruce Charlier (Victoria University of Wellington, New Zealand), who performed the XRF and ICP-MS analyses, respectively, and Daniele Morgavi, Diego Perugini, Maurizio Petrelli and Francesco Vetere (University of Perugia, Italy), who offered insights on chaotic mixing processes and helped with interpretations. Shane Rooyakkers planned the study, performed all fieldwork and sampling, prepared samples for whole-rock analyses, performed EPMA analyses, and wrote the chapter in consultation with, and with editorial input from, John Stix and Kim Berlo (McGill University).

4.1. ABSTRACT

Products of the ca. 110 ka Halarauður ignimbrite eruption (7 ± 6 km^3 magma) linked with major collapse of the Krafla caldera in northeast Iceland show abundant evidence for interactions between basaltic and rhyolitic magmas. We present a detailed petrologic study of these products, including whole-rock major and trace element analyses, and *in situ* major and minor element analyses of crystals, matrix glasses and melt inclusions. Sampling within the stratigraphic

framework of Rooyakkers et al. (2020) allows these data to be placed into time-stratigraphic context. Whole-rock compositions of juvenile products span a continuous range between quartz tholeiite basalt (50.0 wt% SiO_2, 5.0 wt% MgO; Mg# 38) and high-silica rhyolite (74.6 wt% SiO_2). Strongly linear correlations between all major elements are consistent with two-component mixing of sub-equal volumes of these endmember magmas, while correlations between trace elements are more variable and show evidence for diffusive fractionation during chaotic mixing. Evolved compositions (andesite to rhyolite) and marked compositional heterogeneity are typical of early-erupted units, reflecting tapping of the upper, more silicic regions of a compositionally heterogeneous reservoir undergoing chaotic mixing. Compositions of later-erupted deposits are more homogeneous and grade smoothly upward from andesite to basalt, reflecting tapping of denser hybrid magma and underplating basalt from lower levels of the chamber. All erupted products are extremely crystal-poor (<1-2 modal% macrocrysts), implying storage at near-liquidus temperatures prior to mixing. Geobarometry and MELTS modeling suggest shallow storage pressures <1-1.5 kbar (~4-6 km depth) for the endmember basalt, which thus existed in close proximity to the overlying rhyolite body. Large (~1 mm) plagioclase (An_{60-76}) and augite (Mg# 68-75) macrocrysts reflect storage and crystallisation of this basalt for least several decades to centuries prior to interaction with the rhyolite. Sparse glomerocrysts (plagioclase ± augite ± olivine ± orthopyroxene) in late-erupted basaltic material reflect disaggregation of cumulate mush that developed at the base of the chamber. Narrow (<50 μm), sodic rims on 15% of plagioclase crystals from this basalt record short periods of re-equilibration with hybrid magma during mixing, constrained by experimentally-measured plagioclase growth rates as at most two months, and possibly as short as several tens of hours. A second population of calcic plagioclase (cores An_{81-91}) associated with more primitive basaltic glass selvages of Mg# 49-55 occurs sparsely in the

160

volumetrically minor deposits of the first eruptive phase and very rarely in later-erupted units, providing evidence for interaction with a second, more primitive batch of basalt that was of insufficient volume to skew the whole-rock mixing trends. Narrow (<100 μm) sodic rims on these crystals imply interaction with the rhyolite over at most ~15 hours, but glassy basaltic selvages around most crystals imply residence times of at most one hour in the rhyolite before eruptive quenching. The short mixing timescales and evidence for ascent of multiple basaltic magmas from depth reflect a major and rapid destabilisation of the magmatic system immediately prior to the Halarauður event, likely triggered by a crustal rifting episode. Large bodies of crystal-poor magma may be stored for protracted periods in Iceland's rift zones, but can be mobilised over timescales as short as months to hours prior to eruption.

4.2. INTRODUCTION

Effective volcano monitoring and eruption forecasting require a detailed understanding of the architecture of magmatic systems, and the nature and timescales of the processes that occur in them as they move from quiescence towards eruption (e.g., Blundy and Cashman, 2008). Modern instrumentation and observations, coupled with petrologic studies of erupted products, have provided a reasonably clear outline of the present-day configuration of many magmatic systems and the processes of magma ascent, mixing and degassing leading up to small-volume eruptions (e.g., Murphy et al., 2000; Chouet, 2003; Lees, 2007; De Moor et al., 2016; Roman and Cashman, 2018; Stix, 2018, and many others), as well as some moderate-sized events such as the climactic eruptions of Mount Saint Helens in 1980 (Lipman and Mullineaux, 1981) and Pinatubo in 1991 (Newhall and Punongbayan, 1996). Much less is understood about the build-up to large or very large eruptions involving ignimbrite formation and caldera collapse (magma volumes ≥ several

km^3, in some cases up to hundreds or thousands of km^3), even the smallest of which have not been observed with modern instrumentation (e.g., Novarupta-Katmai in 1912; Hildreth and Fierstein, 2012), and the largest of which have not occurred historically (Mason et al., 2004; Self, 2006). Scientific understanding of the processes that occur in the build-up to these events relies heavily on geochemical and petrologic studies of their erupted products, which can provide valuable insights on the generation, assembly and mobilisation of large magma batches to inform future monitoring efforts (e.g., Druitt et al., 2012; Chamberlain et al., 2014; Barker et al., 2016; Allan et al., 2013, 2017; Singer et al., 2016; Budd et al., 2017; Cooper et al., 2017; Reid and Vasquez, 2017; Forni et al., 2016; Matsumoto et al., 2018).

Iceland is one of the most active and productive volcanic regions on Earth (Thordarson and Höskuldsson, 2008). Like many other volcanic regions, the present-day configuration of its magmatic systems and the processes occurring in them before and during recent small to moderate eruptions, including explosive events at Eyjafjallajökull in 2010 and Grímsvötn in 2011, and the effusion of ~1 km^3 of basaltic lava in the 2014-2015 Bárðarbunga-Holuhraun event, have been well documented by modern geophysical, geodetic, geochemical and petrologic methods (e.g., Sigmundsson et al., 2010, 2015; Sigmarsson et al., 2011; Keiding and Sigmarsson, 2012; Hjaltadóttir et al., 2015; Gudmundsson et al., 2016; Viccaro et al., 2016; Einarsson, 2018; Halldórsson et al., 2018; Pankhurst et al., 2018; Woods et al., 2019, and many others). Larger effusive outpourings of basaltic lava involving magma volumes >5 km^3 occur approximately every 500 years in Iceland (Gudmundsson et al., 2008). Although these events have not been observed with modern instrumentation, detailed studies of their erupted products have provided insights into the architecture and dynamics of their source magmatic systems (e.g., Bindeman et al., 2008; Halldorsson et al., 2008; Passmore et al., 2012; Neave et al., 2013, 2017; Hartley et al., 2016).

Explosive silicic ignimbrite-forming events of a similar magnitude, however, are rare in Iceland over human timescales. Only three such events are known from the Quaternary record (Jørgensen, 1980, 1981; Einarsson, 1982; Lacasse et al., 1995; Gudmundsson et al., 2008; Moles et al., 2019; Rooyakkers et al., 2020; Chapter 2), and the magmatic processes that give rise to them have scarcely been studied (Tomlinson et al., 2012). Nonetheless, silicic ignimbrites are common in Iceland's Tertiary volcanic pile (Dearnley, 1954; Tryggvason and White, 1955; Walker, 1962, 1966; Blake, 1969; Schmincke et al., 1982), and the scarcity of younger deposits is likely to be an artefact of glacial erosion, implying that such events are probably more common than the recent geological record suggests (Gudmundsson et al., 2008; Rooyakkers et al., 2020; Chapter 2). How do the magmatic processes prior to these ignimbrite eruptions differ from the more common large-volume lava-forming events, and how might future monitoring efforts anticipate them? Petrologic studies of Icelandic ignimbrites are needed to answer such questions.

We present one such study of erupted products from the ca. 110 ka ignimbrite-forming Halarauður eruption, the largest known eruption of Krafla volcano in northeast Iceland (7 ± 6 km^3 magma; Rooyakkers et al., 2020; Chapter 2). Whole-rock major element data presented by Rooyakkers et al. (2020; Chapter 2) are examined in detail here, together with new whole-rock trace element analyses and *in situ* major element analyses of crystals, matrix glasses and melt inclusions. We then review the textural and chemical evidence for mixing of basaltic and rhyolitic magmas in the Halarauður eruption, and use a combination of geothermobarometry and MELTS thermodynamic modelling to constrain the pre-eruptive architecture of the Halarauður magma system. The Halarauður products reveal evidence for protracted storage and rapid destabilisation of melt-dominant magma bodies in the shallow crust, highlighting the pace at which such systems can move from quiescence to eruption.

4.3. GEOLOGICAL BACKGROUND

4.3.1. Krafla Volcanic System

Krafla is one of five en-echelon volcanic systems located in the Northern Volcanic Zone (NVZ) of Iceland, a segment of the axial rift zone associated with the divergent Eurasian-North American plate boundary (Sæmundsson, 1979). The system, active since at least 300 ka, comprises the Krafla central volcano, a shield of ~25 km diameter with an ~8 x 10 km caldera at its centre, and a 100 km-long, 5-8 km-wide fissure swarm that transects the central volcano from northeast to southwest (Fig.1; Sæmundsson, 1991; Hjartardóttir et al., 2012). Erupted products are compositionally bimodal; basaltic lavas and subglacial hyaloclastites are dominant (>90% by volume), while subordinate rhyolite has erupted in and around the caldera (Nicholson et al., 1991; Sæmundsson, 1991; Jónasson, 1994; Chapter 3). Intermediate products are rare, and those erupted within the caldera show evidence for a hybrid origin by mixing of basalt and rhyolite (Jónasson, 1994).

Recent activity at Krafla has been characterised by interplay between regional tectonics and volcanism, with long (ca. 300-1000 y.) periods of tectonic and volcanic quiescence interrupted by short (<10 y.) rifting events and effusive basaltic fissure eruptions (Thorarinsson, 1979; Sæmundsson, 1991; Hjartardóttir et al., 2016). Two major historic volcanotectonic events have occurred: the 1724-1729 Mývatn Fires, and 1975-1984 Krafla Fires (e.g., Hollingsworth et al., 2012). A zone of shear-wave attenuation at ~3-7 km depth in the central caldera region is inferred to reflect a large active basaltic magma chamber (Einarsson, 1978) or storage zone comprising a network of dikes and sills (Kennedy et al., 2018) that fed much of the recent activity. An active rhyolitic magma body (or bodies) is presently located at ~2 km depth in the central region of the caldera (Elders et al., 2011; Zierenberg et al., 2013), but its dimensions are poorly constrained (see Schuler et al., 2015).
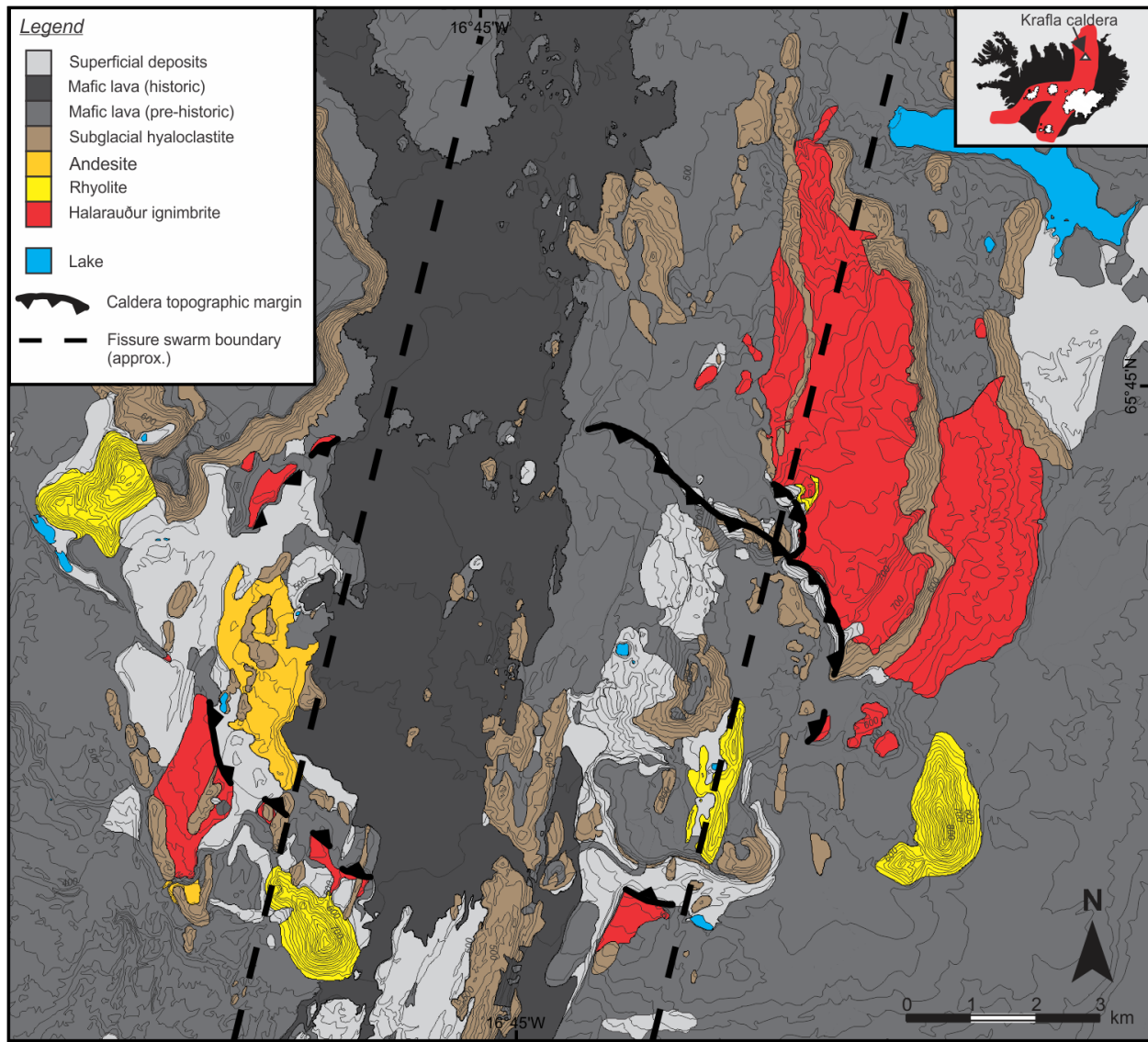
Figure 4.1. Simplified geological map of the Krafla caldera and surrounding area, showing the dispersal of Halarauður deposits around the caldera margin. Modified after Sæmundsson et al. (2012).

4.3.2. The Halarauður Eruption

The ca. 110 ka Halarauður eruption is the largest known eruption from the Krafla system (^{40}Ar/^{39}Ar age from Sæmundsson and Pringle, 2000). Its deposits occur in patchy exposure up to ~7 km from the caldera margin (Fig. 4.1) and were originally interpreted as a welded airfall tuff linked with

caldera formation (Björnsson et al., 1977; Calderone et al., 1990; Sæmundsson, 1991). Rooyakkers et al. (2020; Chapter 2) subsequently presented evidence for lateral emplacement of the deposits, re-interpreting them as the proximal remnants of a once expansive ignimbrite sheet that was largely eroded away during the last glaciation. By reconstructing the original distribution of outflow and intracaldera deposits prior to glaciation and assuming a range of dispersal scenarios and glacial erosion rates, they proposed a total erupted volume of 7 ± 6 km^3 dense rock equivalent (DRE).

Based on detailed field studies and whole-rock major element analyses of the erupted products, Rooyakkers et al. (2020; Chapter 2) subdivided the Halarauður deposits into three units, H1-H3 from base to top. Compositions of juvenile products range from basalt to high-silica rhyolite and become more mafic on average up-section, but with considerable scatter through H1 and most of H2, reflecting tapping of a heterogeneous magma body in which basalt underplated and mixed with rhyolite (Rooyakkers et al., 2020; Chapter 2). Field evidence for significant time breaks within or between units is lacking, hence the entire sequence was interpreted as the product of a single sustained eruption.

H1 deposits (andesite to rhyolite, $60.9 - 74.6$ wt% SiO$_2$; Fig. 4.2), which are absent at most sites and inferred to comprise <5% of the total preserved deposit, consist of valley-ponded pumice- and spatter-bearing lithic breccias, which transition laterally to lithic-poor, spatter-bearing pumiceous ignimbrite at the most distal sites. The occurrence of basal lithic breccias with variable lithic componentry between sites, and the absence of basal fall deposits, were interpreted as evidence for opening of a ring-fracture vent system and rapid column collapse at the onset of the eruption, likely accompanied by incipient caldera subsidence.

H1 deposits grade up into H2, the volumetrically dominant unit (preserved volume ~0.1
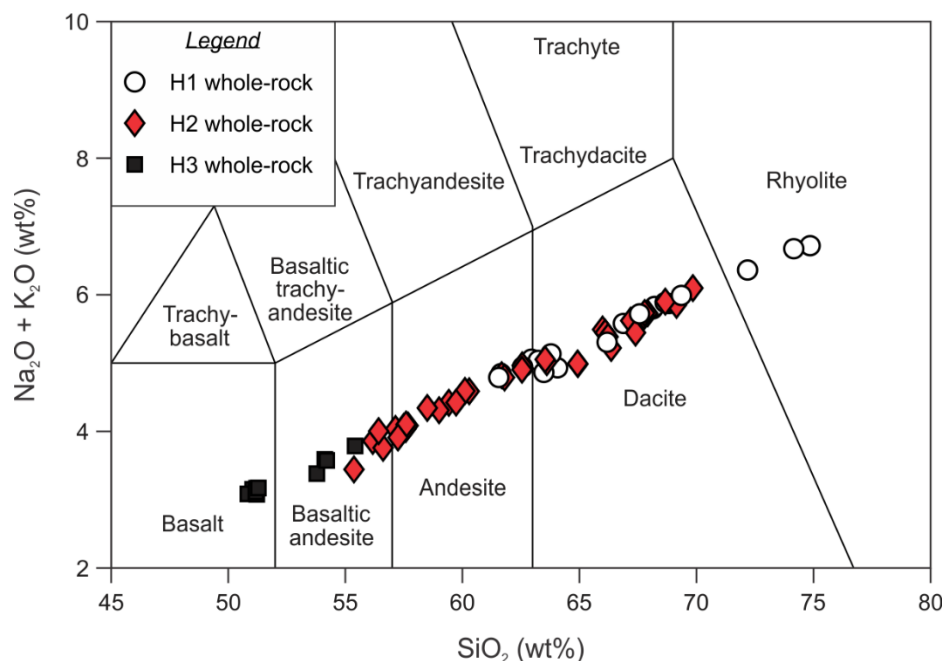
Figure 4.2. Total alkali versus silica (TAS) diagram of Halarauður whole-rock compositions, determined by XRF. Error bars (2σ) are smaller than the symbols.

km^3), which consists of a landscape-burying sheet of variably welded spatter-rich agglomerates, transitioning laterally to spatter-bearing lapilli tuffs at the most distal site. H2 juvenile compositions range from basaltic andesite to rhyodacite (54.5-69.4 wt% SiO$_2$; Fig. 4.2). Rooyakkers et al. (2020; Chapter 2) interpreted the agglomerates as coarse proximal "lag" deposits, analogous to lithic breccias, of spatter-rich pyroclastic density currents, which formed during sustained caldera collapse as fines-rich currents from explosive vents entrained spatter from weak fountains at neighbouring vents around a ring fracture.

The uppermost unit, H3 (preserved volume ~0.04 km^3), consists of a lower sequence of lava-like mafic ignimbrite (basalt to basaltic andesite; 50.0-54.6 wt% SiO$_2$; Fig. 4.2), overlain by welded to nonwelded spatter-bearing basaltic ignimbrite. Rooyakkers et al. (2020; Chapter 2) interpreted the lava-like H3 facies to reflect unusually high mass-flux effusion of gas-poor mafic

magma from the deepest and hottest levels of the chamber, which was squeezed through a highly dilated ring fault vent system by the sinking chamber roof block, forming low collapsing fountains that fed very high temperature pyroclastic density currents. The upper surfaces of H3 deposits are erosional and form the modern landscape surface (± soil cover).

4.4. METHODS AND TERMINOLOGY

4.4.1 Methods

Juvenile Halarauður products were sampled within the stratigraphic framework of Rooyakkers et al. (2020; Chapter 2) for petrologic and chemical analysis during field campaigns in 2016-2018. Single clasts were preferentially sampled where possible; where clast outlines were overprinted by intense welding, a bulk sample was collected. Whole-rock samples were crushed, powdered in an alumina ceramic mill, and analysed for major element contents by X-ray fluorescence spectroscopy (XRF) at the University of Waikato or the University of Auckland (both in New Zealand), as detailed by Rooyakkers et al. (2020; Chapter 2 and Appendix 1).

A subset of whole-rock samples, selected to span the range of major element compositions reported by Rooyakkers et al. (2020; Chapter 2), were analysed for trace element contents by solution inductively-coupled plasma mass spectrometry (ICP-MS) at Victoria University of Wellington, New Zealand. Solutions were prepared using standard HF digestion techniques, and analysed with a Thermo-Fisher Element2 sector-field ICP-MS equipped with an ESI autosampler. Analytical procedures were similar to those of Eggins et al. (1997). Full details of the digestion method, ICP-MS tuning and calibration procedures are found in Appendix 1. Estimates of 2σ analytical precision based on repeat analyses of standard reference materials are ≤6% relative

(usually $\leq$2-3%), and measured values are accurate to within 10% (commonly within 5%) of reference values for most elements.

Major- and minor-element compositions of macrocrysts (defined here as crystals >200 μm in maximum dimension), pyroxene microcrysts (groundmass crystals, $\leq$50 μm in maximum dimension) and glasses were determined *in situ* from polished thin sections or epoxy grain mounts by electron probe microanalysis (EPMA) at McGill University (Montreal, Canada). Plagioclase was analysed by wavelength dispersive spectroscopy (WDS) with a JEOL 8900 electron microprobe, using an accelerating voltage of 15 kV, beam current of 20 nA, and beam diameter of 5 μm, with peak/background counting times of 20 s/10 s for all elements except K and Fe (40 s/20 s). FeO* concentrations for plagioclase analyses within 50 μm of crystal rims were corrected for fluorescence of the surrounding groundmass following Sugawara (2001); all corrections are $\leq$0.16 wt%. Pyroxene, olivine and glass were analysed by WDS with a Cameca SX Five FE electron microprobe using a 15 kV accelerating voltage. For pyroxene and olivine, a 20 nA beam current, 2 μm beam diameter, and 20 s peak/10 s background counting times were used. For glasses, we first used a 2 nA beam current, 10 μm beam diameter and 20 s peak/ 10 s background counting times to analyse major elements, then increased the current to 10 nA and counting times to 60 s peak/30 s background for the minor elements (P, Cl, S and Ti). A zero-time correction for Na, K and Si was applied for glass analyses to account for any possible Na loss. Analytical precision (2σ) estimated from repeat analyses of standard reference materials is <3% relative for elements with concentrations >10 wt%, and <5% relative for elements comprising 1-10 wt% (excluding Na_2O, K_2O and FeO* in glass, and Na_2O in pyroxene; <15%, <9.5%, <5.5% and <7%, respectively). Mean values are accurate to within 5% of reference values for elements comprising >1 wt%,

excluding FeO* and MgO in glass, and Al_2O_3 in pyroxene (within 7.5%, 6.5% and 6.5%, respectively).

4.4.2. Terminology

Studies of the interactions between compositionally contrasting magmas commonly reserve the term "mixing" to describe the complete blending of magmas to form a compositionally homogeneous "hybrid" magma; where magmas are physically intermixed but compositional heterogeneities remain, the terms "mingling" or "commingling" are used (e.g., Sparks and Marshall, 1986). Because we view these terms as descriptors of what is essentially the same process, captured at varying degrees of completion in the erupted products, we here use "mixing" to describe any interactions between magmas in the Halarauður system.

4.5. RESULTS

4.5.1. Textural Evidence for Magma Mixing

The lower stratigraphic units of the Halarauður deposits, H1 and H2, show abundant textural evidence for mixing between mafic and felsic magmas. In H1, red or purple mafic enclaves up to ~1 cm in size are ubiquitous as a minor matrix component, and are interpreted as juvenile products based on their cauliform margins and microcrystalline quench textures (cf. Bacon, 1986). Similar enclaves up to ~3 mm in size occur as inclusions in felsic H1 pumice clasts, comprising ~1-2 vol% of each clast (Fig. 4.3g). In H1 spatter clasts, fluidal streaks or filaments of contrasting melt composition are ubiquitous (most easily seen in thin section; Fig. 4.3e). Silicic domains are

typically glassy with occasional pyroxene microcrysts, whereas mafic domains are devitrified. Similar mixing textures composed of filaments of variably recrystallised felsic (cream or white) to mafic (black, or red-oxidised) melt (Fig. 4.3c) also occur throughout H2 deposits. Whole-rock compositions show considerable heterogeneity throughout these lower parts of the stratigraphy and little systematic variation with stratigraphic height (Fig. 4.3).

4.5.2. Whole-Rock Chemistry

Halarauður whole-rock compositions span a broad and continuous range from quartz tholeiite basalt (50.0 wt% SiO_2, 5.0 wt% MgO; Mg# 38, calculated assuming $Fe^{3+}/\sum Fe = 0.1$; Maclennan, 2008) to high-silica rhyolite (74.6 wt% SiO_2, 2.6 wt% K_2O) (Figs. 4.2, 4.4; all values normalised anhydrous). The most primitive basaltic whole-rock composition is among the most evolved basaltic compositions reported from Krafla (which range between 4.7-9.8 wt% MgO and Mg# 37-69) and similar to the quartz tholeiites erupted in the historic Mývatn and Krafla Fires events, which had MgO contents as low as ~5.2-5.5 wt% and Mg# ~43-44 (Grönvold and Mäkipää, 1978; Grönvold, 1984; Nicholson, 1990; Nicholson et al., 1991; Hemond et al., 1993; Jónasson, 1994; Cooper et al., 2016). The most evolved rhyolite has a metaluminous composition similar to other Krafla rhyolites (Jónasson, 1994; Chapter 3).

As described by Rooyakkers et al. (2020; Chapter 2), whole-rock compositions are increasingly mafic on average up-section, but the correlation between stratigraphic height and
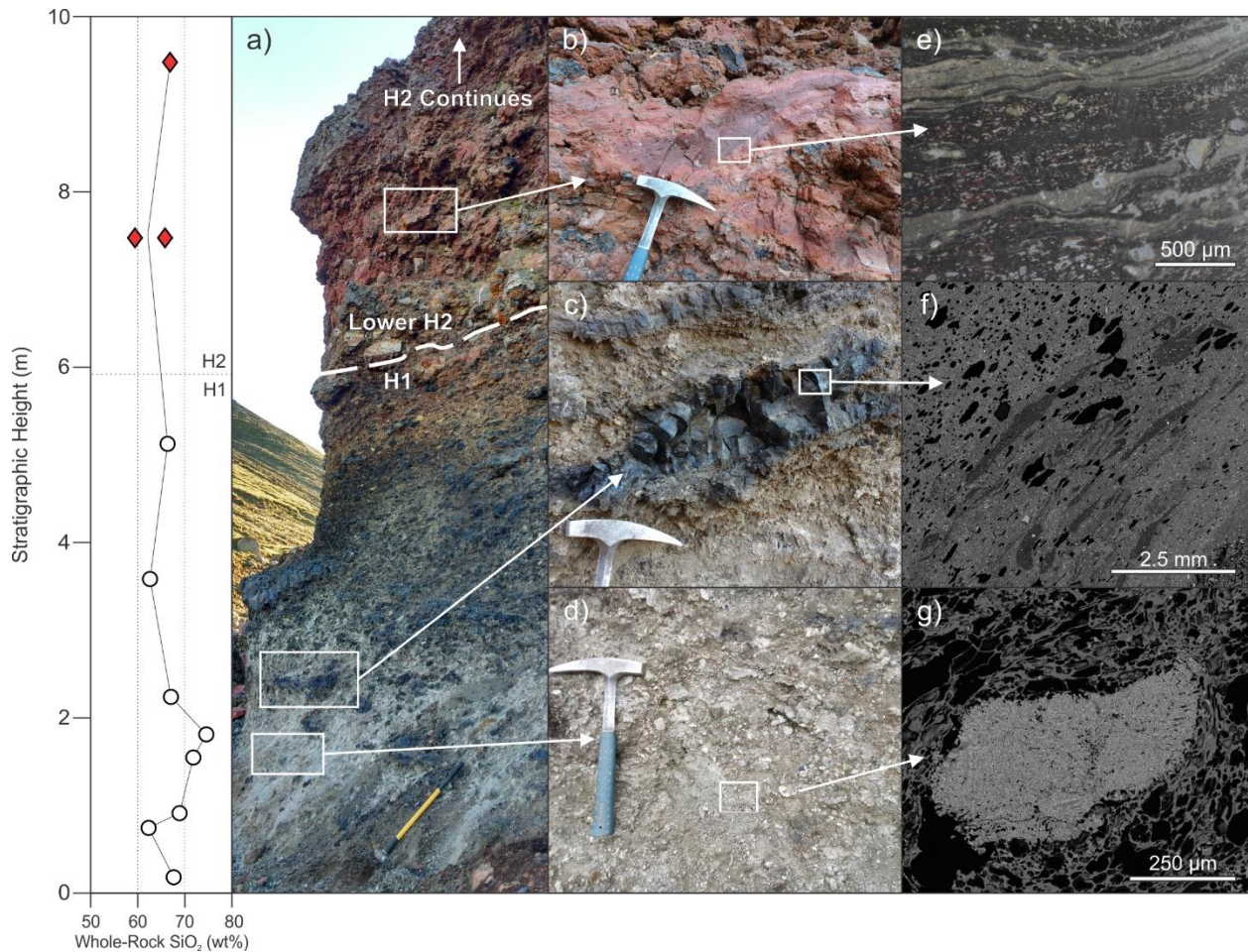
Figure 4.3. Photographs from a section through lower Halarauður deposits (units H1 and lower parts of H2), ~5 km north of the caldera (site F of Rooyakkers et al., 2020; Chapter 2). Note the wide range of whole-rock compositions shown in the leftmost panel (andesite to high-silica rhyolite) and the poor correlation between composition and stratigraphic height. a-d) Outcrop-scale features of the ignimbrite, which ranges from b) welded and strongly oxidised spatter-rich agglomerate (unit H2) to c) spatter-rich and d) spatter-poor pumiceous ignimbrite (unit H1). e-g) Images of micro-scale textures showing interaction between mafic and felsic magmas, including e) photomicrograph (unfiltered light) of mafic (black or red, devitrified) and felsic (cream-coloured, glassy) filaments in welded H2 spatter, f) BSE image of glassy felsic filaments (dark) in more mafic host (bright, devitrified) and g) quenched microcrystalline mafic enclave in H1 pumice clast.

composition is poor throughout H1 and the lower and middle parts of H2 (e.g., Fig. 4.3). Up-section, through uppermost H2 and into H3, whole-rock compositions are more homogeneous at a given stratigraphic level, grading smoothly upwards from andesite (upper H2) to basalt (mid to upper H3) (see Chapter 2, Fig. 2.10). Correlations between all major oxides are strongly linear,
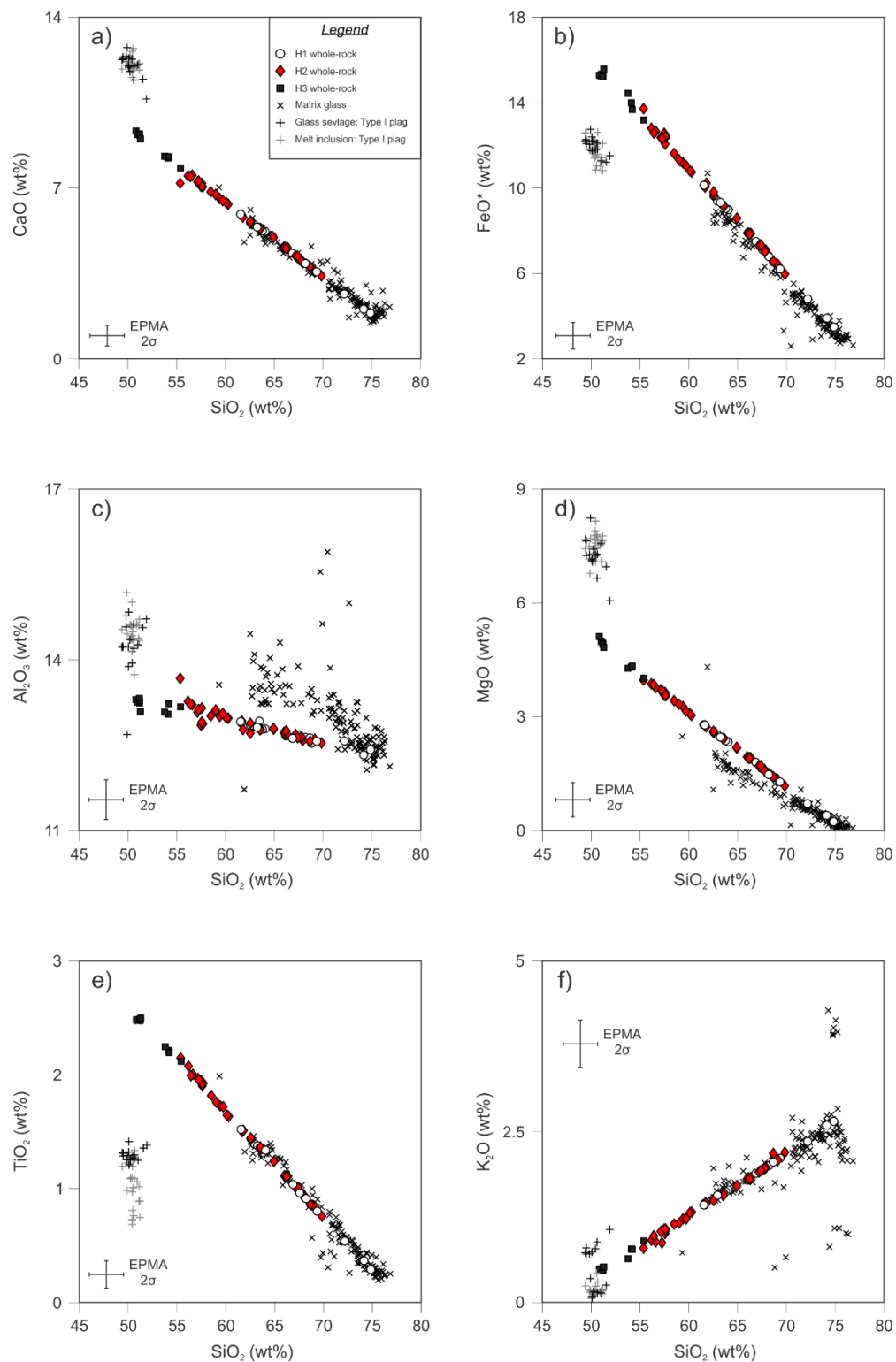
Figure 4.4. Selected Harker diagrams for Halarauður whole-rock and glass compositions (determined by XRF and EPMA, respectively). Error bars show maximum 2σ analytical uncertainty estimates for EPMA analyses based on repeat analyses of VG-2 and VG-A99 basalt and VG-568 rhyolite glass standards. Analytical uncertainties for XRF data are smaller than the symbols.

with R^2 values ≥ 0.95 (usually >0.99); an exception is Al_2O_3, which shows slightly weaker correlations with the other oxides ($R^2 \geq 0.79$).

Trace element concentrations also vary widely through the sequence, ranging between values typical of Krafla rhyolites and basalts (e.g., 102-179 ppm Sr, 201-519 ppm Zr, 142-572 ppm Ba, 17-61 ppm La; Fig. 4.5) . However, unlike the major elements, correlations between trace elements are not always strongly linear. Within groups of elements of similar geochemical behaviour, such as the rare earth (REE; La to Lu) or high field strength elements (HFSE; Zr, Nb, Hf, Ta), correlations between elements are usually strongly linear ($R^2 >0.8$), but correlations between these groups of elements are weaker (Fig. 4.5e). Among the REE, correlations are very strong ($R^2 >0.95$) between elements with similar mass (e.g., between two light REE such as La and Pr; Fig. 4.5a), but become weaker with increasing difference in mass (e.g., between light and heavy REE, such as La and Yb; Fig. 4.5b). Excluding Sc, the transition metals (V, Cr, Co) show strong linear correlations with each other, as well as with the major and high field strength elements. Li, Sc, Cs, W and Pb show weak ($R^2 <0.5$) or very weak ($R^2 <0.2$) correlations with most other elements.

4.5.3. Glass Chemistry

Matrix glasses preserved in the Halarauður deposits are andesitic to rhyolitic (59.3-76.8 wt% SiO_2, normalised anhydrous; Fig. 4.4). Zones of more mafic groundmass are pervasively recrystallised. Glass major element compositions mostly overlap with the whole-rock data, as expected given the very low crystal content (<1-2 modal% macrocrysts) of the Halarauður products (Fig. 4.4). The most notable exception is Al_2O_3, which deflects strongly from the whole-rock trend toward higher
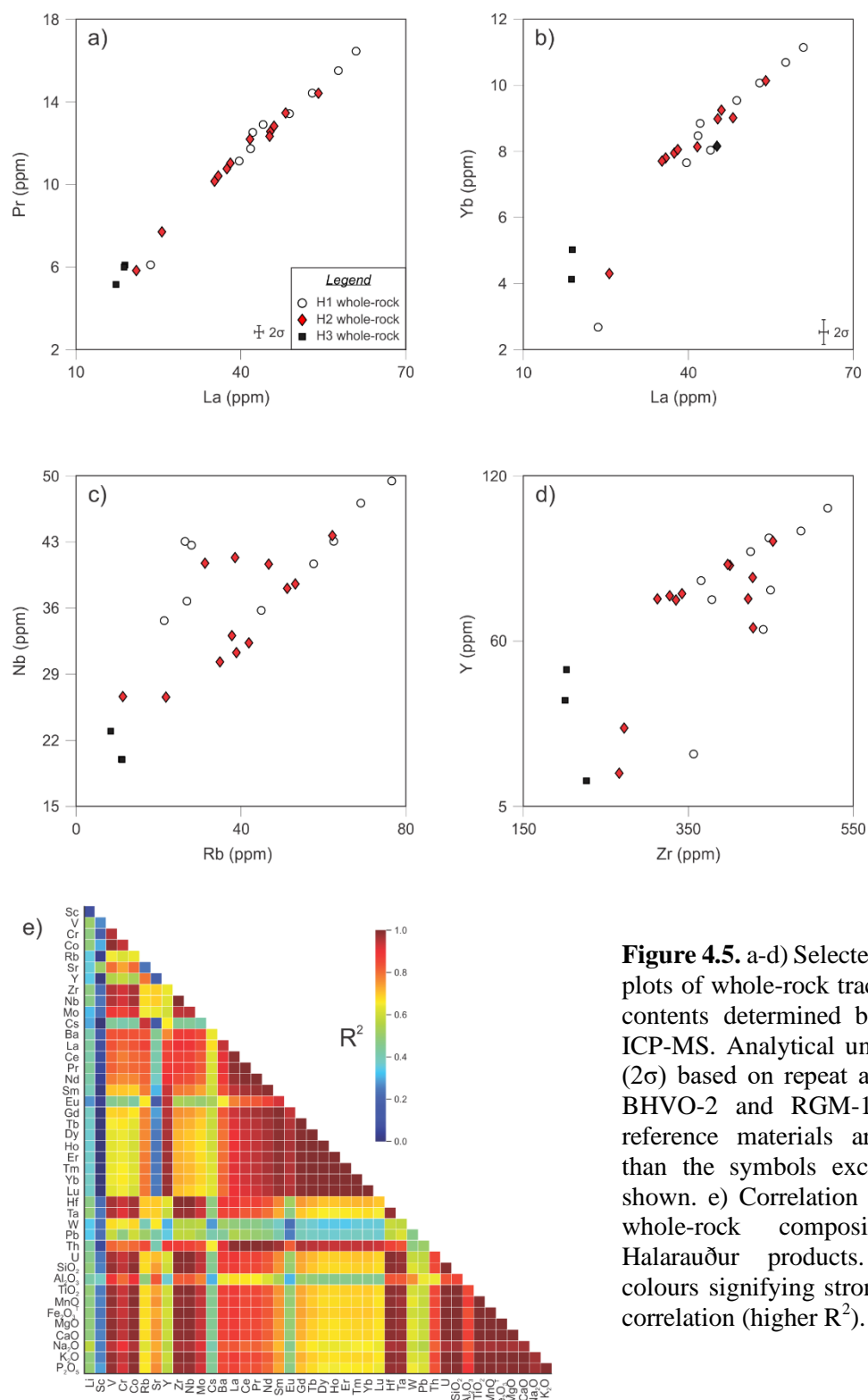
Figure 4.5. a-d) Selected bivariate plots of whole-rock trace element contents determined by solution ICP-MS. Analytical uncertainties (2σ) based on repeat analyses of BHVO-2 and RGM-1 standard reference materials are smaller than the symbols except where shown. e) Correlation matrix for whole-rock compositions of Halarauður products. Warmer colours signifying stronger linear correlation (higher R^2).

concentrations at a given SiO_2 content (Fig. 4.4c). MgO also deviates, toward lower concentrations for a given SiO_2 content (Fig. 4.4d), but the deviation is more subtle than for Al_2O_3. K_2O mainly follows the whole-rock trend, but outliers with anomalously high or low concentrations occur among the more silicic compositions (Fig. 4.4f).

Selvages of basaltic glass occur around some calcic plagioclase crystals (type I plagioclase; see below) in H1 felsic pumice and spatter clasts. With 6.1-8.2 wt% MgO (Mg# 49-55, assuming $Fe^{3+}/\Sigma Fe = 0.1$), they are significantly more primitive than the least-evolved Halarauður whole-rock composition, and plot well away from the trends defined by whole-rock and matrix glass data for most major elements (Fig. 4.4). Melt inclusions in these crystals show nearly complete compositional overlap with the selvages, but extend to slightly lower TiO_2 (Fig. 4.4e) and P_2O_5 (not shown).

4.5.4. Mineral Chemistry

4.5.4.1. Plagioclase

Plagioclase is the dominant macrocryst in the Halarauður deposits, occurring sparsely (<1-2 modal%) through all units. We recognise three populations, types I-III, based on distinct core An and FeO* contents (Fig. 4.6a). Plagioclase microcrysts <20 μm in maximum dimension occasionally occur in devitrified groundmass of welded H3 deposits. These microcrysts are inferred to have grown during slow cooling of the welded ignimbrite sheet, and are not considered further here.
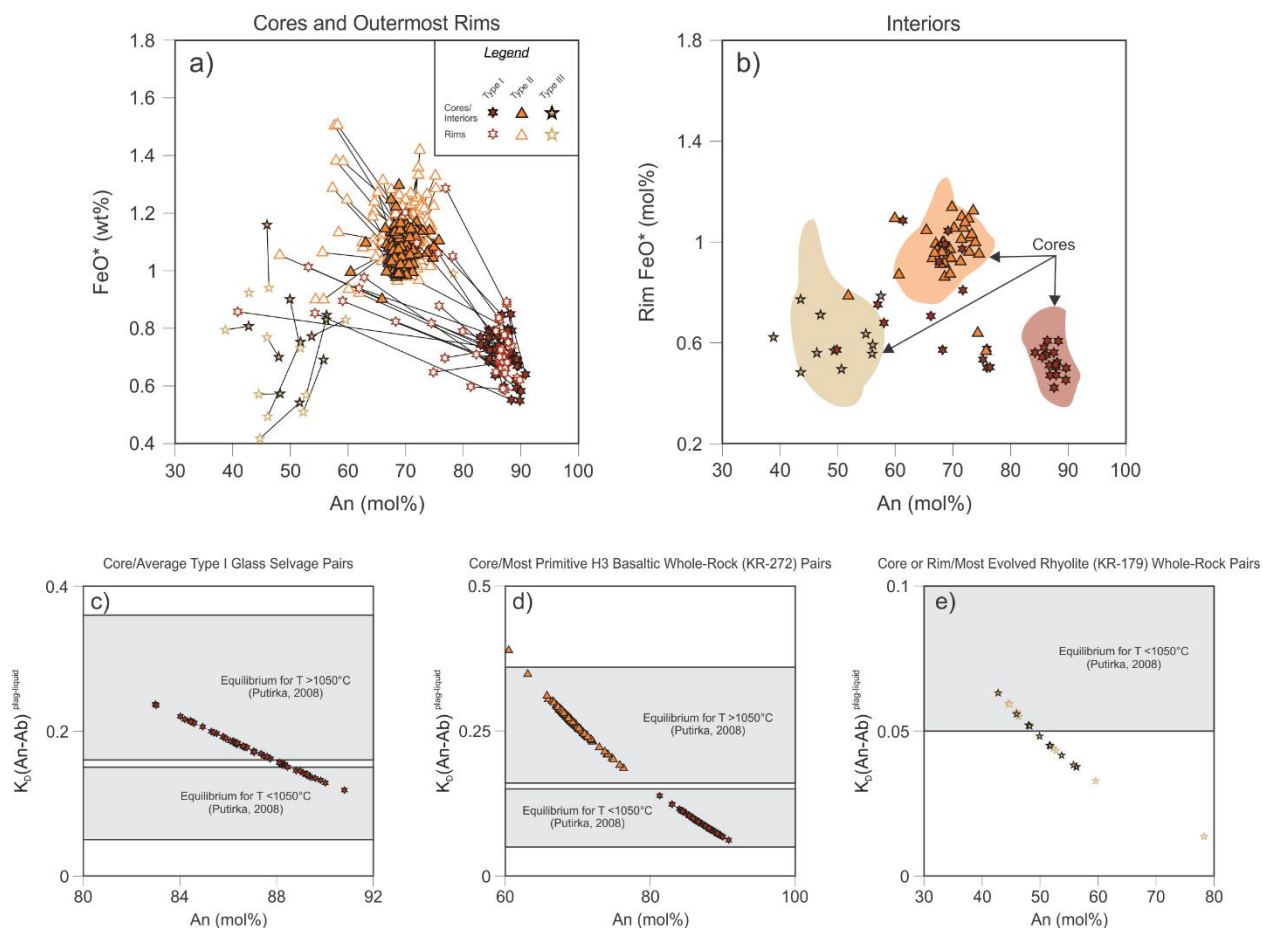
Figure 4.6. Plagioclase a) core and outermost rim (linked by tie-lines), and b) interior compositions, determined by EPMA. c-e) Equilibrium tests applying the K_D criteria of Putirka (2008).

Type I, the most calcic macrocryst population, occurs as discrete euhedral or rarely subhedral phenocrysts up to ~2 mm, commonly with selvages of basaltic glass (see above) (Figs. 4.4, 4.7). Type I crystals are most abundant in H1 deposits, where they comprise approximately one third of plagioclase crystals, but are rare in later-erupted units H2 and H3, where they comprise <5% of crystals and lack primitive selvages. Cores range from An_{81-91} (median = An_{87}), with FeO* contents of 0.55-0.85 wt% (median = 0.70 wt%) (Fig. 4.6a), and are in or very near to equilibrium

with the average composition of the adhering basaltic glass selvages for temperatures >1050°C (assuming $K_D(An\text{-}Ab)^{Pl\text{-}liq}$ = 0.27 ± 0.11 at equilibrium; Putirka, 2008) (Fig. 4.6c). Core compositions are also appropriate for equilibrium with the most primitive Halarauður whole-rock composition at T <1050°C (assuming $K_D(An\text{-}Ab)^{Pl\text{-}liq}$ = 0.10 ± 0.05; Putirka, 2008) (Fig. 4.6d), but we consider this temperature unrealistically low for melts of this composition. Internal zoning in type I plagioclase is usually minor (<5 mol% An) or absent, and most outer rims overlap in composition with type I cores. Narrow (5-100 μm) mantles, trending towards or overlapping with type II or III cores, occur on approximately one third of grains and reach compositions as sodic as An_{41} (Fig. 4.6b). Melt inclusions occur in ~60% of grains and are commonly glassy, with basaltic compositions that largely overlap with the basaltic selvages (Fig. 4.4). Most inclusion-bearing grains host a multitude of inclusions (in some cases >50), which reach up to ~200 μm in size.

Type II plagioclase is the dominant type in all units, occurring as discrete euhedral or rarely subhedral grains up to ~1 mm, and as glomerocrysts (± augite) up to ~2 mm (Fig. 4.7). Cores range from $An_{60\text{-}76}$ (median = An_{69}), with 0.83-1.30 wt% FeO* (median = 1.05 wt%) (Fig. 4.6a), and almost all are in equilibrium with the least evolved basaltic whole-rock composition for T >1050°C (Fig. 4.6d). Minor oscillatory zoning is common, with An variations of <~3 mol% between adjacent zones. Narrow sodic overgrowth rims up to 50 μm thick (typically <10-20 μm) occur on 15% of grains, reaching compositions as evolved as An_{48} . Reverse core-rim zoning occurs in 36% of crystals, but is usually <3-4 mol% (and never >8 mol%). Melt inclusions are scarce (<5% of crystals) and devitrified.

Type III grains reach up to ~1.5 mm and comprise ~5% of the total plagioclase population in all units. They are euhedral or rarely subhedral, and occasionally host small (<100 μm) apatite inclusions. Cores range from $An_{43\text{-}56}$ (median = An_{52}), with 0.54-1.16 wt% FeO* (median = 0.77
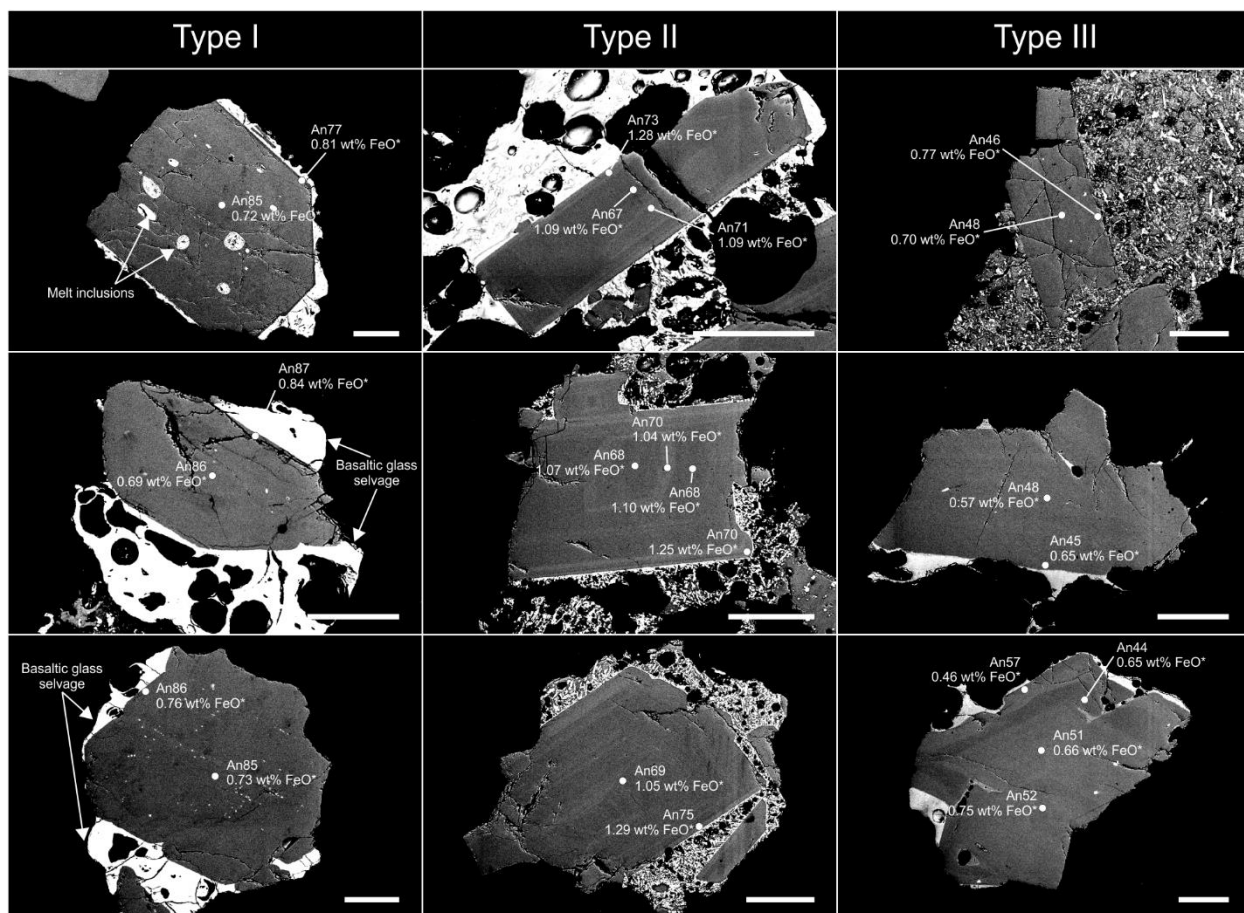
Figure 4.7. Selected back-scattered electron (BSE) images of plagioclase types I-III, labelled with EPMA spots. Scale bars are 200 μm.

wt%) (Fig. 4.6a), and are in or near equilibrium with the most evolved rhyolitic whole-rock composition (Fig. 4.6e). Most crystals are relatively featureless (Fig. 4.7), with smooth normal zoning of <10 mol% An; a minority have resorbed cores with normally zoned overgrowths. Melt inclusions are absent. Rim compositions mainly plot within the field of type III cores. One grain has a markedly more calcic rim of An_{78}.

4.5.4.2. Pyroxene

Euhedral to anhedral augite (Fig. 4.8a, b) macrocrysts up to ~1 mm occur sparsely (<<1 modal%) through all Halarauður units, usually in ~1-2 mm glomerocrysts with type II plagioclase (Fig. 4.9). Core compositions range from $En_{42-49}Fs_{11-22}Wo_{33-41}$ (Mg# 68-81), excluding a single more evolved core of $En_{34}Fs_{28}Wo_{38}$ (Mg# 56) from H1. Those less magnesian than Mg# 75 (excluding the outlier), are in equilibrium with the most primitive basaltic whole-rock composition, assuming $K_D(Fe\text{-}Mg)^{cpx\text{-}liq} = 0.28 \pm 0.08$ at equilibrium (Putirka, 2008) (Fig. 4.8d). Compositions more primitive than Mg# 75 are mainly restricted to H3, rare in H1, and were not observed in H2. In all grains, zoning is minor (Mg# $\leq$5) or absent except for thin (<30 μm) overgrowths at the outermost rim. The overgrowths are commonly dendritic, and usually more Fe-rich than cores, overlapping in composition with groundmass microcrysts. Reverse zoning occurs in only 18% of grains and is limited to Mg# $\leq$4 (excluding the Mg# 56 outlier core from H1, which has a rim of Mg# 63).

Euhedral to subhedral orthopyroxene macrocrysts up to ~1.5 mm were observed only in H3, usually in ~2-4 mm glomerocrysts with plagioclase (± olivine), and occasionally as discrete crystals (Figs. 4.8a, b, 4.9). Core compositions range from $En_{67-71}Fs_{24-28}Wo_{4-5}$ (Mg# 71-75), and all but the most Fe-rich are too magnesian to be in equilibrium with the most primitive basaltic whole-rock composition (Fig. 4.8e). Like augite, zoning is minor (Mg# $\leq$3) or absent except at the outermost rims, which consist of thin (<50 μm) overgrowths of pigeonite ($En_{43-50}Fs_{39-47}Wo_{7-13}$; Mg# 48-55) that overlap in composition with groundmass microcrysts. Plagioclase crystals in glomerocrysts with orthopyroxene texturally resemble type II crystals, but were not analysed by EPMA.

Equant to elongate pyroxene microcrysts ($\leq$50 μm) are pervasive in the deposits of all eruptive phases. Compositions vary widely and overlap with the overgrowth rims on macrocrysts
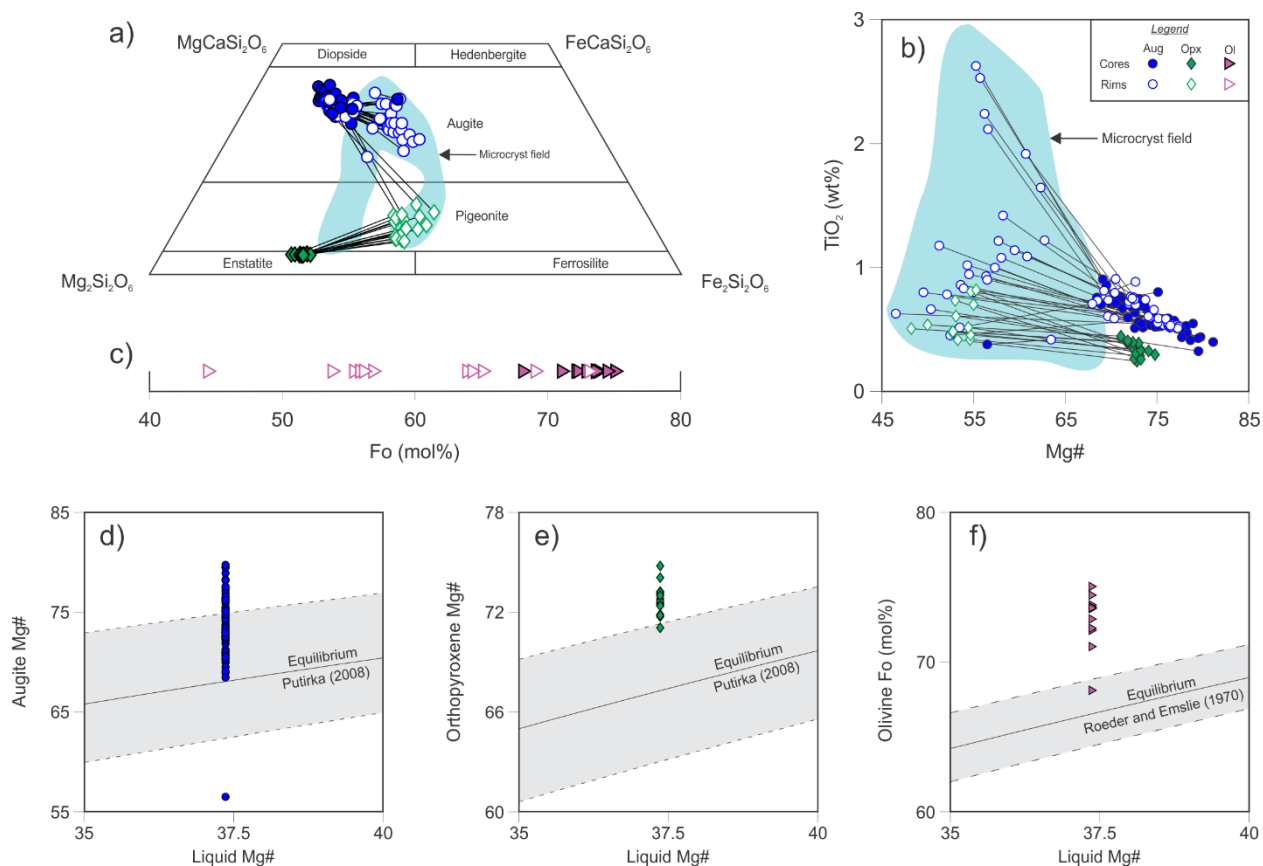
Figure 4.8. a,b) Pyroxene macrocryst core and outermost rim (linked by tie-lines) compositions. Field of microcryst compositions is shown in green. c) Olivine macrocryst core and rim compositions. d-f) Equilibrium tests applying the K_D criteria of Putirka (2008) for cores paired with the most primitive basaltic whole-rock composition (KR-272).

(fields in Figs. 4.8a, b), but show little correlation with stratigraphic position. Most are augite ($En_{32-50}Fs_{21-39}Wo_{21-41}$; Mg#49-69); subordinate pigeonite ($En_{45-63}Fs_{29-46}Wo_{6-17}$; Mg#50-69) occurs in H1 and H2, and a single grain ($En_{38}Fs_{45}Wo_{17}$; Mg# 46) was observed in H3. These groundmass crystals are inferred to record rapid growth during magma ascent and/or mixing (e.g., Shea and Hammer, 2013; Rooyakkers et al., 2018), and are not considered further here.
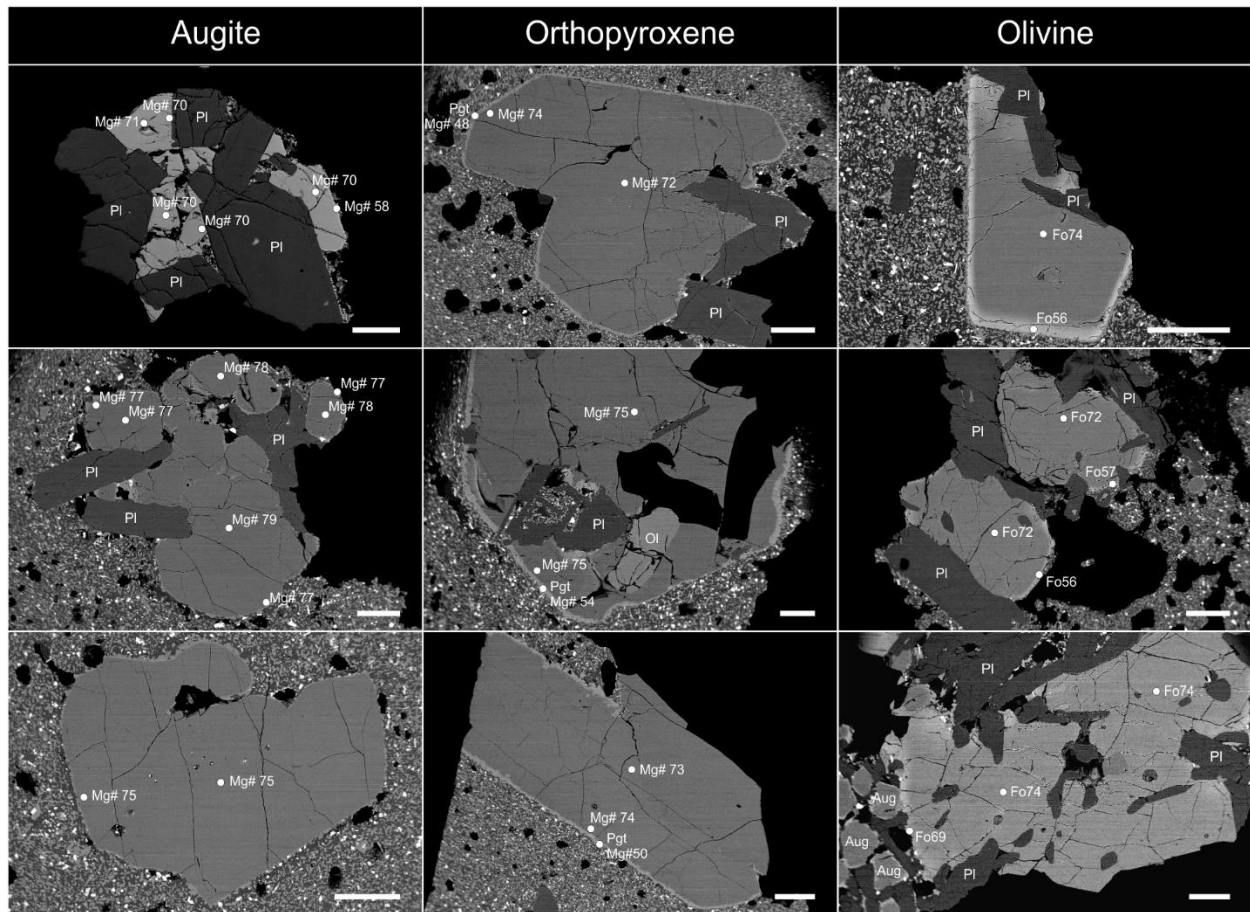
Figure 4.9. Selected back-scattered electron (BSE) images of pyroxene and olivine macrocrysts, labelled with EPMA spots. Scale bars are 200 μm.

4.5.4.3. Olivine

Euhedral to subhedral olivine up to ~1.5 mm was observed only in H3 deposits, exclusively as ~2-4 mm glomerocrysts with plagioclase (± augite and/or orthopyroxene; Fig. 4.9). Some grains have highly irregular forms and are interstitial to network-forming plagioclase laths. Individual grains have large homogeneous cores of Fo_{68-75}, and narrow (~10-50 μm) diffuse rims of more Fe-rich composition, ranging from Fo_{44-69} (excluding a single unzoned grain completely enclosed by orthopyroxene) (Fig. 4.8c).

4.6. DISUCISSION

4.6.1. Basalt-Rhyolite Mixing in the Halarauður System

The quenched mafic enclaves in H1 deposits, streaks and filaments of contrasting melt composition in H1 and H2 spatter clasts, whole-rock and glass compositions ranging from basalt to rhyolite, and diverse macrocryst assemblages throughout the erupted products all provide unambiguous evidence for basalt-rhyolite mixing in the Halarauður eruption. Similar mafic-silicic interactions are common in Icelandic magmatic systems, and have been described from the products of explosive and effusive eruptions (e.g., Prestvik, 1980; Sparks et al., 1977; Sigurdsson and Sparks, 1981; Blake, 1984; McGarvie, 1984; Mørk 1984; Macdonald et al., 1987; McGarvie et al., 1990; Larsen et al., 2001; Sverrisdottir, 2007; Sigmarsson et al. 2011; Keiding and Sigmarsson, 2012; Charreteur and Tegner, 2013), including ignimbrites (Blake, 1969; Jørgensen, 1980, 1981; Tomlinson et al., 2012), and from exhumed hypabyssal and plutonic rocks in the cores of extinct Tertiary systems (e.g., Blake et al., 1965; Walker and Skelhorn, 1966; Furman et al., 1992b; Padilla et al., 2016).

The strong co-linearity of all Halarauður whole-rock major element concentrations (Fig. 4.4) corresponds with the trend predicted by classical two-component mixing, in which the composition of the resulting hybrid magma is related to the proportions of the two endmember magmas by the mixing equation (e.g., Langmuir, 1978):

$$C_H = C_F x + C_M(1-x) \tag{4.1}$$

where C_H, C_F and C_M are the compositions of the hybrid, most-evolved and least-evolved endmembers, respectively, and x is the mass fraction of the most evolved endmember. Rearranging variables yields:

$$C_H - C_M = x(C_F - C_M) \qquad\qquad (4.2)$$

As shown by Fourcade and Allegre (1981), equation 4.2 implies that a plot of $C_H - C_M$ vs. C_F-C_M for all elements should yield a straight line with a slope of x. Hence, if the endmember and hybrid magma compositions are known, the proportions of the two endmembers involved in mixing can be calculated. Here we use our most and least-evolved whole-rock analyses as the rhyolitic and basaltic endmembers, respectively. The hybrid composition can be estimated by considering the distribution of compositions through the system. As mixing progresses, compositions evolve from the two endmembers towards a Gaussian distribution with a central peak that corresponds with the hybrid composition (Perugini et al., 2004, 2008). If the mixing process runs to completion, this Gaussian curve collapses inward, and the system comprises a single homogeneous magma with the hybrid composition. Although there is noise due to the relatively small number of whole-rock analyses, compositional histograms of Halarauður whole-rock major oxide compositions from units H1 and H2 approximate the expected Gaussian distributions (Fig. 4.10). H3 compositions are more homogeneous and showno textural evidence for mixing, so we infer that this late-erupted unit reflects tapping of deeper magma that underwent little to no mixing, and H3 compositions are not used for estimating the hybrid composition. For each oxide, we take the median concentration from H1 and H2 analyses as our best estimate of the hybrid composition. With 63.0 wt% SiO_2 (normalised anhydrous; Table 4.1), our calculated hybrid composition sits on the compositional boundary between andesite and dacite (cf. Fig. 4.2). As predicted by Fourcade and Allegre (1981), a plot of $C_H - C_M$ vs. C_F-C_M for all elements yields a straight line ($R^2 = 1.00$), and x, the proportion of the rhyolitic endmember, is 0.53 (Fig. 4.11). We conclude that our whole-rock major element data are well-explained by classical two-component mixing of sub-equal proportions of rhyolite and basalt. For convenience, these magmas, represented by the most and least evolved whole-rock
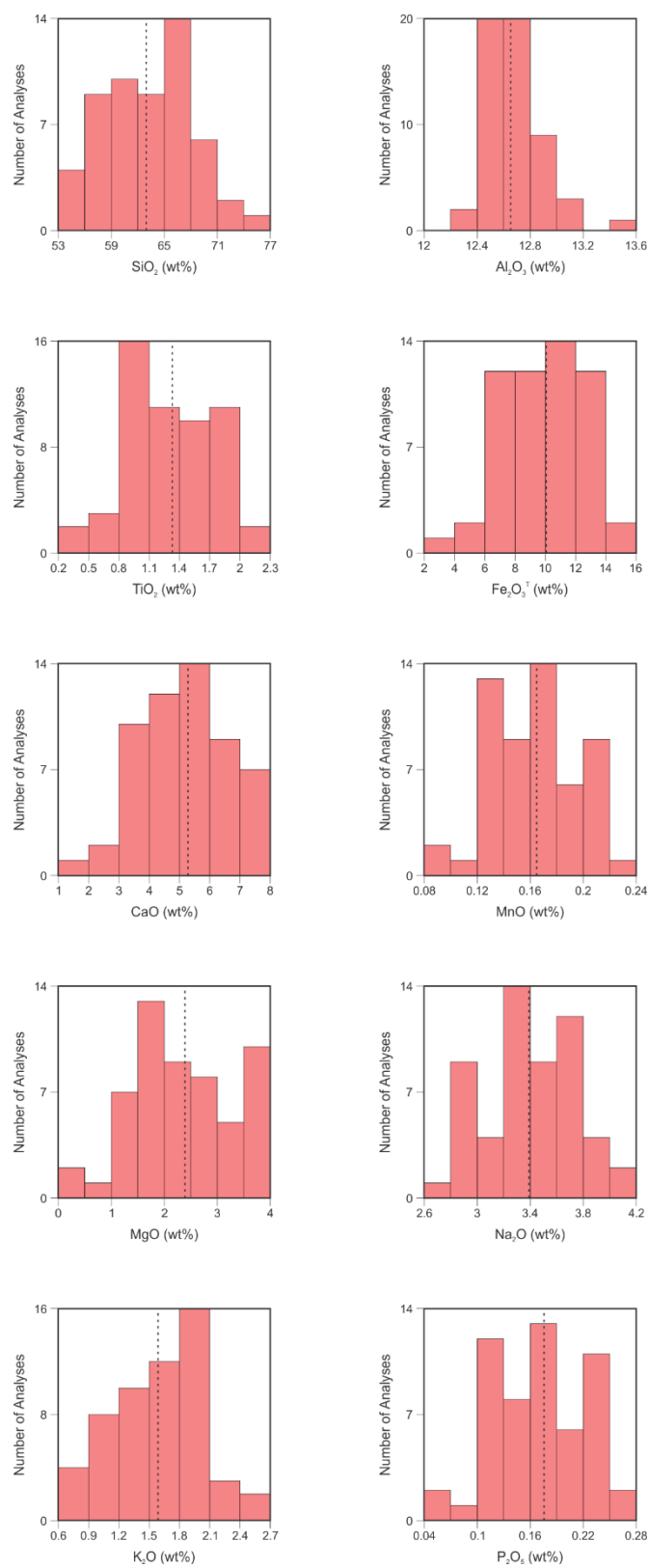
Figure 4.10. Histograms of whole-rock major oxide compositions for H1 and H2 (determined by XRF). Vertical dashed lines show the median concentration for each oxide.

185
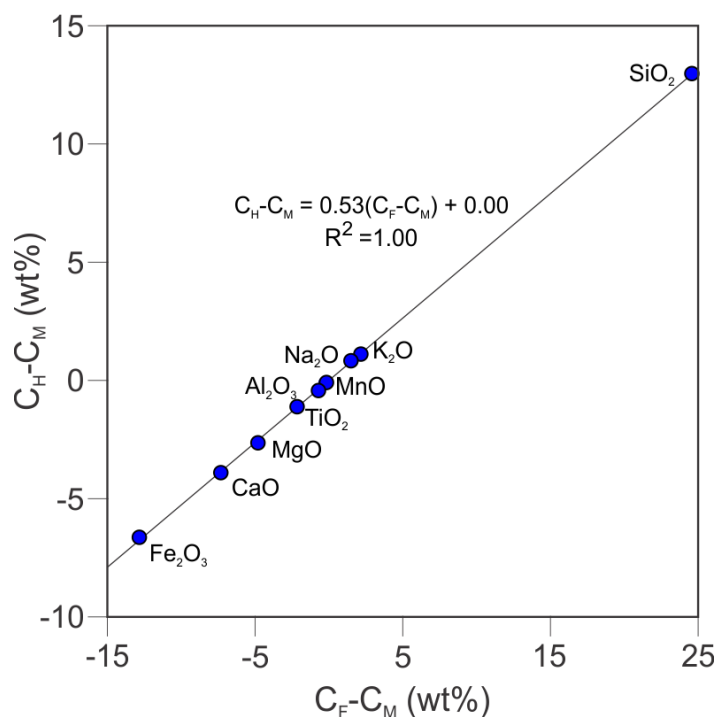
Figure 4.11. Plot of C_H-C_M vs. C_F-C_M after Fourcade and Allegre (1981) for H1 and H2 whole-rock compositions, where C_H, C_F and C_M are the concentrations of each major oxide for the hybrid magma and felsic and mafic endmembers, respectively. The gradient of the regression line is equivalent to the weight fraction of the felsic endmember in the mixed system.

compositions, will be referred to as the "endmember" rhyolite and basalt hereafter. We emphasise that the proportion of the endmember basalt calculated above is averaged across H1 and H2; the general trend towards more mafic compositions up-section implies that the proportion of basalt relative to rhyolite increased with depth in the chamber, and most H1 whole-rock major element compositions are consistent with contamination of the endmember rhyolite by <20 wt% basalt. The presence of quenched mafic enclaves in H1 deposits is also consistent with a smaller volume of basalt relative to rhyolite in the upper (first-tapped) parts of the system (cf. Sparks and Marshall, 1986).

TABLE 4.1. MAJOR ELEMENT COMPOSITIONS OF ENDMEMBER MAGMAS AND THEORETICAL HYBRID										
	SiO_2	TiO_2	Al_2O_3	$Fe_2O_3^T$	CaO	MgO	MnO	Na_2O	K_2O	P_2O_5	Total
Endmember rhyolite	74.57	0.29	12.37	3.86	1.86	0.22	0.09	4.05	2.64	0.04	100
Endmember basalt	49.99	2.44	13.08	16.70	9.18	5.03	0.25	2.56	0.47	0.30	100
Calculated hybrid composition	62.97	1.33	12.65	10.06	5.28	2.39	0.16	3.39	1.59	0.18	100

Note: Endmember compositions were determined by XRF. Theoretical hybrid was calculated from the median composition for each oxide from analyses of H1 and H2 products (see text).

The strong evidence for two-component mixing in our major element data is perhaps surprising given the presence of three distinct plagioclase populations in the Halarauður products (Fig. 4.6). The most primitive population, type I, is associated with a distinct population of basaltic glass (Fig. 4.4) and is not in equilibrium with the more evolved endmember basalt. We thus interpret type I plagioclase and its adhering glass selvages as cryptic evidence for a second, more primitive basaltic magma (hereafter the "primitive basalt") that also interacted with the Halarauður rhyolite. Because the whole-rock data are not skewed towards these more primitive compositions (Fig. 4.4), we infer that the volume of this second basalt was insignificant compared with the other two magmas. Type I plagioclases are most abundant in H1 deposits (approximately one third of plagioclase crystals), which comprise <5% of the preserved Halarauður deposits (Rooyakkers et al., 2020; Chapter 2), but are rare throughout H2 and H3 (<5% of crystals). Hence, we suggest that the small volume of primitive basalt mainly interacted with the upper, more silicic parts of the magmatic system that vented first (see Rooyakkers et al., 2020; Chapter 2). The origins of the primitive basalt and its calcic plagioclase population are considered further below.

According to the above equations, the concentrations of all trace elements should also vary co-linearly in a system undergoing two-component mixing (e.g., Langmuir, 1978; Fourcade and Allegre, 1981). However, as shown by the correlation matrix in Fig. 4.5e, many trace elements in our whole-rock dataset are poorly correlated. Although some of this scatter could be caused by three-component mixing that also involved the more primitive basalt, the insignificant volumes of this third magma indicated by the major element data (see discussion above) imply that its involvement would not be sufficient to significantly skew the linear trends predicted by the mixing equation. Instead, the strong linear correlations between geochemically similar groups of elements

such as the REE or HFSE suggest a different reason for the differing strengths of correlations between elements.

Motivated by recognition that the kinematics of magma mixing are governed by the same repeated stretching and folding processes that characterize chaotic dynamics (e.g., Ottino, 1989), recent experimental and numerical studies have applied chaos theory to advance understanding of the morphological and chemical of evolution of magmas during mixing (e.g., Perugini et al., 2006, 2008; De Campos et al., 2008, 2011; Morgavi et al., 2013a, b). The onset of chaos during mixing generates complex, scale-invariant (i.e., fractal) patterns of lamellar structures (filaments) as the magmatic mass is repeatedly stretched and folded back onto itself. This process exponentially increases the interface between the two magmas, thereby enabling rapid chemical exchanges by diffusion over short length scales (e.g., Petrelli et al., 2011). These fractal patterns of filaments have been observed in both natural volcanic rocks (Wada, 1995; Flinders and Clemens, 1996; Poli and Perugini, 2002; Perugini et al., 2002, 2003) and silicate magmas mixed experimentally under chaotic conditions (De Campos et al., 2004, 2008, 2011; Perugini et al., 2008; Morgavi et al., 2013c), providing strong evidence for chaotic dynamics during magma mixing. A key outcome of these studies is recognition that the coupled action of advection and chemical diffusion during chaotic mixing causes a diffusive fractionation of elements. Differences in the relative mobility of elements are accentuated by the action of chaotic flow fields, causing a rapid de-coupling in concentrations of elements with different mobilities (Perugini et al., 2006; 2008, 2015; De Campos et al., 2008, 2011; Morgavi et al., 2013a, b). A result of this decoupling is that the linear correlations between elements break down. As mixing progresses, correlations remain approximately linear between elements with similar mobilities, such as REE or HFSE, but trends between elements with different mobilities become highly scattered as they redistribute through

the system at different rates (Perugini et al., 2006, 2008, 2013; De Campos et al., 2008, 2011; Morgavi et al., 2013a, b).

The varying strengths of correlations between trace elements, and stronger correlations between elements with similar geochemical behaviour, agree with the trends expected from chaotic mixing. Magma mixing experiments have revealed a systematic decrease in mobility of the REE with increasing mass (excluding Eu, which may exist in a divalent state and is thus more mobile than the other REE; Morgavi et al., 2013b; Perugini et al., 2013, 2015), consistent with the progressively weaker correlations that we observe between these elements as their difference in mass increases (Fig. 4.5e). Similarly, the HFSE and most major elements have similar mobilities during mixing (Perugini et al., 2013; Morgavi et al., 2013b), in agreement with the strong correlations within and between these element groups, and their weaker correlations with the REE (Fig. 4.5e). Strong linear correlations between the major elements imply that they had similar mobilities during mixing. Al_2O_3 shows the weakest correlations with other major elements, followed by Na_2O, consistent with a slightly greater mobility relative to other major elements (cf. Perugini et al., 2013). Hence, we conclude that our whole-rock trace element data provide strong evidence for chaotic two-component mixing of the basaltic and rhyolitic endmembers in the Halarauður system.

4.6.1.1. Mixing Timescales

4.6.1.1.1. Primitive Basalt/Rhyolite Interaction

Evidence for re-equilibration of the highly calcic type I plagioclase macrocrysts during mixing into the Halarauður rhyolite is limited to narrow (5-100 μm) sodic rims on approximately one third

of grains. Given that the proportion of basalt that interacted with the upper parts of the magmatic system was small (<~20 wt%; see discussion above), we assume that the small volume of primitive basalt incorporated into the H1 deposits was chilled almost to the liquidus temperature of the Halarauður rhyolite (~900°C), and thus experienced an undercooling (ΔT) of ~250-300°C. To the best of our knowledge, plagioclase growth rates have not been measured at such high undercoolings in basaltic melts, but Schiavi et al. (2009) report rates of 1.9-4.9 x 10^{-9} m s^{-1} for isothermal crystallisation of a dry basaltic andesite at $\Delta T = 330$°C. At similar rates, a 100 μm rim could grow on a type I plagioclase core in approximately 5.5-15 hours, which we propose as a maximum timescale for the duration of interaction between the primitive basalt and Halarauður rhyolite.

Most type I crystals have glassy selvages that are generally completely free of quench crystals, implying that interactions between the primitive basalt and endmember rhyolite were short. Experimentally-determined glass transition temperatures for basaltic melts are <750°C even for extremely rapid cooling rates (Giordano et al., 2005; Potuzak et al., 2008), well below the inferred storage temperature for the Halarauður rhyolite (~900°C; see discussion below). Hence, the selvages must have quenched to glass upon eruption rather than during thermal equilibration with the rhyolite at depth. Assuming a thermal diffusivity of 3 x 10^{-7} m^2 s^{-1} (Sparks et al., 1977), typical selvages of ~200-300 μm thickness would quench to the ambient temperature of the host rhyolite in less than a second. At ΔT of ~250-300°C, nucleation of abundant quench crystals is to be expected in addition to heterogeneous nucleation and growth on pre-existing crystals (e.g., Shea and Hammer, 2013; Rooyakkers et al., 2018). Hence the absence of quench crystals in most selvages and absence of overgrowths on most type I plagioclase crystals imply that the timescales of basalt-rhyolite interaction were faster than the kinetics of nucleation. Nucleation delay times in

basalts are inversely proportional to undercooling (e.g., Donaldson, 1979; Corrigan, 1982; Polacci et al., 2018), but have not been measured at $\Delta T > \sim 100°C$. However, delays of approximately one hour have been determined for homogeneous nucleation of plagioclase in basalts at undercoolings of $\sim 50\text{-}100°C$ (Corrigan, 1982), and for pyroxenes at undercoolings of $\sim 40\text{-}50°C$ (Corrigan, 1982; Polacci et al., 2018). We therefore suggest one hour as a conservative maximum residence time for selvages free of quench crystals in the Halarauður rhyolite. Assuming the rhyolite ascended from ~ 3 km depth (see discussion below) at rates similar to those determined for the onset of caldera-forming silicic eruptions (0.06-13 m s^{-1}; Myers et al., 2018), these inferred mixing timescales are comparable to or shorter than the expected duration of magma ascent (4 minutes to 14 hours). We thus infer that either the rhyolite and admixed primitive basalt were drawn into the conduit almost immediately after the primitive basalt was injected, or a laterally-propagating dike of the primitive basalt intercepted the ascending rhyolite at shallow depth in the conduit (cf. Allan et al., 2012).

4.6.1.1.2. Endmember Basalt/Rhyolite Interaction

The type II plagioclase crystals native to the endmember basalt also show limited evidence for re-equilibration during mixing with the rhyolite. Sodic overgrowth rims suggestive of growth from a cooler, more evolved hybrid melt occur on only 15% of grains and are <50 μm thick (usually <10-20 μm). In the early stages of chaotic mixing involving subequal volumes of the endmember magmas, temperatures and melt compositions are highly heterogeneous throughout the magmatic mass. The sodic overgrowths therefore likely grew at a wide range of undercoolings in compositionally diverse melts, so estimating growth rates is difficult. Conservatively assuming a slow rate of 10^{-11} m s^{-1}, appropriate for rhyodacite melt at $\Delta T < 50\text{-}100°C$ (Hammer and Rutherford,

2002; Shea and Hammer, 2013), sodic rims of 50 μm thickness could grow in about 2 months, which we propose as a maximum estimate for the duration of interaction between the endmember magmas. Growth in andesitic or basaltic andesitic melts at similar ΔT is typically 1-2 orders of magnitude faster than this minimum rate (see Fig. 12 of Shea and Hammer, 2013), hence a crystal resident in relatively mafic hybridised melt could grow a 50 μm rim in several days to as little as ~14 hours. Given the absence of sodic rims on most type II grains, we suggest that these shorter timescales are more realistic.

4.6.2. Architecture and Evolution of the Halarauður Magmatic System

Having identified the three magma batches involved in the Halarauður eruption and the evidence for their short interactions, we now consider the origin and pre-eruptive storage conditions for each magma. We integrate the results of geothermobarometry and MELTS modeling to constrain the pre-eruptive architecture of the Halarauður magmatic system, and compare the Halarauður magmas and their crystal cargoes with similar magmas from Krafla and elsewhere in Iceland.

4.6.2.1. Storage and Origin of the Endmember Basalt

The core compositions of almost all type II plagioclase and the most evolved augite macrocrysts (Mg# ≤75), which occur together as glomerocrysts throughout the Halarauður sequence, have euhedral forms and core/interior compositions in equilibrium with the endmember basalt whole-rock composition (Figs. 4.6, 4.8). These compositions are typical of relatively evolved Icelandic quartz tholeiites (cf. Hemond et al., 1993), and we thus infer that these crystals are phenocrystic to this basalt. This assemblage is consistent with other evolved basalts from Krafla, which

commonly lack olivine (Nicholson, 1990). Zoning in both phases is essentially limited to narrow ($\leq$50-100 µm) rim overgrowths, which likely record late-stage (likely syn-eruptive) growth during ascent and/or magma mixing. Hence, crystal-liquid thermobarometry pairing their core or interior compositions with the melt composition of the endmember basalt prior to mixing should provide robust estimates of magmatic storage conditions prior to the Halarauður event. The absence of groundmass glass in samples of the endmember basalt, which are pervasively devitrified, precludes a direct pairing of crystal and pre-mixing carrier melt compositions. However, because the Halarauður products are extremely crystal-poor ($\leq$2 modal% macrocrysts), the endmember basalt whole-rock composition closely approximates the composition of the carrier melt prior to mixing, and we use it here for thermobarometry.

The plagioclase-liquid thermometers of Putirka (2008; equation 24a) and Waters and Lange (2015) were applied to type II plagioclase cores paired with the basaltic endmember whole-rock composition (sample KR-272) for a range of pressure and melt H_2O input estimates (P = 1-5 kbar, melt H_2O = 0.1-1 wt%, typical values for Icelandic tholeiites; Maclennan et al., 2001; Nichols et al., 2002; Neave et al., 2013; Neave and Putirka, 2017; Bali et al., 2018; Hartley et al., 2018). Results from both thermometers overlap within their respective calibration errors [standard errors of estimate (SEE) are ±36°C for the Putirka (2008) model and ±12°C for Waters and Lange (2015)]. Temperature estimates for the driest melts (0.1 wt% H_2O) cluster between ~1000-1050°C (Fig. 4.12a), mostly within error of the minimum 1050°C expected for equilibrium at the measured K_D values (Fig. 4.6d; Putirka, 2008). Temperatures calculated for higher melt H_2O inputs are systematically lower. At melt H_2O contents of 1 wt%, temperatures from the Waters and Lange (2015) model are between ~975-1000°C, too low for equilibrium at the measured K_D values, while
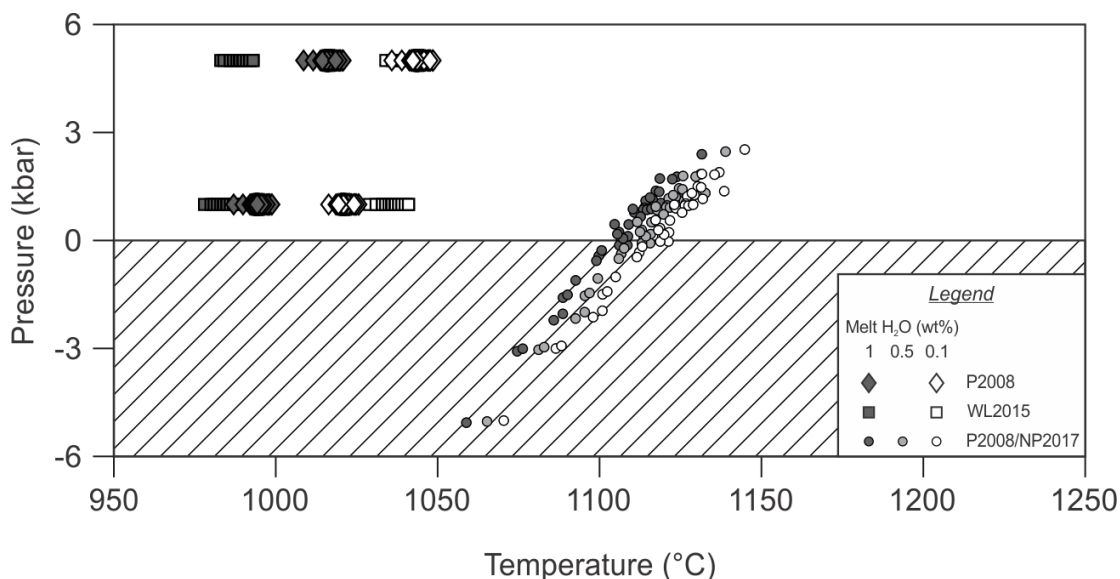
Figure 4.12. Results of geothermobarometry for type II plagioclase or augite paired with the most primitive basaltic whole-rock composition. P2008 = Putirka (2008) plagioclase-melt thermometer; WL2015 = Waters and Lange (2015) plagioclase-melt thermometer; P2008/NP2017 = Putirka (2008) clinopyroxene-melt thermometer and Neave and Putirka (2017) clinopyroxene-melt barometer, solved iteratively.

the Putirka (2008) model returns temperatures within error of the equilibrium criterion T >1050°C only at high pressures (Fig. 4.12).

The clinopyroxene-liquid barometer of Neave and Putirka (2017) and thermometer of Putirka (2008; equation 36) were applied to augite cores paired with the basaltic endmember whole-rock composition. These formulations require temperature and pressure as inputs, respectively, so were solved together iteratively following Neave and Putirka (2017) for melt H_2O estimates of 0.1-1 wt% (see above). Calculated temperatures for equilibrium pairs range between ~1060-1140 °C (±56°C SEE), but most cluster between ~1100-1140°C (Fig. 4.12), exceeding the maximum temperature estimates from plagioclase-melt thermometry. Median temperatures differ by <10°C across the range of H_2O inputs. Calculated pressures are ≤2.5 kbar (±1.5 kbar SEE) and correlate positively with temperature (Fig. 4.12). Pressure estimates are negative for temperatures

<~1100°C, consistent with the poor performance of this thermometer-barometer pairing at <1100°C noted by Neave and Putirka (2017). Discarding any P results for T <1100°C yields median pressure estimates of 0.9 kbar for all H_2O inputs.

The very low macrocryst content (≤2 modal%) of the erupted products implies that the Halarauður magmas were stored near their liquidus temperatures prior to their interaction. Hence, to further investigate P-T storage conditions of the endmember basalt and to address the discrepancies between mineral thermometry for plagioclase-melt and clinopyroxene-melt thermometry outlined above, we compare the observed mineral assemblages with the near-liquidus phase relations predicted by equilibrium crystallisation calculations using rhyolite-MELTS (a modified version of the MELTS calibration optimised for silicic magmas but also applicable to basalts; Gualda et al., 2012). Isobaric cooling calculations were performed using the most primitive basaltic whole-rock composition with 0.1, 0.5 and 1 wt% H_2O at pressures of 0.5, 1, 3 and 5 kbar (see above). Oxygen fugacity was fixed at one log unit below the fayalite-magnetite-quartz buffer (FMQ-1), a typical value for Krafla tholeiites (Nicholson, 1990). The phase relations predicted by rhyolite-MELTS are shown in Fig. 4.13. Liquidus temperatures are between ~1100–1230°C over the full P-X_{H_2O} space. Pigeonite is the liquidus phase in all models at P >~2 kbar, and in some cases down to 0.5 kbar, but was not observed in Halarauður products except as microcrysts and narrow overgrowth rims on some macrocrysts. Augite occurs on or within 20°C of the liquidus for intermediate to high melt H_2O contents, and 30-50°C below in the driest melt. Compositions of the first-crystallising augites ($En_{41-46}Fs_{17-22}Wo_{32-39}$) predicted by rhyolite-MELTS over the full P-X_{H_2O} range modelled are in excellent agreement with observed augite core compositions ($En_{42-49}Fs_{11-22}Wo_{33-41}$). Plagioclase appears on or within ~10°C of the liquidus for low to intermediate melt H_2O contents (0.1-0.5 wt%) at P <2-3 kbar, shifting further below liquidus with increasing
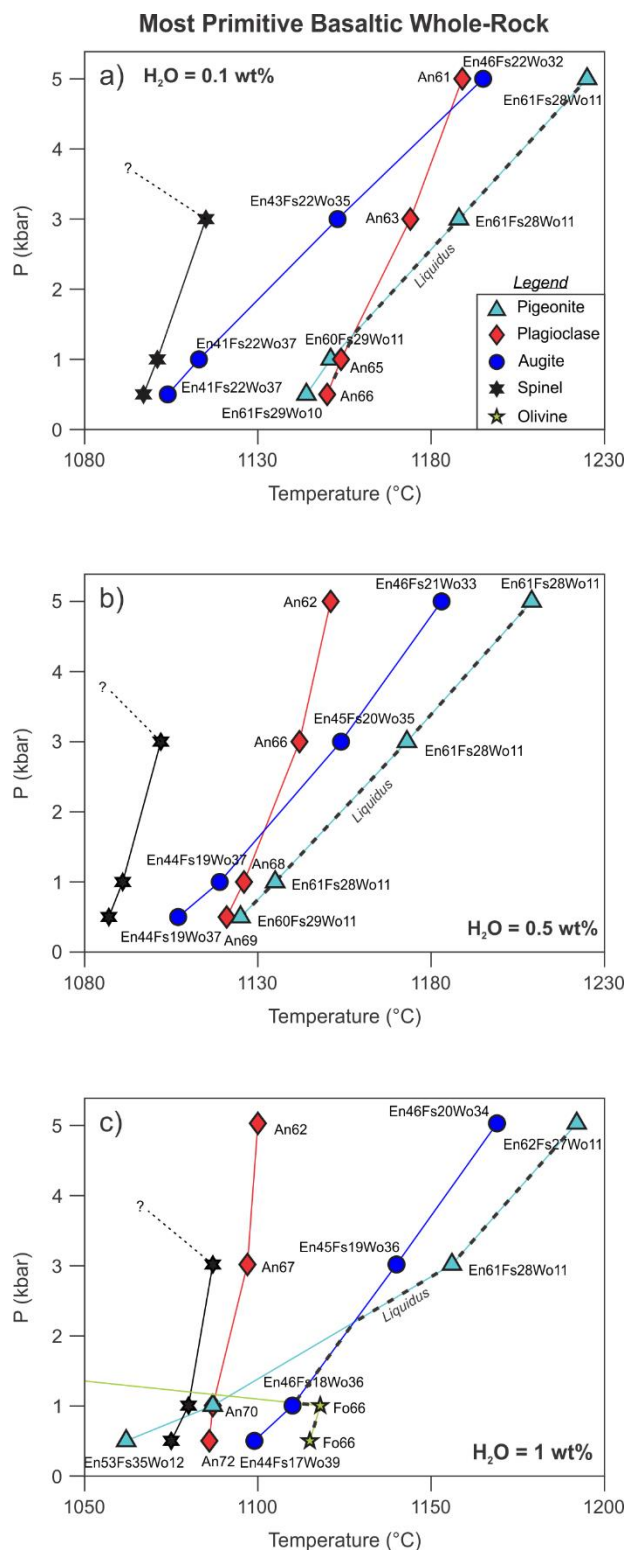
Figure 4.13. Phase diagrams for the most primitive basaltic whole-rock composition determined from rhyolite-MELTS equilibrium crystallisation calculations (Gualda et al., 2012) for melt H_2O contents of 0.1, 0.5 and 1 wt% (labelled on diagrams). Mineral-in curves are labelled with the first-crystallising compositions of their respective phase.

pressure or H_2O. Predicted compositions of the first-crystallising plagioclases (An_{61-72}) largely overlap with type II cores (An_{60-76}), with best agreement at melt H_2O contents ≥ 0.5 wt% and P ≤ 1-1.5 kbar. Olivine (Fo_{66}) is the liquidus phase for the wettest melt at P ≤ 1 kbar, but is otherwise absent. Spinel occurs at temperatures $\geq 30°C$ below liquidus, but was not observed in the Halarauður products. Crystallisation of plagioclase and/or augite in the absence of pigeonite and spinel is only predicted at pressures $<\sim 1.5$ kbar (equivalent to a depth of ~ 6.1 km, assuming an average crustal density of 2490 kg m^{-3}; Árnason et al., 2009) and at moderate to high melt H_2O contents (>0.5 but <1 wt%). This pressure constraint is in good agreement with the median pressure estimate of 0.9 kbar (depth of ~ 3.7 km) from augite-melt thermobarometry, suggesting storage at depths overlapping with the present-day shallow basaltic storage zone that extends from ~ 3 to ~ 7 km depth (Einarsson, 1978; Kelley and Barton, 2008, and references therein) and fed eruptions of compositionally similar evolved quartz tholeiites during the historic Mývatn and Krafla Fires events (Grönvold and Mäkipää, 1978; Grönvold, 1984, 2006). Temperatures of 1100-1150°C are also consistent with augite-melt thermometry (Fig. 4.12). We infer that the low temperatures predicted by plagioclase-melt thermometry, which are well below liquidus (cf. Fig. 4.13), are in error, possibly a consequence of pairing mineral compositions with the whole-rock composition rather than a true magmatic liquid.

The low macrocryst content of all Halarauður products imply that the endmember magmas were stored as crystal-poor bodies prior to their interaction. Large, homogenous, melt-dominant bodies of evolved basalt are typical of large-volume lava-forming basaltic eruptions in Iceland, such as events at Laki in 1783-1784 and Bárðarbunga-Holuhraun in 2014-2015 (see Halldórsson et al., 2018). These magmas are thought to experience a complex early magmatic history involving extensive fractional crystallisation, crustal assimilation and mixing of discrete basaltic magma

batches at a range of crustal levels (Bindeman et al., 2008; Neave et al., 2013), before homogenisation in a large, well-mixed, melt-dominant reservoir prior to eruption (Edmonds et al., 2016; Halldórsson et al., 2018). The evolved composition of the Halarauður basaltic endmember implies a similar protracted evolution from parental mantle-derived basalts, which likely involved fractional crystallisation, assimilation and mixing processes at various depths before assembly of the final erupted magma body. However, the scarcity of intra-crystal zoning in type II plagioclase and co-existing augite macrocrysts, as well as equilibrium between their cores and the endmember whole-rock composition, implies that these crystal populations experienced storage and growth under relatively stable magmatic conditions (pressure, temperature and melt composition) in the evolved endmember basaltic magma prior to eruption. At growth rates typical of plagioclase in shallow basaltic systems (10^{-12} – 10^{-13} m s^{-1}; Cashman, 1993), the largest type II crystals, ~1 mm in size, could grow in approximately 30-300 years. Hence, we infer that the large melt-dominant body of evolved endmember basalt was stored in its final, well-mixed state for at least decades to centuries in the upper crust prior to the Halarauður event.

4.6.2.1.1. Basal Cumulate Mush

The olivine, orthopyroxene and primitive augite (Mg# >75) that occur in glomerocrysts in the late-vented deposits (unit H3) are too magnesian for equilibrium with the endmember basalt (Fig. 4.8d-f). Although some of these compositions are in or close to equilibrium with the primitive basalt associated with type I plagioclase, the absence of olivine and orthopyroxene in H1 deposits, where type I plagioclase is most abundant, implies that they have a different origin. The plagioclase crystals in the H3 glomerocrysts were not analysed by EPMA, but texturally resemble the type II

crystals associated with the endmember basalt and lack the abundant melt inclusions characteristic of type I.

Aggregates of crystals too primitive to be in equilibrium with their carrier melt are common in Icelandic basalts, and generally interpreted as fragments of disaggregated cumulate mush (e.g., Hansen and Grönvold, 2000; Neave et al., 2014, 2017; Hartley et al, 2016). Textures of the H3 glomerocrysts are consistent with such an origin. The crystals comprising the glomerocrysts commonly impinge at high angles, typical of highly porous, plagioclase-dominated mushes (Holness et al., 2005, 2012), and void spaces between crystals, inferred to have been originally occupied by interstitial melt, are common. The parallel alignment of crystals expected for aggregates formed by synneusis is absent (Vance, 1969). Although most minerals in the aggregates are too primitive for equilibrium with their carrier melt, most are close to equilibrium and have compositions typical of relatively evolved basalts. We thus interpret the H3 glomerocrysts as fragments of antecrystic cumulate mush from the basal region of the endmember basalt magma body, which were disaggregated and entrained into the more evolved overlying melt, probably during the eruption (cf. Hartley et al., 2016; Neave et al., 2017) as the lower regions of the chamber were disturbed by decompression and tapping of the overlying melt-rich body. The presence of olivine and orthopyroxene only in the basal cumulate zone likely reflects their negative buoyancy in basaltic melt, which allowed them to settle to the base of the chamber while less dense plagioclase (± small adhering augites) remained suspended (cf. Neave et al., 2014). The narrow Fe-rich rims on olivines likely formed after these crystals were entrained into the more evolved overlying melt-dominant body. Narrow Fe-rich rims on olivines from the Laki eruption were interpreted by Hartley et al. (2016) in a similar way, and constrained by diffusion modeling to have formed over a period of ~6-10 days.

4.6.2.2. Storage and Origin of the Endmember Rhyolite

Type III plagioclase is the only macrocryst population in the Halarauður products that has compositions appropriate for equilibrium with rhyolitic melt. Cores and most rims are in or near equilibrium with the most evolved Halarauður whole-rock composition, and most rims (those with <53 mol% An) are in equilibrium with the most evolved matrix glass. We thus infer that type III plagioclase is phenocrystic to the Halarauður rhyolite. These crystals are rare in all units, however, and we infer that the rhyolite was nearly aphyric and stored at very close to liquidus temperature. Rhyolite-MELTS predicts liquidus temperatures of ~880-930°C for pressure inputs of 0.5-2 kbar, melt H_2O of 2-4 wt%, and fO_2 at the FMQ buffer (typical values for Krafla rhyolites; see Chapter 3).

We do not have an independent constraint on the storage pressure of the Halarauður rhyolite due to an absence of phases suitable for geobarometry. However, venting of the most silicic compositions in the first eruptive phase, followed by a shift towards more mafic compositions in later phases, implies that the rhyolite body was stored above the endmember basalt and tapped first. Rhyolitic magmas at Krafla are thought to form by partial melting or assimilation of low $\delta^{18}O$ hydrothermally altered crust (plus some degree of fractional crystallisation; see Chapter 3) around the margins of upper-crustal basaltic magma bodies (Jónasson, 1994; Pope et al., 2013). Whole-rock $\delta^{18}O$ values have not been measured for the Halarauður rhyolite, but similar trace element systematics and parallel REE patterns among the Halarauður and younger Krafla rhyolites (see Chapter 3) imply that all were generated by a common process. We thus suggest that the Halarauður rhyolite likely formed by assimilation or crustal melting above the large shallow mafic system, and was stored in the uppermost crust (i.e., at P less than the minimum ~1.5 kbar determined for the endmember basalt; see above). Prior to the Halarauður eruption, close proximity

to the large volume of underlying endmember basalt likely maintained high (near-liquidus) magmatic temperatures in the rhyolite, consistent with the scarcity of rhyolite-derived crystals in the Halarauður products. A similar configuration was recently identified at Krafla, where an active crystal-poor rhyolite body at ~850-920°C was intercepted during a geothermal drilling project at ~2.1 km depth (Elders et al., 2011; Zierenberg et al., 2013). Similarly, a separate body of rhyolite was stored above a large basaltic body at ~1 kbar at the nearby Askja system prior to its 1875 C.E. Plinian eruption (Kuritani et al., 2011).

4.6.2.3. Origin and Ascent of the Primitive Basalt

Highly calcic plagioclases (An >85 mol%) similar to type I crystals are relatively common in Icelandic rift zone basalts, often as cores that are surrounded by more sodic overgrowths and not in equilibrium with their carrier melt (e.g., Halldórsson et al., 2008, 2018). These primitive cores are usually interpreted to reflect entrainment of primitive mid- or lower-crustal crystal mush into a more evolved basaltic liquid (e.g., Hansen and Grönvold, 2000; Neave et al., 2014, 2017). However, type I Halarauður plagioclase crystals are in or near equilibrium with their adhering primitive basaltic glass selvages, providing direct evidence for interaction of a primitive melt and its native phenocrysts with the shallow Halarauður system.

Like the type II grains native to the endmember basalt, the more primitive type I crystals show little or no intra-crystal zoning except at their outermost rims, reflecting protracted growth under stable magmatic conditions. We thus suggest that the small body of primitive basalt involved in the Halarauður event was likely stored at stable P-T conditions while crystallising the type I grains, then was mobilised and ascended to higher crustal levels immediately prior to or during the

first eruptive phase. Rhyolite-MELTS calculations using the average basaltic glass composition and the same P, H_2O and fO_2 inputs as for the endmember basalt offer little insight on these storage conditions, as predicted compositions for the first-crystallising plagioclase are more sodic (An_{73-83}) than all but the most evolved type I grains across the full range of model inputs. However, similar primitive melts and calcic plagioclase are generally thought to derive from the mid or lower crust in the rift zones (e.g., Hansen and Grönvold, 2000), and we assume a similar origin.

Type I crystals are most abundant in H1 deposits and very scarce in later-vented units, implying that interactions between the primitive basalt and shallow system mainly occurred in its upper, more silicic levels. This suggests that at least some of the primitive basalt was able to bypass the lower basaltic parts of the Halarauður magma system rather than being trapped by the large body of endmember basalt, perhaps propagating around the edge of the shallow basaltic magma chamber, or laterally along the fissure swarm at shallow depths. Co-eruption of compositionally distinct basaltic magmas was also observed during the 1975-1984 Krafla Fires episode, where evolved quartz tholeiite similar to the endmember basalt was erupted above the shallow magma storage zone inside the caldera, while more primitive olivine tholeiite, inferred to derive from a deeper source, was vented along fissures north of the caldera (Grönvold and Mäkipää, 1978; Grönvold, 2006). Ascent and eruption of distinct basaltic magmas derived from separate sources also occurred along the nearby Askja fissure swarm during its 1874-1876 C.E. rifting episode (Hartley and Thordarson, 2013). Basaltic upwelling beneath the Askja central volcano ultimately triggered the explosive eruption of ~0.3 km^3 (DRE) of rhyolite in 1875 (e.g., Sparks et al., 1981; Carey et al., 2010). Mixed pumices from this event host streaks of basaltic glass with compositions ranging from ~4.0-7.0 wt% MgO (Sigurdsson and Sparks, 1981). The least evolved of these glasses are considerably more primitive than the evolved basalts vented elsewhere along the fissure swarm

during this episode, and in subsequent eruptions within the caldera, which are inferred to derive from a large shallow (~3 km depth) magma chamber beneath the central volcano (Kuritani et al., 2011; Hartley and Thordarson, 2013). Kuritani et al. (2011) thus proposed that the primitive glasses in the 1875 pumices reflect ascent of a relatively primitive basalt from depth, which bypassed the shallow chamber of evolved basalt, ultimately intercepting and triggering eruption of a separate overlying rhyolite body.

4.6.3. Sequence of Magmatic Events in the Halarauður System

The lines of evidence outlined above imply a complex history for the Halarauður magma system, involving assembly and storage of separate large crystal-poor basaltic and rhyolitic magma bodies in the shallow crust, followed by rapid destabilisation and mixing of these bodies and ascent of more primitive basalt from depth. Here we summarise the inferred sequence of events, linking our petrologic data and the field constraints of Rooyakkers et al. (2020; Chapter 2) to provide a comprehensive overview of the magmatic events occurring in the build up to, and during, Krafla's largest eruption.

The early history of the Halarauður endmember basalt is poorly constrained, but, like other large-volume evolved Icelandic basalts, likely involved protracted fractionation, crustal assimilation and mixing of distinct magma batches at a range of crustal levels before assembly of the final erupted magma body in the shallow crust. Equilibrium between type II plagioclase and most augite cores and the endmember basalt whole-rock composition implies that these crystals grew after assembly of the final, well-mixed magma body, which was stored in its crystal-poor state for at least several decades to centuries prior to eruption. During this time an olivine- and

203

orthopyroxene-bearing cumulate mush layer developed by crystal settling near the base of the chamber as the overlying melt underwent minor cooling and crystallisation (Fig. 4.14).

Like other Krafla rhyolites, the endmember rhyolite probably formed above the shallow mafic system by crustal melting and some degree of subsequent crystal fractionation over several millennia (Chapter 3; Hampton et al., in prep), but the details of its assembly are poorly resolved due to the scarcity of rhyolite-derived crystals in the Halarauður products. We suggest that close proximity to the large underlying body of endmember basalt maintained near-liquidus temperatures in the rhyolite in the later stages of its evolution, during which only minor crystallisation of type III plagioclase occurred. Evidence for interactions with intruding basalt during crystal growth, such as prominent resorption surfaces with reverse-zoned Fe-rich overgrowths, is not observed in type III plagioclase, implying that the endmember magma bodies existed separately with little to no interaction during storage and crystal growth in the upper crust (Fig. 4.14a).

This stable configuration was disrupted shortly before eruption. Mafic enclaves, filaments of hybrid melt, and crystals derived from both the primitive and endmember basalts (types I and II plagioclase, respectively) occur in the lowermost deposits of the first eruptive phase (unit H1 of Rooyakkers et al., 2020; Chapter 2), implying that interactions between the rhyolite and both basalts began before vents opened. Mixing timescales, however, were short: less than two months but possibly as short as a few tens of hours for the endmember basalt, and at most several hours for the primitive basalt. We thus infer that the eruption was triggered by a major destabilisation of the magmatic system, during which two distinct basaltic magmas ascended and intercepted the shallow rhyolite body. As in the recent Krafla Fires volcanotectonic episode, the ascent of multiple basaltic magmas from depth likely reflects a major rifting event in the Krafla system, in which
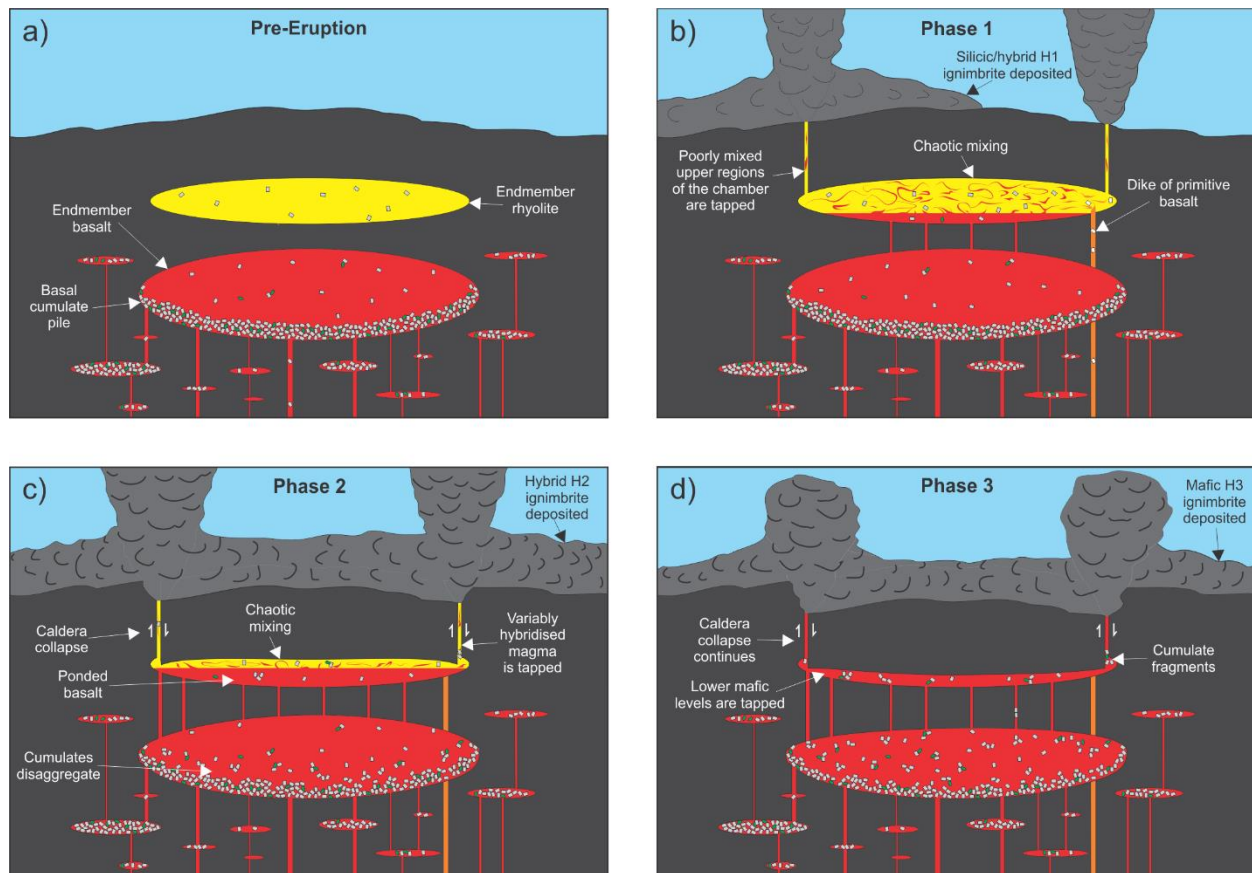
Figure 4.14. Schematic diagrams showing key magmatic events in the Halarauður eruption. a) Separate, crystal-poor bodies of the endmember basalt and rhyolite are assembled and stored in the shallow crust. The endmember basalt forms a basal cumulate layer by crystal settling. b) The stable configuration in a) is disrupted by rifting, and endmember basalt is injected into the overlying rhyolite less than two months before eruption. Chaotic mixing occurs between the two magmas in the upper regions of the magma body. A small volume of the more primitive basalt is injected into the rhyolite body or shallow conduit and mixes with the rhyolite. Initial vents open at most a few hours after injection of primitive basalt. c) Chaotic mixing continues as the eruption intensifies in phase 2 and large-scale caldera collapse occurs. Variably hybridised magma is tapped from the upper levels of the chamber, while the basal cumulate mush in the underlying basaltic chamber disaggregates. Continued ascent of endmember basalt from the lower chamber continues, feeding a layer of ponded basalt at the base of the upper chamber. d) Dense mafic magma from the lower levels of the upper chamber hosting disaggregated cumulate fragments is tapped as the sinking roof block nears the chamber floor.

dikes were injected into the fissure swarm from both the shallow endmember basalt reservoir and

a deeper body of the primitive basalt.

Injection of the endmember basalt into the overlying rhyolite triggered chaotic mixing of the two magmas. During the early stages of interaction, a gravitationally stable layer of dense endmember basalt likely ponded beneath the less dense rhyolite body (e.g., Wiebe, 1994). Thermal equilibration of the upper parts of the layer against the cooler rhyolite above caused rapid crystallisation and volatile exsolution in the basalt, lowering its density and eventually causing overturn of the upper parts of the ponded layer (Huppert et al., 1982) and chaotic mixing with the rhyolite (Fig. 4.14b). Shortly after these interactions began, a small dike of the primitive basalt carrying type I plagioclase ascending from deeper levels intercepted the rhyolite body or conduit (Fig. 4.14b). Initial vent opening occurred around a developing ring fracture within minutes to at most several hours of injection of the primitive basalt, followed by rapid column collapse and emplacement of H1 ignimbrite deposits (see Rooyakkers et al., 2020; Chapter 2).

The onset of major caldera collapse followed soon after initial vent opening (Rooyakkers et al., 2020; Chapter 2), with early collapse favoured by the shallow depth of the magma body and low chamber roof aspect ratio (Roche and Druitt, 2001). Chaotic mixing of subequal volumes of the endmember basalt and rhyolite continued in this phase, likely enhanced by stirring induced by subsidence of the caldera roof block (Kennedy et al., 2008), as variably hybridised magma from the upper levels of the chamber were tapped and erupted from ring fault vents to form the compositionally heterogeneous lower H2 ignimbrite deposits (Rooyakkers et al., 2020; Chapter 2) (Fig. 4.14c). As the magmatic system was decompressed and magma withdrawn, basal cumulate mush in the lower chamber disaggregated, and mush fragments were transported into the upper chamber during continued ascent of the endmember basalt, collecting in a dense ponded layer of basalt at the base of the upper chamber. Relatively homogenous hybrid andesitic magma, likely

206

formed in a well-mixed convective layer above the ponded basalt (cf. Blake et al., 1992; Plail et al., 2018), was tapped during the later stages of phase 2 to form the upper H2 deposits.

The relatively homogeneous mafic compositions of late-erupted products (unit H3), which transition smoothly upward from basaltic andesite to basalt, reflect tapping of the dense basal levels of the upper chamber during the final stages of caldera collapse. All silicic magma in the upper chamber had been completely depleted in the final eruptive stage, as pure endmember basalt containing disaggregated mush fragments was squeezed through the ring fault vent system (see Rooyakkers et al., 2020; Chapter 2) and erupted to form the homogeneous basaltic upper H3 deposits (Fig. 4.14d).

4.7. CONCLUSIONS

Deposits of the Halarauður ignimbrite eruption provide evidence for complex but short-lived interactions between basaltic and rhyolitic magmas during a major destabilisation of the Krafla magmatic system. We conclude the following:

1. Large, separate, crystal-poor magma bodies of rhyolite and evolved basalt developed in close proximity in the upper crust beneath Krafla, and co-existed without interaction for at least several decades to centuries.

2. The stable shallow magmatic system was disrupted very shortly prior to eruption, when the evolved basalt ascended and intercepted the overlying rhyolite body. Mixing between these magmas occurred over less than two months, and possibly as little as a few tens of hours, before vents opened. Interactions between the rhyolite and small volumes of a second, more

primitive basaltic magma occurred over similar or shorter timescales, at most ~15 hours. Crystals derived from this basalt with adhering glass selvages free of quench crystals had residence times in the rhyolite of less than one hour. These short mixing timescales highlight the rapid pace at which magmatic systems can move from stability towards catastrophic eruption. Large silicic magma bodies in the shallow Icelandic crust may be mobilised over similar short timescales, and a rapid transition from quiescence to eruption should be anticipated if such bodies are detected.

3. Ascent of multiple basaltic magmas from distinct storage zones in the Halarauður eruption is similar to events in the recent volcanotectonic episodes at Krafla (1975-1984) and in the nearby Askja system (1874-1876), suggesting that triggering of the Halarauður eruption was probably linked with onset of a similar rifting event. The interplay between volcanism and tectonics that has characterised recent activity at Krafla has likely occurred throughout much or all of the system's lifespan, and is associated with large explosive mixed-magma eruptions as well as smaller effusive events.

5. Summary and Conclusions

The central purpose of this thesis is to expand understanding of rhyolitic and mixed rhyolitic-basaltic magmatism and volcanism at Krafla. Here we summarise the major findings of this work and their implications for understanding the present state of the silicic system at Krafla and hazards associated with rhyolitic eruptions in the Icelandic rift zones. We conclude by considering areas where further work is needed and offer some suggestions for further research on topics explored in this thesis.

5.1. SUMMARY AND IMPLICATIONS OF KEY FINDINGS

5.1.1. Size, Style and Dynamics of the Halarauður Eruption and Links with Caldera Collapse

The new field observations and interpretations of deposits of the ca. 110 ka Halarauður eruption presented in Chapter 2 provide insights to an extreme scenario of explosive Icelandic volcanism. By reconstructing the original distribution of the outflow deposits prior to glaciation for a plausible range of dispersal scenarios and erosion rates, we proposed a total erupted magma volume of 7 ± 6 km^3 for the Halarauður event. The large uncertainty in this value and poor preservation of the deposits highlight the challenges of reconstructing eruption histories and magnitude-frequency relationships for young ignimbrite eruptions in Iceland due to the erosive effects of Quaternary glaciations. Major ignimbrite-forming eruptions are thus likely to be much more common in Iceland than the onshore geological record suggests, and the hazards associated with such events deserve greater scientific attention.

Dynamics of the Halarauður event were strongly influenced by early caldera collapse, which was favoured by shallow storage of the magma bodies. Early formation of a ring fault conduit system and rapid onset of caldera collapse during initial explosive venting of silicic magma had a runaway effect, with variably degassed and hybridised magma from deeper levels subsequently driven into the conduit system by pressure exerted by the subsiding chamber roof. Unusual lithofacies characteristics of the deposits, including proximal spatter agglomerate facies, more distal spatter-bearing ignimbrite, and welding of basaltic ignimbrite, reflect the effect of this process of magma "squeeze out" on fragmentation styles and effusion rates around the ring fault vent system. Co-eruption of explosive collapsing plumes and weak spatter fountains throughout much of the event reflects variable ascent rates and outgassing through the variably dilated caldera fault system, while late-stage explosive venting of basalt and welding of basaltic ignimbrite reflects the uncharacteristically high effusion rates achieved as gas-poor basalt from deep levels was forced through the mature and open conduit system in the final stages of caldera collapse. The devasting link between explosive venting of shallow silicic magma, early caldera collapse, and unusually vigorous and explosive venting of large volumes of basaltic magma exemplified by the Halarauður eruption is uncommon, reflecting a possible extreme eruption scenario in an Icelandic rift setting where large shallow rhyolitic and basaltic magma bodies may be stored in close proximity at shallow depths.

5.1.2. Pre- and Syn-Eruptive Processes in the Halarauður Magmatic System

Detailed petrologic studies of the Halarauður products, presented in Chapter 4 and tied to the stratigraphic framework of Chapter 2, provide key insights on magmatic processes in the build-up to and during the Halarauður eruption. Whole-rock data imply venting of sub-equal volumes of

crystal-poor high-silica rhyolite and evolved basalt. Crystal chemistry, geobarometry and MELTS modeling imply that both magmas were stored as large, separate, well-mixed crystal-poor magma bodies in the upper crust (<4-6 km depth) for at least decades to centuries prior to eruption, and then mixed over timescales of at most two months and possibly as little as several tens of hours before venting. Small volumes of a second, more primitive basalt, evidenced by a highly calcic plagioclase population with primitive glass selvages, interacted with upper parts of the magmatic system over <15 hours. The eruption thus reflects a rapid destabilisation of the magmatic system, likely triggered by crustal rifting, after assembly and storage of large crystal-poor magma bodies in the shallow crust. A rapid transition from protracted storage to eruption should be anticipated if similarly large melt-dominant magma bodies are geophysically detected in the shallow crust of the Icelandic rift zones.

5.1.3. Generation and Assembly of Krafla Rhyolites

The crystal-chemical and melt inclusion data presented in Chapter 3 predominantly record crystal growth from evolved melts, and very few crystals are in equilibrium with basalt. Some crystals, however, are not in equilibrium with high-silica rhyolite. These grains, interpreted here as antecrysts derived from less evolved but co-genetic silicic magmas, provide evidence for crystal fractionation in the generation of Krafla rhyolites in addition to crustal melting or assimilation processes. In agreement with the presence of these antecrysts, experimental literature on partial melting of hydrothermally altered basalts and our trace element modeling both imply that generation of eruptible volumes of high-silica rhyolite by a pure partial melting process alone is unlikely. Instead, trace element models imply that assimilation fractional crystallization (AFC) from basaltic parental melts plays a central role in producing Krafla rhyolites, consistent with the

presence of occasional antecrysts and evidence for cooling and differentiation in mineral zoning patterns.

Although rhyolitic eruptions at Krafla have varied markedly in size and style, similar trace element systematics and parallel REE patterns among the Halarauður rhyolite and all younger units imply that petrogenetic processes have been similar throughout much of the system's history. There is, however, some evidence for subtle differences in the generation and sequestration of rhyolites that fed small versus large eruptions. Similar highly incompatible trace element ratios among the larger-volume units (Halarauður rhyolite and the extra-caldera ridges) imply compositionally similar sources for these magmas, likely reflecting melting and magma assembly across a large source area. In contrast, ratios for smaller-volume rhyolites (the oldest rhyolite, Hrafntinnuhryggur, Víti) are distinct from the larger units and one another, likely reflecting local heterogeneities in parental melt and/or crustal assimilant compositions sampled over smaller source areas. A second difference is in the diverse mineral compositions and abundance of internal resorption surfaces in crystals from the Víti rhyolite. Masotta et al. (2018) recently proposed that the IDDP-1 rhyolite derives from remelting of a previously solidified felsite intrusion, and we suggest that the above features of the Víti crystals reflect mixing of small silicic magma batches derived from similar remelting and recycling of compositionally diverse sub-solidus felsite bodies. Such a process is also consistent with the presence of partially melted felsite xenoliths among the Víti eruption products (Sigurdsson, 1968). Internal resorption surfaces are less abundant in crystals from the older and larger-volume rhyolites and these crystals show less compositional diversity, consistent with predominantly closed-system storage and differentiation of these rhyolites. The smaller volumes of recent rhyolites favour rapid freezing and possible later thermal rejuvenation

by similar silicic magma ascending from depth, and such processes are likely to be involved in assembling eruptible rhyolite bodies in the near future at Krafla.

5.1.4. Interactions with Mafic Magmas

Mineral compositions and zoning patterns in Krafla rhyolites discussed in Chapter 3 provide very little evidence for mafic recharge events during magma storage. In other words, despite their proximity to shallow basaltic magma bodies, Krafla rhyolites are assembled and stored largely in isolation from coeval basaltic magmas, and encounters between the two magma types generally occur only very shortly prior to eruption, if at all. Where mafic and rhyolitic magmas do meet, however, pre-eruptive mixing timescales may be extremely short, and in the case of the Víti event were too short for crystals to record. Products of the two most recent eruptions involving rhyolite at Krafla (the 1724 C.E. Víti pumice and ca. 9000 B.P. Hveragil tephra) show direct textural evidence for interactions with basalt, implying an important triggering role for basalt in recent small-volume events. We suggest that similar explosive events, rapidly triggered by intersection of ascending mafic dikes with shallow rhyolite bodies, are the most likely hazard associated with rhyolitic magmatism in the near future at Krafla and should be anticipated during future unrest.

5.1.5. Links Between the Active Molten Rhyolite Bodies and Previously Erupted Rhyolites

Silicic melts sampled from the KJ-39 well in 2008 show considerable compositional diversity and bear little resemblance to any of the erupted rhyolites at Krafla or elsewhere in Iceland. In agreement with Mortensen et al. (2010), we suggest that this well did not encounter a melt-dominant magma body, but rather sampled small and heterogeneous (likely centimetre to

decimetre scale) pockets and veins of partial melt in wallrock around the margins of an active intrusion. The possibility that these melts reflect the incipient stages of rhyolite generation and could in future be extracted from their source zone, homogenised, and fractionated in a manner similar to the two-stage process suggested above to produce a magma resembling the erupted rhyolites warrants consideration.

By contrast, the compositionally homogeneous magma sampled from the IDDP-1 well shows close similarity with previously erupted Krafla rhyolites, and is essentially petrologically indistinguishable from the 1724 C.E. Víti rhyolite. Given this similarity, as well as the spatial proximity of the IDPP-1 well to the Víti vent area, we suggest that the IDDP-1 well either sampled the same magma body that was tapped in the Víti event, or a related body derived from remelting of the same felsite intrusion (cf. Masotta et al., 2018). Two questions immediately arise: 1) If the former scenario is correct, why did the IDDP-1 rhyolite not erupt during the recent Krafla Fires activity? 2) If the latter scenario is correct, how long has the magma body been in place, and what was the heat source that mobilised it? Distinguishing between these scenarios is difficult at present, but we speculate that possible basaltic intrusion in the IDDP-1/Víti area during the Krafla Fires may have provided heat to remobilise near- or sub-solidus rhyolite previously erupted from Víti. Further knowledge of the nature and dimensions of the IDDP-1 magma body derived from future drilling campaigns (Eichelberger et al., 2019), coupled with thermal models, should help to distinguish between the possible scenarios. Regardless of its ultimate origin, the explosive eruption of compositionally similar magma from Víti and evidence for extremely rapid basalt triggering of this event presented in Chapter 3 highlight the hazard associated with possible future eruption of the IDDP-1 rhyolite body, and the extremely short warning times that might be expected in such an event. At least until more is known about the size and state of the IDDP-1 rhyolite body, an

explosive eruption of this rhyolite should be considered a real and immediate hazard in the event of dike intrusion occurring in the central caldera region.

5.2. SUGGESTIONS FOR FUTURE RESEARCH

The findings of this thesis research raise a number of further questions regarding processes of rhyolitic and mixed rhyolitic-basaltic magmatism and volcanism at Krafla and elsewhere that warrant investigation. Some suggested topics for future research include the following:

1. Detailed field and petrologic studies of Icelandic ignimbrites. Poor preservation of the Halarauður deposits exemplifies the challenges of understanding the frequency, size and dynamics of Quaternary ignimbrites in Iceland, and much remains to be learned about these events. The relative abundance of ignimbrites in the Tertiary volcanic sequence, however, offers an opportunity for field and petrologic studies aimed at reconstructing the magmatic and volcanic processes associated with Iceland's largest explosive eruptions. To date these deposits have been studied only in outline, if at all, and there is much room for further work.

2. Phase equilibria studies of Icelandic rhyolites. The relatively Fe-rich and K-poor compositions typical of the rift zone rhyolites differ strongly from the calc-alkaline rhyolites more typical of most silicic systems. These calc-alkaline magmas commonly bear quartz, alkali-feldspar and/or hydrous phases, all of which are rare in Icelandic rhyolites. Reasons for these differences are not well-understood, but previous suggestions that the absence of hydrous phases reflects very low magmatic H_2O

215

contents are increasingly being debunked by volatile studies. The high Fe contents of the rift zone rhyolites means that phase equilibria are likely to be highly sensitive to fO_2, but its effect has not been well-constrained. To date, very little experimental work has been performed on Icelandic rhyolites, and there is ample room for experimental studies to better constrain the evolution and storage conditions of rhyolites at Krafla and elsewhere.

3. Petrologic studies of felsite and granophyre xenoliths. Texturally variable xenoliths of felsite and granophyre showing varying degrees of remelting were ejected in the Víti event, and also occur in the Halarauður deposits, and were sampled during this work. Petrologic studies of these xenoliths offer a contrasting perspective on silicic magmatism at Krafla that may yield valuable insights on magmatic processes. How chemically similar are these products to the erupted magmas? To what extent is remelting of felsite or granophyre involved in assembling eruptible rhyolite bodies at Krafla? Can low-degree partial melting of felsitic or granophyric wallrock influence the trace element compositions of rhyolite magmas during storage? How compositionally variable are near- or sub-solidus felsic intrusions adjacent to active rhyolitic magma bodies at Krafla? Studies of xenolith populations will allow these and other questions to be addressed.

4. Dating and/or modeling studies aimed at understanding the tempo of rhyolitic magmatism in Icelandic central volcanoes. This thesis and other work highlight marked variations in the tempo of rhyolitic magmatism at Krafla and other Icelandic systems through time, but the reasons for this variability are not yet understood. Perhaps

surprisingly, close chemical similarities among large- and small-volume Krafla rhyolites imply that petrogenetic processes are similar for large and small rhyolite bodies. Why is this the case, and what controls the rates of rhyolite generation? Is magma flux into the mafic system the dominant control, as we speculated in Chapter 3? Are other factors involved? Does glacial loading or unloading influence rates of rhyolite production? Why is the spike in mafic output at Krafla in the early postglacial period not reflected by a corresponding spike in silicic eruptions? Further detailed geochronology studies of rhyolitic magmatism in Icelandic systems and modeling studies aimed at investigating links between the thermal state of the crust, rates of shallow mafic intrusion and rates of rhyolite production will help to answer such questions.

6. References

Agustsdottir, T., Gudmundsson, M. T., and Einarsson, P., 2010, A gravity study of silicic domes in the Krafla area, N-Iceland: Jökull, v. 60, p. 135-148.

Allan, A. S. R., Wilson, C. J. N., Millet, M. A., and Wysoczanski, R. J., 2012, The invisible hand: Tectonic triggering and modulation of a rhyolitic supereruption: Geology, v. 40, p. 563-566.

Allan, A. S. R., Morgan, D. J., Wilson, C. J. N., and Millet, M. A., 2013, From mush to eruption in centuries: assembly of the super-sized Oruanui magma body: Contributions to Mineralogy and Petrology, v. 166, p. 143-164.

Allan, A. S. R., Barker, S. J., Millet, M.-A., Morgan, D. J., Rooyakkers, S. M., Schipper, C. I., and Wilson, C. J. N., 2017, A cascade of magmatic events during the assembly and eruption of a super-sized magma body: Contributions to Mineralogy and Petrology, v. 172, p. 49.

Allègre, C. J., and Minster, J. F., 1978, Quantitative models of trace element behavior in magmatic processes: Earth and Planetary Science Letters, v. 38, p. 1-25.

Allen, R. M., Nolet, G., Morgan, W. J., Vogfjörd, K., Bergsson, B. H., Erlendsson, P., Foulger, G. R., Jakobsdóttir, S., Julian, B. R., Pritchard, M., Ragnarsson, S., and Stefánsson, R., 1999, The thin hot plume beneath Iceland: Geophysical Journal International, v. 137, p. 51-63.

Allen, S. R., 2005, Complex spatter- and pumice-rich pyroclastic deposits from an andesitic caldera-forming eruption: the Siwi pyroclastic sequence, Tanna, Vanuatu: Bulletin of Volcanology, v. 67, p. 27-41.

Almeev, R. R., Bolte, T., Nash, B. P., Holtz, F., Erdmann, M., and Cathey, H. E., 2012, High-temperature, low-H_2O silicic magmas of the Yellowstone hotspot: an experimental study of rhyolite from the Bruneau–Jarbidge eruptive center, central Snake River Plain, USA: Journal of Petrology, v. 53, p. 1837-1866.

Ármannsson, H., Guðmundsson, Á., and Steingrímsson, B. S., 1987, Exploration and development of the Krafla geothermal area: Jökull, v. 37, p. 13-30.

Andersen, D. J., Lindsley, D. H., and Davidson, P. M., 1993, QUILF: A pascal program to assess equilibria among Fe-Mg-Mn-Ti oxides, pyroxenes, olivine, and quartz: Computers & Geosciences, v. 19, p. 1333-1350.

Andersen, N. L., Singer, B. S., Costa, F., Fournelle, J., Herrin, J. S., and Fabbro, G. N., 2018, Petrochronologic perspective on rhyolite volcano unrest at Laguna del Maule, Chile: Earth and Planetary Science Letters, v. 493, p. 57-70.

Ármannsson, H., Guðmundsson, Á., and Steingrímsson, B. S., 1987, Exploration and development of the Krafla geothermal area: Jökull, v. 37, p. 13-30.

Árnadóttir, T., Sigmundsson, F., and Delaney, P. T., 1998, Sources of crustal deformation associated with the Krafla, Iceland, eruption of September 1984: Geophysical Research Letters, v. 25, p. 1043-1046.

Árnason, K., 2020, New conceptual model for the magma-hydrothermal-tectonic system of Krafla, NE Iceland: Geosciences, v. 10, p. 34.

Árnason, K., Vilhjálmsson, A. M., and Björnsdóttir, T., 2009, A study of the Krafla volcano using gravity, micro earthquake and MT data: ÍSOR Report 2009/067, 14 p.

Astbury, R. L., Petrelli, M., Ubide, T., Stock, M. J., Arienzo, I., D'Antonio, M., and Perugini, D., 2018, Tracking plumbing system dynamics at the Campi Flegrei caldera, Italy: High-resolution trace element mapping of the Astroni crystal cargo: Lithos, v. 318, p. 464-477.

Austin, W. E. N., Wilson, L. J., and Hunt, J. B., 2004, The age and chronostratigraphical significance of North Atlantic Ash zone II: Journal of Quaternary Science, v. 19, p. 137-146.

Bali, E., Hartley, M. E., Halldórsson, S. A., Gudfinnsson, G. H., and Jakobsson, S., 2018, Melt inclusion constraints on volatile systematics and degassing history of the 2014–2015 Holuhraun eruption, Iceland: Contributions to Mineralogy and Petrology, v. 173, p. 9.

Bachmann, O., and Bergantz, G. W., 2004, On the origin of crystal-poor rhyolites: Extracted from batholithic crystal mushes: Journal of Petrology, v. 45, p. 1565-1582.

Bacon, C. R., 1986, Magmatic inclusions in silicic and intermediate volcanic rocks: Journal of Geophysical Research: Solid Earth, v. 91, p. 6091-6112.

Banik, T. J., Miller, C. F., Fisher, C. M., Coble, M. A., and Vervoort, J. D., 2018, Magmatic-tectonic control on the generation of silicic magmas in Iceland: Constraints from Hafnarfjall-Skarðsheiði volcano: Lithos, v. 318-319, p. 326-339.

Barker, S. J, Rotella, M. D., Wilson, C. J. N., Wright, I. C., and Wysoczanski, R. J., 2012, Contrasting pyroclast density spectra from subaerial and submarine silicic eruptions in the Kermadec arc: implications for eruptive processes and dredge sampling: Bulletin of Volcanology, v. 74, p. 1425-1443.

Barker, S. J., Wilson, C. J. N., Smith, E. G. C., Charlier, B. L. A., Wooden, J. L., Hiess, J., and Ireland, T. R., 2014, Post-supereruption magmatic reconstruction of Taupo volcano (New Zealand), as reflected in zircon ages and trace elements: Journal of Petrology, v. 55, p. 1511-1533.

Barker, S. J., Wilson, C. J. N., Allan, A. S. R., and Schipper, C. I., 2015, Fine-scale temporal recovery, reconstruction and evolution of a post-supereruption magmatic system: Taupo (New Zealand): Contributions to Mineralogy and Petrology, v. 170, p. 5.

Barker, S. J., Wilson, C. J. N., Morgan, D. J., and Rowland, J. V., 2016, Rapid priming, accumulation, and recharge of magma driving recent eruptions at a hyperactive caldera volcano: Geology, v. 44, p. 323-326.

Barsotti, S., Di Rienzo, D. I., Thordarson, T., Björnsson, B. B., and Karlsdóttir, S., 2018, Assessing impact to infrastructures due to tephra fallout from Öræfajökull volcano (Iceland) by using a scenario-based approach and a numerical model: Frontiers in Earth Science, v. 6, p. 196.

Bear, A. A., Cas, R. A. F., and Giordano, G., 2009, The implications of spatter, pumice and lithic clast rich proximal co-ignimbrite lag breccias on the dynamics of caldera forming eruptions: The 151 ka Sutri eruption, Vico Volcano, Central Italy: Journal of Volcanology and Geothermal Research, v. 181, p. 1-24.

Beard, J. S., and Lofgren, G. E., 1989, Effect of water on the composition of partial melts of greenstone and amphibolite: Science, v. 244, p. 195.

Beard, J. S., and Lofgren, G. E., 1991, Dehydration melting and water-saturated melting of basaltic and andesitic greenstones and amphibolites at 1, 3, and 6.9 kb: Journal of Petrology, v. 32, p. 365-401.

Behncke, B., 2009, Hazards from pyroclastic density currents at Mt Etna (Italy): Journal of Volcanology and Geothermal Research, v. 180, p. 148-160.

Bergþórsdóttir, I. A., 2018, The Role of Apatite in Hekla Magmas: Trace Element Partitioning Between Minerals and Melt [MS thesis]: Reykjavík, Iceland, University of Iceland, 113 p.

Bijwaard, H., and Spakman, W., 1999, Tomographic evidence for a narrow whole mantle plume below Iceland: Earth and Planetary Science Letters, v. 166, p. 121-126.

Bindeman, I., Gurenko, A., Sigmarsson, O., and Chaussidon, M., 2008, Oxygen isotope heterogeneity and disequilibria of olivine crystals in large volume Holocene basalts from Iceland: Evidence for magmatic digestion and erosion of Pleistocene hyaloclastites: Geochimica et Cosmochimica Acta, v. 72, p. 4397-4420.

Bindeman, I., Gurenko, A., Carley, T., Miller, C., Martin, E., and Sigmarsson, O., 2012, Silicic magma petrogenesis in Iceland by remelting of hydrothermally altered crust based on oxygen isotope diversity and disequilibria between zircon and magma with implications for MORB: Terra Nova, v. 24, p. 227-232.

Björnsson, A., 1985, Dynamics of crustal rifting in NE Iceland: Journal of Geophysical Research: Solid Earth, v. 90, p. 10151-10162.

Björnsson, A., Sæmundsson, K., Einarsson, P., Tryggvason, E., and Grönvold, K., 1977, Current rifting episode in north Iceland: Nature, v. 266, p. 318-323.

Björnsson, A., Johnsen, G., Sigurdsson, S., Thorbergsson, G., and Tryggvason, E., 1979, Rifting of the plate boundary in north Iceland 1975–1978: Journal of Geophysical Research: Solid Earth, v. 84, p. 3029-3038.

Blake, D. H., 1969, Welded tuffs and the Maelifell caldera, Alftafjordur volcano, south-eastern Iceland: Geological Magazine, v. 106, p. 531-541.

Blake, D. H., Elwell, R. W. D., Gibson, I. L., Skelhorn, R. R., and Walker, G. P. L., 1965, Some relationships resulting from the intimate association of acid and basic magmas: Quarterly Journal of the Geological Society of London, v. 121, p. 31-49.

Blake, S., 1984, Magma mixing and hybridization processes at the alkalic, silicic, Torfajökull Central volcano triggered by tholeiitic Veidivötn fissuring, South Iceland: Journal of Volcanology and Geothermal Research, v. 22, p. 1-31.

Blake, S., Wilson, C. J. N., Smith, I. E. M., and Walker, G. P. L., 1992, Petrology and dynamics of the Waimihia mixed magma eruption, Taupo volcano, New Zealand: Journal of the Geological Society, v. 149, p. 193-207.

Blundy, J., and Cashman, K., 2008, Petrologic reconstruction of magmatic system variables and processes: Rev Mineral Geochem, v. 69, p. 179-239.

Blundy, J. D., and Wood, B. J., 1991, Crystal-chemical controls on the partitioning of Sr and Ba between plagioclase feldspar, silicate melts, and hydrothermal solutions: Geochimica et Cosmochimica Acta, v. 55, p. 193-209.

Blundy, J., and Wood, B., 1994, Prediction of crystal–melt partition coefficients from elastic moduli: Nature, v. 372, p. 452-454.

Boehnke, P., Watson, E. B., Trail, D., Harrison, T. M., and Schmitt, A. K., 2013, Zircon saturation revisited: Chemical Geology, v. 351, p. 324-334.

Bolte, T., Holtz, F., Almeev, R., and Nash, B., 2015, The Blacktail Creek Tuff: an analytical and experimental study of rhyolites from the Heise volcanic field, Yellowstone hotspot system: Contributions to Mineralogy and Petrology, v. 169, p. 15.

Brandsdóttir, B., and Einarsson, P., 1979, Seismic activity associated with the September 1977 deflation of the Krafla central volcano in northeastern Iceland: Journal of Volcanology and Geothermal Research, v. 6, p. 197-212.

Brandsdóttir, B., and Menke, W. H., 1992, Thin low-velocity zone within the Krafla caldera, NE-Iceland attributed to a small magma chamber: Geophysical Research Letters, v. 19, p. 2381-2384.

Brandsdóttir, B., and Menke, W. H., 2008, The seismic structure of Iceland: Jökull, v. 58, p. 17-34.

Brandsdóttir, B., Menke, W., Einarsson, P., White, R. S., and Staples, R. K., 1997, Färoe-Iceland Ridge Experiment 2. Crustal structure of the Krafla central volcano: Journal of Geophysical Research: Solid Earth, v. 102, p. 7867-7886.

Branney, M. J., and Kokelaar, P., 1992, A reappraisal of ignimbrite emplacement: progressive aggradation and changes from particulate to non-particulate flow during emplacement of high-grade ignimbrite: Bulletin of Volcanology, v. 54, p. 504-520.

Branney, M. J., and Kokelaar, B. P., 2002, Pyroclastic Density Currents and the Sedimentation of Ignimbrites: Geological Society of London Memoir 27, 143 p.

Branney, M. J., Kokelaar, B. P., and McConnell, B. J., 1992, The Bad Step Tuff: a lava-like rheomorphic ignimbrite in a calc-alkaline piecemeal caldera, English Lake District: Bulletin of Volcanology, v. 54, p. 187-199.

Branney, M. J., Bonnichsen, B., Andrews, G. D. M., Ellis, B., Barry, T. L., and McCurry, M., 2008, 'Snake River (SR)-type' volcanism at the Yellowstone hotspot track: distinctive products from unusual, high-temperature silicic super-eruptions: Bulletin of Volcanology, v. 70, p. 293-314.

Brown, R. J., and Andrews, G. D. M., 2015, Deposits of pyroclastic density currents, *in* Sigurdsson, H., Houghton, B., McNutt, S. R., Rymer, H., and Stix, J., eds., Encyclopedia of Volcanoes (second edition): New York, Elsevier, p. 631-648.

Brown, R. J., and Branney, M. J., 2004, Event stratigraphy of a caldera-forming ignimbrite eruption on Tenerife: the 273 ka Poris Formation: Bulletin of Volcanology, v. 66, p. 392-416.

Brown, R. J., Blake, S., Thordarson, T., and Self, S., 2014, Pyroclastic edifices record vigorous lava fountains during emplacement of a flood basalt flow field, Roza Member, Columbia River basalt province, USA: Geological Society of America Bulletin, v. 126, p. 875-891.

Brophy, J. G., 2009, La–SiO_2 and Yb–SiO_2 systematics in mid-ocean ridge magmas: implications for the origin of oceanic plagiogranite: Contributions to Mineralogy and Petrology, v. 158, p. 99-111.

Brugman, K. K., and Till, C. B., 2019, A low-aluminum clinopyroxene-liquid geothermometer for high-silica magmatic systems: American Mineralogist, v. 104, p. 996-1004.

Buck, W. R., Einarsson, P., and Brandsdóttir, B., 2006, Tectonic stress and magma chamber size as controls on dike propagation: Constraints from the 1975-1984 Krafla rifting episode: Journal of Geophysical Research: Solid Earth, v. 111.

Budd, D. A. Budd, D. A. Troll, V. R., Deegan, F. M., Jolis, E. M., Smith, V. C., Whitehouse, M. J., Harris, C., Freda, C., Hilton, D. R., Halldórsson, S. A., and Bindeman, I. N., 2017, Magma reservoir dynamics at Toba caldera, Indonesia, recorded by oxygen isotope zoning in quartz: Scientific Reports, v. 7, p. 40624.

Burgisser, A., 2005, Physical volcanology of the 2,050 BP caldera-forming eruption of Okmok volcano, Alaska: Bulletin of Volcanology, v. 67p. 497-525.

Bunsen, R., 1851, Ueber die processe der vulkanischen gesterinsbildungen Islands (On the process of volcanic rock formation in Iceland): Annalen der Physik und Chemie, v. 83, p. 197-272.

Calderone, G. M., Grönvold, K., and Oskarsson, N., 1990, The welded air-fall tuff layer at Krafla, northern Iceland: a composite eruption triggered by injection of basaltic magma: Journal of Volcanology and Geothermal Research, v. 44, p. 303-314.

Capaccioni, B., and Cuccoli, F., 2005, Spatter and welded air fall deposits generated by fire-fountaining eruptions: Cooling of pyroclasts during transport and deposition: Journal of Volcanology and Geothermal Research, v. 145, p. 263-280.

Carey, R. J., Houghton, B. F., and Thordarson, T., 2008a, Contrasting styles of welding observed in the proximal Askja 1875 eruption deposits I: Regional welding: Journal of Volcanology and Geothermal Research, v. 171, p. 1-19.

Carey, R. J., Houghton, B. F., and Thordarson, T., 2008b, Contrasting styles of welding observed in the proximal Askja 1875 eruption deposits II: Local welding: Journal of Volcanology and Geothermal Research, v. 171, p. 20-44.

Carey, R. J., Houghton, B. F., and Thordarson, T., 2010, Tephra dispersal and eruption dynamics of wet and dry phases of the 1875 eruption of Askja Volcano, Iceland: Bulletin of Volcanology, v. 72, p. 259-278.

Carley, T. L., Miller, C. F., Wooden, J. L., Bindeman, I. N., and Barth, A. P., 2011, Zircon from historic eruptions in Iceland: reconstructing storage and evolution of silicic magmas: Mineralogy and Petrology, v. 102, p. 135-161.

Carley, T. L., Miller, C. F., Wooden, J. L., Padilla, A. J., Schmitt, A. K., Economos, R. C., Bindeman, I. N., and Jordan, B. T., 2014, Iceland is not a magmatic analog for the Hadean: Evidence from the zircon record: Earth and Planetary Science Letters, v. 405, p. 85-97.

Carley, T. L., Miller, C. F., Sigmarsson, O., Coble, M. A., Fisher, C. M., Hanchar, J. M., Schmitt, A. K., and Economos, R. C. 2017: Geosphere, v. 13, p. 1640-1663.

Carley, T. L., Miller, C. F., Fisher, C. M., Hanchar, J. M., Vervoort, J. D., Schmitt, A. K., Economos, R. C., Jordan, B. T., Padilla, A. J., and Banik, T. J., 2020, Petrogenesis of silicic magmas in Iceland through space and time: The isotopic record preserved in zircon and whole rocks: The Journal of Geology, v. 128, p. 1-28.

Carmichael, I. S. E., 1964, The petrology of Thingmuli, a Tertiary volcano in eastern Iceland: Journal of Petrology, v. 5, p. 435-460.

Carmichael, I. S. E., 1967, The iron-titanium oxides of salic volcanic rocks and their associated ferromagnesian silicates: Contributions to Mineralogy and Petrology, v. 14, p. 36-64.

Cashman, K. V., 1993, Relationship between plagioclase crystallization and cooling rate in basaltic melts: Contributions to Mineralogy and Petrology, v. 113, p. 126-142.

Caulfield, J. T., Cronin, S. J., Turner, S. P., and Cooper, L. B., 2011, Mafic Plinian volcanism and ignimbrite emplacement at Tofua volcano, Tonga: Bulletin of Volcanology, v. 73, p. 1259-1277.

Chamberlain, K. J., Morgan, D. J., and Wilson, C. J. N., 2014, Timescales of mixing and mobilisation in the Bishop Tuff magma body: perspectives from diffusion chronometry: Contributions to Mineralogy and Petrology, v. 168, p. 1034.

Charreteur, G., and Tegner, C., 2013, Magmatic emulsion texture formed by mixing during extrusion, Rauðafell composite complex, Breiðdalur volcano, eastern Iceland: Bulletin of Volcanology, v. 75, p. 721.

Charreteur, G., Tegner, C., and Haase, K., 2013, Multiple ways of producing intermediate and silicic rocks within Thingmúli and other Icelandic volcanoes: Contributions to Mineralogy and Petrology, v. 166, p. 471-490.

Chouet, B., 2003, Volcano seismology: Pure and Applied Geophysics, v. 160, p. 739-788.

Clay, P. L., Busemann, H., Sherlock, S. C., Barry, T. L., Kelley, S. P., and McGarvie, D. W., 2015, $^{40}Ar/^{39}Ar$ and residual volatile contents in degassed subaerial and subglacial glassy volcanic rocks from Iceland: Chemical Geology, v. 403, p. 99-110.

Colgan, P. M., Bierman, P. R., Mickelson, D. M., and Caffee, M., 2002, Variation in glacial erosion near the southern margin of the Laurentide Ice Sheet, south-central Wisconsin, USA: Implications for cosmogenic dating of glacial terrains: Geological Society of America Bulletin, v. 114, p. 1581-1591.

Condomines, M., Grönvold, K., Hooker, P. J., Muehlenbachs, K., O'Nions, R. K., Óskarsson, N., and Oxburgh, E. R., 1983, Helium, oxygen, strontium and neodymium isotopic relationships in Icelandic volcanics: Earth and Planetary Science Letters, v. 66, p. 125-136.

Cooper, G. F., Morgan, D. J., and Wilson, C. J. N., 2017, Rapid assembly and rejuvenation of a large silicic magmatic system: Insights from mineral diffusive profiles in the Kidnappers and Rocky Hill deposits, New Zealand: Earth and Planetary Science Letters, v. 473, p. 1-13.

Cooper, K. M., 2017, What does a magma reservoir look like? The "crystal's-eye" view: Elements, v. 13, p. 23-28.

Cooper, K. M., and Kent, A. J. R., 2014, Rapid remobilization of magmatic crystals kept in cold storage: Nature, v. 506, p. 480-483.

Cooper, K. M., Sims, K. W. W., Eiler, J. M., and Banerjee, N., 2016, Timescales of storage and recycling of crystal mush at Krafla Volcano, Iceland: Contributions to Mineralogy and Petrology, v. 171, p. 1-19.

Coote, A. C., and Shane, P., 2016, Crystal origins and magmatic system beneath Ngauruhoe volcano (New Zealand) revealed by plagioclase textures and compositions: Lithos, v. 260, p. 107-119.

Corrigan, G. M., 1982, Supercooling and the crystallization of plagioclase, olivine, and clinopyroxene from basaltic magmas: Mineralogical Magazine, v. 46, p. 31-42.

Couch, S., Sparks, R. S. J., and Carroll, M. R., 2001, Mineral disequilibrium in lavas explained by convective self-mixing in open magma chambers: Nature, v. 411, p. 1037-1039.

Darbyshire, F. A., Priestley, K. F., White, R. S., Stefánsson, R., Gudmundsson, G. B., and Jakobsdóttir, S. S., 2000, Crustal structure of central and northern Iceland from analysis of teleseismic receiver functions: Geophysical Journal International, v. 143, p. 163-184.

Dearnley, D. R., 1954, A contribution to the geology of Loðmundarfjörður: Acta Naturalia Islandica, v. 1, 29 p., 2 pl.

De Campos, C. P., Dingwell, D. B., and Fehr, K. T., 2004, Decoupled convection cells from mixing experiments with alkaline melts from Phlegrean Fields: Chemical Geology, v. 213, p. 227-251.

De Campos, C. P., Dingwell, D. B., Perugini, D., Civetta, L., and Fehr, T. K., 2008, Heterogeneities in magma chambers: Insights from the behavior of major and minor elements during mixing experiments with natural alkaline melts: Chemical Geology, v. 256, p. 131-145.

De Campos, C. P., Perugini, D., Ertel-Ingrisch, W., Dingwell, D. B., and Poli, G., 2011, Enhancement of magma mixing efficiency by chaotic dynamics: an experimental study: Contributions to Mineralogy and Petrology, v. 161, p. 863-881.

De Moor, J. M., Aiuppa, A., Avard, G., Wehrmann, H., Dunbar, N., Muller, C., Tamburello, G., Giudice, G., Liuzzo, M., Moretti, R., Conde, V., and Galle, B., 2016, Turmoil at Turrialba Volcano (Costa Rica): Degassing and eruptive processes inferred from high-frequency gas monitoring: Journal of Geophysical Research: Solid Earth, v. 121, p. 5761-5775.

de Zeeuw-van Dalfsen, E., Pedersen, R., Sigmundsson, F., and Pagli, C., 2004, Satellite radar interferometry 1993–1999 suggests deep accumulation of magma near the crust-mantle boundary at the Krafla volcanic system, Iceland: Geophysical Research Letters, v. 31.

de Zeeuw-van Dalfsen, E., Rymer, H., Williams-Jones, G., Sturkell, E., and Sigmundsson, F., 2006, Integration of micro-gravity and geodetic data to constrain shallow system mass changes at Krafla Volcano, N Iceland: Bulletin of Volcanology, v. 68, p. 420-431.

Di Genova, D., Sicola, S., Romano, C., Vona, A., Fanara, S., and Spina, L., 2017, Effect of iron and nanolites on Raman spectra of volcanic glasses: A reassessment of existing strategies to estimate the water content: Chemical Geology, v. 475, p. 76-86.

Dirscherl, M., and Rossi, C., 2018, Geomorphometric analysis of the 2014-2015 Bárðarbunga volcanic eruption, Iceland: Remote Sensing of Environment, v. 204, p. 244-259.

Donaldson, C. H., 1979, An experimental investigation of the delay in nucleation of olivine in mafic magmas: Contributions to Mineralogy and Petrology, v. 69, p. 21-32.

Druitt, T. H., and Sparks, R. S. J., 1982, A proximal ignimbrite breccia facies on Santorini, Greece: Journal of Volcanology and Geothermal Research, v. 13, p. 147-171.

Druitt, T. H., Mellors, R. A., Pyle, D. M., and Sparks, R. S. J., 1989, Explosive volcanism on Santorini, Greece: Geological Magazine, v. 126, p. 95-126.

Dufek, J., and Bachmann, O., 2010, Quantum magmatism: Magmatic compositional gaps generated by melt-crystal dynamics: Geology, v. 38, p. 687-690.

Dufek, J., Wexler, J., and Manga, M., 2009, Transport capacity of pyroclastic density currents: Experiments and models of substrate-flow interaction: Journal of Geophysical Research: Solid Earth, v. 114.

Druitt, T. H., Costa, F., Deloule, E., Dungan, M., and Scaillet, B., 2012, Decadal to monthly timescales of magma transfer and reservoir growth at a caldera volcano: Nature, v. 482, p. 77-80.

Edmonds, M., Hartley, M. E., Morgan, D. J., Maclennan, J., Mutch, E. J. F., and Neave, D., 2016, How long does it take to assemble the magmas that feed large basaltic fissure eruptions?: Abstract V53B-3083 presented at 2016 Fall Meeting, AGU, San Francisco, California, 12-16 December.

Eggins, S. M., Woodhead, J. D., Kinsley, L. P. J., Mortimer, G. E., Sylvester, P., McCulloch, M. T., Hergt, J. M., and Handler, M. R., 1997, A simple method for the precise determination of ≥ 40 trace elements in geological samples by ICPMS using enriched isotope internal standardisation: Chemical geology, v. 134, p. 311-326.

Eichelberger, J. C., 2019, Magma: A journey to inner space: Eos, v. 100, p. 26-31.

Eichelberger, J. C., and Koch, F. G., 1979, Lithic fragments in the Bandelier Tuff, Jemez Mountains, New Mexico: Journal of Volcanology and Geothermal Research, v. 5, p. 115-134.

Eiler, J. M., 2001, Oxygen Isotope variations of basaltic Lavas and upper mantle rocks: Reviews in Mineralogy and Geochemistry, v. 43, p. 319-364.

Einarsson, E. H., 1982, Súra gjóskubergid á Sólheimum og vídar í Myrdal (The acid tephra layer in Solheimar and elsewhere in Myrdalur) Eldur er í Nordri (Fire in the north): Reykjavik, Sögufélag, p. 17-28.

Einarsson, P., 1978, S-wave shadows in the Krafla Caldera in NE-Iceland, evidence for a magma chamber in the crust: Bulletin Volcanologique, v. 41, p. 187-195.

Einarsson, P., 1991a, Earthquakes and present-day tectonism in Iceland: Tectonophysics, v. 189, p. 261-279.

Einarsson, P., 1991b, Umbrotin við Kröflu 1975-89 (The Krafla volcano-tectonic episode 1975-1989) *in* Garðarson, A., and Einarsson, Á., eds., Náttúra Mývatns (Mývatn's Nature): Reykjavík, Hid íslenska náttúrufræðifélag, p. 97–139.

Einarsson, P., 2008, Plate boundaries, rifts and transforms in Iceland: Jökull, v. 58, p. 35-58.

Einarsson, P., 2018, Short-term seismic precursors to Icelandic eruptions 1973–2014: Frontiers in Earth Science, v. 6, p. 45.

Einarsson, P., and Brandsdóttir, B., 1980, Seismological evidence for lateral magma intrusion during the July 1978 deflation of the Krafla volcano in NE-Iceland: Journal of Geophysics v. 47, p. 160-165.

Elders, W. A., Friðleifsson, G. Ó., Zierenberg, R. A., Pope, E. C., Mortensen, A., Guðmundsson, Á., Lowenstern, J. B., Marks, N. E., Owens, L., Bird, D. K., Reed, M., Olsen, N. J., and Schiffman, P., 2011, Origin of a rhyolite that intruded a geothermal well while drilling at the Krafla volcano, Iceland: Geology, v. 39, p. 231-234.

Erdmann, M., Fischer, L. A., France, L., Zhang, C., Godard, M., and Koepke, J., 2015, Anatexis at the roof of an oceanic magma chamber at IODP Site 1256 (equatorial Pacific): an experimental study: Contributions to Mineralogy and Petrology, v. 169, p. 39.

Ewart, J. A., Voight, B., and Björnsson, A., 1991, Elastic deformation models of Krafla Volcano, Iceland, for the decade 1975 through 1985: Bulletin of Volcanology, v. 53, p. 436-459.

Firth, C. W., Cronin, S. J., Turner, S. P., Handley, H. K., Gaildry, C., and Smith, I., 2015, Dynamics and pre-eruptive conditions of catastrophic, ignimbrite-producing eruptions from the Yenkahe Caldera, Vanuatu: Journal of Volcanology and Geothermal Research, v. 308, p. 39-60.

Fisher, R. V., 1961, Proposed classification of volcaniclastic sediments and rocks: Geological Society of America Bulletin, v. 72, p. 1409-1414.

Flinders, J., and Clemens, J. D., 2011, Non-linear dynamics, chaos, complexity and enclaves in granitoid magmas: Earth and Environmental Science Transactions of the Royal Society of Edinburgh, v. 87, p. 217-223.

Flude, S. Burgess, R., and McGarvie, D. W., 2008, Silicic volcanism at Ljósufjöll, Iceland: Insights into evolution and eruptive history from Ar–Ar dating: Journal of Volcanology and Geothermal Research, v. 169, p. 154-175.

Flude, S., McGarvie, D. W., Burgess, R., and Tindle, A. G., 2010, Rhyolites at Kerlingarfjöll, Iceland: the evolution and lifespan of silicic central volcanoes: Bulletin of Volcanology, v. 72, p. 523-538.

Forni, F., Bachmann, O., Mollo, S., De Astis, G., Gelman, S. E., and Ellis, B. S., 2016, The origin of a zoned ignimbrite: Insights into the Campanian Ignimbrite magma chamber (Campi Flegrei, Italy): Earth and Planetary Science Letters, v. 449, p. 259-271.

Fourcade, S., and Allegre, C. J., 1981, Trace elements behavior in granite genesis: A case study: The calc-alkaline plutonic association from the Querigut complex (Pyrénées, France): Contributions to Mineralogy and Petrology, v. 76, p. 177-195.

France, L., Koepke, J., Ildefonse, B., Cichy, S. B., and Deschamps, F., 2010, Hydrous partial melting in the sheeted dike complex at fast spreading ridges: experimental and natural observations: Contributions to Mineralogy and Petrology, v. 160, p. 683-704.

Freundt, A., 1998, The formation of high-grade ignimbrites, I: Experiments on high- and low-concentration transport systems containing sticky particles: Bulletin of Volcanology, v. 59, p. 414-435.

Freundt, A., and Schmincke, H. U., 1995, Eruption and emplacement of a basaltic welded ignimbrite during caldera formation on Gran Canaria: Bulletin of Volcanology, v. 56, p. 640-659.

Freundt, A., Wilson, C. J. N., and Carey, S. N., 2000, Ignimbrites and block-and-ash flow deposits, *in* Sigurdsson, H., Houghton, B., McNutt, S. R., Rymer, H., and Stix, J., eds., Encyclopedia of Volcanoes: New York, Academic Press, p. 581-599.

Friðleifsson, G. Ó., and Elders, W. A., 2005, The Iceland Deep Drilling Project: a search for deep unconventional geothermal resources: Geothermics, v. 34, p. 269-285.

Friðleifsson G. Ó., Elders, W. A., and Albertsson, A., 2014, The concept of the Iceland deep drilling project: Geothermics, v. 49, p. 2-8.

Furman, T., Frey, F. A., and Meyer, P. S., 1992a, Petrogenesis of evolved basalts and rhyolites at Austurhorn, southeastern Iceland: the role of fractional crystallization: Journal of Petrology, v. 33, p. 1405-1445.

Furman, T., Meyer, P. S., and Frey, F., 1992b, Evolution of Icelandic central volcanoes: evidence from the Austurhorn intrusion, southeastern Iceland: Bulletin of Volcanology, v. 55, p. 45-62.

Gaete, A., Kavanagh, J. L., Rivalta, E., Hilmi Hazim, S., Walter, T. R., and Dennis, D. J. C., 2019, The impact of unloading stresses on post-caldera magma intrusions: Earth and Planetary Science Letters, v. 508, p. 109-121.

Gardner, J. E., Befus, K. S., Gualda, G. A. R., and Ghiorso, M. S., 2014, Experimental constraints on rhyolite-MELTS and the Late Bishop Tuff magma body: Contributions to Mineralogy and Petrology, v. 168, p. 1051.

Gautason, B., and Muehlenbachs, K., 1998, Oxygen isotopic fluxes associated with high-temperature processes in the rift zones of Iceland: Chemical Geology, v. 145, p. 275-286.

Geirsdóttir, Á., Miller, G. H., and Andrews, J. T., 2007, Glaciation, erosion and landscape evolution of Iceland: Journal of Geodynamics, v. 43, p. 170-186.

Geirsdóttir, Á., Miller, G. H., Axford, Y., and Ólafsdóttir, S., 2009, Holocene and latest Pleistocene climate and glacier fluctuations in Iceland: Quaternary Science Reviews, v. 28, p. 2107-2118.

Ghiorso, M. S., and Sack, R. O., 1995, Chemical mass transfer in magmatic processes IV. A revised and internally consistent thermodynamic model for the interpolation and extrapolation of liquid-solid equilibria in magmatic systems at elevated temperatures and pressures: Contributions to Mineralogy and Petrology, v. 119, p. 197-212.

Gibb, F. G. F., 1974, Supercooling and the crystallization of plagioclase from a basaltic magma: Mineralogical Magazine, v. 39, p. 641-653.

Gibson, I. L., Origin of some Icelandic pitchstones: Lithos, v. 2, p. 343-349.

Gibson, I. L., Kirkpatrick, R. J., Emmerman, R., Schmincke, H.-U., Pritchard, G., Oakley, P. J., Thorpe, R. S., and Marriner, G. F., 1982, The trace element composition of the lavas and dikes from a 3-km vertical section through the lava pile of eastern Iceland: Journal of Geophysical Research: Solid Earth, v. 87, p. 6532-6546.

Gillis, K. M., and Coogan, L. A., 2002, Anatectic migmatites from the roof of an ocean ridge magma chamber: Journal of Petrology, v. 43, p. 2075-2095.

Ginibre, C., Kronz, A., and Wörner, G., 2002a, High-resolution quantitative imaging of plagioclase composition using accumulated backscattered electron images: new constraints on oscillatory zoning: Contributions to Mineralogy and Petrology, v. 142, p. 436-448.

Ginibre, C., Wörner, G, and Kronz, A., 2002b, Minor- and trace-element zoning in plagioclase: implications for magma chamber processes at Parinacota volcano, northern Chile: Contributions to Mineralogy and Petrology, v. 143, p. 300-315.

Ginibre, C., Worner, G., and Kronz, A., 2007, Crystal zoning as an archive for magma evolution: Elements, v. 3, p. 261-266.

Giordano, D., Nichols, A. R. L., and Dingwell, D. B., 2005, Glass transition temperatures of natural hydrous melts: a relationship with shear viscosity and implications for the welding process: Journal of Volcanology and Geothermal Research, v. 142, p. 105-118.

Giordano, G., De Benedetti, A. A., Diana, A., Diano, G., Gaudioso, F., Marasco, F., Miceli, M., Mollo, S., Cas, R. A. F., and Funicello, R., 2006, The Colli Albani mafic caldera (Roma, Italy): stratigraphy, structure and petrology: Journal of Volcanology and Geothermal Research, v. 155, p. 49-80.

Grönvold, K., 1972, Structural and Petrochemical Studies in the Kerlingarfjöll Region, Central Iceland [Ph.D. thesis]: Oxford, United Kingdom, University of Oxford, 237 p.

Grönvold, K., 1984, Mývatn fires 1724-1729: Chemical composition of the lava: Nordic Volcanological Institute Report 84 01, 30 p.

Grönvold, K., 2006, Composition of Krafla lavas 1975-84, Abstract T33E-08 presented at 2006 Fall Meeting, AGU, San Francisco, California, 11-15 December.

Grönvold, K., and Mäkipää, H., 1978, Chemical composition of Krafla lavas 1975-1977: Nordic Volcanological Institute Report 78 16, 49 p.

Grönvold, K., Óskarsson, N., Johnsen, S. J., Clausen, H. B., Hammer, C. U., Bond, G., and Bard, E., 1995, Ash layers from Iceland in the Greenland GRIP ice core correlated with oceanic and land sediments: Earth and Planetary Science Letters, v. 135, p. 149-155.

Gualda, G. A. R., Ghiorso, M. S., Lemons, R. V., and Carley, T. L., 2012, Rhyolite-MELTS: a modified calibration of MELTS optimized for silica-rich, fluid-bearing magmatic systems: Journal of Petrology, v. 53, p. 875-890.

Gudmundsson, A., 1988, Formation of collapse calderas: Geology, v. 16, p. 808-810.

Gudmundsson, A., 1995, Infrastructure and mechanics of volcanic systems in Iceland: Journal of Volcanology and Geothermal Research, v. 64, p. 1-22.

Gudmundsson, A., 2000, Dynamics of volcanic systems in Iceland: Example of tectonism and volcanism at juxtaposed hot spot and mid-ocean ridge systems: Annual Review of Earth and Planetary Sciences, v. 28, p. 107-140.

Gudmundsson, A., 2015, Collapse-driven large eruptions: Journal of Volcanology and Geothermal Research, v. 304, p. 1-10.

Gudmundsson, A., and Nilsen, K., 2006, Ring-faults in composite volcanoes: Structures, models and stress fields associated with their formation, in Troise, C., De Natale, G., and Kilburn, C. R. J., eds., Mechanisms of Activity and Unrest at Large Calderas: Geological Society, London, Special Publication 269, p. 83-108.

Gudmundsson, M. T., Larsen, G., Höskuldsson, Á., and Gylfason, Á. G., 2008, Volcanic hazards in Iceland: Jökull, v. 58, p. 251-268.

Gudmundsson, M. T., Jónsdóttir, K., Hooper, A., Holohan, E. P., Halldórsson, S. A., Ófeigsson, B. G., Cesca, S., Vogfjörd, K. S., Sigmundsson, F., Högnadóttir, T., Einarsson, P., Sigmarsson, O., Jarosch, A. H., Jónasson, K., Magnússon, E., Hreinsdóttir, S., Bagnardi, M., Parks, M. M., Hjörleifsdóttir, V., Pálsson, F., Walter, T. R., Schöpfer, M. P. J., Heimann, S., Reynolds, H. I., Dumont, S., Bali, E., Gudfinnsson, G. H., Dahm, T., Roberts, M. J., Hensch, M., Belart, J. M. C., Spaans, K., Jakobsson, S., Gudmundsson, G. B., Fridriksdóttir, H. M., Drouin, V., Dürig, T., Aðalgeirsdóttir, G., Riishuus, M. S., Pedersen, G. B. M., van Boeckel, T., Oddsson, B., Pfeffer, M. A., Barsotti, S., Bergsson, B., Donovan, A., Burton, M. R., and Aiuppa, A.., 2016, Gradual caldera collapse at Bárdarbunga volcano, Iceland, regulated by lateral magma outflow: Science, v. 353, p. 262-271.

Guðmundsson, Á, Sigursteinsson, D., Guðmundsson, G., Friðleifsson, G., and Tryggvason, H., 1983, Krafla, Hola KJ-22: Orkustofnun Report OS 8-070, 12 p.

Guilbaud, M. -N., Blake, S., Thordarson, T., and Self, S., 2007, Role of syn-eruptive cooling and degassing on textures of lavas from the AD 1783–1784 Laki eruption, South Iceland: Journal of Petrology, v. 48, p. 1265-1294.

Guillou, H., Scao, V., Nomande, S., Van Viet-Lanoë, B., Liorzou, C., and Guðmundsson, Á., 2019, $^{40}Ar/^{39}Ar$ dating of the Thorsmork ignimbrite and Icelandic sub-glacial rhyolites: Quaternary Science Reviews, v. 209, p. 52-62.

Gunnarsson, B., Marsh, B. D., and Taylor, H. P., 1998, Generation of Icelandic rhyolites: silicic lavas from the Torfajökull central volcano: Journal of Volcanology and Geothermal Research, v. 83, p. 1-45.

Gurenko, A. A., Bindeman, I. N., and Sigurdsson, I. A., 2015, To the origin of Icelandic rhyolites: insights from partially melted leucocratic xenoliths: Contributions to Mineralogy and Petrology, v. 169, p. 49.

Haggerty, S. E., 1991, Oxide textures; a mini-atlas: Reviews in Mineralogy and Geochemistry, v. 25, p. 129-219.

Halldorsson, S. A., Oskarsson, N., Gronvold, K., Sigurdsson, G., Sverrisdottir, G., and Steinthorsson, S., 2008, Isotopic-heterogeneity of the Thjorsa lava—Implications for mantle sources and crustal processes within the Eastern Rift Zone, Iceland: Chemical Geology, v. 255, p. 305-316.

Halldórsson, S. A., Bali, E., Hartley, M. E., Neave, D. A., Peate, D. W., Guðfinnsson, G. H., Bindeman, I., Whitehouse, M. J., Riishuus, M. S., Pedersen, G. B. M., Jakobsson, S., Askew, R., Gallagher, C. R., Guðmundsdóttir, E. R., Gudnason, J., Moreland, W. M., Óskarsson, B. V., Nikkola, P., Reynolds, H. I., Schmith, J., and Thordarson, T., 2018, Petrology and geochemistry of the 2014–2015 Holuhraun eruption, central Iceland: compositional and mineralogical characteristics, temporal variability and magma storage: Contributions to Mineralogy and Petrology, v. 173, p. 64.

Hammer, J. E., and Rutherford, M. J., 2002, An experimental study of the kinetics of decompression-induced crystallization in silicic melt: Journal of Geophysical Research-Solid Earth, v. 107, p. 1-24.

Hampton, R.L., Bindeman, I. N., Stern, R. A., Coble, M. A., and Rooyakkers, S. M., in prep., A microanalytical isotopic investigation of rhyolite petrogenesis at the Krafla volcanic center, Iceland.

Hansen, H., and Grönvold, K., 2000, Plagioclase ultraphyric basalts in Iceland: the mush of the rift: Journal of Volcanology and Geothermal Research, v. 98, p. 1-32.

Hards, V. L., Kempton, P. D., Thompson, R. N., and Greenwood, P. B., 2000, The magmatic evolution of the Snæfell volcanic centre; an example of volcanism during incipient rifting in Iceland: Journal of Volcanology and Geothermal Research, v. 99, p. 97-121.

Hartley, M. E., and Thordarson, T., 2013, The 1874-1876 volcano-tectonic episode at Askja, North Iceland: Lateral flow revisited: Geochemistry, Geophysics, Geosystems, v. 14, p. 2286-2309.

Hartley, M. E., Morgan, D. J., Maclennan, J., Edmonds, M., and Thordarson, T., 2016, Tracking timescales of short-term precursors to large basaltic fissure eruptions through Fe–Mg diffusion in olivine: Earth and Planetary Science Letters, v. 439, p. 58-70.

Hartley, M. E., Bali, E., Maclennan, J., Neave, D. A., and Halldórsson, S. A., 2018, Melt inclusion constraints on petrogenesis of the 2014–2015 Holuhraun eruption, Iceland: Contributions to Mineralogy and Petrology, v. 173, p. 10.

Hattori, K., and Muehlenbachs, K., 1982, Oxygen isotope ratios of the Icelandic crust: Journal of Geophysical Research: Solid Earth, v. 87, p. 6559-6565.

Hellstrom, J., Paton, C., Woodhead, J. D., and Hergt, J. M., 2008, Iolite: software for spatially-resolved LA-(quad and MC) ICPMS analysis, in Sylvester, P., ed., Laser Ablation ICPMS in the Earth Sciences: Current Practises and Outstanding Issues. Mineralogical Association of Canada Short Course Series, v. 40, p. 343–348.

Hemond, C., Arndt, N. T., Lichtenstein, U., Hofmann, A. W., Oskarsson, N., and Steinthorsson, S., 1993, The heterogeneous Iceland plume: Nd-Sr-O isotopes and trace element constraints: Journal of Geophysical Research: Solid Earth, v. 98, p. 15833-15850.

Henry, C. D., and Wolff, J. A., 1992, Distinguishing strongly rheomorphic tuffs from extensive silicic lavas: Bulletin of Volcanology, v. 54, p. 171-186.

Hildreth, W., and Fierstein, J., 2012, The Novarupta-Katmai eruption of 1912 – Largest eruption of the twentieth century: Centennial perspectives: U.S. Geological Survey Professional Paper 1791, 260 p.

Hjaltadóttir, S., Vogfjörd, K. S., Hreinsdóttir, S., and Slunga, R., 2015, Reawakening of a volcano: Activity beneath Eyjafjallajökull volcano from 1991 to 2009: Journal of Volcanology and Geothermal Research, v. 304, p. 194-205.

Hjartardóttir, Á. R., Einarsson, P., Bramham, E., and Wright, T. J., 2012, The Krafla fissure swarm, Iceland, and its formation by rifting events: Bulletin of Volcanology, v. 74, p. 2139-2153.

Hjartardóttir, Á. R., Einarsson, P., Magnúsdóttir, S., Björnsdóttir, Þ., and Brandsdóttir, B., 2016, Fracture systems of the Northern Volcanic Rift Zone, Iceland: an onshore part of the Mid-Atlantic plate boundary, *in* Wright, T. J., Ayele, A., Ferguson, D. J., Kidane, T. & Vye-Brown, C., eds., Geological Society, London, Special Publication 420, p. 297-314.

Hollingsworth, J., Leprince, S., Ayoub, F., and Avouac, J.-P., 2012, Deformation during the 1975–1984 Krafla rifting crisis, NE Iceland, measured from historical optical imagery: Journal of Geophysical Research: Solid Earth, v. 117, p. 1-24.

Hollingsworth, J., Leprince, S., Ayoub, F., and Avouac, J.-P., 2013, New constraints on dike injection and fault slip during the 1975–1984 Krafla rift crisis, NE Iceland: Journal of Geophysical Research: Solid Earth, v. 118, p. 3707-3727.

Holness, M. B., Cheadle, M. J., and McKenzie, D., 2005, On the use of changes in dihedral angle to decode late-stage textural evolution in cumulates: Journal of Petrology, v. 46, p. 1565-1583.

Holness, M. B., Humphreys, M. C. S., Sides, R., Helz, R. T., and Tegner, C., 2012, Toward an understanding of disequilibrium dihedral angles in mafic rocks: Journal of Geophysical Research: Solid Earth, v. 117, p. 1-31.

Holtz, F., Johannes, W., Tamic, N., and Behrens, H., 2001, Maximum and minimum water contents of granitic melts generated in the crust: a reevaluation and implications: Lithos, v. 56, p. 1-14.

Houghton, B. F., and Wilson, C. J. N., 1989, A vesicularity index for pyroclastic deposits: Bulletin of Volcanology, v. 51, p. 451-462.

Humphreys, M. C. S., Blundy, J. D., and Sparks, R. S. J., 2006, Magma evolution and open-system processes at Shiveluch Volcano: Insights from phenocryst zoning: Journal of Petrology, v. 47, p. 2303-2334.

Humphreys, M. C. S., Edmonds, M., and Klöcking, M. S., 2016, The validity of plagioclase-melt geothermometry for degassing-driven magma crystallization: American Mineralogist, v. 101, p. 769-779.

Huppert, H. E., Sparks, R. S. J., and Turner, J. S., 1982, Effects of volatiles on mixing in calc-alkaline magma systems: Nature, v. 297, p. 554-557.

Iacovino, K., Kim, J. S., Sisson, T. W., Lowenstern, J. B., Jang, J. N., Song. K. H., Ham. H. H., Ri, K. H., Donovan, A. R., Oppenheimer, C., Hammond, J. O. S., Weber Liu, K., and Ryu, K. R., 2015, New constraints on the geochemistry of the Millennium eruption of Mount Peaktu (Changbaishan), Democratic People's Republic of Korea/China, Abstract V43B-3114 presented at 2015 Fall Meeting, AGU, San Francisco, California, 14-18 December.

Imsland, P., 1983, Iceland and the ocean floor. Comparison of chemical characteristics of the magmatic rocks and some volcanic features: Contributions to Mineralogy and Petrology, v. 83, p. 31-37.

Ingólfsson, Ó., Norðdahl, H., and Schomacker, A., 2010, Deglaciation and Holocene glacial history of Iceland, *in* Schomacker, A., Krüger, J., and Kjær, K. H., eds., Developments in Quaternary Sciences, v. 13, p. 51-68.

Inman, D. L., 1952, Measures for describing the size distribution of sediments: Journal of Sedimentary Research, v. 22, p. 125-145.

Jakobsson, S. P., 1972, Chemistry and distribution pattern of recent basaltic rocks in Iceland: Lithos, v. 5, p. 365-386.

Jakobsson, S. P., 1979, Outline of the petrology of Iceland: Jökull, v. 29, p. 57-73.

Janebo, M. H., Thordarson, T., Houghton, B. F., Bonadonna, C., Larsen, G., and Carey, R. J., 2016, Dispersal of key subplinian-Plinian tephras from Hekla volcano, Iceland: implications for eruption source parameters: Bulletin of Volcanology, v. 78, p. 66.

Jóhannesson, H., 1975, Structure and Petrochemistry of the Reykjadalur Central Volcano and the Surrounding Areas, Midwest Iceland [Ph.D. thesis]: Durham, United Kingdom, Durham University, 273 p.

Jóhannesson, H., and Sæmundsson, K., 1998, Geological map of Iceland, bedrock geology: Náttúrufræðistofnun Íslands, Reykjavík, scale 1: 500,000.

Jónasson, K., 1994, Rhyolite volcanism in the Krafla central volcano, north-east Iceland: Bulletin of Volcanology, v. 56, p. 516-528.

Jónasson, K., 2007, Silicic volcanism in Iceland: Composition and distribution within the active volcanic zones: Journal of Geodynamics, v. 43, p. 101-117.

Jørgensen, K. A., 1980, The Thorsmörk Ignimbrite: An unusual comenditic pyroclastic flow in southern Iceland: Journal of Volcanology and Geothermal Research, v. 8, p. 7-22.

Jørgensen, K. A., 1981, The Thorsmörk Ignimbrite: A review, *in* Self, S., and Sparks, R. S. J., eds., Tephra Studies: Proceedings of the NATO Advanced Study Institute "Tephra Studies as a Tool in Quaternary Research", Laugarvatn and Reykjavík, June 1980: Dordrecht, D. Riedel Publishing Company, p. 347-354.

Jull, M., and McKenzie, D., 1996, The effect of deglaciation on mantle melting beneath Iceland: Journal of Geophysical Research: Solid Earth, v. 101, p. 21815-21828.

Keiding, J. K., and Sigmarsson, O., 2012, Geothermobarometry of the 2010 Eyjafjallajökull eruption: New constraints on Icelandic magma plumbing systems: Journal of Geophysical Research: Solid Earth, v. 117, p. 1-15.

Kelley, D. F., and Barton, M., 2008, Pressures of crystallization of Icelandic magmas: Journal of Petrology, v. 49, p. 465-492.

Kennedy, B., Wilcock, J., and Stix, J., 2012, Caldera resurgence during magma replenishment and rejuvenation at Valles and Lake City calderas: Bulletin of Volcanology, v. 74, p. 1833-1847.

Kennedy, B. M., Holohan, E. P., Stix, J., Gravely, D. M., Davidson, J. R. J., and Cole, J. W., 2018, Magma plumbing beneath collapse caldera volcanic systems: Earth-Science Reviews, v. 177, p. 404-424.

Kim, D., Brown, L. D., Árnason, K., Águstsson, K., and Black, H., 2017, Magma reflection imaging in Krafla, Iceland, using microearthquake sources: Journal of Geophysical Research: Solid Earth, v. 122, p. 5228-5242.

Kim, D., Brown, L. D., Árnason, K., Gudmundsson, Ó., Ágústsson, K, and Flóvenz, Ó., 2020, Magma "bright spots" mapped beneath Krafla, Iceland, using RVSP imaging of reflected waves from microearthquakes: Journal of Volcanology and Geothermal Research, v. 291, p. 106365.

Koepke, J., Feig, S. T., Snow, J., and Freise, M., 2004, Petrogenesis of oceanic plagiogranites by partial melting of gabbros: an experimental study: Contributions to Mineralogy and Petrology, v. 146, p. 414-432.

Kokelaar, P., 2007, Friction melting, catastrophic dilation and breccia formation along caldera superfaults: Journal of the Geological Society, v. 164, p. 751-754.

Kokelaar, P., Raine, P., and Branney, M. J., 2007, Incursion of a large-volume, spatter-bearing pyroclastic density current into a caldera lake: Pavey Ark ignimbrite, Scafell caldera, England: Bulletin of Volcanology, v. 70, p. 23-54.

Koyaguchi, T., 1985, Magma mixing in a conduit: Journal of Volcanology and Geothermal Research, v. 25, p. 365-369.

Kristmannsdottir, H., 1979, Alteration of basaltic rocks by hydrothermal activity at 100-300°C, *in* Mortland, M. M., and Farmer, V. C., eds., Developments in Sedimentology: Amsterdam, Elsevier, v. 27, p. 359-367.

Kueppers, U., Scheu, B., Spieler, O., and Dingwell, D. B., 2006, Fragmentation efficiency of explosive volcanic eruptions: A study of experimentally generated pyroclasts: Journal of Volcanology and Geothermal Research, v. 153, p. 125-135.

Kuritani, T., Yokoyama, T., Kitagawa, H., Kobayashi, K., and Nakamura, E., 2011, Geochemical evolution of historical lavas from Askja Volcano, Iceland: Implications for mechanisms and timescales of magmatic differentiation: Geochimica et Cosmochimica Acta, v. 75, p. 570-587.

Lacasse, C., and Garbe-Schönberg, C. D., 2001, Explosive silicic volcanism in Iceland and the Jan Mayen area during the last 6 Ma: sources and timing of major eruptions: Journal of Volcanology and Geothermal Research, v. 107, p. 113-147.

Lacasse, C., Sigurdsson, H., Jóhannesson, H., Paterne, M., and Carey, S., 1995, Source of Ash Zone 1 in the North Atlantic: Bulletin of Volcanology, v. 57, p. 18-32.

Lacasse, C., Sigurdsson, H., Carey, S. N., Jóhannesson, H., Thomas, L. E., and Rogers, N. W., 2007, Bimodal volcanism at the Katla subglacial caldera, Iceland: Insights into the geochemistry and petrogenesis of rhyolitic magmas: Bulletin of Volcanology, v. 69, p. 373-399.

Laeger, K., Petrelli, M., Andronico, D., Misiti, V., Scarlato, P., Cimarelli, C., Taddeucci, J., Del Bello, E., and Perugini, D., 2017, High-resolution geochemistry of volcanic ash highlights complex magma dynamics during the Eyjafjallajökull 2010 eruption: American Mineralogist, v. 102, p. 1173-1186.

Langmuir, C. H., Vocke, R. D., Hanson, G. N., and Hart, S. R., 1978, A general mixing equation with applications to Icelandic basalts: Earth and Planetary Science Letters, v. 37, p. 380-392.

Larsen, G., and Eiríksson, J., 2007, Late Quaternary terrestrial tephrochronology of Iceland – frequency of explosive eruptions, type and volume of tephra deposits: Journal of Quaternary Science, v. 23, p. 109-120.

Larsen, G., and Thorarinsson, S. (1977) H-4 and other acid Hekla tephra layers: Jökull, v. 27, p. 28-46.

Larsen, G., Dugmore, A., and Newton, A., 1999, Geochemistry of historical-age silicic tephras in Iceland: The Holocene, v. 9., p. 463-471.

Larsen, G., Newton, A. J., Dugmore, A. J., and Vilmundardóttir, E. G., 2001, Geochemistry, dispersal, volumes and chronology of Holocene silicic tephra layers from the Katla volcanic system, Iceland: Journal of Quaternary Science, v. 16, p. 119-132.

Larsen, J.F., Neal, C., Schaefer, J., Beget, J., and Nye, C., 2007, Late Pleistocene and Holocene caldera-forming eruptions of Okmok caldera, Aleutian Islands, Alaska, *in* Eichelberger, J., Gordeev, E., Izbekov, P., Kasahara, M., and Lees, J., eds., Volcanism and Subduction: The Kamchatka Region: American Geophysical Union Geophysical Monograph 172, p. 343–364.

Lee, B., Unsworth, M., Árnason, K., and Cordell, D., 2020, Imaging the magmatic system beneath the Krafla geothermal field, Iceland: A new 3-D electrical resistivity model from inversion of magnetotelluric data: Geophysical Journal International, v. 220, p. 541-567.

Lees, J. M., 2007, Seismic tomography of magmatic systems: Journal of Volcanology and Geothermal Research, v. 167, p. 37-56.

Leonard, G. S., Cole, J. W., Nairn, I. A., and Self, S., 2002, Basalt triggering of the c. AD 1305 Kaharoa rhyolite eruption, Tarawera Volcanic Complex, New Zealand: Journal of Volcanology and Geothermal Research, v. 115, p. 461-486.

Lipman, P. W., 1984, The roots of ash flow calderas in western North America: Windows into the tops of granitic batholiths: Journal of Geophysical Research: Solid Earth, v. 89, p. 8801-8841.

Lipman, P. W., 1997, Subsidence of ash-flow calderas: relation to caldera size and magma-chamber geometry: Bulletin of Volcanology, v. 59, p. 198-218.

Lohmar, S., Robin, C., Parada, M. A., López-Escobar, L., Moreno, H., and Naranjo, J., 2005, The two major postglacial (13-14,000 BP) pyroclastic eruptions of Llaima and Villarrica volcanoes (Southern Andes): A comparison: 6th International symposium on Andean Geodynamics, Barcelona, Extended Abstracts: Paris, Institut de recherche pour le développement, p. 442-445.

Lohmar, S., Robin, C., Gourgand, A., Clavero, J., Parada, M. A., Moreno, H., Ersoy, O., López-Escobar, L, and Naranjo, J.-A., 2007, Evidence of magma-water interaction during the 13,800 years BP explosive cycle of the Licán Ignimbrite, Villarrica volcano (southern Chile): Andean Geology, v. 34, p. 233-247.

Long, D. A., 1977, Raman Spectroscopy: New York, McGraw-Hill, 276 p.

Lucic, G., Berg, A.-S., and Stix, J., 2016, Water-rich and volatile-undersaturated magmas at Hekla volcano, Iceland: Geochemistry, Geophysics, Geosystems, v. 17, p. 3111-3130.

Lundgaard, K. L., and Tegner, C., 2004, Partitioning of ferric and ferrous iron between plagioclase and silicate melt: Contributions to Mineralogy and Petrology, v. 147, p. 470-483.

Macdonald, R., Sparks, R. S. J., Sigurdsson, H., Mattey, D. P., McGarvie, D. W., and Smith, R. L., 1987, The 1875 eruption of Askja volcano, Iceland: combined fractional crystallization and selective contamination in the generation of rhyolitic magma: Mineralogical Magazine, v. 51, p. 183-202.

Macdonald, R., McGarvie, D. W., Pinkerton, H., Smith, R. L., and Palacz, A., 1990, Petrogenetic evolution of the Torfajökull volcanic complex, Iceland I. Relationship between the magma types: Journal of Petrology, v. 31, p. 429-459.

Maclennan, J., 2008, Concurrent mixing and cooling of melts under Iceland: Journal of Petrology, v. 49, p. 1931-1953.

Maclennan, J., Mkenzie, D., Gronvöld, K., and Slater, L., 2001, Crustal accretion under northern Iceland: Earth and Planetary Science Letters, v. 191, p. 295-310.

Maclennan, J., Jull, M., McKenzie, D., Slater, L., and Grönvold, K., 2002, The link between volcanism and deglaciation in Iceland: Geochemistry, Geophysics, Geosystems, v. 3, p. 1-25.

Mahood, G. A., and Hildreth, W., 1986, Geology of the peralkaline volcano at Pantelleria, Strait of Sicily: Bulletin of Volcanology, v. 48, p. 143-172.

Manga, M., and Brodsky, E., 2006, Seismic triggering of eruptions in the far field: Volcanoes and geysers: Annual Review of Earth and Planetary Sciences, v. 34, p. 263-291.

Marquart, G., and Jacoby, W, 1985, On the mechanism of magma injection and plate divergence during the Krafla Rifting Episode in NE Iceland: Journal of Geophysical Research: Solid Earth, v. 90, p. 10178-10192.

Marsh, B. D., Gunnarsson, B., Congdon, R., and Carmody, R., 1991, Hawaiian basalt and Icelandic rhyolite: Indicators of differentiation and partial melting: Geologische Rundschau, v. 80, p. 481-510.

Martí, J., Folch, A., Neri, A., Macedonio, G., 2000, Pressure evolution during explosive caldera-forming eruptions: Earth and Planetary Science Letters, v. 175, p. 275-287.

Martin, A. P., Smellie, J. L., Cooper, A. F., and Townsend, D. B., 2018, Formation of a spatter-rich pyroclastic density current deposit in a Neogene sequence of trachytic-mafic igneous rocks at Mason Spur, Erebus volcanic province, Antarctica: Bulletin of Volcanology, v. 80, p. 13.

Martin, E., and Sigmarsson, O., 2007, Crustal thermal state and origin of silicic magma in Iceland: the case of Torfajökull, Ljósufjöll and Snæfellsjökull volcanoes: Contributions to Mineralogy and Petrology, v. 153, p. 593-605.

Martin, E., and Sigmarsson, O., 2010, Thirteen million years of silicic magma production in Iceland: Links between petrogenesis and tectonic settings: Lithos, v. 116, p. 129-144.

Martin, E., Martin, H., and Sigmarsson, O., 2008, Could Iceland be a modern analogue for the Earth's early continental crust?: Terra Nova, v. 20, p. 463-468.

Mason, B. G., Pyle, D. M., and Oppenheimer, C., 2004, The size and frequency of the largest explosive eruptions on Earth: Bulletin of Volcanology, v. 66, p. 735-748.

Masotta, M., Mollo, S., Nazzari, M., Tecchiato, V., Scarlato, P., Papale, P., and Bachmann, O., 2018, Crystallization and partial melting of rhyolite and felsite rocks at Krafla volcano: A comparative approach based on mineral and glass chemistry of natural and experimental products: Chemical Geology, v. 483, p. 603-618.

Matsumoto, A., Hasegawa, T., and Nakagawa, M., 2018, Petrology of the 120 ka caldera-forming eruption of Kutcharo volcano, eastern Hokkaido, Japan: Coexistence of multiple silicic magmas and their relationship with mafic magmas: Journal of Petrology, v. 59, p. 771-793.

McDonough, W. F., and Sun, S.-s., 1995, The composition of the Earth: Chemical Geology, v. 120, p. 223-253.

McGarvie, D. W., 1984, Torfajokull - a volcano dominated by magma mixing: Geology, v. 12, p. 685-688.

McGarvie, D. W., 1985, Volcanology and Petrology of Mixed Magmas and Rhyolites from the Torfajokull Volcano, Iceland [Ph.D. thesis]: Lancaster, United Kingdom, University of Lancaster, 255 p.

McGarvie, D., 2009, Rhyolitic volcano–ice interactions in Iceland: Journal of Volcanology and Geothermal Research, v. 185, p. 367-389.

McGarvie, D. W., Macdonald, R., Pinkerton, H., and Smith, R. L., 1990, Petrogenetic evolution of the Torfajökull volcanic complex, Iceland II. The role of magma mixing: Journal of Petrology, v. 31, p. 461-481.

Mellors, R. A., and Sparks, R. S. J., 1991, Spatter-rich pyroclastic flow deposits on Santorini, Greece: Bulletin of Volcanology, v. 53, p. 327-342.

Merle, O., Barde-Cabusson, S., and van Wyk de Vries, B., 2010, Hydrothermal calderas: Bulletin of Volcanology, v. 72, p. 131-147.

Michon, L., Massin, F., Famin, V., Ferrazzini, V., and Roult, G., 2011, Basaltic calderas: Collapse dynamics, edifice deformation, and variations of magma withdrawal: Journal of Geophysical Research: Solid Earth, v. 116, p. 1-18.

Moles, J. D., McGarvie, D., Stevenson, J. A., Sherlock, S. C., Abbott, P. M., Jenner, F. E., and Halton, A. M., 2019, Widespread tephra dispersal and ignimbrite emplacement from a subglacial volcano (Torfajökull, Iceland): Geology, v. 47, p. 577-580.

Mollo, S., Putirka, K., Iezzi, G., and Scarlato, P., 2013, The control of cooling rate on titanomagnetite composition: implications for a geospeedometry model applicable to alkaline rocks from Mt. Etna volcano: Contributions to Mineralogy and Petrology, v. 165, p. 457-475.

Moorbath, S., and Walker, G. P. L., 1965, Strontium isotope investigation of igneous rocks from Iceland: Nature, v. 207, p. 837-840.

Morgavi, D., Perugini, D., De Campos, C. P., Ertl-Ingrisch, W., Lavallée, Y., Morgan, L., and Dingwell, D. B., 2013a, Interactions between rhyolitic and basaltic melts unraveled by chaotic mixing experiments: Chemical Geology, v. 346, p. 199-212.

Morgavi, D., Perugini, D., De Campos, C. P., Ertel-Ingrisch, W., and Dingwell, D. B., 2013b, Time evolution of chemical exchanges during mixing of rhyolitic and basaltic melts: Contributions to Mineralogy and Petrology, v. 166, p. 615-638.

Morgavi, D., Perugini, D., De Campos, C. P., Ertel-Ingrisch, W., and Dingwell, D. B., 2013c, Morphochemistry of patterns produced by mixing of rhyolitic and basaltic melts: Journal of Volcanology and Geothermal Research, v. 253, p. 87-96.

Mortensen, A. K., Grönvold, K., Guðmundsson, Á., Steingrímsson, B., and Egilson, T., 2010, Quenched silicic glass from well KJ-39 in Krafla, north-eastern Iceland, *in* Proceedings, World Geothermal Congress, Bali, Indonesia, April 2010: Bochum, International Geothermal Association, paper 1284.

Mortensen, A. K., Egilson, Þ., Gautason, B., Árnadóttir, S., and Guðmundsson, Á, 2014, Stratigraphy, alternation mineralogy, permeability and temperature conditions of well IDDP-1, Krafla, NE-Iceland: Geothermics, v. 49, p. 31-41.

Mørk, M. B. E., 1984, Magma mixing in the post-glacial Veidivötn fissure eruption, southeast Iceland: a microprobe study of mineral and glass variations: Lithos, v. 17, p. 55-75.

Mucek, A. E., Danišík, M., de Silva, S. L., Schmitt, A. K., Pratomo, I., and Coble, M. A., 2017, Post-supereruption recovery at Toba Caldera: Nature Communications, v. 8, p. 15248.

Muehlenbachs, K., 1973, The oxygen isotope geochemistry of siliceous volcanic rocks from Iceland: Carnegie Institution of Washington Yearbook, v. 72, p. 593-597.

Muehlenbachs, K., Anderson, A. T., and Sigvaldason, G. E., 1974, Low-O^{18} basalts from Iceland: Geochimica et Cosmochimica Acta, v. 38, p. 577-588.

Mueller, S. B., Houghton, B. F., Swanson, D. A., Poret, M., and Fagents, S. A., 2019, Total grain size distribution of an intense Hawaiian fountaining event: case study of the 1959 Kilauea Iki eruption: Bulletin of Volcanology, v. 83, p. 43.

Murphy, M. D., Sparks, R. S. J., Barclay, J., Carroll, M. R., and Brewer, T. S., 2000, Remobilization of andesite magma by intrusion of mafic magma at the Soufriere Hills Volcano, Montserrat, West Indies: Journal of Petrology, v. 41, p. 21-42.

Mutch, E. J. F., Maclennan, J., Shorttle, O., Edmonds, M., and Rudge, J. F., 2019, Rapid transcrustal magma movement under Iceland: Nature Geoscience, v. 12, p. 569-574.

Myers, M. L., Wallace, P. J., Wilson, C. J. N., Watson, J. M., and LIU, Y., 2018, Ascent rates of rhyolitic magma at the onset of three caldera-forming eruptions: American Mineralogist, v. 103, p. 952-965.

Namiki, A, and Manga, M., 2008, Transition between fragmentation and permeable outgassing of low viscosity magmas: Journal of Volcanology and Geothermal Research, v. 169, p. 48-60.

Neave, D. A., and Putirka, K. D., 2017, A new clinopyroxene-liquid barometer, and implications for magma storage pressures under Icelandic rift zones: American Mineralogist, v. 102, p. 777-794.

Neave, D. A., Passmore, E., Maclennan, J., Fitton, G., and Thordarson, T., 2013, Crystal–melt relationships and the record of deep mixing and crystallization in the AD 1783 Laki eruption, Iceland: Journal of Petrology, v. 54, p. 1661-1690.

Neave, D. A., Maclennan, J., Hartley, M. E., Edmonds, M., and Thordarson, T., 2014, Crystal storage and transfer in basaltic systems: the Skuggafjöll eruption, Iceland: Journal of Petrology, v. 55, p. 2311-2346.

Neave, D. A., Buisman, I., and Maclennan, J., 2017, Continuous mush disaggregation during the long-lasting Laki fissure eruption, Iceland: American Mineralogist, v. 102, p. 2007-2021.

Newhall, C. G., and Self, S., 1982, The volcanic explosivity index (VEI): An estimate of explosive magnitude for historical volcanism: Journal of Geophysical Research, v. 87, p. 1231-1238.

Nichols, A. R. L., Carroll, M. R., and Höskuldsson, Á., 2002, Is the Iceland hot spot also wet? Evidence from the water contents of undegassed submarine and subglacial pillow basalts: Earth and Planetary Science Letters, v. 202, p. 77-87.

Nicholson, H., 1990, The Magmatic Evolution of Krafla, NE Iceland [Ph.D. thesis]: Edinburgh, Scotland, University of Edinburgh, 286 p.

Nicholson, H., Condomines, M., Fitton, J. G., Fallick, A. E., Grönvold, K., and Rogers, G., 1991, Geochemical and isotopic evidence for crustal assimilation beneath Krafla, Iceland: Journal of Petrology, v. 32, p. 1005-1020.

O'Nions, R. K., and Grönvold, K., 1973, Petrogenetic relationships of acid and basic rocks in Iceland: Sr-isotopes and rare-earth elements in late and postglacial volcanics: Earth and Planetary Science Letters, v. 19, p. 397-409.

Óskarsson, N., Sigvaldason, G. E., and Steinthórsson, S., 1982, A dynamic model of rift zone petrogenesis and the regional petrology of Iceland: Journal of Petrology, v. 23, p. 28-74.

Oskarsson, N., Steinthorsson, S., and Sigvaldason, G. E., 1985, Iceland geochemical anomaly: Origin, volcanotectonics, chemical fractionation and isotope evolution of the crust: Journal of Geophysical Research: Solid Earth, v. 90, p. 10011-10025.

Oswald, P., Geist, D., Harpp, K., Christensen, B., and Wallace, P., 2007, Differentiation of historical Hekla magmas: Abstract V13C-1493 presented at 2007 Fall Meeting, AGU, San Francisco, California, 10-14 December.

Ottino, J. M., 1989, The Kinematics of Mixing: Stretching, Chaos, and Transport: Cambridge, United Kingdom, Cambridge University Press, 396 p.

Owen, J., Tuffen, H., and McGarvie, D. W., 2013a, Explosive subglacial rhyolitic eruptions in Iceland are fuelled by high magmatic H_2O and closed-system degassing: Geology, v. 41, p. 251-254.

Owen, J., Tuffen, H., and McGarvie, D. W., 2013b, Pre-eruptive volatile content, degassing paths and depressurisation explaining the transition in style at the subglacial rhyolitic eruption of Dalakvísl, South Iceland: Journal of Volcanology and Geothermal Research, v. 258, p. 143-162.

Padilla, A. J., Miller, C. F., Carley, T. L., Economos, R. C., Schmitt, A. K., Coble, M. A., Wooden, J. L., Fisher, C. M., Vervoort, J. D., and Hanchar, J. M., 2016, Elucidating the magmatic history of the Austurhorn silicic intrusive complex (southeast Iceland) using zircon elemental and isotopic geochemistry and geochronology: Contributions to Mineralogy and Petrology, v. 171, p. 69.

Palladino, D. M., and Simei, S., 2005, Eruptive dynamics and caldera collapse during the Onano eruption, Vulsini, Italy: Bulletin of Volcanology, v. 67, p. 423-440.

Pankhurst, M. J., Morgan, D. J., Thordarson, T., and Loughlin, S. C., 2018, Magmatic crystal records in time, space, and process, causatively linked with volcanic unrest: Earth and Planetary Science Letters, v. 493, p. 231-241.

Parnell-Turner, R., White, N., Henstock, T., Murton, B., Maclennan, J., and Jones, S. M., 2014, A continuous 55-million-year record of transient mantle plume activity beneath Iceland: Nature Geoscience, v. 7, p. 914.

Passmore, E., Maclennan, J., Fitton, G., and Thordarson, T., 2012, Mush disaggregation in basaltic magma chambers: Evidence from the AD 1783 Laki eruption: Journal of Petrology, v. 53, p. 2593-2623.

Pearce, J. A., and Cann, J. R., 1973, Tectonic setting of basic volcanic rocks determined using trace element analysis: Earth and Planetary Science Letters, v. 19, p. 290-300.

Pérez, W., and Freundt, A., 2006, The youngest highly explosive basaltic eruptions from Masaya Caldera (Nicaragua): Stratigraphy and hazard assessment, *in* Rose, W. I., Bluth, G. J. S., Carr, M. J., Ewert, J. W., Patino, L. C., and Vallance, J. W., eds., Volcanic Hazards in Central America, Geological Society of America Special Paper 412, p. 189-207.

Perrotta, A., and Scarpati, C., 1994, The dynamics of the Breccia Museo eruption (Campi Flegrei, Italy) and the significance of spatter clasts associated with lithic breccias: Journal of Volcanology and Geothermal Research, v. 59, p. 335-355.

Perugini, D., Poli, G., and Gatta, G. D., 2002, Analysis and simulation of magma mixing processes in 3D: Lithos, v. 65, p. 313-330.

Perugini, D., Poli, G., and Mazzuoli, R., 2003, Chaotic advection, fractals and diffusion during mixing of magmas: evidence from lava flows: Journal of Volcanology and Geothermal Research, v. 124, p. 255-279.

Perugini, D., Ventura, G., Petrelli, M., and Poli, G., 2004, Kinematic significance of morphological structures generated by mixing of magmas: a case study from Salina Island (southern Italy): Earth and Planetary Science Letters, v. 222, p. 1051-1066.

Perugini, D., Petrelli, M., and Poli, G., 2006, Diffusive fractionation of trace elements by chaotic mixing of magmas: Earth and Planetary Science Letters, v. 243, p. 669-680.

Perugini, D., De Campos, C. P., Dingwell, D. B., Petrelli, M., and Poli, G., 2008, Trace element mobility during magma mixing: Preliminary experimental results: Chemical Geology, v. 256, p. 146-157.

Perugini, D., De Campos, C. P., Dingwell, D. B., and Dorfman, A., 2013, Relaxation of concentration variance: A new tool to measure chemical element mobility during mixing of magmas: Chemical Geology, v. 335, p. 8-23.

Perugini, D., De Campos, C. P., Petrelli, M., and Dingwell, D. B., 2015, Concentration variance decay during magma mixing: a volcanic chronometer: Scientific Reports, v. 5, p. 14225.

Petrelli, M., Poli, G., Perugini, D., and Peccerillo, A., 2005, PetroGraph: A new software to visualize, model, and present geochemical data in igneous petrology: Geochemistry, Geophysics, Geosystems, v. 6, p. 1-15.

Petrelli, M., Perugini, D., and Poli, G., 2011, Transition to chaos and implications for time-scales of magma hybridization during mixing processes in magma chambers: Lithos, v. 125, p. 211-220.

Petrelli, M., Morgavi, D., Vetere, F., and Perugini, D., 2016, Elemental imaging and petro-volcanological applications of an improved laser ablation inductively coupled quadrupole plasma mass spectrometry: Periodico di Mineralogia, v. 85, p. 25-39.

Pioli, L., and Rosi, M., 2005, Rheomorphic structures in a high-grade ignimbrite: the Nuraxi tuff, Sulcis volcanic district (SW Sardinia, Italy): Journal of Volcanology and Geothermal Research, v. 142, p. 11-28.

Plail, M., Edmonds, M., Woods, A. W., Barclay, J., Humphreys, M. C. S., Herd, R. A., and Christopher, T., 2018, Mafic enclaves record syn-eruptive basalt intrusion and mixing: Earth and Planetary Science Letters, v. 484, p. 30-40.

Polacci, M., Arzilli, F. La Spina, G. Le Gall, N. Cai, B. Hartley, M. E. Di Genova, D. Vo, N. T. Nonni, S. Atwood, R. C. Llewellin, E. W. Lee, P. D., and Burton, M. R., 2018, Crystallisation in basaltic magmas revealed via in situ 4D synchrotron X-ray microtomography: Scientific Reports, v. 8, p. 8377.

Poli, G., and Perugini, D., 2002, Strange attractors in magmas: evidence from lava flows: Lithos, v. 65, p. 287-297.

Pope, E. C., Bird, D. K., and Arnórsson, S., 2013, Evolution of low-^{18}O Icelandic crust: Earth and Planetary Science Letters, v. 374, p. 47-59.

Porter, C., Morin, P., Howat, I., Noh, M.-J., Bates, B., Peterman, K., Keesey, S., Schlenk, M., Gardiner, J., Tomko, K., Willis, M., Kelleher, C., Cloutier, M., Husby, E., Foga, S., Nakamura, H., Platson, M., Wethington, M., Jr., Williamson, C., Bauer, G., Enos, J., Arnold, G., Kramer, W., Becker, P., Doshi, A., D'Souza, C., Cummens, P., Laurier, F., and Bojesen, M., 2018, Arctic DEM: Harvard Dataverse, v. 1, https://www.pgc.umn.edu/data/arcticdem/.

Portnyagin, M., Hoernle, K., Storm, S., Mironov, N., van den Bogaard, C., and Botcharnikov, R., 2012, H_2O-rich melt inclusions in fayalitic olivine from Hekla volcano: Implications for phase relationships in silicic systems and driving forces of explosive volcanism on Iceland: Earth and Planetary Science Letters, v. 357-358, p. 337-346.

Potuzak, M., Nichols, A. R. L., Dingwell, D. B., and Clague, D. A., 2008, Hyperquenched volcanic glass from Loihi Seamount, Hawaii: Earth and Planetary Science Letters, v. 270, p. 54-62.

Prestvik, T., 1980, Petrology of hybrid intermediate and silicic rocks from Öræfajökull, southeast Iceland: Geologiska Föreningen i Stockholm Förhandlingar, v. 101, p. 299-307.

Prestvik, T., Goldberg, S., Karlsson, H., and Grönvold, K., 2001, Anomalous strontium and lead isotope signatures in the off-rift Öræfajökull central volcano in south-east Iceland: Evidence for enriched endmember(s) of the Iceland mantle plume?: Earth and Planetary Science Letters, v. 190, p. 211-220.

Putirka, K. D., 2008, Thermometers and barometers for volcanic systems: Reviews in Mineralogy and Geochemistry, v. 69, p. 61-120.

Reid, M. R., and Vazquez, J. A., 2017, Fitful and protracted magma assembly leading to a giant eruption, Youngest Toba Tuff, Indonesia: Geochemistry, Geophysics, Geosystems, v. 18, p. 156-177.

Reimink, J. R., Chacko, T., Stern, R. A., and Heaman, L. M., 2010, Earth's earliest evolved crust generated in an Iceland-like setting: Nature Geoscience, v. 7, p. 529-533.

Robert, G., Andrews, G. D. M., Ye, J., and Whittington, A. G., 2013, Rheological controls on the emplacement of extremely high-grade ignimbrites: Geology, v. 41, p. 1031-1034.

Robin, C., Eissen, J. P., and Monzier, M., 1994, Ignimbrites of basaltic andesite and andesite compositions from Tanna, New Hebrides Arc: Bulletin of Volcanology, v. 56, p. 10-22.

Robin, C., Eissen, J.-P., and Monzier, M., 1995, Mafic pyroclastic flows at Santa Maria (Gaua) Volcano, Vanuatu: the caldera formation problem in mainly mafic island arc volcanoes: Terra Nova, v. 7, p. 436-443.

Roche, O., and Druitt, T., 2001, Onset of caldera collapse during ignimbrite eruptions: Earth and Planetary Science Letters, v. 191, p. 191-202.

Roman, D. C., and Cashman, K. V., Top-down precursory volcanic seismicity: Implications for 'stealth' magma ascent and long-term eruption forecasting: Frontiers in Earth Science, v. 6, p. 124.

Rooyakkers, S. M., Wilson, C. J. N., Schipper, C. I., Barker, S. J., and Allan, A. S. R., 2018, Textural and micro-analytical insights into mafic–felsic interactions during the Oruanui eruption, Taupo: Contributions to Mineralogy and Petrology, v. 173, p. 35.

Rooyakkers, S. M., Stix, J., Berlo, K., and Barker, S. J., 2020, Emplacement of unusual rhyolitic to basaltic ignimbrites during collapse of a basalt-dominated caldera: The Halarauður eruption, Krafla (Iceland): Geological Society of America Bulletin, (in press).

Rosi, M., Vezzoli, L., Aleotti, P., and De Censi, M., 1996, Interaction between caldera collapse and eruptive dynamics during the Campanian Ignimbrite eruption, Phlegraean Fields, Italy: Bulletin of Volcanology, v. 57, p. 541-554.

Ruprecht, P., and Wörner, G., 2007, Variable regimes in magma systems documented in plagioclase zoning patterns: El Misti stratovolcano and Andahua monogenetic cones: Journal of Volcanology and Geothermal Research, v. 165, p. 142-162.

Sable, J. E., Houghton, B. F., Wilson, C. J. N., and Carey, R. J., 2006, Complex proximal sedimentation from Plinian plumes: The example of Tarawera 1886: Bulletin of Volcanology, v. 69, p. 89-103.

Sæmundsson, K., 1974, Evolution of the axial rifting zone in northern Iceland and the Tjörnes Fracture Zone: Geological Society of America Bulletin, v. 85, p. 495-504.

Sæmundsson, K, 1978, Fissure swarms and central volcanoes of the neovolcanic zones of Iceland: Geological Journal, special issue, v. 10, p. 415-432.

Sæmundsson, K, 1979, Outline of the geology of Iceland: Jökull, v. 29, p. 7-27.

Sæmundsson, K., 1982, Öskjur á virkum eldfjallasvæðum á Íslandi (Calderas within the active volcanic zones of Iceland), *in* Þórarinsdóttir, H., Óskarsson, O.H., Stein*þór*sson, S., and Einarsson, Th., eds., Eldur er í norðri (Fire in the north): Reykjavik, Sögufélag, p. 221-239.

Sæmundsson, K., 1991, Jarðfræði Kröflukerfisins (Geology of the Krafla volcanic system), *in* Garðarson, A., and Einarsson, Á., eds., Náttúra Mývatns (Mývatn's Nature): Reykjavík, Hid íslenska náttúrufræðifélag, p. 24–95.

Sæmundsson, K., 2008, Krafla. Geological Map: Iceland Geosurvey and Landsvirkjun, scale 1:25,000.

Sæmundsson, K., and Pringle, M. S., 2000, Um aldur berglaga Í Kröflukerfinu (On the age of rock strata in the Krafla system): Geoscience Society of Iceland Spring Meeting, Reykjavík, Abstracts, p. 26-27.

Sæmundsson, K., Hjartarson, Á., Kaldal, I., Sigurgeirsson, M. A., Kristinsson, S. G., and Vikingsson, S., 2012, Geological map of the Northern volcanic zone, Iceland, Northern part: Iceland Geosurvey and Landsvirkjun, scale 1:100,000.

Schattel, N., Portnyagin, M., Golowin, R., Hoernle, K., and Bindeman, I., 2014, Contrasting conditions of rift and off-rift silicic magma origin on Iceland: Geophysical Research Letters, v. 41, p. 5813-5820.

Schiavi, F., Walte, N., and Keppler, H., 2009, First in situ observation of crystallization processes in a basaltic-andesitic melt with the moissanite cell: Geology, v. 37, p. 963-966.

Schiffman, P., Zierenberg, R. A., Mortensen, A. K., Friðleifsson, G. Ó., and Elders, W. A., 2014, High temperature metamorphism in the conductive boundary layer adjacent to a rhyolite intrusion in the Krafla geothermal system, Iceland: Geothermics, v. 49, p. 42-48.

Schmincke, H. U., Viereck, L. G., Griffin, B. J., and Pritchard, R. G., 1982, Volcaniclastic rocks of the Reydarfjördur drill hole, eastern Iceland: 1. Primary features: Journal of Geophysical Research: Solid Earth, v. 87, p. 6437-6458.

Schuler, J., Greenfield, T., White, R. S., Roecker, S. W., Brandsdóttir, B., Stock, J. M., Tarasewicz, J., Martens, H. R., and Pugh, D., 2015, Seismic imaging of the shallow crust beneath the Krafla central volcano, NE Iceland: Journal of Geophysical Research: Solid Earth, v. 120, p. 7156-7173.

Selbekk, R. S., and Trønnes, R. G., 2007, The 1362 AD Öræfajökull eruption, Iceland: Petrology and geochemistry of large-volume homogeneous rhyolite: Journal of Volcanology and Geothermal Research, v. 160, p. 42-58.

Self, S., 2006, The effects and consequences of very large explosive volcanic eruptions: Philosophical Transactions of the Royal Society a-Mathematical Physical and Engineering Sciences, v. 364, p. 2073-2097.

Sharma, K., Self, S., Blake, S., Thordarson, T., and Larsen, G., 2008, The AD 1362 Öræfajökull eruption, S.E. Iceland: Physical volcanology and volatile release: Journal of Volcanology and Geothermal Research, v. 178, p. 719-739.

Shea, T., and Hammer, J. E., 2013, Kinetics of cooling- and decompression-induced crystallization in hydrous mafic-intermediate magmas: Journal of Volcanology and Geothermal Research, v. 260, p. 127-145.

Shea, T., Gurioli, L., Houghton, B. F., Cioni, R., and Cashman, K. V., 2011, Column collapse and generation of pyroclastic density currents during the A.D. 79 eruption of Vesuvius: The role of pyroclast density: Geology, v.39, p. 695-698.

Sigmarsson, O., Hémond, C., Condomines, M., Fourcade, S., and Oskarsson, N., 1991, Origin of silicic magma in Iceland revealed by Th isotopes: Geology, v. 19, p. 621-624.

Sigmarsson, O., Condomines, M., and Fourcade, S., 1992, A detailed Th, Sr and O isotope study of Hekla: differentiation processes in an Icelandic Volcano: Contributions to Mineralogy and Petrology, v. 112, p. 20-34.

Sigmarsson, O., Vlastelic, I., Andreasen, R., Bindeman, I., Devidal, J. L., Moune, S., Keiding, J. K., Larsen, G., Höskuldsson, A., Thordarson, T., 2011, Remobilization of silicic intrusion by mafic magmas during the 2010 Eyjafjallajökull eruption: Solid Earth, v. 2, p. 271-281.

Sigmundsson, F., 2006, Iceland Geodynamics: Crustal Deformation and Divergent Plate Tectonics: Berlin, Springer-Verlag, 214 p.

Sigmundsson, F., Hreinsdóttir, S., Hooper, A., Árnadóttir, T., Pedersen, R., Roberts, M. J., Óskarsson, N., Auriac, A., Decriem, J., Einarsson, P., Geirsson, H., Hensch, M., Ófeigsson, B. G., Sturkell, E., Sveinbjörnsson, H., and Feigl, K. L., 2010, Intrusion triggering of the 2010 Eyjafjallajökull explosive eruption: Nature, v. 468, p. 426-430.

Sigmundsson, F., Hooper, A., Hreinsdóttir, S., Vogfjörd, K. S., Ófeigsson, B. G., Heimisson, E. R., Dumont, S., Parks, M., Spaans, K., Gudmundsson, G. B., Drouin, V., Árnadóttir, T., Jónsdóttir, K., Gudmundsson, M. T., Högnadóttir, T., Fridriksdóttir, H. M., Hensch, M., Einarsson, P., Magnússon, E., Samsonov, S., Brandsdóttir, B., White, R. S., Ágústsdóttir, T., Greenfield, T., Green, R. G., Hjartardóttir, Á R., Pedersen, R., Bennett, R. A., Geirsson, H., la Femina, P. C., Björnsson, H., Pálsson, F., Sturkell, E., Bean, C. J., Möllhoff, M., Braiden, A. K., and Eibl, E. P. S.., 2015, Segmented lateral dyke growth in a rifting event at Bárðarbunga volcanic system, Iceland: Nature, v. 517, p. 191-195.

Sigmundsson, F, Einarsson, P., Hjartardóttir, Á. R., Drouin, V., Jónsdóttir, K., Árnadóttir, T., Geirsson, H., Hreinsdóttir, S., Li, S., and Ófeigsson, B. G., 2020, Geodynamics of Iceland and the signatures of plate spreading: Journal of Volcanology and Geothermal Research, v. 391, p. 106436.

Sigurdsson, H., 1968, Petrology of acid xenoliths from Surtsey: Geological Magazine, v. 105, p. 440-453.

Sigurdsson, H., 1970, The petrology and chemistry of the Setberg volcanic region and of the intermediate and acid rocks of Iceland [Ph.D. thesis]: Durham, United Kingdom, Durham University, 321 p.

Sigurdsson, H., 1971, Feldspar relations in Icelandic alkalic rhyolites: Mineralogical Magazine, v. 38, p. 503-510.

Sigurdsson, H., 1977, Generation of Icelandic rhyolites by melting of plagiogranites in the oceanic layer: Nature, v. 269, p. 25-28.

Sigurdsson, H., and Carey, S., 1989, Plinian and co-ignimbrite tephra fall from the 1815 eruption of Tambora volcano: Bulletin of Volcanology, v. 51, p. 243-270.

Sigurdsson, H., and Sparks, R. S. J., 1978, Rifting episode in north Iceland in 1874–1875 and the eruptions of Askja and Sveinagja: Bulletin Volcanologique, v. 41, p. 149-167.

Sigurdsson, H., and Sparks, R. S. J., 1981, Petrology of rhyolitic and mixed magma ejecta from the 1875 Eruption of Askja, Iceland: Journal of Petrology, v. 22, p. 41-84.

Sigvaldason, G. E., 1974, The petrology of Hekla and origin of silicic rocks in Iceland, in Einarsson, T., Kjartansson, G., and Thorarinsson, S., eds., The Eruption of Hekla 1947-1948, Volume 1: Reykjavik, Societas Scientiarum Islandica, p. 1-44.

Sigvaldason, G. E., 1979, Rifting, magmatic activity and interaction between acid and basic liquids: Nordic Volcanological Institute Report 79 03, 54 p.

Sigvaldason, G. E., 2002, Volcanic and tectonic processes coinciding with glaciation and crustal rebound: an early Holocene rhyolitic eruption in the Dyngjufjöll volcanic centre and the formation of the Askja caldera, north Iceland: Bulletin of Volcanology, v. 64, p. 192-205.

Silva Parejas, C., Druitt, T. H., Robin, C., Moreno, H., and Naranjo, J.-A., 2010, The Holocene Pucón eruption of Volcán Villarrica, Chile: deposit architecture and eruption chronology: Bulletin of Volcanology, v. 72, p. 677-692.

Simakin, A. G., and Bindeman, I. N., 2012, Remelting in caldera and rift environments and the genesis of hot, "recycled" rhyolites: Earth and Planetary Science Letters, v. 337-338, p. 224-235.

Simmons, J. M., Cas, R. A. F., Druitt, T. H., and Carey, R. J., 2017, The initiation and development of a caldera-forming Plinian eruption (172 ka Lower Pumice 2 eruption, Santorini, Greece): Journal of Volcanology and Geothermal Research, v. 341, p. 332-350.

Singer, B. S., Costa, F., Herrin, J. S., Hildreth, W., and Fierstein, J., 2016, The timing of compositionally-zoned magma reservoirs and mafic 'priming' weeks before the 1912 Novarupta-Katmai rhyolite eruption: Earth and Planetary Science Letters, v. 451, p. 125-137.

Slater, L., Jull, M., McKenzie, D., and Gronvöld, K., 1998, Deglaciation effects on mantle melting under Iceland: results from the northern volcanic zone: Earth and Planetary Science Letters, v. 164, p. 151-164.

Smallwood, J. R., and White, R. S., 2002, Ridge-plume interaction in the North Atlantic and its influence on continental breakup and seafloor spreading: Geological Society, London, Special Publications, v. 197, p. 15-37.

Smith, P. M., and Asimow, P. D., 2005, Adiabat_1ph: A new public front-end to the MELTS, pMELTS, and pHMELTS models: Geochemistry, Geophysics, Geosystems, v. 6, p. 1-8.

Smith, R. L., 1960, Ash flows: Geological Society of America Bulletin, v. 71, p. 795-841.

Smith, R. L., and Bailey, R. A., 1966, The Bandelier Tuff: A study of ash-flow eruption cycles from zoned magma chambers: Bulletin Volcanologique, v. 29, p. 83-103.

Snyder, D., Crambes, C., Tait, S., and Wiebe, R. A., 1997, Magma mingling in dikes and sills: Journal of Geology, v. 105, p. 75-86.

Sparks, R. S. J., 1976, Grain size variations in ignimbrites and implications for the transport of pyroclastic flows: Sedimentology, v. 23, p. 147-188.

Sparks, R. S. J., and Marshall, L. A., 1986, Thermal and mechanical constraints on mixing between mafic and silicic magmas: Journal of Volcanology and Geothermal Research, v. 29, p. 99-124.

Sparks, R. S. J., and Walker, G. P. L., 1977, Significance of vitric-enriched air-fall ashes associated with crystal-enriched ignimbrites: Journal of Volcanology and Geothermal Research, v. 2, p. 329-341.

Sparks, S. R. J., Sigurdsson, H., and Wilson, L., 1977, Magma mixing: A mechanism for triggering acid explosive eruptions: Nature, v. 267, p. 315-318.

Sparks, R. S. J., Wilson, L., and Hulme, G., 1978, Theoretical modeling of the generation, movement, and emplacement of pyroclastic flows by column collapse: Journal of Geophysical Research: Solid Earth, v. 83, p. 1727-1739.

Sparks, R. S. J., Wilson, L., and Sigurdsson, H., 1981, The pyroclastic deposits of the 1875 eruption of Askja, Iceland: Philosophical Transactions of the Royal Society of London A: Mathematical and Physical Sciences, v. 299, p. 241-273.

Spulber, S. D., and Rutherford, M. J., 1983, The origin of rhyolite and plagiogranite in oceanic crust: An experimental study: Journal of Petrology, v. 24, p. 1-25.

Staples, R. K., White, R. S., Brandsdóttir, B., Menke, W., Maguire, P. K. H., and McBride, J. H., 1997, Färoe-Iceland Ridge Experiment 1. Crustal structure of northeastern Iceland: Journal of Geophysical Research: Solid Earth, v. 102, p. 7849-7866.

Steinthórsson, S., Óskarsson, N., Arnórsson, S., and Gunnlaugsson, E., 1987, Metasomatism in Iceland: Hydrothermal alteration and remelting of oceanic crust, *in* Helgeson, H. C., ed., Chemical Transport in Metasomatic Processes: Dordrecht, Netherlands, D. Riedel Publishing Company, p. 355-387.

Stix, J., 2018, Understanding fast and slow unrest at volcanoes and implications for eruption forecasting: Frontiers in Earth Science, v. 6, p. 56.

Stock, M. J., Humphreys, M. C. S., Smith, V. C., Isaia, R., and Pyle, D. M., 2016, Late-stage volatile saturation as a potential trigger for explosive volcanic eruptions: Nature Geoscience, v. 9, p. 249-254.

Stormer, J. C., 1983, The effects of recalculation on estimates of temperature and oxygen fugacity from analyses of multicomponent iron-titanium oxides: American Mineralogist, v. 68, p. 586-594.

Stormer, J. C., and Nicholls, J., 1978, XLFRAC: A program for the interactive testing of magmatic differentiation models: Computers & Geosciences, v. 4, p. 143-159.

Stroeven, A. P., Fabel, D., Harbor, J., Hättestrand, C., and Kleman, J., 2016, Quantifying the erosional impact of the Fennoscandian ice sheet in the Torneträsk-Narvik corridor, northern Sweden, based on cosmogenic radionuclide data. Gografiska Annaler: Series A, Physical Geography, v. 84, p. 275-283.

Sugawara, T., 2001, Ferric iron partitioning between plagioclase and silicate liquid: thermodynamics and petrological applications: Contributions to Mineralogy and Petrology, v. 141, p. 659-686.

Sumner, J., 1998, Formation of clastogenic lava flows during fissure eruption and scoria cone collapse: the 1986 eruption of Izu-Oshima Volcano, eastern Japan: Bulletin of Volcanology, v. 60, p. 195-212.

Sumner, J. M., and Branney, M. J., 2002, The emplacement history of a remarkable heterogeneous, chemically zoned, rheomorphic and locally lava-like ignimbrite: 'TL' on Gran Canaria: Journal of Volcanology and Geothermal Research, v. 115, p. 109-138.

Sun, S.-s., and McDonough, W. F., 1989, Chemical and isotopic systematics of oceanic basalts: implications for mantle composition and processes, *in* Coe, K., ed., Magmatism in the Ocean Basins: Geological Society, London, Special Publications 42, p. 313-345.

Sverrisdottir, G., 2007, Hybrid magma generation preceding Plinian silicic eruptions at Hekla, Iceland: evidence from mineralogy and chemistry of two zoned deposits: Geological Magazine, v. 144, p. 643-659.

Swanson, D. A., Rose, T. R., Mucek, A. E., Garcia, M. O., Fiske, R. S., and Mastin, L. G., 2014, Cycles of explosive and effusive eruptions at Kīlauea Volcano, Hawai'i: Geology, v. 42, p. 631-634.

Thomas, R. M. E., and Sparks, R. S. J., 1992, Cooling of tephra during fallout from eruption columns: Bulletin of Volcanology, v. 54, p. 542-553.

Thorarinsson, S., 1951, Laxárgljúfur and Laxárhraun: a tephrochronological study: Geografiska Annaler, v. 33, p. 1-88.

Thorarinsson, S., 1958, The Öræfajökull eruption of 1362: Acta Naturalia Islandica, v. 2, p. 1-100.

Thorarinsson, S., 1967a, The eruptions of Hekla in historical times: a tephrochronological study, in Einarsson, T., Kjartansson, G., and Thorarinsson, S., eds., The Eruption of Hekla 1947-1948: Reykjavík, Societas Scientiarum Islandica, p. 1-68.

Thorarinsson, S., 1967b, Some problems of volcanism in Iceland: Geologische Rundschau, v. 57, p. 1-20.

Thórarinsson, S. 1969, Ignimbrít í Þórsmórk: Náttúrufræðingurinn, v. 39, p. 139–155.

Thorarinsson, S., 1979, The postglacial history of the Mývatn area: Oikos, v. 32, p. 17-28.

Thorarinsson, S., 1981, Greetings from Iceland: Ash-falls and volcanic aerosols in Scandinavia: Geografiska Annaler. Series A, Physical Geography, v. 63, p. 109-118.

Thordarson, T., and Höskuldsson, Á., 2008, Postglacial volcanism in Iceland: Jökull, v. 58, p. 197-228.

Thordarson, T., and Larsen, G., 2007, Volcanism in Iceland in historical time: Volcano types, eruption styles and eruptive history: Journal of Geodynamics, v. 43, p. 118-152.

Thordarson, T., and Self, S., 1993, The Laki (Skaftár-Fires) and Grímsvötn eruptions in 1783-1785: Bulletin of Volcanology, v. 55, p. 233-263.

Thy, P., Beard, J. S., and Lofgren, G. E., 1990, Experimental constraints on the origin of Icelandic rhyolites: The Journal of Geology, v. 98, p. 417-421.

Tomlinson, E. L., Thordarson, T., Müller, W., Thirlwall, M., and Menzies, M. A., 2010, Microanalysis of tephra by LA-ICP-MS — Strategies, advantages and limitations assessed using the Thorsmörk ignimbrite (Southern Iceland): Chemical Geology, v. 279, p. 73-89.

Tomlinson, E. L., Thordarson, T., Lane, C. S., Smith, V. C., Manning, C. J., Müller, W., and Menzies, M. A., 2012, Petrogenesis of the Sólheimar ignimbrite (Katla, Iceland): Implications for tephrostratigraphy: Geochimica et Cosmochimica Acta, v. 86, p. 318-337.

Trigila, R., and Walker, G. P. L., 1986, The Onano spatter flow, Italy: Evidence for a new ignimbrite depositional mechanism, in International Association of Volcanology and Chemistry of the Earth's Interior (IAVCEI) Volcanological Congress 1986 Abstracts: IAVCEI, p. 81.

Tryggvason, E., 1980, Subsidence events in the Krafla area, North-Iceland, 1975-1979: Journal of Geophysics, v. 47, p. 141-153.

Tryggvason, E., 1984, Widening of the Krafla fissure swarm during the 1975–1981 volcano-tectonic episode: Bulletin Volcanologique, v. 47, p. 47-69.

Tryggvason, E., 1986, Multiple magma reservoirs in a rift zone volcano: Ground deformation and magma transport during the September 1984 eruption of Krafla, Iceland: Journal of Volcanology and Geothermal Research, v. 28, p. 1-44.

Tryggvason, E., 1994, Surface deformation at the Krafla volcano, North Iceland, 1982–1992: Bulletin of Volcanology, v. 56, p. 98-107.

Tryggvason, T, and White, D. E., 1955, Rhyolitic tuffs in lower Tertiary plateau basalts of eastern Iceland: American Journal of Science, v. 253, p. 26-38.

Tuffen, H., and Castro, J. M., 2009, The emplacement of an obsidian dyke through thin ice: Hrafntinnuhryggur, Krafla Iceland: Journal of Volcanology and Geothermal Research, v. 185, p. 352-366.

Turbeville, B. N., 1992, Tephra fountaining, rheomorphism, and spatter flow during emplacement of the Pitigliano Tuffs, Latera caldera, Italy: Journal of Volcanology and Geothermal Research, v. 53, p. 309-327.

Ubide, T., and Kamber, B. S., 2018, Volcanic crystals as time capsules of eruption history: Nature communications, v. 9, p. 326.

Valentine, G. A., Perry, F. V., and WoldeGabriel, G., 2000, Field characteristics of deposits from spatter-rich pyroclastic density currents at Summer Coon volcano, Colorado: Journal of Volcanology and Geothermal Research, v. 104, p. 187-199.

Vance, J. A., 1969, On synneusis: Contributions to Mineralogy and Petrology, v. 24, p. 7-29.

Van Vliet-Lanoë, B., Bourgeois, O., Dauteuil, O., Embry, J. C., Schneider, J. L., and Guillou, H., 2005, Deglaciation and volcano-seismic activity in Northern Iceland: Holocene and early Eemian: Geodinamica Acta, v. 18, p. 81-100.

Van Vliet-Lanoë, B., Guðmundsson, A., Guillou, H., Guégan, S., van Loon, A. J., and De Vleeschouwer, F., 2010, Glacial terminations II and I as recorded in NE Iceland: Geologos, v. 16, p. 201-222.

Venezky, D. Y., and Rutherford, M. J., 1999, Petrology and Fe-Ti oxide reequilibration of the 1991 Mount Unzen mixed magma: Journal of Volcanology and Geothermal Research, v. 89, p. 213-230.

Viccaro, M., Giuffrida, M., Nicotra, E., and Cristofolini, R., 2016, Timescales of magma storage and migration recorded by olivine crystals in basalts of the March–April 2010 eruption at Eyjafjallajökull volcano, Iceland: American Mineralogist, v. 101, p. 222-230.

Vink, G. E., 1984, A hotspot model for Iceland and the Vøring Plateau: Journal of Geophysical Research: Solid Earth, v. 89, p. 9949-9959.

Wada, K., 1995, Fractal structure of heterogeneous ejecta from the Me-akan volcano, eastern Hokkaido, Japan: implications for mixing mechanism in a volcanic conduit: Journal of Volcanology and Geothermal Research, v. 66, p. 69-79.

Walker, G. P. L., 1962, Tertiary welded tuffs in eastern Iceland: Quarterly Journal of the Geological Society, v. 118, p. 275-290.

Walker, G. P. L., 1963, The Breiddalur central volcano, eastern Iceland: Quarterly Journal of the Geological Society, v. 119, p. 29.

Walker, G. P. L., 1966, Acid volcanic rocks in Iceland: Bulletin Volcanologique, v. 29, p. 375-402.

Walker, G. P. L., 1985, Origin of coarse lithic breccias near ignimbrite source vents: Journal of Volcanology and Geothermal Research, v. 25, p. 157-171.

Walker, G. P. L., 1988, Three Hawaiian calderas: An origin through loading by shallow intrusions?: Journal of Geophysical Research: Solid Earth, v. 93, p. 14773-14784.

Walker, G. P. L., and Skelhorn, R. R., 1966, Some associations of acid and basic igneous rocks: Earth Science Reviews, v. 2, p. 93-109.

Warshaw, C. M., and Smith, R. L., 1988, Pyroxenes and fayalites in the Bandelier Tuff, New Mexico; temperatures and comparison with other rhyolites: American Mineralogist, v. 73, p. 1025-1037.

Wastegård, S., and Davies, S. M., 2009, An overview of distal tephrochronology in northern Europe during the last 1000 years: Journal of Quaternary Science, v. 24, p. 500-512.

Waters, L. E., and Lange, R. A., 2015, An updated calibration of the plagioclase-liquid hygrometer-thermometer applicable to basalts through rhyolites: American Mineralogist, v. 100, p. 2172-2184.

Watson, E. J., Swindles, G. T., Savov, I. P., Lawson, I. T., Connor, C. B., and Wilson, J. A., 2017, Estimating the frequency of volcanic ash clouds over northern Europe: Earth and Planetary Science Letters, v. 460, p. 41-49.

Weber, G., and Castro, J. M., 2017, Phase petrology reveals shallow magma storage prior to large explosive silicic eruptions at Hekla volcano, Iceland: Earth and Planetary Science Letters, v. 466, p. 168-180.

Weisenberger, T. B., Axelsson, G., Arnaldsson, A., Blischke, A., Óskarsson, F., Ármannsson, H., Blanck, H., Helgadóttir, M., Berthet, J. -C. C., Árnason, K., Ágústsson, K., Gylfadóttir, S. S., and Guðmundsdóttir, V., 2015, Revision of the conceptual model of the Krafla geothermal system: Landsvirkjun Report LV-2015-040, 111 p.

Welke, H., Moorbath, S., Cumming, G. L., and Sigurdsson, H., 1968, Lead isotope studies on igneous rocks from Iceland: Earth and Planetary Science Letters, v. 4, p. 221-231.

Wendt, K., Möller, D., and Ritter, B., 1985, Geodetic measurements of surface deformations during the present rifting episode in NE Iceland: Journal of Geophysical Research: Solid Earth, v. 90, p. 10163-10172.

White, R. S., 1997, Rift–plume interaction in the North Atlantic: Philosophical Transactions of the Royal Society of London A: Mathematical, Physical and Engineering Sciences, v. 355, p. 319-339.

Wiebe, R. A., 1994, Silicic magma chambers as traps for basaltic magmas: the Cadillac Mountain intrusive complex, Mount Desert Island, Maine: Journal of Geology, v. 102, p. 423-437.

Willbold, M., Hegner, E., Stracke, A., and Rocholl, A., 2009, Continental geochemical signatures in dacites from Iceland and implications for models of early Archaean crust formation: Earth and Planetary Science Letters, v. 279, p. 44-52.

Willcock, M. A. W., Cas, R. A. F., Giordano, G., and Morelli, C., 2013, The eruption, pyroclastic flow behaviour, and caldera in-filling processes of the extremely large volume (> 1290 km^3), intra- to extra-caldera, Permian Ora (Ignimbrite) Formation, Southern Alps, Italy: Journal of Volcanology and Geothermal Research, v. 265, p. 102-126.

Williams, S. N., 1983, Geology and Eruptive Mechanisms of Masaya Caldera Complex, Nicaragua [Ph.D. thesis]: Hanover, New Hampshire, Dartmouth College, 169 p.

Wilson, C. J. N., and Hildreth, W., 1997, The Bishop Tuff: New insights from eruptive stratigraphy: The Journal of Geology, v. 105, p. 407-440.

Wilson, C. J. N., and Hildreth, W., 2003, Assembling an ignimbrite: Mechanical and thermal building blocks in the Bishop Tuff, California: The Journal of Geology, v. 111, p. 653-670.

Wolfe, C. J., Bjarnason, I. T., VanDecar, J. C., and Solomon, S. C., 1997, Seismic structure of the Iceland mantle plume: Nature, v. 385, p. 245-247.

Wolff, J. A., and Sumner, J. M., 2000, Lava fountains and their products, *in* Sigurdsson, H., Houghton, B., McNutt, S. R., Rymer, H., and Stix, J., eds., Encyclopedia of Volcanoes: New York, Academic Press, p. 321-330.

Wood, B. J., and Blundy, J. D., 1997, A predictive model for rare earth element partitioning between clinopyroxene and anhydrous silicate melt: Contributions to Mineralogy and Petrology, v. 129, p. 166-181.

Wood, D. A., 1978, Major and trace element variations in the Tertiary lavas of eastern Iceland and their significance with respect to the Iceland geochemical anomaly: Journal of Petrology, v. 19, p. 393-436.

Wood, D. A., Gibson, I. L., and Thompson, R. N., 1976, Elemental mobility during zeolite facies metamorphism of the Tertiary basalts of eastern Iceland: Contributions to Mineralogy and Petrology, v. 55, p. 241-254.

Woods, J., Winder, T., White, R. S., and Brandsdóttir, B., 2019, Evolution of a lateral dike intrusion revealed by relatively-relocated dike-induced earthquakes: The 2014–15 Bárðarbunga–Holuhraun rifting event, Iceland: Earth and Planetary Science Letters, v. 506, p. 53-63.

Wright, F. E., 1915, Obsidian from Hrafntinnuhryggur, Iceland: Its lithophysae and surface markings: Geological Society of America Bulletin, v. 26, p. 255-286.

Wright, T. J., Sigmundsson, F., Pagli, C., Belachew, M., Hamling, I. J., Brandsdóttir, B., Keir, D., Pedersen, R., Ayele, A., Ebinger, C., Einarsson, P., Lewi, E., and Calais, E., 2012, Geophysical constraints on the dynamics of spreading centres from rifting episodes on land: Nature Geoscience, v. 5, p. 242-250.

Zellmer, G. F., Rubin, K. H., Grönvold, K., and Jurado-Chichay, Z., 2008, On the recent bimodal magmatic processes and their rates in the Torfajökull–Veidivötn area, Iceland: Earth and Planetary Science Letters, v. 269, p. 388-398.

Zierenberg, R. A., Schiffman, P., Barfod, G. H., Lesher, C. E., Marks, N. E., Lowenstern, J. B., Mortensen, A. K., Pope, E. C., Bird, D. K., Reed, M. H., Friðleifsson, G. O., and Elders, W. A., 2013, Composition and origin of rhyolite melt intersected by drilling in the Krafla geothermal field, Iceland: Contributions to Mineralogy and Petrology, v. 165, p. 327-347.

Appendix 1. Supplemental Methods: Halarauður Deposits

A1.1. Grain Size Analysis

Grain size analyses were performed on non-welded deposits using standard sieving techniques. Deposits were dry-sieved and weighed in the field at 1 ϕ intervals (ϕ = -log$_2$[grain size in mm]) from -6 ϕ (64 mm) to -2 ϕ (4 mm). Approximately 500 g of the sub- -2 ϕ fraction were then sub-sampled for completion in the lab. Each sub-sample was weighed, dried in an oven overnight at 60°C, and then re-weighed to calculate a moisture correction factor for the size classes measured in the field. The sub-samples were then dry-sieved and weighed at 1 ϕ intervals down to 4 ϕ (63 µm). Area fractions for clasts coarser than -6 ϕ were determined from photographs using ImageJ (https://imagej.nih.gov/ij/) and converted to weight % values from clast and matrix densities measured in the lab (following Druitt and Sparks, 1982). Grain size parameters Md$_\phi$ and σ$_\phi$ were calculated after Inman (1952). Considerable breakage of large clasts occurred during sampling for grain size analyses, so grain size data reported here are skewed towards finer sizes.

A1.2. Tephra Componentry Analysis

Tephra componentries (by weight) were determined in the field for all size fractions coarser than -2 ϕ where a significant number of clasts (>100) could be sampled. Clasts in each size fraction were classified as either lithic, white/grey pumice, black pumice, purple/red juvenile scoria, or free crystals. Componentries for the finer fractions down to 2ϕ (250 µm) were determined in the lab from random sub-samples of ≥500 grains. The grains were washed in an ultrasonic bath and dried

overnight in an oven, before classifying for componentry under a binocular microscope. Each class was then weighed on a high-precision balance.

A1.3. Clast Density and Vesicularity Analysis

Densities of coherent welded blocks were determined using techniques similar to Wilson and Hildreth (2003). Fist-sized blocks were dried overnight in an oven at 60° C, before weighing on a laboratory balance (precise to two decimal places). Block volumes were then determined by water displacement, after pre-soaking overnight to prevent ingress of water during measurement. During each measurement, water was displaced through a siphon tube and collected in a beaker on a pre-tared balance. Displaced volumes were calculated assuming a water density of 1000 kg m^{-3}. The water displacement procedure was repeated ten times for each block, yielding a maximum density error estimate of $\pm$ 50 kg m^{-3} (1 σ).

We determined vesicularities of juvenile clasts from non-welded deposits following Houghton and Wilson (1989) and Barker et al. (2012). Clasts from the -4 to -5 ϕ size fraction (16 – 32 mm) were dried in an oven overnight at 60°C, before coating with silicone waterproofing spray to prevent water ingress during measurement. Those with large vesicles (>2 mm) were also wrapped in Parafilm^{TM}, but this was rarely required. Clast densities were then calculated by comparing their weight in air and in water (Archimedes' principle), and converted to vesicularities using measured dense-rock equivalent (DRE) densities (2400 kg m^{-3} for H1, 2600 kg m^{-3} for H2, 2900 kg m^{-3} for H3). Repeat measurements (n = 10) on several representative clasts suggest 2σ precisions of <0.3% and <1.5 % vesicularity for samples measured with and without Parafilm^{TM},

respectively. Use of Parafilm™ introduced a positive bias of 2-5% vesicularity, but because few clasts required this approach, we did not apply a correction.

A1.4. Lithic Componentry Analysis

Lithic componentries for a given stratigraphic interval were determined by classifying a minimum of 150 (usually >200) lithic clasts. We used a broad classification scheme (Table A1.1) to easily classify lithics in the field. Although our scheme is simple, componentry variations were readily captured within single outcrops and between sites.

TABLE A1.1. LITHIC CLASSIFICATION SCHEME

Lithic type	Description
Crystal-poor vesicular basalt	Black or grey (or red-oxidised). ϕ >10%, vesicles mm- to cm-scale. <10 modal% phenocrysts (dominantly plagioclase with subordinate mafic phases). Microcrystalline groundmass.
Dense crystal-poor basalt	Black or grey (or red-oxidised). ϕ <10%, commonly nonvesicular. Porphyritic (or aphyric) with <10 modal% phenocrysts, dominantly mm-scale euhedral plagioclase with subordinate mafic phases (pyroxene + Fe-Ti oxides, olivine rarely present). Microcrystalline groundmass.
Crystal-rich basalt	Black or grey (or red-oxidised). >10 modal% phenocrysts, dominantly mm-scale euhedral plagioclase with subordinate mafic phases (typically pyroxene + Fe-Ti oxides, rarely olivine). Glomerocrysts common. ϕ = 0-30 vol%.
Obsidian	Black glassy groundmass with >20 modal% euhedral plagioclase up to ~2 mm.
Gabbro	Medium- to coarse-grained, phaneritic. Typically porphyritic with ~20-40 modal% white plagioclase phenocrysts, most ~2-5 mm, set in coarse crystalline groundmass of ~40-60 modal% plagioclase and ~40-60 modal% black pyroxene. Generally nonvesicular; a few exceptions contain minor mm-scale voids (ϕ <5%). Most grains >1 mm.
Microgabbro/microdiorite	Fine-grained, phaneritic. Equigranular, or porphyritic with ~5-30 modal% plagioclase phenocrysts up to ~2-3 mm. Light- to dark-grey phaneritic groundmass of ~30-70 modal% plagioclase and ~30-70 modal% black mafic phases (pyroxene + oxides) up to ~1 mm.
Felsite	Fine-grained, phaneritic. Largest grains ~2 mm. ~80-90 modal% felsic minerals (including granophyric quartz-feldspar intergrowths) with ~10-20 modal% equant to elongate black mafic minerals (pyroxene + oxides).
Hyaloclastite	Brown, cemented, palagonitised ash, occasionally hosting angular mafic lapilli. Soft, sandy texture.
Amygdular basalt	Slightly altered basalt with >10 vol% amygdules of white or red secondary minerals. Groundmass may be greenish.
Hydrothermally altered	Blue-grey or red-brown, soft and crumbly, clay-rich with dried/cracked appearance. Occasionally bleached. Easily broken by hand.

A1.5. Whole-Rock Major Element Analysis – X-Ray Fluorescence Spectroscopy (XRF)

Juvenile products were sampled through the stratigraphy at key sites and analyzed for major element contents by X-ray fluorescence spectroscopy (XRF). Single clasts were preferentially sampled where possible; where clast outlines were overprinted by strong to very strong welding, a bulk block was collected. Samples were coarsely crushed, and 50-100 g of ~5 mm fresh chips were hand-picked under a binocular microscope, with care taken to remove any chips containing lithic fragments. The chips were then washed twice with nanopore water in an ultrasonic bath for ~30 minutes, dried overnight in an oven at 60°C, and powdered in an alumina-ceramic mill. Powders were analyzed at either the University of Waikato or the University of Auckland (both in New Zealand). For samples analyzed at Waikato, loss on ignition (LOI) values were calculated after heating in a Nabertherm muffle furnace at 1100°C for one hour. Fusion beads were then prepared in a Claisse Le Neo furnace with a 12:22 ratio of sample to lithium flux, and analyzed with a Bruker S8 Tiger (1kW) XRF spectrometer. For samples analyzed at Auckland, LOI was conducted on all sample powders after heating at 900°C for 16 h. Fusion beads were made from a 2:1 mixture (by mass) of non-ignited powder and lithium meta (64.7%) / tetra (36.3%) borate fused in a PANalytical Eagon 2 at 1000°C for 85 min and analyses were performed on a PANalytical Axios XRF spectrometer. Estimates of analytical precision from repeat analyses of in-house and international standard reference materials at both Auckland and Waikato (detailed in the electronic appendix) are $\leq$3% relative (2σ) for all major elements (usually <1% relative). Mean values are accurate to within 5% (usually within 1-2%) of accepted values.

A1.6. Whole-Rock Trace Element Analysis – Solution Inductively-Coupled Plasma Mass Spectrometry (ICP-MS)

Powdered rock samples were prepared for solution ICP-MS using standard HF digestion techniques in the ultra-clean Geochemistry Laboratory at Victoria University of Wellington (VUW). All procedures used sub-boiling-distilled acids and reagents. Approximately 50 mg of sample powder was weighed into pre-cleaned 23 ml Savillex Teflon® screw-top vials using a high precision balance (to ±0.0001 g), to which ~2 mL of concentrated hydrofluoric acid (29 M HF) and ~0.5 ml HNO_3 (16 M HNO_3) were added. The vials were then capped and placed on a hotplate at 120°C for 3-4 days to ensure complete sample digestion. Following digestion, each solution was evaporated to incipient dryness to prevent sample loss and formation of insoluble fluorides, then refluxed twice in ~2 mL of 6M HCl. The final solutions were checked visually for the presence of any insoluble residues. The final digested solutions were diluted gravimetrically using 3% HNO_3 in pre-cleaned polyethylene labware to a final dilution factor of ~100,000.

Tuning of the ICP-MS was undertaken using a 1 ppb multi-element standard, and the torch position and gas flows adjusted to optimise performance (i.e. low relative standard deviations of <1-2%; low oxide abundances: UO^+/U^+ <6-7 %, BaO^+/Ba^+ <2 %; low doubly charged production: Ba^{++}/Ba^+ <5 %). Some isotopes were analysed at higher resolution to resolve the relevant peak from neighbouring interferences (Sc^{45}, V^{51}, Cr^{52}, Co^{59}, Ni^{60}, Cu^{63}, Zn^{66}, Ga^{69}, Sr^{88}, Zr^{90}, Ba137, Hf177, Ta181) or to attenuate counts on highly abundant isotopes (Ti^{47}, Mn^{55}, Fe^{56}). Solutions were analysed for ~90 s and were preceded by a 240 s washout using 3 % HNO_3.

Concentrations in the unknowns were calculated relative to a calibration curve generated from measurements of multiple dilutions (0.1 ppb, 0.2 ppb, 0.5 ppb, 1 ppb, 2 ppb). These were prepared gravimetrically from a 1 ppm standard solution comprising a mixture of 39 elements which in turn was prepared from commercially available single element 1000 ppm stock solutions. The 0.2 ppb calibration solution was replicated every five samples to monitor and correct for

instrumental drift. Total procedural blanks were <0.1 ppb for all elements, with most within the range of background counts. Estimates of 2σ analytical precision based on repeat analyses of standard reference materials (detailed in the electronic appendix) are $\leq 6\%$ relative (usually ≤ 2-3%), and measured values are accurate to within 10% (commonly within 5%) of reference values for most elements.

Appendix 2. Stratigraphic Logs and Volume Reconstructions for Halarauður Deposits
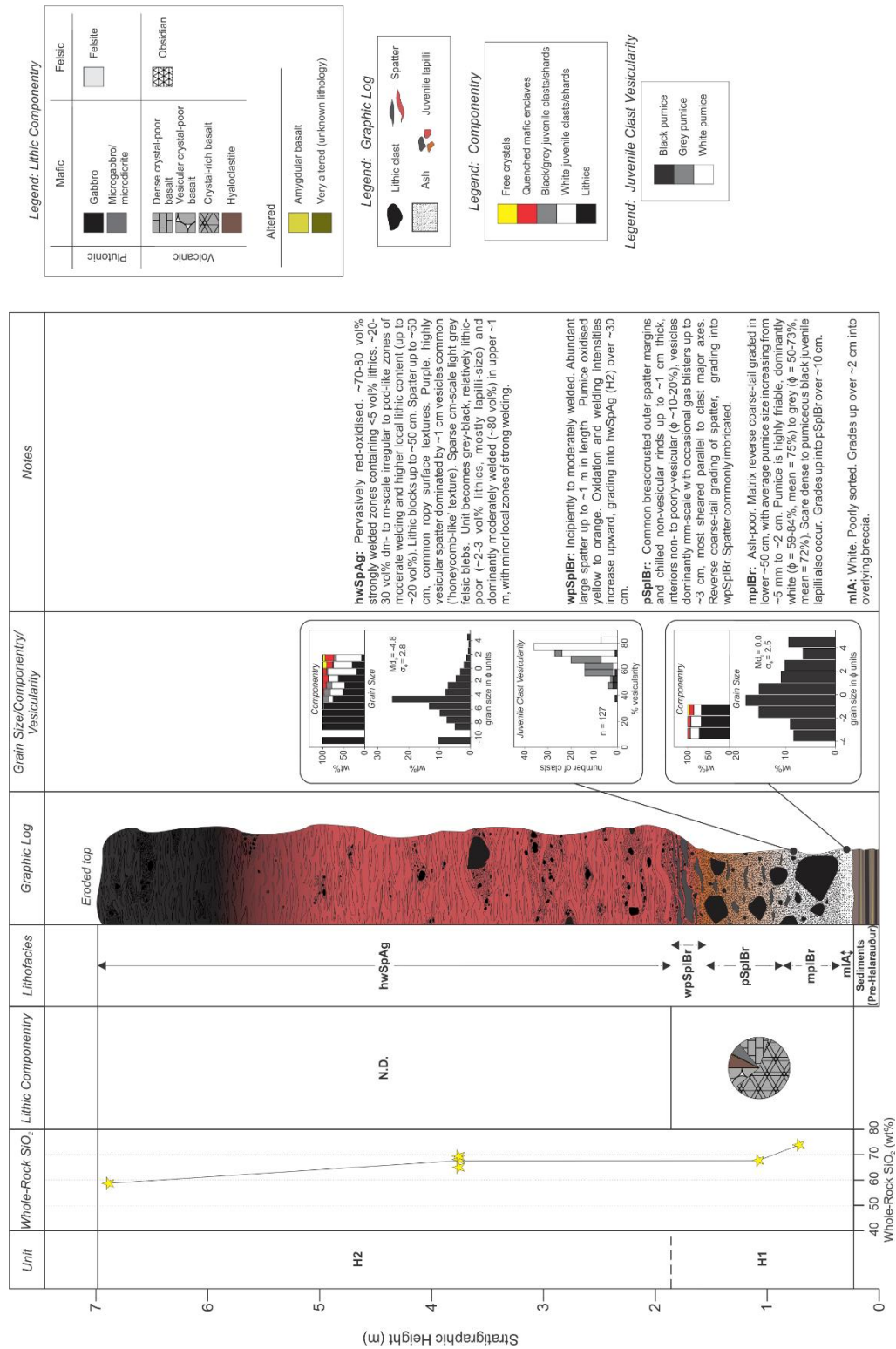

Figure A2.1. Stratigraphic log of site C, showing vertical variations in lithofacies, bulk composition and componentry.
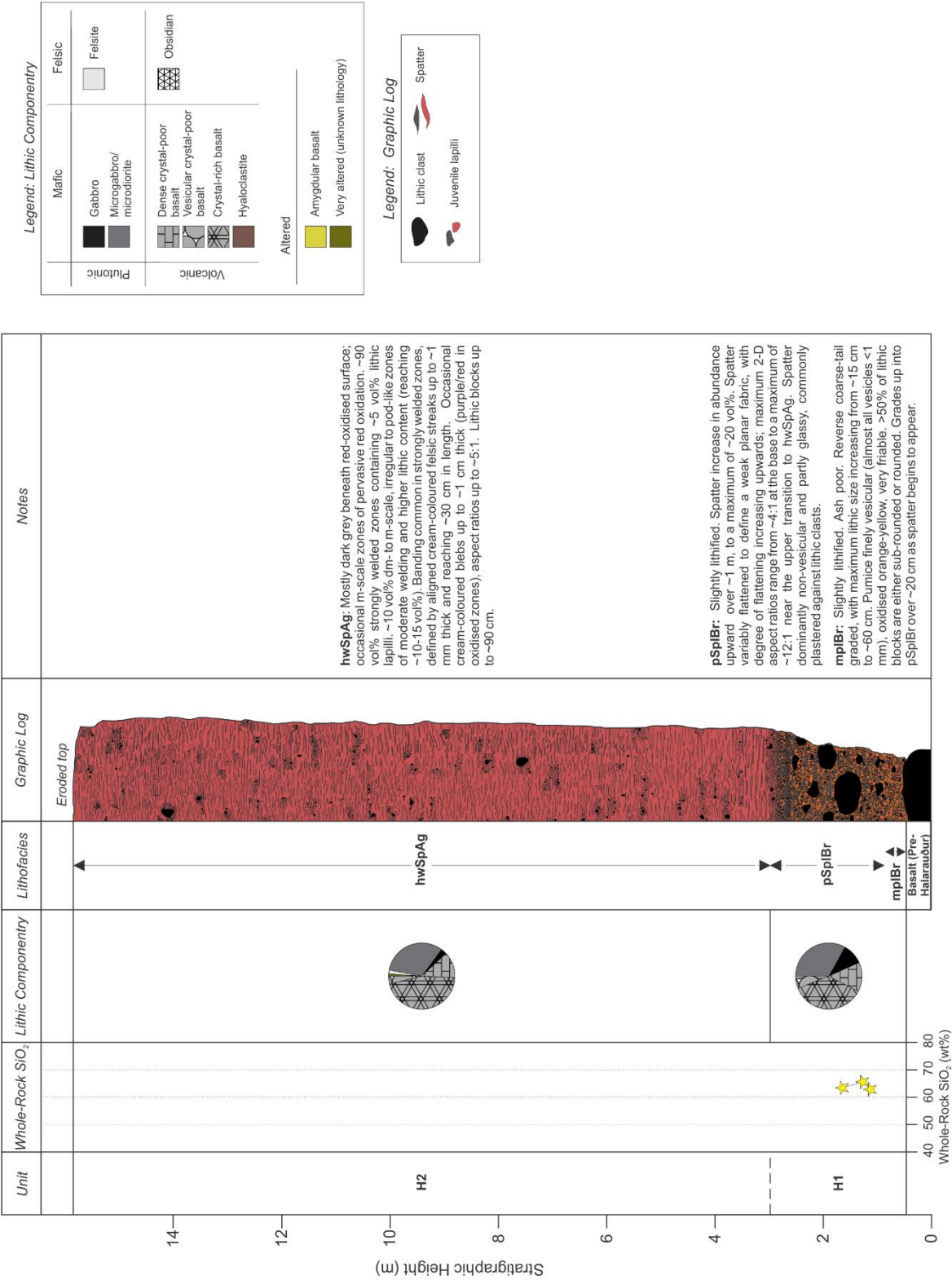
Figure A2.2. Stratigraphic log of site H, showing vertical variations in lithofacies, bulk composition and lithic componentry.
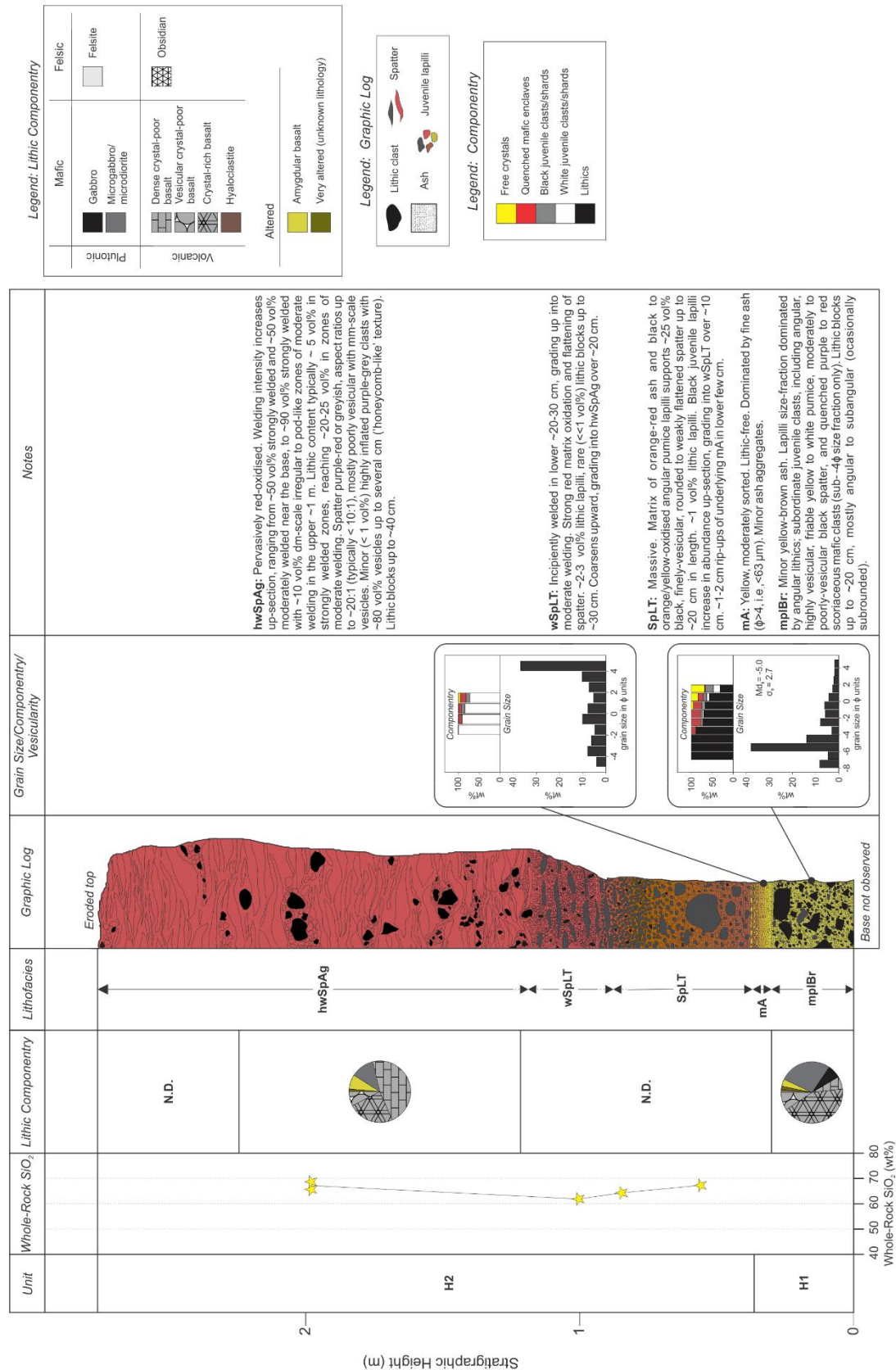
Figure A2.3. Stratigraphic log of site E, showing vertical variations in lithofacies, bulk composition and lithic componentry.

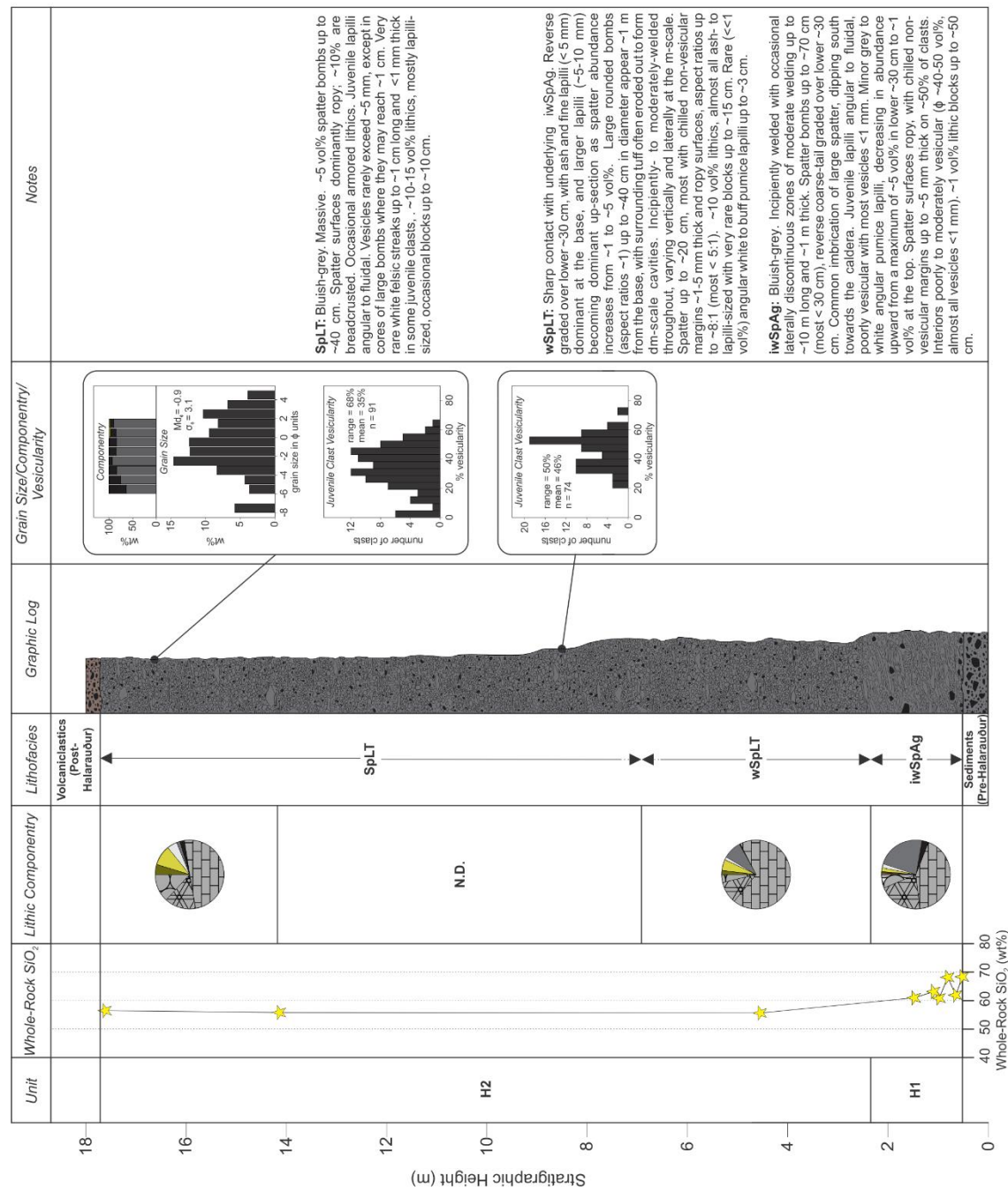**Figure A2.4.** Stratigraphic log of site G, showing vertical variations in lithofacies, bulk composition and lithic componentry.

Figure A2.5. Stratigraphic log of site J, showing vertical variations in lithofacies, bulk composition and componentry.
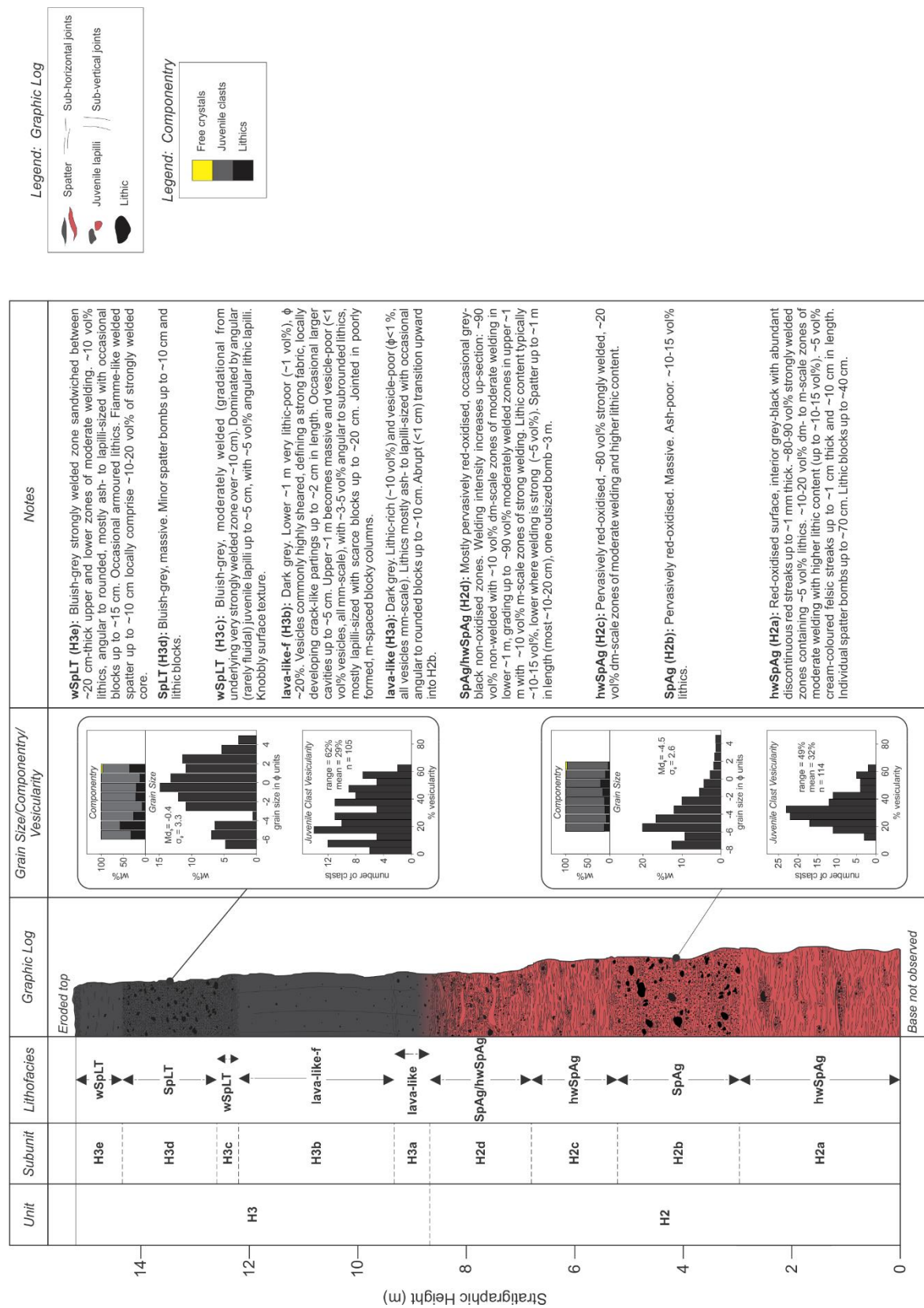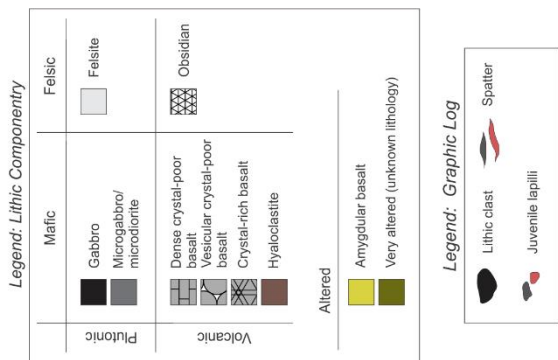
256
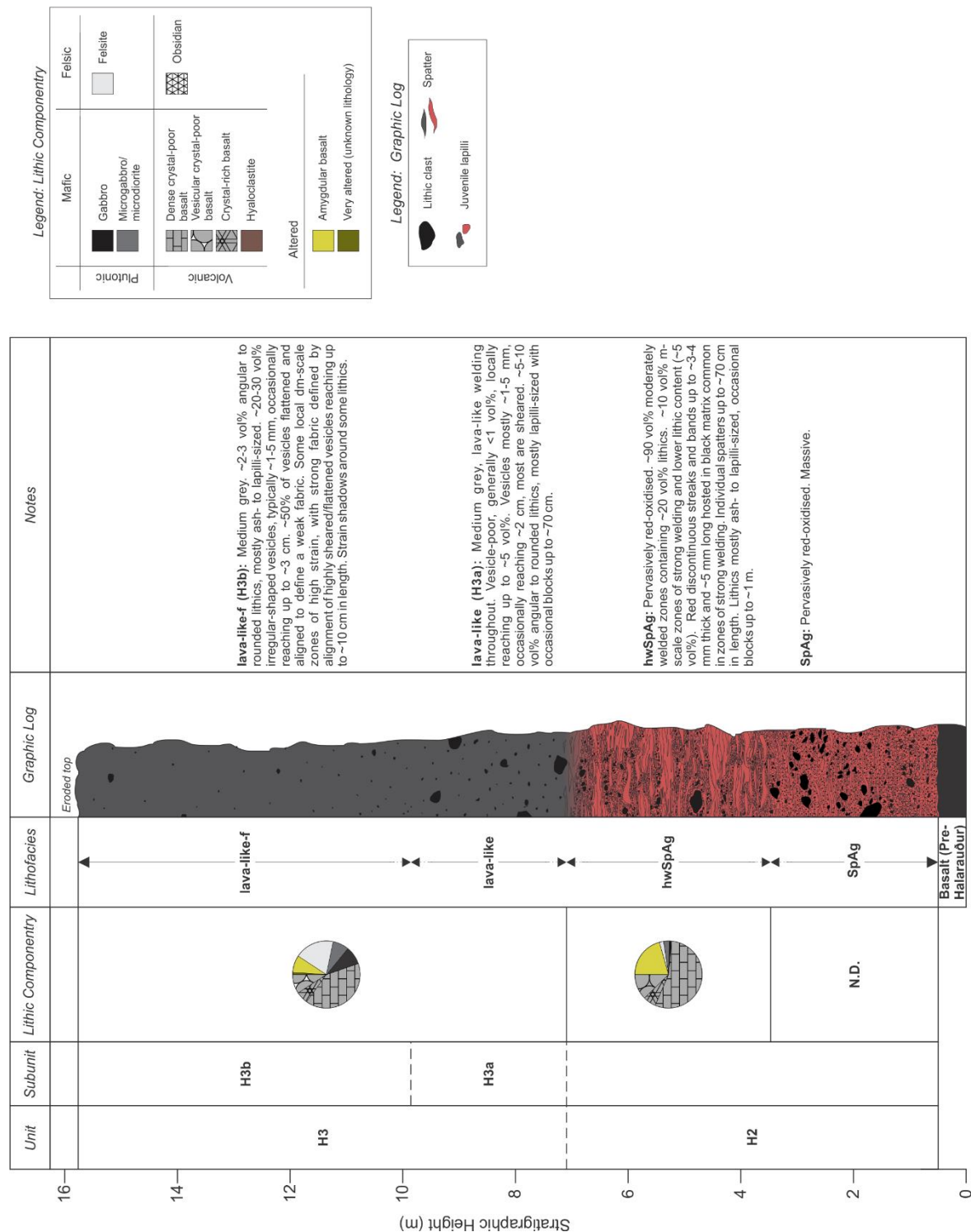
Figure A2.6. Stratigraphic log of site K, showing vertical variations in lithofacies, bulk composition and lithic componentry.

257
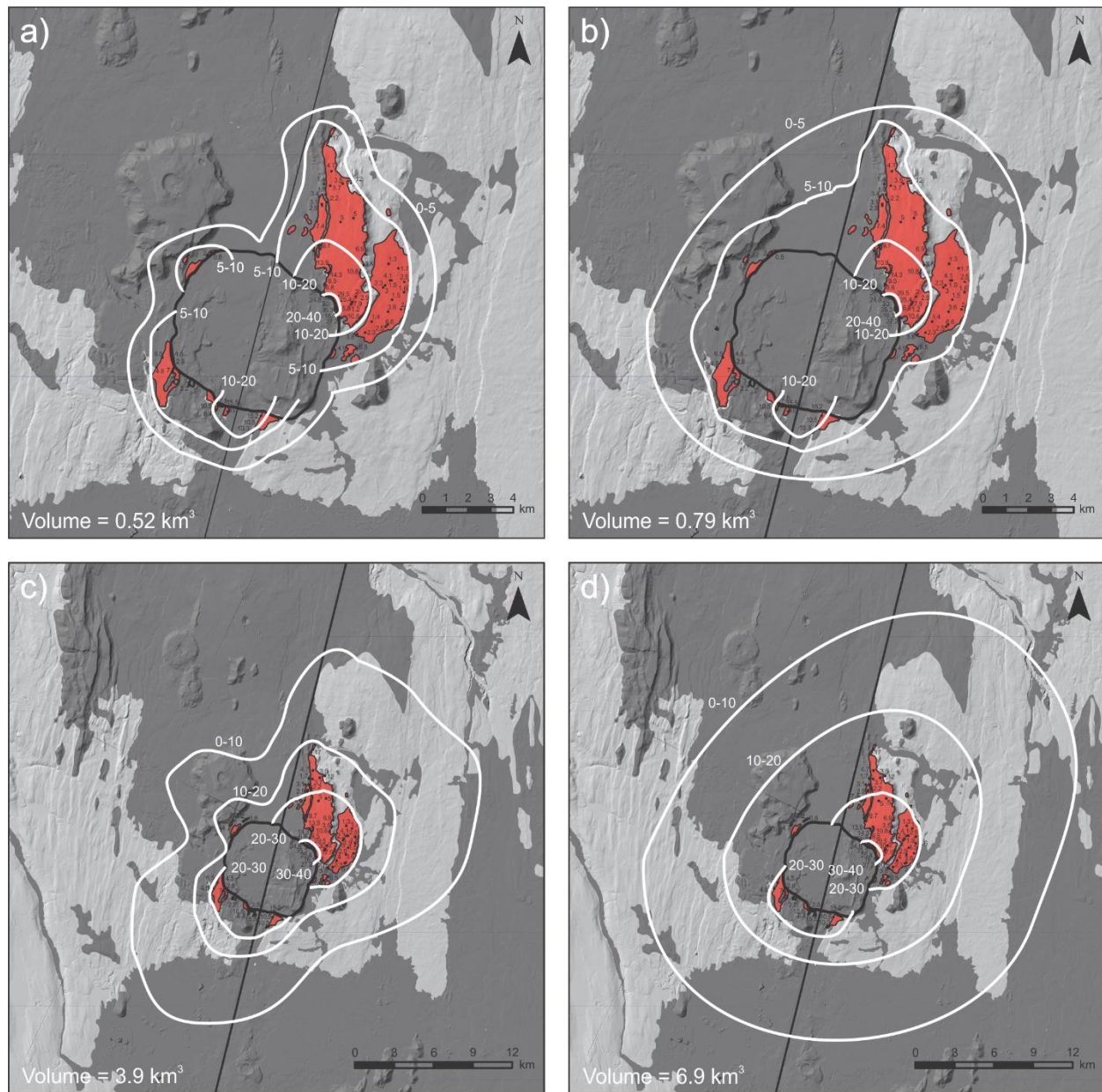
Figure A2.7. Isopachs (white, in meters) for reconstructed original distributions of the Halarauður outflow deposits, assuming a-b) 5 m and c-d) 15 m of glacial erosion. Present-day thicknesses of the full Halarauður sequence are labelled. a) and c) are conservative reconstructions, assuming an original distribution in lobes centered around current outcrops. b) and d) are less conservative, assuming a more radial original distribution. Areas shaded dark grey represent post- Halarauður units (after Sæmundsson, 2008; Sæmundsson et al., 2012) or lakes, which may cover the ignimbrite deposits. To account for post-eruptive spreading of the plate boundary, the area was closed by 2.2 km across the central axis of the fissure swarm (dashed line).

Appendix 3. Supplemental Methods: Rhyolite Petrology

A3.1. Whole-Rock Major Element Analysis – X-Ray Fluorescence Spectroscopy (XRF)

Fresh ~5 mm-sized chips (~50-100 g) were handpicked under a binocular microscope from 49 crushed whole-rock samples. Chips were washed twice with nanopore water in an ultrasonic bath for ~30 minutes, dried overnight in an oven at 60 °C, and powdered in an alumina-ceramic (n = 38) or tungsten-carbide (n = 11) mill. Major element compositions of whole-rock powders were determined by X-ray fluorescence spectroscopy (XRF) in New Zealand at either the University of Waikato (all Halarauður, Víti and Hrafntinnuhryggur samples, plus KR-246 from Hlídarfjall) or the University of Auckland (all Jörundur, Gæsafjallarani and oldest rhyolite samples, and all but one sample from Hlídarfjall). Individual pumice samples from Víti and the Halarauður ignimbrite were too small for XRF analysis, so whole-rock data for these units are combinations of several pumice clasts. For samples analyzed at Waikato, loss on ignition (LOI) values were calculated after heating in a Nabertherm muffle furnace at 1100 °C for one hour. Fusion beads were then prepared in a Claisse Le Neo furnace with a 12:22 ratio of sample to lithium flux, and analyzed with a Bruker S8 Tiger (1kW) XRF spectrometer. For samples analyzed at Auckland, LOI was conducted on all sample powders after heating at 900 °C for 16 h. Fusion beads were made from a 2:1 mixture (by mass) of non-ignited powder and lithium meta (64.7%)/tetra (36.3%) borate fused in a PANalytical Eagon 2 at 1000 °C for 85 min and analyses were performed on a PANalytical Axios XRF spectrometer. Estimates of analytical precision from repeat analyses of in-house and international standard reference materials at both Auckland and Waikato are $\leq$3% relative (2σ) for all major elements (usually < 1% relative). Mean values are accurate to within 5% (usually within 1-2%) of accepted values. LOI values are $\leq$2.1 wt%.

A3.2. Whole-Rock Trace Element Analysis – Solution Inductively-Coupled Plasma Mass Spectrometry (ICP-MS)

Whole-rock trace element analysis was performed by Actlabs (Ancaster, Ontario) on a subset of 22 samples, selected to cover the full range of major element compositions for each unit. For each sample, ~0.5 g of rock powder was fused with a lithium metaborate/tetraborate mix and the resulting molten beads were digested in weak HNO_3. The fusion technique ensures the complete dissolution of refractory minerals, including zircon. Solutions were analysed by inductively-coupled plasma mass spectrometry (ICP-MS). Estimates of 2σ analytical precision based on replicate analyses of RGM-1 standard reference material are <5% relative for all elements excluding Lu (<7%) and Pb (<10%). Measured values for RGM-1 and GSP-2 are accurate to within 10% (usually within 5%) of accepted values, excluding Tb, Dy and Er (within $\leq$13%), Tl and Cu (within $\leq$18%), and Pb (within $\leq$30%). Co and Ta concentrations were elevated for samples powdered in tungsten carbide, so are not reported for these samples.

A3.3. *In-Situ* Mineral and Glass Major and Minor Element Analysis – Electron Probe Microanalysis (EPMA)

Mineral and glass major- and minor-element compositions for each rhyolite were analysed from polished thin sections and/or epoxy grain mounts by wavelength-dispersive spectroscopy (WDS) at the McGill University electron microprobe facility (Montreal, Canada). Calibration was performed using a combination of natural and synthetic standards. Minerals were analysed with a JEOL 8900 electron microprobe using an accelerating voltage of 15 kV (plagioclase, pyroxene) or 20 kV (Fe-Ti oxides, fayalite), beam current of 20 nA (plagioclase) or 30 nA (pyroxene, Fe-Ti

260

oxides, fayalite) and beam diameters of 5 μm (plagioclase and pyroxene) or 1 μm (fayalite and Fe-Ti oxides). Peak and background counting times were 20 s and 10 s, respectively, for all elements except K and Fe in plagioclase (40 s peak and 20 s background). Groundmass glasses and melt inclusions were analysed with a Cameca SX Five FE using a 15 kV accelerating voltage and 10 μm beam diameter. Major elements were analysed with a 2 nA beam current and 20 s peak/10 s background counting times, analysing Na first and applying a zero-time correction for Na, K and Si to correct for any possible Na loss. Minor elements (P, Cl, S and Ti) were then analysed with a 10 nA beam current and peak/background counting times of 60 s/30 s.

Analytical precision (2σ) for EPMA analyses determined by repeat analysis of standard reference materials is <3% relative for elements with concentrations >10 wt%, and <5% relative for elements comprising 1-10 wt% (excluding Na2O, K2O and FeO* in glass; < 12%, <9% and <5%, respectively). Precision is lower but variable for minor elements (<1 wt%). Mean values are accurate to within 1% of reference values for elements present at >1 wt%, excluding Na_2O, Al_2O_3, K_2O and FeO* in glass (within 4%, 4%, 2.5% and 7.5%, respectively).

A3.4. *In-Situ* Glass H_2O Analysis – Confocal Raman Spectroscopy

H_2O contents of glassy plagioclase- and augite-hosted melt inclusions were analysed by Raman spectroscopy at McGill University following methods similar to Di Genova et al. (2017). Spectra were acquired at a depth of 5 μm below the surface of polished, epoxy-mounted samples using a Reinshaw InVia confocal micro-Raman spectrometer equipped with a 532 nm wavelength laser and optical microscope, calibrated daily with a silicon standard. Instrumental settings consisted of a 1200 grooves mm^{-1} grating density, 25 μm slit diameter, 1.5 mW laser power and 100x objective

lens, with an exposure time of 60 s for 5 accumulations. Backscattered Raman radiation was collected over the 200 – 1500 cm^{-1} (LW; low wavenumber) and 2750 – 3900 cm^{-1} (HW; high wavenumber) spectral regions. Spectra were treated using a modified version of the MATLAB code from Di Genova et al. (2017), applying the temperature and excitation line correction of Long (1977) and a cubic spline baseline subtraction. Calibration curves for the linear relationship between glass H_2O content and the ratio of areas under the LW and HW bands were measured daily with a suite of three in-house standards of known water content, independently determined by ion probe.

Appendix 4. Inverse Fractional Crystallisation Models

TABLE A4.1. INVERSE FRACTIONAL CRYSTALLISATION MASS BALANCE CALCULATIONS FOR JÖRUNDUR SAMPLE KR-128

	SiO_2	Al_2O_3	TiO_2	MnO	FeO*	MgO	CaO	Na_2O	K_2O	Total	Density (g cm^{-3})	Modal %	wt% of Fractionated Assemblage
Final Composition: KR-128 (Jörundur)	74.84	12.15	0.31	0.09	3.82	0.16	1.80	4.18	2.64	100			
Plagioclase (An$_{41}$)	59.34	25.62	-	-	0.48	-	8.06	6.21	0.30	100	2.7	4.2	78.3
Titanomagnetite (Usp$_{58}$)	-	1.55	19.98	0.73	77.35	0.39	-	-	-	100	5	0.2	6.9
Augite (Mg# 30)	48.86	0.71	0.33	0.92	25.43	6.10	17.44	0.19	0.01	100	3.4	0.4	9.4
Fayalite (Fo$_{13}$)	30.52	0.01	0.01	1.94	61.77	5.38	0.38	-	-	100	4.4	0.2	3.0
Pigeonite (Mg# 33)	49.06	0.39	0.14	1.24	33.69	11.68	3.77	0.03	-	100	3.4	0.2	2.3
Bulk Composition of Fractionated Assemblage	53.14	20.25	1.41	0.22	10.77	1.04	8.05	4.88	0.23	100			
Starting Composition: 50% Crystallisation	63.99	16.20	0.86	0.16	7.30	0.60	4.92	4.53	1.44	100			
Starting Composition: 40% Crystallisation	66.16	15.39	0.75	0.15	6.60	0.51	4.30	4.46	1.68	100			
Starting Composition: 30% Crystallisation	68.33	14.58	0.64	0.13	5.90	0.42	3.67	4.39	1.92	100			
Starting Composition: 20% Crystallisation	70.50	13.77	0.53	0.12	5.21	0.33	3.05	4.32	2.16	100			
Starting Composition: 10% Crystallisation	72.67	12.96	0.42	0.11	4.51	0.24	2.43	4.25	2.40	100			

TABLE A4.2. INVERSE FRACTIONAL CRYSTALLISATION MASS BALANCE CALCULATIONS FOR VÍTI SAMPLE KR-14-o

	SiO_2	Al_2O_3	TiO_2	MnO	FeO*	MgO	CaO	Na_2O	K_2O	Total	Density (g cm^{-3})	Modal %	wt% of Fractionated Assemblage
Final Composition: KR-14-o (Víti)	74.34	12.52	0.38	0.09	3.62	0.33	1.92	3.92	2.89	100			
Plagioclase (An$_{50}$)	57.28	26.82	0.00	0.00	0.63	0.00	9.42	5.54	0.30	100	2.7	3	82.8
Titanomagnetite (Usp$_{62}$)	0.00	1.82	21.05	0.69	75.71	0.74	0.00	0.00	0.00	100	5	0.2	10.2
Augite (Mg# 50)	50.75	0.98	0.33	0.72	18.81	10.38	17.97	0.18	0.00	100	3.4	0.1	3.5
Pigeonite (Mg# 33)	49.06	0.39	0.14	1.24	33.69	11.68	3.77	0.03	0.00	100	3.4	0.1	3.5
Bulk Composition of Fractionated Assemblage	50.91	22.45	2.17	0.14	10.09	0.84	8.56	4.59	0.25	100			
Starting Composition: 50% Crystallisation	62.62	17.49	1.27	0.11	6.85	0.59	5.24	4.25	1.57	100			
Starting Composition: 40% Crystallisation	64.97	16.49	1.10	0.11	6.21	0.54	4.58	4.19	1.83	100			
Starting Composition: 30% Crystallisation	67.31	15.50	0.92	0.10	5.56	0.49	3.91	4.12	2.10	100			
Starting Composition: 20% Crystallisation	69.65	14.51	0.74	0.10	4.91	0.44	3.25	4.05	2.36	100			
Starting Composition: 10% Crystallisation	71.99	13.51	0.56	0.09	4.26	0.38	2.59	3.99	2.62	100			